TESIS DOCTORAL

FRANCISCO MIGUEL MOREIRA MARTINS FERNANDES

# On the structural and functional properties of sepiolite in polymer-clay nanocomposites and materials derived thereof

Director:

**Prof. Eduardo Ruiz Hitzky**

Dpto de Nuevas Arquitecturas en Química de Materiales

Instituto de Ciencia de Materiales de Madrid (ICMM), CSIC

Dpto. De Química Física Aplicada

Facultad de Ciencias

Universidad Autónoma de Madrid,

Mayo 2011

# Resumen

El estudio de los denominados Polymer-Clay Nanocomposites ( PCN ) remonta a aproximadamente dos décadas cuando Y. Fukushima y otros investigadores de Toyota Research Laboratories lograron por primera vez la polimerización in situ, es decir entre las laminas de arcillas de estructura laminar (esmectitas), partiendo de monómeros intercalados y generando nuevos materiales de aplicación industrial como son las arcillas combinadas con poliamidas. Siguiendo esos pasos distintos grupos desarrollaron metodologías que permitieron intercalar otros monómeros en diversos silicatos laminares e incluso especies poliméricas.

La sepiolita es una arcilla con características morfológicas y texturales marcadamente distintas de las mencionadas previamente. Aprovechando sus dimensiones nanométricas, así como su gran razón de aspecto, distintos estudios han propuesto la introducción de dichas fibras naturales en matrices poliméricas para promover su refuerzo mecánico. Otra caracteristica de gran interés de la sepiolita es su gran disponibilidad de grupos silanoles (Si-OH) disponibles en su superficie. Dichas características ha llevado al desarrollo de forma continuada la modificación de la química superficial de la sepiolita. Dichas modificaciones, basadas sobretodo en la condensación de alcoxisilanos con los grupos silanoles de la sepiolita, permite gran flexibilidad a la hora de preparar materiales híbridos compuestos por fibras inorgánicas (el mismo silicato) que disponen de distintas fracciones orgánicas ancladas en su superficie. Además de la utilización de la sepiolita como agente de refuerzo mecánico en matrices poliméricas, la sepiolita ha sido recientemente utilizada como sustrato para la formación de materiales carbonosos a partir de fuentes de materia orgánica de bajo coste.

Uno de los principales objetivos de esta tesis doctoral fue la determinación de las propiedades mecánicas de la sepiolita a diferentes escalas de ensayo. En este contexto se pudo determinar, mediante la aplicación de técnicas de microscopia de fuerzas atómicas que el módulo elástico de las nanofibras individuales de sepiolita se encuentra sobre los 10 GPa. Sin embargo, el análisis del mismo material a escalas superiores (bloque de sepiolita obtenido directamente de la cantera) reveló un importante efecto de escala sobre sus propiedades elásticas, ya que los módulos determinados son sustancialmente más bajos.

El segundo objetivo planteado fue complementario al primero ya que se cuantificó el aporte mecánico de la sepiolita así como de sus derivados en el contexto de un nanocomposite basado en un polímero de origen biológico (gelatina). Así, se estudiaron dos efectos fundamentales: por una parte el mismo efecto de refuerzo de la matriz polimérica basándose en los valores previamente determinados del modulo elástico de la sepiolita; y por la otra una evaluación del efecto de la introducción de las nanofibras de sepiolita sobre la organización cristalina de la matriz polimérica. Se concluyó que el aporte mecánico impartido por la sepiolita sobre la matriz polimérica de gelatina se relaciona esencialmente con un cambio conformacional de polímero en presencia de las fibras de sepiolita no modificadas.

Un tercero objetivo se centró en la preparación de materiales carbonosos a partir de los híbridos sepiolita-biopolímero preparados en el marco del segundo objetivo. En este apartado se logró preparar materiales conductores basados en una combinación del silicato con la fase carbonosa generada a partir del biopolímero utilizado. Además de lograr conductividad electrónica, el método de preparación de materiales carbonosos soportados sobre la arcilla fibrosa permitió controlar la morfología de las partículas generadas a raiz del efecto

plantilla de la sepiolita. En este apartado de la presente tesis doctoral se desarrollaron materiales de gran utilidad en el refuerzo funcional de distintas matrices poliméricas de aplicación industrial como son por ejemplo las resinas epoxi.

Finalmente el último objetivo de esta tesis doctoral fue el de determinar el papel de las propiedades reológicas de la sepiolita en la preparación de dispersiones acuosas de nanopartículas funcionales como los nanotubos de carbono. La preparación de dichas dispersiones homogéneas compuestas por fibras de sepiolita y nanotubos de carbono multipared (MWCNTs) se planteó como una vía eficaz de lograr la homogeneidad de materiales compuestos por MWCNTs así como de promover el uso de estos en el refuerzo de matrices poliméricas. Se verificó que la dispersión ultrasónica de los MWCNTs en presencia de sepiolita (cuando la concentración de esta última se encuentra por encima de la percolación reológica) es estable durante largos periodos de tiempo. Esta metodología permitió la preparación de materiales híbridos autosoportados provistos de conductividad eléctrica de gran utilidad en la preparación de sensores. Como prueba de concepto se desarrolló un biosensor amperométrico para detección catalítica de peróxidos.

# Figure and Scheme List

# Table list

# Index

# 1. Introduction

This introductory chapter intends to review some of the key concepts that constitute the foundations of the work reported in this dissertation. In first place, general concepts such as nanoparticle or composite are addressed in the context of physical and materials chemistry. These ideas, although mentioned with the required brevity are fundamental as they enclose some of the more specific concepts reviewed subsequently. Secondly, more specific concepts such as hybrid material, nanocomposite and bionanocomposite are disclosed. Being significantly closer to the work reported in this dissertation, these concepts are the object of a more detailed bibliographic analysis, where the main landmarks are briefly reviewed. Finally, the dissertation's main objectives are disclosed.

## 1.1. Nanomaterials

The concept of nanomaterial (alongside with nanotechnology, nanoscience or nanoparticle) is nowadays perfectly established and widely disseminated across many scientific areas. In fact, the boom mediatization of this type of particles, due to the likely benefits that they carry along, has even led the concept to be familiar to the general public. To some extent, such mediatization caused some misuse of the concept based on its marketing power. If such inaccurate use of the concept of nanoparticle is somehow understandable in non-scientific environments, it carries far more importance in the scientific context. To cope with this effect, authoritative definitions are nowadays available from different sources (Hatto, 2008). The most common definition is based on the length of at least one of the dimensions of the particle which should be comprised between 1 and 100 nm.

Different criteria are available to characterize nanoparticles. One of the most widespread relates to the morphology of the particle. Typically the form of nanoparticles is classified into spheres, rods or discs (plates) which can be classified according to the number of dimensions in the nanoscale (Hatto, 2008). Using this definition, spheres (or any low aspect ratio particle) corresponds to three, rods or fibers correspond to two and discs or platelets correspond to one nano-dimension respectively. An alternative way to describe the preceding morphologies is the analogy with geometrical entities such as point, line or plane. Using this approach, a spherical nanoparticle is considered as a point and therefore as a dimensionless entity (0D), while nanofibers and nanorods are considered as equivalent to lines (1D) and plate like nano-objects as two-dimensional entities (2D). This work uses the first definition where the number of dimension in the nanoscale defined the “nanodimensionality” of the particle.

Other important concepts when considering nanoparticles regards the chemical nature of the particle. A brief outlook of the bibliography related with nanoparticles renders quite diverse chemical nature for these materials. Gold nanoparticles, for instance, are one of the most common and versatile metallic NPs (Daniel and Astruc, 2003). Also metal oxides can be found found in the form of nanoparticles as the case of magnetite (Burgos-Asperilla, Darder et al., 2007). Other nanoparticles frequently found in the literature are of carbonaceous (Iijima, 1991) or siliceous nature (Caruso, 2001). Putting it brief, practically all solid materials can be found in the form of nanoparticles.

As can be deduced from the above definition, nanoparticles are, in most cases, not necessarily related to high-technology materials. They are just small particles! One can find nanoparticles from the exhaust smoke of combustion engines (Kittelson, 1998) to the decorative stained glass in the windows of medieval European churches (Daniel and Astruc, 2003).

### 1.1.1 Size matters!

The statement that nanoparticles (NPs) are just small particles, might seem an oversimplification, especially when confronted with the common attributes usually associated with NPs (enhanced reactivity, electronic, magnetic, thermal, mechanical or optical properties). But in fact, the main difference between most materials and nano-particulate materials is their size. However, the effects of reducing the size of a particle enclose more consequences than those expected in a first consideration. A simple exercise, considering the relationship between the volume of one material in the form of spheres and the correspondent surface area as a function of the radius of the sphere, is paradigmatic. One cubic meter composed of compact spheres of a given material with a radius of 10 cm yields a surface area of 30 $m^2$, on the other hand, the same volume composed of spheres with 10 nm corresponds to a surface area of $3x10^8$ $m^2$.

This simple example demonstrates how the dimension of a particle is related to the specific surface area. It is not difficult to imagine that the interface phenomena taking place on this material's surface will not occur in the same manner (or at least with the same intensity) in the finely divided material as in the bulk material. Another feature that derives from the reduction in the size of a particle is the variation in the relative importance of the forces to which it is submitted. For a sphere with radius equal to 10 cm the Van der Waals forces established with a similar sphere are irrelevant as they are not comparable with gravitational force. However, if the radius reduces significantly (and the specific weight is maintained), the surface phenomena gain importance and the referred Van der Waals forces might have a significant impact on the aggregation state with similar nanoparticles.

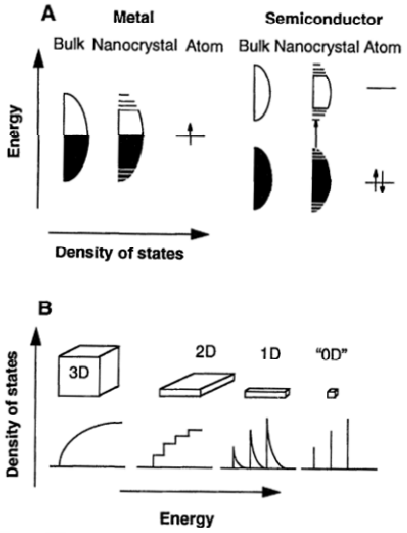


**Figure 1.1 –** Schematic representation of the changes in enegetic states of materials as a function of their dimensionality. A) Schematic illustration of the density of states in metal and semiconductor clusters. B) Density of states in one band of a semiconductor as a function of dimension. Reproduced with permission from AAAS from reference (Alivisatos, 1996).

Another relevant effect of reduced size (especially in metallic and semiconductor nanoparticles) is the progressive discretization of energy levels associated with the corresponding electrons when compared with bulk as

depicted in figure 1.1. The seminal work by Alivisatos firstly described NPs as a transition state of matter between the continuous valence band typical of bulk materials and the single energy level typical of the atomic scale (Alivisatos, 1996).

This effect is of paramount importance in the use of nanoparticles as it permits to fine tune the electronic (optical, conducting, etc.) properties of the materials by a precise control of their size and morphology. A revealing example is that of metal nanoparticles whose size and shape are used to tailor the surface plasmon band and consequently the chromatic aspect of the resulting colloids (Liz-Marzán, 2005).

The specific surface area and the electronic properties of NPs are important but insufficient examples of how the physical and chemical properties of materials scale with particle size. The deep understanding of such scaling laws is the keystone to fully explore the potentialities of nanoscale materials (Ozin and Arsenault, 2005).

### 1.1.2 Top down vs. bottom up

Another fundamental idea behind the use and understanding of nanoparticles is the methodology employed to achieve them. The two main approaches are those of *top down* and *bottom up* (Ozin and Arsenault, 2005). The first refers to a strategy in which nanomaterials are obtained by systematically dividing bulk materials into nanosized objects. Richard Feynman's laid ground for this approach in his inspired talk "*There is plenty of room at the bottom*" back in 1959 (Feynman, 1960). In such communication he conjectured the possibilities inherent to the size reduction of materials. In fact, his talk stands as the first description of one half of nanotechnology as we know it nowadays.

The **bottom up** approach is the flip side of the coin to Feynman's engineering based approach. It was introduced later by several other researchers. Among

them, Heinz A. Lowenstam (Lowenstam, 1981; Lowenstam and Weiner, 1989), Jean Marie Lehn (Lehn, 1988) and George M. Whitesides (Whitesides, Mathias et al., 1991) offered a new vision on materials science and nanotechnology, its basic mechanisms, and most of all how nanomaterials can be built based on a completely diverse strategy from the proposed by Feynman. The first brought into play concepts like the interactions between biopolymers and minerals in the construction of complex biomineral architectures in living organisms while the last focused on supramolecular chemistry and self-assembly. Their approach is based on the construction of complex materials based on the assembly of molecular or macromolecular building blocks (Ruiz-Hitzky, Aranda et al., 2011). Other complementary concepts such as *crystal engineering* or *molecular architecture* were also developed aiming at predetermining hybrid materials properties from their synthetic procedures (Ruiz-Hitzky, 1988). In fact, modern materials science heavily relies in these approaches. They provide the understanding of how simple and small building blocks can generate complex hierarchical architectures that cope with extreme service requirements (Fratzl and Weinkamer, 2007).

## 1.2 Composites

A material resulting from the combination of two or more materials in which at least one of them forms a continuous phase is commonly called a composite material. Historically, bringing two different materials together in order to obtain a final material that combines the properties of both or, in some cases displays synergistic behaviour, has been a universal strategy. Most of the construction techniques, ancient and new, across the globe rely on composites. Paradigm examples are adobe, a mixture of dry mud and straw assembled into a stable and durable construction material (Moropoulou, Bakolas et al., 2005).

Historically the production of composites was closely related to the improvement of the mechanical properties of the materials (Bledzki and Gassan, 1999; Wan, Wang et al., 2000; Liu, Barber et al., 2005; Moropoulou, Bakolas et al., 2005; Coleman, Khan et al., 2006a; Xie, Zhang et al., 2007; Bhattacharya, Maiti et al., 2009; Fernandes, Ruiz et al., 2009). Nevertheless, recent developments have proved that the same strategy used for centuries to improve the mechanical properties of construction materials was also effective in enhancing some functional properties such as fire resistance (Ruiz-Hitzky, Aranda et al., 2010), gas barrier properties (Sinha Ray and Bousmina, 2005), electrical conductivity (Fernandez-Saavedra, Darder et al., 2008), among other properties.

### 1.2.1 Structural organization

An analysis of the structure of composites leads to two main concepts, the continuous and the disperse phase. These constitutive elements are briefly analyzed in the following sections.

*a) Continuous phase – metals, ceramics and polymers*

The continuous phase consists, as the name indicates, on a phase within the composite which spans throughout the entire volume of the sample in a continuous manner. In general, such phase is considered as the matrix, whose properties are to be improved by the addition of another (or more than one) disperse phase. It is also important to note that being the continuous phase or the matrix is not necessarily related to being the biggest material fraction in the composite, even if these two separate features coincide frequently.

There is a multitude of examples of matrices which have been used in the form of composites, from metals to ceramics. Although metals are more commonly

reinforced by the addition of another metal with the consequent formation of an alloy, several examples refer to metal matrix composites where metals such as titanium (Mileiko, Rudnev et al., 1995) or aluminum (Kamrani, Hesabi et al.) are reinforced with carbon fibers or SiC particles. Also ceramic materials such as alumina (Sun, Gao et al., 2002), silica (Gong, Zhang et al., 2004) or titanium dioxide (Gao, Chen et al., 2009) have been reinforced using a composite approach.

Nevertheless, most metal and ceramic matrices possess quite satisfactory properties (especially mechanical) which leads to the fact that its use in composite materials is practically restricted to the improvement of their functional properties. Polymers, on the other hand, also possess very interesting properties such as low density and relatively easy processing technology. However their mechanical properties are in general poor when compared to most structural materials (metal alloys, ceramics, etc.). In an effort to maximize their mechanical properties (Young's modulus, tensile strength, strain at break, etc.) these materials have been systematically reinforced with other particles.

The first systematic attempt to produce polymer based composites seems to arise together with the mass production of polymers as a structural material. Nowadays there is no restriction regarding which polymers may serve as a continuous matrix in composites, from thermosetting resins to thermoplastics.

*b) Disperse phase - straw, glass and carbon*

The disperse phase (commonly called as *filler*) regards the particles introduced in a continuous matrix that intend to improve a given property of a material. Historically many types of particles have served as fillers in numerous types of matrices. Some of the most ancient examples consist on the dispersion of fibers of biological origin such as straw, hemp or flax fibers (John and Thomas, 2008).

In fact these materials are recently resurging as alternatives to synthetic reinforcing fibers. The main advantage related to the use of these materials relates to their excellent mechanical properties. Such mechanical properties derive mainly from the Young's modulus of cellulose crystal that compose them, which have been determined to be close to 140 GPa (Sturcová, Davies et al., 2005).

Also inorganic fillers have been widely used in the reinforcement of polymeric matrices. One of the most notorious is glass fiber that has been applied to a variety of polymers from polycarbonate to epoxy resins improving both the elastic modulus and tensile strength (Laura, Keskkula et al., 2000; Cheng, Xue et al., 2002; Zheng, Zhang et al., 2003; Chang and Chow, 2010). Also carbon fiber has been widely applied in the context of mechanical reinforcement of polymeric compounds. In fact, using carbon fiber also yields conductive composites once a percolating network of conductive fibers is formed, which is of great utility in many applications (Hammel, Tang et al., 2004).

### 1.2.2 Mechanics of composite materials

As mentioned before, one of the major goals in preparing composites is to enhance the mechanical properties of the resulting material. Among the different mechanical properties that describe the structural behavior of a given material, the elastic modulus is possibly the most relevant parameter.

The mechanical properties of nanocomposites, especially the elastic properties, can be predicted from a wide number of composite models. These seek to explain and predict how factors such as the matrix elastic modulus, filler elastic modulus, filler aspect ratio, filler concentration and filler packing efficiency (in oriented reinforced composites) influence the composite modulus. A brief selection of some elastic properties composite models leads us to explore three simple yet paradigmatic composite models based on the mean field theory. The

first of such is the Rule Of Mixtures (ROM), followed by the Inverse Rule Of Mixtures (IROM) and the Halpin-Tsai Model (HT). There are other models which aim at explaining the mechanical behavior of composite materials such as the Mori-Tanaka model (Mori and Tanaka, 1973) or the Hashin-Shtrikman bounds (Hashin, 1983). However such models will not be addressed as a comprehensive analysis of all models is both long and, in most cases, redundant (as many of the models are based in similar assumptions). ROM and IROM models define the physical boundaries of the elastic modulus of composite materials as compared to its components elastic modulus. The ROM model (eq. 1.1) assumes that the elastic properties of the composite scale linearly with the volume fraction of each component.

$$E_c = E_f \phi + E_m (1 - \phi) \qquad \text{(eq. 1.1)}$$

where $E_c$ stands for the composite modulus, $E_m$ stands for the matrix moduls, $E_f$ stands for the filler modulus and ϕ stands for the filler volume fraction.

The flip side of the coin to the ROM model is the IROM model (eq. 1.2) where the composite modulus scales inversely with the volume fraction of each component.

$$E_c = \left( \frac{\phi}{E_f} + \frac{(1-\phi)}{E_m} \right)^{-1} \qquad \text{(eq. 1.2)}$$

The derivation of these two simple models that explain the behavior of the elastic properties of composites is based on very simple assumptions which are presented briefly in figure 1.2.

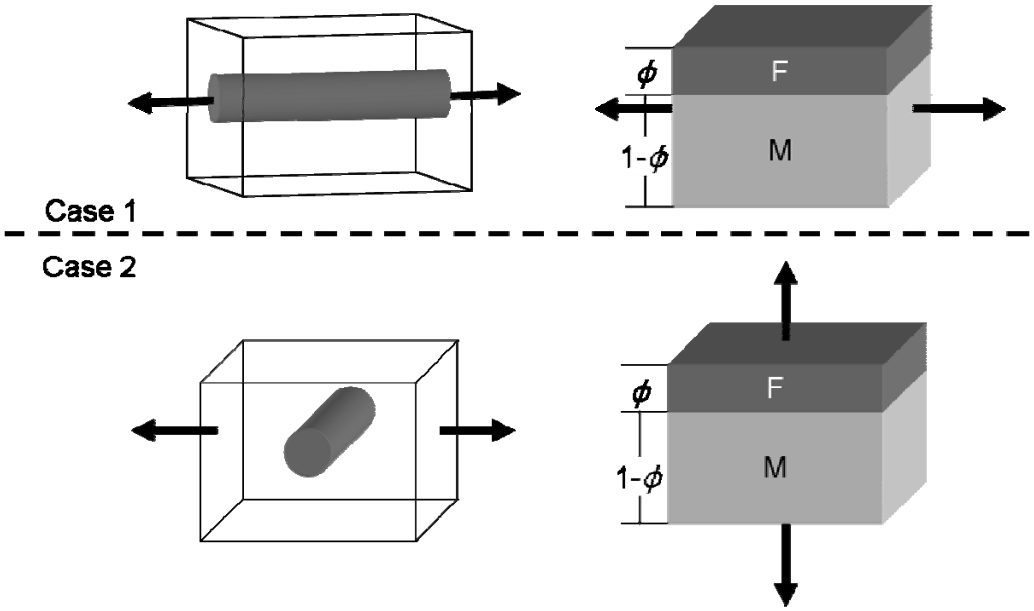


**Figure 1.2 –** Schematic representation of two situations where a high aspect ratio filler reinforced composite is submitted to traction. The left diagrams represent the orientation of the filler with respect to the loading direction and the right diagrams represent the mechanical analogy showing the filler (Φ) and matrix (1-Φ) fraction. Case 1 corresponds to axial loading and case 2 to transverse loading.

Taking into account that the elastic modulus is a measure of the elasticity of a material in its elastic regime, the Hooke's law relation between stress and strain hold (eq. 1.3),

$$\sigma = E\varepsilon \qquad \text{(eq. 1.3)}$$

where σ corresponds to the stress, E to the elastic modulus and ε to the strain. Assuming that both phases are totally adhered to each other and therefore there is no slippage between them; and assuming also that in case 1 the total strain is common to the two phases ($\varepsilon_c=\varepsilon_m=\varepsilon_f$), and the total stress ($\sigma_T$), which is force per unit area, corresponds to the sum of stresses of fraction A and B (eq 1.5), comes

$$\varepsilon_c = \varepsilon_m = \frac{\sigma_m}{E_m} = \varepsilon_f = \frac{\sigma_f}{E_f} \qquad \text{(eq. 1.4)}$$

$$\sigma_c = (1-\phi)\sigma_m + \phi\sigma_f \qquad \text{(eq. 1.5)}$$

Combining equations 1.3 and 1.5 results in equation 1.6, which can be further simplified to the form presented in equation 1.1.

$$E_c\varepsilon_c = (1-\phi)E_m\varepsilon_m + \phi E_f\varepsilon_f \quad \text{(eq. 1.6)}$$

The IROM (depicted in case 2, Fig. 1.2) is based on a similar argument. In that case, the equal stress assumption has to be made (eq. 1.7).

$$\sigma_c = \sigma_m = E_m\varepsilon_m = \sigma_f = E_f\varepsilon_f \quad \text{(eq. 1.7)}$$

On the other hand the composite strain is given by,

$$\varepsilon_c = (1-\phi)\varepsilon_m + \phi\varepsilon_f \quad \text{(eq. 1.8)}$$

Combining equations 1.7 and 1.8, comes that the composite modulus according to the IROM is given by equation 1.9, that can be further simplified to the form exposed in equation 1.2.

$$E_c = \frac{\sigma_c}{\varepsilon_c} = \frac{\sigma_f}{(1-\phi)\varepsilon_m + \phi\varepsilon_f} \quad \text{(eq. 1.9)}$$

The preceding models (ROM and IROM) stand as natural limits of the reinforcing behavior of composites.

The other, and slightly more complex, model is the HT model (Halpin and Kardos, 1976). It has been developed by Halpin, Tsai and Kardos and aims at explaining the mechanics of composites based on the same factors, filler volume fraction, matrix and filler modulus but takes into account the filler aspect ratio. Equation 1.10 reproduces the HT model for aligned fibers.

$$E_c = \left( \frac{1 + 2\alpha\eta\phi}{1 - \eta\phi} \right) E_m$$
$$\eta = \frac{Ef\ /\ Em - 1}{Ef\ /\ Em + 2\alpha} \qquad \text{(eq. 1.10)}$$

Where α corresponds to the filler aspect ratio. One interesting feature of the HT model is that it reduces simply at interesting limits (Schaefer and Justice, 2007). For instance in the dilute stiff fiber limit ($\phi << 1$, $E_f >> E_m$), the equation reduces to:

$$\frac{E_c}{E_m} = 1 + 2\alpha \left( \frac{E_f / E_m}{E_f / E_m + 2\alpha} \right) \phi \qquad \text{(eq. 1.11)}$$

On the other hand, in the long fiber limit ($2\alpha >> E_f/E_m$) the resulting equation reduces to the ROM (eq. 1.1). In the dilute short fiber limit ($\alpha << E_f/E_m$), equation 1.11 becomes independent of the fiber elastic properties (eq. 1.12).

$$Ec = (1 + 2\alpha\phi) E_m \qquad \text{(eq. 1.12)}$$

A brief analysis of the equations displayed above as well as its limits renders a clear picture of the key factors behind an effective reinforcement of polymer matrices. The first idea is that the volume fraction of the filler plays a critical role in the enhancement of the elastic properties. Moreover, the filler aspect ratio is decisive in improving such properties as can be observed in equation 12, where the composite elastic modulus becomes independent of the elastic properties of the filler when low aspect ratio fillers are used. Another critical parameter is the relation between the filler and matrix mechanical properties.

### 1.2.3 Recent developments – Nanocomposites

The composite examples mentioned previously (§ 1.2) are well known, and the majority of them find place in day-to-day life. Equally, the referred composite

theories are well established and in some situations regarded as standard predictive models in costume-designed composites. However, the advent of nanomaterials, mentioned earlier (§ 1.1) induced a dramatic change in composite materials. The rationale behind such evolution in composites (called *nanocomposites* when nanofillers are used instead of the common fillers) was that using nanosized materials as fillers, the reinforcement efficiency would be maximized. There are two main reasons behind such effect. The first is the acknowledgement that besides the factors described before, the reinforcement of polymeric matrices was also dependent on the interface between the polymer and the filler. In that sense, the reduction of dimensions of the filler would account for a tremendous enhancement of the contact area between the continuous and disperse phases (see example relating particle size and specific surface area, § 1.1.1). This reason opened way to the so called *Polymer-Clay Nanocomposites* (PCN). The other reason is the discovery of materials such as *carbon nanotubes* (CNT) and *graphene* with extraordinary mechanical and functional properties. These two directions in the production of nanocomposites are addressed separately in the following sections.

*a) Polymer-Clay Nanocomposites, PCN*

The development of PCNs is the turning point in the approach towards modern composites. Nevertheless, a thorough description of the fundamental concepts behind the use of layered silicates such as *montmorillonite* in the reinforcement of polymer highly depends on a huge amount of work previously initiated with this type of layered materials, clay-organic hybrids (Theng, 1974; Aranda, Serratosa et al., 2004; Bergaya, Theng et al., 2006)! The first reports describing the introduction of an organic moieties of diverse nature into sodium montmorillonite ($Na^+$ MMT) were by Gieseking (Gieseking, 1939), Hendricks (Hendricks, 1941), MacEwan (MacEwan, 1946) and Bradley (Bradley, 1945).

Talibudeen reported the formation of complexes between proteins and the layered silicate (Talibudeen, 1950; Talibudeen, 1955). Later other authors such as Brindley, Serratosa, Martland, Ruiz-Hitzky, Detellier, Cloos, Kuroda and Ogawa published extensive work on clay-organic interactions regarding the adsorption of diverse organic molecules into the interlamellar space of montmorillonite and other layered clays. From that point onwards, the interest in the structures formed by the intercalation of layered inorganic species and organic moieties spread radially, with the focus laid on the adsorbed (or guest) species. Several authors devoted their research to the adsorption of polymeric species reaching extended basal spacing in the modified layered structure due to the presence of the polymer chains (Theng, 1979). Another field of research related to the intercalation of organics species into natural clays was the formation molecular assemblies (mainly by using surfactants) to promote a controllable variation of the basal spacing of the modified clays (Jordan, 1949; Jones, 1983). Other authors have centered their research on the intercalation of functional species as conducting polymers like polyethylene oxide or macrocyclic compounds like crown ethers which found use in electrochemical applications (Ruiz-Hitzky and Aranda, 1990; Aranda and Ruiz-Hitzky, 1992; Ruiz-Hitzky, 1993).

Blumstein was the first to report the adsorption and *in-situ* polymerization of a monomer (methyl methacrylate, MMA) inside the galleries of a natural montmorillonite (Blumstein, 1965). Nevertheless the most important breakthrough in the development of nanocomposites was impelled by the work developed at the Toyota Research Labs group headed by Y. Fukushima, who have successfully polymerized polyamide 6 in the interlayer space of a homoionic MMT achieving at the same time the exfoliation of the clay layers (Fukushima, Okada et al., 1988; Kojima, Usuki et al., 1993; Usuki, Kojima et al., 1993). The preparation proceeded through the intercalation of 12-aminolauric acid into the clay layers, followed by the mixture of the modified MMT with ε-

caprolactone. This approach permitted for the first time to prepare a fully exfoliated nanocomposite where the contact between the polymer and the clay lamellae surface was maximized with an important effect on the mechanical properties. In fact, the close interaction between the exfoliated clay layers and the polymeric matrix has also led some thermo-mechanical properties such as heat deflection temperature (HDT) to be greatly improved (Kojima, Usuki et al., 1993). The introduction of the clay onto the polyamide also meant increased gas barrier properties due to the tortuous path imposed on the diffusing molecules by the clay platelets dispersed on the matrix (Yano, Usuki et al., 1993).

Other layered inorganic systems such as kaolinite, Layered Double Hydroxides (LDH) or polysilicates have also been used as host species for the intercalation of organic moieties and subsequent exfoliation into polymer nanocomposites (Pinnavaia and Beall, 2000; Leroux and Besse, 2001). Similarly the guest species and the polymer matrix have been systematically studied generating a wide array of materials (LeBaron, Wang et al., 1999; Pinnavaia and Beall, 2000), some of which are presently in the market (Ruiz-Hitzky and Van Meerbeek, 2006).

*b) Carbon Nanotubes*

The reinforcement of polymeric matrices using carbon materials such as carbon fibers and carbon black has long been used in the modification of the properties of polymeric matrices, namely thermosetting resins (Mizutani and Iwatsu, 1980) and rubbers (Parkinson, 1951), respectively. However the definitive breakthrough in achieving high efficiency nanocomposites was linked to the discovery of Carbon Nanotubes (CNTs) (Iijima, 1991; Monthioux and Kuznetsov, 2006) and their mechanical properties (Salvetat, Bonard et al., 1999; Salvetat-Delmotte and Rubio, 2002). The report on these structures

produced huge expectations since nanotubes seemed to condense very interesting and diverse properties. Just after their discovery, CNTs were presented as a mixture of the chemistry of fullerenes, the conductivity of graphite and the Young's modulus of diamond. In fact, CNT's properties have actually surpassed those predictions. Some of the outstanding properties of CNTs are summarized in review articles such as the one published by Dresselhaus and co-workers (Dresselhaus, Dresselhaus et al., 2004). The preparation of nanocomposites based on CNTs as filler is, however, a matter which is not exempt of difficulties. The first report on CNT-polymer nanocomposites is by Ajayan and coworkers (Ajayan, Stephan et al., 1994), who after dispersing multi-walled carbon nanotubes CNT in a commercial epoxy resin matrix, microtomed the nanocomposite inducing some orientation of the filler with respect to the polymer matrix. Although exceptionally relevant in the context of CNT-based nanocomposites, the mentioned report was more focused in establishing a manner to orient the CNTs to measure their mechanical properties, not the composite's. Naturally, the development in nanocomposites using CNTs has evolved dramatically since that report. Nevertheless, there are some difficulties and inconsistencies. Dispersing CNTs in a polymer matrix is difficult due to CNT's low surface energy responsible for the difficulties in dispersing them in polymeric matrices. Several processing methods have been used to attain good dispersion in CNT-based thermoplastic nanocoposites. The most common is solvent casting (Cadek, Coleman et al., 2002) alongside with melt processing (Manchado, Valentini et al., 2005) and other techniques such as in-situ polymerization and extrusion or injection (Coleman, Khan et al., 2006b). Paired with the improvement in the mechanical properties, the electrical properties can also be significantly improved by the addition of CNTs. Although there is considerable scattering regarding the percolation threshold due to differences in composite processing, nanotube type (single or multi-wall) and nanotube production method (arc discharge, chemical

vapor deposition, laser vaporization), the electrical properties can be tailored to attain conductive materials based on insulating polymeric matrix (Bauhofer and Kovacs, 2009).

Apart from the mechanical reinforcement and electrical conductivity, other properties can be explored using CNT-based nanocomposites. Some of the most interesting examples regard the preparation of electromechanical actuators (Baughman, Cui et al., 1999) or electrochemical sensors (Xu, Zhu et al., 2003; Merkoci, 2006; Lin, He et al., 2009; Qureshi, Kang et al., 2009; Jacobs, Peairs et al., 2010).

## 1.3 Bionanocomposites

Bionanocomposite is a newly defined concept (Ruiz-Hitzky, Aranda et al., 2008; Ruiz-Hitzky, Darder et al., 2010) describing a wide range of materials, natural and synthetic, old and new, functional and structural. The word itself is self explanatory (etymologically), being the prefix *bio* attached to the concept of biological origin, application or inspiration, the prefix *nano* describing the dimension of (typically) the disperse phase, and *composite* describing the hybrid and multiphase character of such materials. A brief analysis of the group of materials comprised in the wide definition provided by the term itself renders two main divisions, *Natural bionanocomposites* and *Synthetic bionanocomposites*. The following sections aim at unveiling the main features and potentialities of these materials, trying to establish the natural comparison between the inspiring materials (bone, nacre, etc.) and the new materials that try to mimic them in both architecture and function.

### 1.3.1 Natural bionanocomposites

Biomineralization is a central biological phenomenon in the synthesis of structural and functional hybrid materials by living organisms. The first global view (not the first report on biomineralization) at this phenomenon was reported by Lowenstam who systematically analyzed the different inorganic materials synthesized by living organisms, from vertebrates to diatoms (Lowenstam, 1981). The paper attempted to find some common ground in the different biomineralization processes and proposed a general scheme for the interaction of the organic and the inorganic phases. Other authors followed this route trying to clarify the mechanisms behind the formation of each crystal phase but also aiming at elucidating the mechanism controlling the formation of such complex architectures (Addadi and Weiner, 1985; Addadi and Weiner, 1986; Mann, 1986b; Mann, 1986a; Mann, Hannington et al., 1986; Lowenstam and Weiner, 1989; Franckel and Mann, 1994; Xu, Ma et al., 2007).

At first sight, the strategies behind the formation of such complex and diverse materials seem to be similar to each others. However, in these processes, the different living organisms secrete different biomacromolecules that act as organic templates for the nucleation and growth of the inorganic counterpart (carbonates, phosphates, silica, and iron oxide). The differences in the secreted macromolecules and the available ions seem to control the wide variety of final materials obtained, as well as the corresponding architectures (Ruiz-Hitzky, Aranda et al., 2008).

A wide array of natural bionanocomposites is available in Nature. Some of the most interesting are eggshell, bone, enamel, fish scales, antler, nacre or the siliceous diatom exoskeleton. As a full overview covering all of these structures is impractical, two examples are addressed. On the one hand bone, possibly the most complex hierarchical bionanocomposite serving both a structural and functional role. On the other hand nacre, the paradigmatic example of layer-by-

layer material possessing a simple yet highly efficient brick and mortar architecture and serving as a structural bionanocomposite designed to protect abalone from mechanical action.

*a) Bone*

Bone is one of the most complex natural bionanocomposite present in Nature. It is composed of hydroxyapatite (HAP) nanocrystals organized along a collagen matrix which together, form the bone's basic building block, the mineralized collagen fibril (Fratzl, Gupta et al., 2004). This structure is composed of highly oriented collagen triple α-helixes associated with nanosized HAP crystals which are placed in a staggered form between adjacent collagen molecules. The period characterizing the displacement of one inorganic moiety associated with one collagen triple helix from the adjacent is around 67 nm (Fratzl, Gupta et al., 2004). Another important structural feature in bone is the size of the HAP crystal that has been reported to be between 2 and 4 nm in thickness, and in the order of tens of nanometers in both width and length. An array of parallel mineralized collagen fibril composes the collagen fiber which, in turn, is the building block of bone lamella. These last structures are organized in a concentric manner around Harvesian channels forming osteons. In summary, bone is organized in a hierarchical fashion from the basic building block, the mineralized collagen triple helix (Rho, Kuhn-Spearing et al., 1998).

A remarkable characteristic of bone is the huge variety in form, density, organization and other characteristics that it is capable of displaying although it is essentially built from this same building block throughout the majority of species. A simple visual inspection of a human femoral head demonstrates the diversity in architecture that can be attained in bone within the same organ. It displays a compact outer shell named (compact or cortical bone) and a foam-like spongy interior (named trabecular or cancelous bone) with distinct

structures, functions, apparent densities and mechanical properties. Compact bone for instance, presents as the name indicates, a denser structure with highly anisotropic mechanical properties. The stiffness for this type of bone structure is substantially higher than that of the spongy part. Along the principal direction of the collagen fibers, compact bone presents an elastic modulus around 25 GPa, whereas in the transverse direction it usually lies around 16 GPa (Fratzl, Gupta et al., 2004). The mechanical behavior of trabecular bone is more isotropic and presents a much lower stiffness (although a high degree of variability is reported in the literature) (Rho, Kuhn-Spearing et al., 1998; Fratzl, Gupta et al., 2004). The main structural function is to support compression forces by dissipating the stress across its structures. In fact the amount and nature of stress applied to bone is determinant in modeling and remodeling trabecular bone, as it will adapt to the typical stress lines providing effective stress distribution.

The composite behavior of bone is therefore a compromise, maintaining a high (though lowered) stiffness, while enhancing the fracture strain from pure mineral about 10-fold. Putting it brief, bone is stiff like HAP but also tough like collagen (Fratzl, Gupta et al., 2004).

The other central aspect of bone is related to its functionality. To address this matter (even if briefly) it is fundamental to understand that bone is usually formed by 50 to 74 % (w/w) HAP being the rest practically all collagen and water, other entities play a determinant role in bone formation and maintainance, cells. Osteocytes, osteoblasts and osteoclasts are the main type of cells responsible for the regulation between bone formation and bone resorption and also for the balance of the oxygen levels inside bone lacuna.

*b) Nacre*

Another paradigmatic material fitting the natural bionanocomposite materials classification is nacre. Nacre is the structural bionanocomposite material from which abalone shell formed. It is composed of aragonite platelet-crystals bound together by a thin layer of proteins and polysaccharides such as conchiolin, lustrin, chitin, etc (Ruiz-Hitzky, Aranda et al., 2008). One of the most distinct features is the regular pattern that characterizes the microstructure of nacre (Ruiz-Hitzky, Aranda et al., 2008; Dunlop and Fratzl). Figure 1.3 depicts the typical brick and mortar structure of nacre.

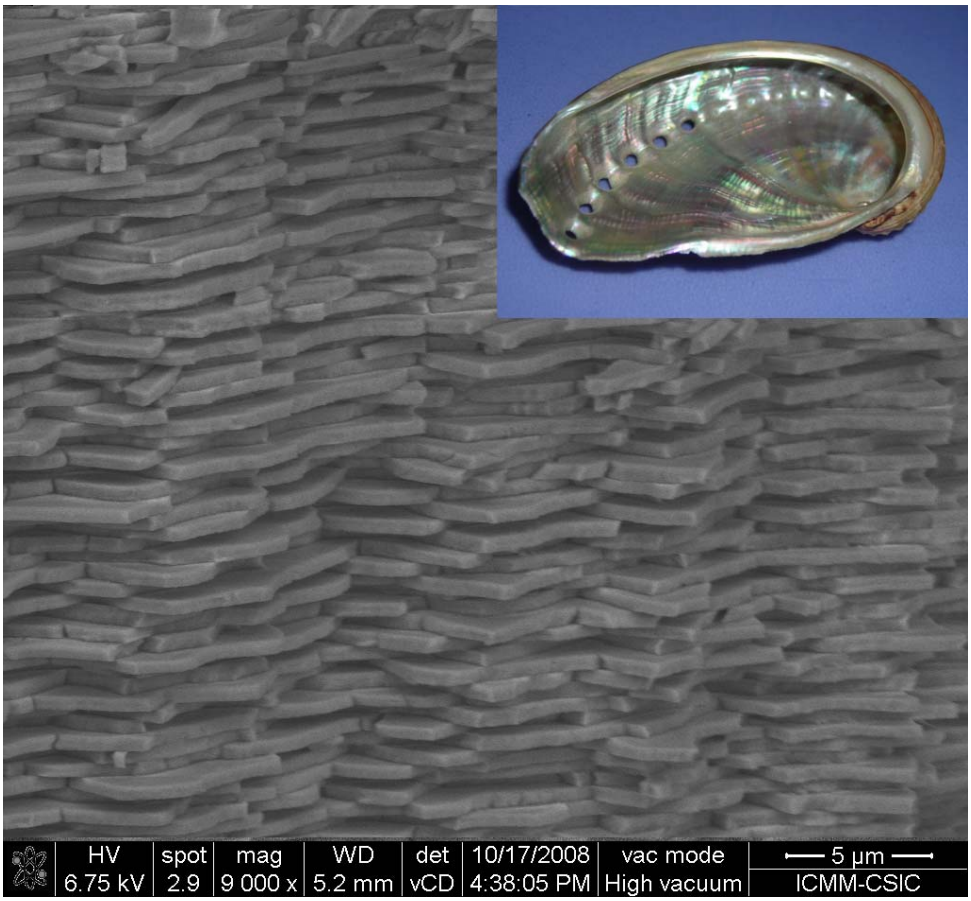


**Figure 1.3 –** FE-SEM micrograph of nacre from abalone shell displaying the aragonite crystals stacked in brick and mortar geometry. The inset shows a macroscopic image of the same abalone shell (*Haliotis sp.*).

Several mechanisms were suggested to describe the mechanical properties of nacre (especially the deformation mechanisms) (Wang, Suo et al., 2001; Ji and

Gao, 2004; Li, Chang et al., 2004). The cooperativeness between the polymeric layers and the aragonite platelets yields elastic modulus values ranging between 60 and 80 GPa (Li, Chang et al., 2004). These values are consistent with the elastic modulus of the constituents and their volume fraction (Ji and Gao, 2004). However it is especially interesting to note that the tensile strength of nacre is not a cooperative effect between the net tensile strengths of aragonite crystals and the proteinous layer. In fact nacre exhibits a synergetic behavior in tensile strength as its value (100-300 MPa) is clearly superior to each of components tensile strength (20 and 30 MPa for protein and mineral respectively) (Ji and Gao, 2004).

The most surprising feature in nacre is the simplicity of the hybrid nanostructure paired with the dramatic improvement of the mechanical properties when compared with the composing phases.

### 1.3.2 Synthetic bionanocomposites

Synthetic bionanocomposites are expanding rapidly. This class of materials is the result of the understanding that the lessons from nature in designing materials (as seen in the natural bionanocomposites) are valuable and enclose strategies that had not been explored before (Bensaude-Vincent, Arribart et al., 2002; Sanchez, Arribart et al., 2005). Even if these materials are inspired by the natural counterparts, they benefit from a wider range of raw materials. Natural bionanocomposites are, in general restricted to a few biopolymers such as proteins and polysaccharide and some minerals (Dunlop and Fratzl, 2010). Synthetic bionanocomposites benefit from a wider range of biopolymers and minerals, giving place to a wide and highly unexplored array of possible combinations (Ruiz-Hitzky, Darder et al., 2010). The following sections refer to some of the most interesting combinations between biopolymers and inorganic phases such as silica, clay minerals, carbonates, phosphates and CNTs. Also

the range of application of this class of materials is widespread. Each of the sections will be accompanied by some applicative examples where specific bionanocomposites have been designed for a specific function.

*a) Clay-based bionanocomposites*

Several clay minerals have been used in the preparation of bionanocomposites. Following to some extent the work on traditional polymer-clay nanocomposites (Fukushima, Okada et al., 1988; Kojima, Usuki et al., 1993; Usuki, Kojima et al., 1993), the first synthetic bionanocomposites were prepared from smectite clays such as montmorillonite, beidellite, saponite, hectorite and nontronite (Darder, Colilla et al., 2003; Darder, Colilla et al., 2005; Ruiz-Hitzky, Darder et al., 2005; Ruiz-Hitzky, Aranda et al., 2008). Also microfibrous clay minerals such as sepiolite and palygorskite have been compatibilized with biopolymers to form synthetic bionanocomposites (Darder, Lopez-Blanco et al., 2006; Chivrac, Pollet et al., 2010). Given the diversity of clay minerals and the intrinsic differences in biopolymers, it is impossible to establish a single mechanism responsible for the interaction between both phases. Depending on the used raw materials the resulting hybrid may present from ion-exchange processes to Van der Waals interactions (Ruiz-Hitzky, Aranda et al., 2008). A case by case analysis is required to establish the driving force in the association of the two moieties.

One interesting example of clay based synthetic bionanocomposite is the preparation of chitosan-MMT hybrid (Darder, Colilla et al., 2003; Darder, Colilla et al., 2005). Chitosan is a positively charged polysaccharide derived from the deacetilation of chitin. It interacts with sodium montmorillonite ($Na^+$MMT) by an ion-exchange mechanism generating intercalated compounds with interesting ion-exchange properties. By finely controlling the extent of intercalation, the authors were able to Chitosan-MMT based potentiometric sensors whose

sensitivity could be adjusted to either cations or anions (Darder, Colilla et al., 2005).

Another interesting example of the materials obtained from the association of layered clay minerals and biopolymers is the use of gelatin in $Na^+$MMT. Talibudeen was the first to recognize that this collagen derivative could be intercalated in MMT by adjusting the medium pH (Talibudeen, 1950; Talibudeen, 1955). Later, the preparation of similar bionanocomposites where the layered silicate had been previously modified with the cationic dye Methyl Red, permitted to obtain self supported bionanocomposite films for pH sensing (Fernandes, Ruiz et al., 2009). The composite film color turned from yellow to pink when exposed to an acidic atmosphere opening way to its application as active phase in optical systems.

Also fibrous clay minerals such as sepiolite have found utility in the preparation of synthetic bionanocomposites (Perez-Castells, Alvarez et al., 1985; Darder, Lopez-Blanco et al., 2006; Ruiz-Hitzky, Darder et al., 2009; Chivrac, Pollet et al., 2010; Ruiz-Hitzky, Aranda et al., 2010). Among these examples it is particularly interesting to note the bionanocomposite where xanthan, a negatively charged polysaccharide is heavily adsorbed by sepiolite (Ruiz-Hitzky, Darder et al., 2009). Such association occurs mainly via hydrogen bonding between the silanol groups on the external clay particles and the hydroxyl from xanthan. This hybrid material with anionic character is then capable of establishing electrostatic interactions with the positively charged molecules of influenza H5N1 virus capsids. The assembly between the bionanocomposite and the viral particles has proven to be highly effective as an adjuvant for intra-nasal vaccines for H5N1 virus tested in mice (Ruiz-Hitzky, Darder et al., 2009).

The preparation of structural synthetic bionanocomposites has also been subject of several efforts as reviewed recently (Sinha Ray and Bousmina, 2005).

*b) Synthetic –Carbonate and –Phosphate bionanocomposites*

Synthetic bionanocomposites based on carbonate and phosphate moieties are mostly related with the direct reproduction of previously mentioned natural bionanocomposites, bone and nacre (Ruiz-Hitzky, Aranda et al., 2008), for biomedical and structural applications, respectively.

Differently from clay based materials, bionanocomposite composed of carbonates and/or phosphate tend to be prepared in a biomimetic manner. This is due to the fact that clay minerals are fully developed crystals which are not expected to grow. On the other hand, carbonates and phosphates are able to grow (given the necessary conditions such as the presence of the corresponding ions) under mild (*e.g.* physiological) conditions. This feature is determinant when aiming at producing artificial bone or nacre.

An interesting approach to prepare synthetic bionanocomposite materials that emulate bone are those based on the precipitation of HAP from simulated body fluid (SBF) over a biopolymer matrix. One of the earliest examples following this strategy reports the deposition of nanocrystalline HAP from SBF onto poly-L-lactide (PLLA) (Zhang and Ma, 1999). The same strategy has subsequently been followed to adapt other polymers to artificial bone applications (Kim, Kishimoto et al., 1999; Zhang and Ma, 2004; Oyane, Uchida et al., 2005; Kong, Gao et al., 2006).

Another interesting examples of biomimetic growth of artificial bone (with special focus on the nanostructure) was reported by Kikuchi et al. who developed a pH controlled co-precipitation system that regulated the delivery of the components (Kikuchi, Itoh et al., 2001; Kikuchi, Ikoma et al., 2004). Pig skin derived collagen was added to an aqueous solution of $H_3PO_4$ and added as the acid component while $Ca(OH)_2$ was added as the basic component. By varying different synthesis temperatures and pH conditions the authors achieved a biomimetic HAP-colagen composite material where the HAP c-axis was aligned with the collagen orientation (Kikuchi, Itoh et al., 2001). After 12 weeks

implantation in dog's tibiae the bionanocomposite material had been integrated/replaced by newly formed bone. The subsequent histological observation revealed that both osteoblasts and osteoclasts were present in the vicinity of the implant, indicating good compatibility.

The use of carbonate-based bionanocomposites is not as widespread as the phosphate based counterparts.

Kuang and co-authors have prepared a bionanocomposite based on calcium carbonate mineralization inside poly(n-isopropylacrylamide) (PNIPAM) hydrogel spheres (Kuang, Wang et al., 2005). According to the authors the mineralization of calcium carbonate particles within the hydrogel is comparable to the biomineralization processes occurring in single cellulous organisms.

Also layered examples of carbonate based bionanocomposites have been reported. Layer-by-layer techniques were applied to the preparation of bionanocomposites $CaCO_3$ layered materials (Wakayama, Hall et al., 2005; Wei, Ma et al., 2007).

*c) CNT-based bionanocomposites*

Another important combination that joins biopolymers and inorganic particles to build up bionanocomposites relies on the use of CNTs. A wide amount of work has been done in this subject, especially regarding the association of CNT with electroactive species of biological origin such as enzymes for the preparation of biosensors (Merkoci, 2006; Jacobs, Peairs et al., 2010). However the groundbreaking work associating CNTs with biopolymers comes with the work by Zheng *et al.*, who firstly described the wrapping of DNA chains around CNTs (Zheng, Jagota et al., 2003). The described association between these biological macromolecules and CNTs intended initially to enhance the dispersability of CNTs in aqueous media. However the work has, above all, served to disclose the affinity between species of biological interest and CNTs.

Following that work, several authors have prepared CNT based bionanocomposites for different applications. One of the most relevant materials regards the assembly of carboxylic acid functionalized carbon nanotubes (CNT-COOH) and collagen for the preparation of scaffold materials for tissue engineering applications (MacDonald, Laurenzi et al., 2005). The bionanocomposite materials were seeded with rat aortic smooth muscle cells as model system to study the viability of living cell in the CNT-COOH loaded materials. After 3 and 7 days the cell viability was assessed yielding some unexpected results. When compared to the collagen construct, CNT-COOH loaded materials showed enhanced cell viability, suggesting that these materials could be successfully implemented as scaffolds in tissue regeneration. Other biopolymers have been compatibilized with CNTs in order to prepare bionanocomposites that could benefit from the excellent mechanical properties of CNTs. Other authors have used the same type of modified carbon nanotubes (CNT-COOH) in the preparation of chitosan based bionanocomposites, reaching a 93% improvement in the tensile modulus by the incorporation of 0.8 wt.% (CNT-COOH) in a chitosan matrix (Wang, Shen et al., 2005).

The preparation of macroporous materials using CNT-COOH and biopolymers has also been addressed (Nabeta and Sano, 2005). These authors prepared a CNT-gelatin gel from a dispersion of oxidized SWCNTs in a gelatin aqueous solution. Upon freezing and subsequent freeze-drying a cellular macroporous material was obtained. The gelatin fraction was later removed by thermal oxidation rendering a foam-like material composed of CNT-COOH. Several other preparations and applications have been reported in the assembly of biopolymers and CNTs. However it is especially relevant to refer the work by Potschke and co-workers who have prepared a CNT based sensor for liquids (Pötschke, Andres et al., 2010). Their approach focused on the melt-spinning of PLLA and CNT to produce bionanocomposite fibers between 100 and 600 μm

in diameter for liquid sensing. The fibers were placed in different solvents and their resistivity measured along time allowing discriminating between the nature of the solvent.

## 1.4 Objectives of this dissertation

The objectives of this dissertation are directly related to the preparation and the understanding of novel nanocomposites based on a specific clay mineral, sepiolite.

Firstly the mechanical properties of sepiolite are addressed. Although several examples of sepiolite based nanocomposites (Nohales, Solar et al., 2006; Zheng and Zheng, 2006; Bilotti, Zhang et al., 2009) and bionancomposites (Darder, Lopez-Blanco et al., 2006; Fernandes, Ruiz et al., 2009; Chivrac, Pollet et al., 2010) prepared for reinforcing purposes have been described in the literature, the intrinsic mechanical properties of sepiolite are unknown. As the knowledge of the elastic properties of the reinforcing phase is critical in all composite models, the determination of such properties was considered as a first step in the rational design of composites based on this clay mineral.

Another important objective relates to the application of sepiolite in bionanocomposites. Sepiolite-gelatin materials are taken as a model of the interactions established between a complex biopolymer such as gelatin (a collagen derivative) and sepiolite. To fully explore the nature of the interaction between both phases several factors are studied such as the surface chemistry of sepiolite and how it affects the clay-biopolymer interactions. A full insight on

the reinforcing capacity of sepiolite in biopolymeric matrices is addressed, using the data previously determined for the elastic properties of sepiolite.

A third objective relates to the use of sepiolite-biopolymers in the preparation of electrically conductive materials. Benefiting from the close interaction between the clay mineral and gelatin determined in the preceding point, a detailed analysis of the potentialities of preparing hybrid silicate-carbon materials is addressed. Also the potentialities of gelatin to form stable physical gels are explored in the context of producing electrically conductive foams.

Finally, sepiolite is analyzed from the point of view of its dispersing and stabilizing power. Its rheological properties are explored to produce stable aqueous dispersions of carbon nanotubes materials, whose difficulties to be dispersed in water constitute a major drawback in the wide application of these carbon based materials. The concomitant use of sepiolite and non-oxidized CNTs are explored in the context of bionanocomposite materials and its reinforcing ability is analyzed. Simultaneously, the rich sol-gel chemistry characteristic of fibrous silicates is fully explored in the presence of a conductive matrix giving rise to electroanalytical tools such as enzyme based biosensors.

In summary, sepiolite is analyzed in the wide panorama of bionanocomposites, from the mechanical to the electrical fundamentals and applications. It is the main ambition of this dissertation to provide a close regard at the multiple roles that sepiolite can assume in the growing field of bionanocomposites as well as exploring the related applications.

# 2. Experimental section

## 2.1 Starting materials

### 2.1.1 Sepiolite

Sepiolite is a hydrated magnesium silicate belonging to the clay minerals group. It is formed from alternating Tetrahedral Si : Octahedral Mg : Tetrahedral Si (TOT) ribbons (talc-like units) that present a periodic inversion of the silicon tetrahedron each six silicon atoms, generating a checkboard pattern as is depicted in the crystalline structure presented in figure 2.1.

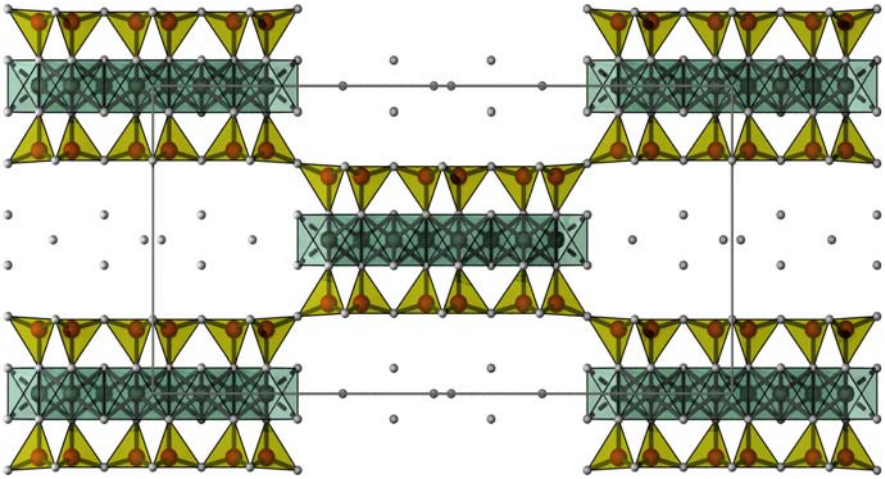

**Figure 2.1 –** Sepiolite crystalline structure viewed along the c axis according to Brunauer and Preisiger (Brunauer and Preisinger, 1956).

Sepiolite's half-unit formula is $Si_{12}O_{30}Mg_8(OH,F)_4(H_2O)_4 \bullet 8H_2O$ (Brunauer and Preisinger, 1956; Santaren, Sanz et al., 1990). The crystalline arrangement of this silicate is substantially different from the majority of clay minerals such as montmorillonite, kaolinite or illite which present a layered two-dimensional structure. Another exception along with sepiolite is the fibrous silicate palygorskite which also presents a quasi one-dimensional structure. Sepiolite's morphology consists of inorganic fibers that may range from a few to about 50 nanometers in diameter, whereas the fiber length is substantially higher than its diameter. It ranges from one micrometer to exceptionally large fibers as in the

case for Ampandrandava (Madagascar) sepiolite which might attain centimeters in length (Galán and Singer, 1984).

In this work, sepiolite was obtained from the Vallecas-Vicalvaro (Spain) deposit. It is a whitish powdery commercial product available under the trade name Pangel® S9 and was generously supplied by Tolsa S.A. Macroscopic block of sepiolite directly extracted from the same deposit was also used in the macro-mechanical characterization of sepiolite. Such block was of irregular shape and approximately 5 cm in its longest axis. The block was machined to regular 0.8 cm sided cubes for mechanical characterization.

### 2.1.2 Gelatin

Gelatine is a water soluble structural protein-like material derived from collagen. It is readily obtained from the parent protein by two simple procedures, acid-curing or lime-curing of animal skin, bone, tendons, yielding type A or type B gelatins respectively. These two types of preparative procedures are related to the origin of tissues employed. While bovine derived gelatin can be processed by the two curing processes, gelatin derived from other animal sources such as porcine or fish can only be processed via the acid procedure. After processing, gelatin can be further categorized according to its characteristics. The most notable are the isoelectric point and the bloom index. The isoelectric point (IP) describes the pH at which the positive charges from the amino groups present in the biopolymer backbone are compensated by the negative charges associated with the carboxylic acids. The relative amount of positive and negative charges is, evidently, highly dependent on the preparation procedures. Type A gelatins usually present an IP between 6 and 9 while type B gelatins usually display more acidic IP, around 4.5. The bloom index is a simple yet effective measure of the gel strength at predetermined conditions (temperature and concentration). Although this is not a fundamental measure of any gelatine

property it is convenient as an empirical index to describe the mechanical properties of gelatin gels.

Another relevant characteristic of gelatin relates to its amino-acid composition. Being a derivate of the structural protein collagen, gelatin considerably maintains its residue composition. This is characterized by a (Gly-Xaa-Yaa) repeat unit with high glycine (Gly) content and where Xaa and Yaa positions are normally occupied by proline and/or hydroxyproline residues respectively. This residue composition along with the minoritary residues introduced in the collagen denaturation process such as glutamic acid or arginine (Veis, 1964; Chiellini, Cinelli et al., 2001; Darder, Ruiz et al., 2006) account for the characteristic polyampholytic and polyelectrolytic behaviour of gelatine.

Gelatin can be viewed as a biocompatible and biodegradable (Zhuang, Zheng et al., 2007) denatured state of the structural protein collagen, from which inherits part of its structure. On the other hand above certain temperature it behaves as a high linear polymer with random spatial arrangement (Veis, 1964). Although the transition between these two states is widely known, it carries along critical consequences to the preparation and application of gelatine-based composites as, for instance, its mechanical properties vary dramatically as a function of the protein conformational state (Bigi, Panzavolta et al., 2004). But this protein's complexity does not stick to its conformational transitions between triple helix and random coil, as previously mentioned, gelatin preserves in some extent the primary structure of collagen. Thus, a comprehensive regard at gelatin and derived materials must consider the following aspects (Fernandes, Darder et al., 2011):

1) Gelatin can be viewed as a physical gel exhibiting collagen-like triple helix conformation below transition temperature;
2) Gelatin has a linear random polymer conformation above transition temperature; and

3) It presents polyampholytic behaviour due to anionic and cationic residues in the polymer backbone.

In this work type A porcine gelatin was obtained from Aldrich and used without further purification steps. It consists on a finely ground pale yellow powder. According to the supplier it presents an IP of *circa* 9 and a bloom index close to 300.

### 2.1.3 Polyvinyl alcohol

Polyvinyl alcohol (PVA) is a hydrophilic polymer with repeating unit consisting of $CH_2$-CH(OH). This thermoplastic polymer is usually obtained by deacetilation of polyvinyl acetate instead of polymerization reactions. Due to the preparative route it is common to find residual acetate functions in its backbone. Industrially, PVA is largely applied in the paper industry where it acts as a sizing agent. Among its main characteristics, PVA shows biodegradability and biocompatibility along with an outstanding affinity to other polymeric materials forming especially interesting mixtures with polysaccharides (Cascone, Barbani et al., 2001). These characteristics impelled PVA to be applied in a wide diversity of materials for bioapplications such as drug delivery (Cascone, Barbani et al., 2001), cell transportation systems (Li, 1998) or scaffold materials (Nuttelman, Henry et al., 2002; Chua, Leong et al., 2004; Kobayashi, Chang et al., 2005).

In this work PVA was obtained from Sigma Aldrich under the trade name Mowiol® 20-98. Its degree of polymerization is around 2800 (Mw~125 kDa) and contains approximately 98% deacetilated units and ester number between 15 and 25.

### 2.1.4 Multi-Wall carbon nanotubes, MWCNTs

Carbon nanotubes (CNTs) are carbon nanomaterials possessing a tubular structure and nanometric diameter. Chemically, they are composed of rolled-up concentric layers of graphene forming tubular structures that are in some occasions capped by fullerene-like structures. The number of composing layers forming the nanotube varies greatly, from a single layer that forms a single-wall carbon nanotube (SWCNT) to several layers forming a multi-wall carbon nanotube (MWCNT). Although the discovery of SWCNTs is nowadays somewhat controversial (Monthioux and Kuznetsov, 2006), the first definitive report on these remarkable structures was published by Iijima in 1991 (Iijima, 1991).

In this work, pristine MWCNT produced by Catalytic Carbon Vapor Deposition, which can be considered a particular case of Chemical Vapor Deposition (CVD) method, were acquired from Dropsens (Oviedo, Spain) and used as received. According to the supplier the nanotubes consist on a majority of open end structures with an average diameter and length of 10 nm and 1.5 μm, respectively.

### 2.1.5 Horseradish Peroxidase, HRP

Horseradish peroxidase (HRP) is an oxyreductase enzyme obtained from horseradish (*Armoracia rusticana*) known to use hydrogen peroxide to oxidize a variety of organic and inorganic species (Veitch, 2004). In general horseradish peroxidase is composed of different isoenzymes from which isoenzyme C is the most abundant (Veitch, 2004). This isoenzyme is composed of 308 amino-acid residues linked through 4 disulfide bridges. Aside from the amino-acid composition, HRP contains two different types of metal centre that are key to its bioactivity, iron(III) protoporphyrin IX (usually referred to as the heme group)

and two calcium atoms stabilized by hydrogen bonds with adjacent aminoacid residues (Veitch, 2004).

Horseradish peroxidase was obtained from Sigma Aldrich and stored at -20 ºC.

### 2.1.6 Other reagents and starting materials

**Table 2.1 –** Main reagents used in the course of the work, corresponding chemical structure, purity and the supplier.

| Reagent | Chemical Structure | Purity | Supplier |
|---|---|---|---|
| Poly(propyleneglycol (bis-2-aminoether)) | 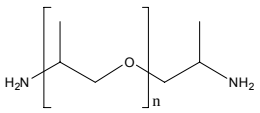 | - | Sigma-Aldrich |
| Bisphenol A diglycidyl ether | 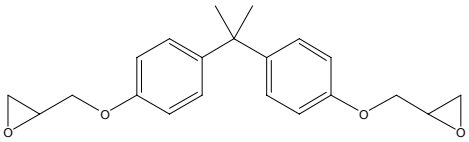 | - | Sigma-Aldrich |
| (3-Aminopropyl) Trimethoxysilane (APS) | 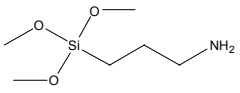 | 97 % | Fluka |
| (3-Glycidyloxypropyl) Trimethoxysilane (GOPS) | 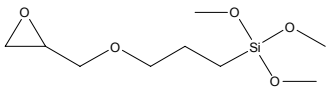 | >97 % | Fluka |
| 2,2′-Azino-bis(3-ethylbenzothiazoline -6-sulfonic acid) diammonium salt (ABTS) | 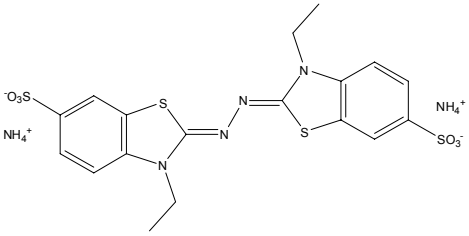 | >99 % | Sigma-Aldrich |
| Potassium ferricyanide | $K_3Fe(CN)_6$ | >99 % | Sigma-Aldrich |
| Hydrogen peroxide | $H_2O_2$ | 35 wt.% | Sigma-Aldrich |

## 2.2 Synthesis and preparation methods

### 2.2.1 Sepiolite derivatives

*a) Preparation of sepiolite organosilane derivatives by covalent grafting*

The synthesis of organic derivatives of sepiolite by the grafting of alkoxysilanes or chlorosilanes onto the mineral available silanol groups is a well established method (Ruiz-Hitzky and Fripiat, 1976; Van Meerbeek and Ruiz-Hitzky, 1979; Ruiz-Hitzky, 2004). It implies the condensation of an organosilane or a chloro-organosilane onto the silanol groups of the silicate in presence of an organic solvent with the release of the corresponding alcohol. In this work, chemical modification of sepiolite was performed by grafting two different organo-alkoxysilanes, (3-aminopropyl)trimethoxysilane (APS) and (3-glycidyloxypropyl)trimethoxysilane (GOPS) to the mineral surface. The general reaction scheme of the grafting of an alkoxysilane to a silanol group is depicted in Scheme 2.1.

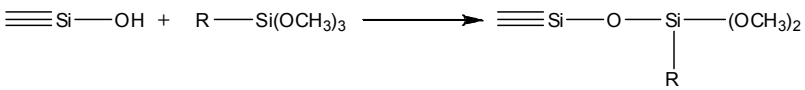


**Scheme 2.1** – General reaction scheme for the grafting of an organo alkoxysilane to the silanol groups on the surface of sepiolite.

Sepiolite (3 % w/v) was dispersed in 200 ml of isopropanol in a two neck round bottom flask equipped with a reflux column. After vigorous agitation the temperature was set to 65 ºC and 25 ml of the corresponding organosilane were added. The reaction was left to proceed overnight. After cooling the mixture down to room temperature, it was filtered and thoroughly washed with water:methanol (1:1) mixture. The resulting solids were dried at 60 ºC under dynamic vacuum for 24 hours and stored in plastic vessels. The resulting organo-modified sepiolites were named Sep-APS and Sep-GOPS according to the organosilane and characterized by CHN chemical analysis and FTIR.

*b) Preparation of sepiolite derivatives obtained by thermal treatment*

Another strategy used to promote specific modifications on sepiolite is to use thermal treatment to induce phase variations. Sepiolite is known to give origin to a semi-dehydrated phase called monohydrated sepiolite when heated to temperatures above approximately 450 ºC (Serna, Ahlrichs et al., 1975; Perraki and Orfanoudaki, 2008). This phase is mainly characterized by a partial collapse (structural folding) of the intracrystalline tunnels and external channels of sepiolite as can be appreciated in figure 2.2.

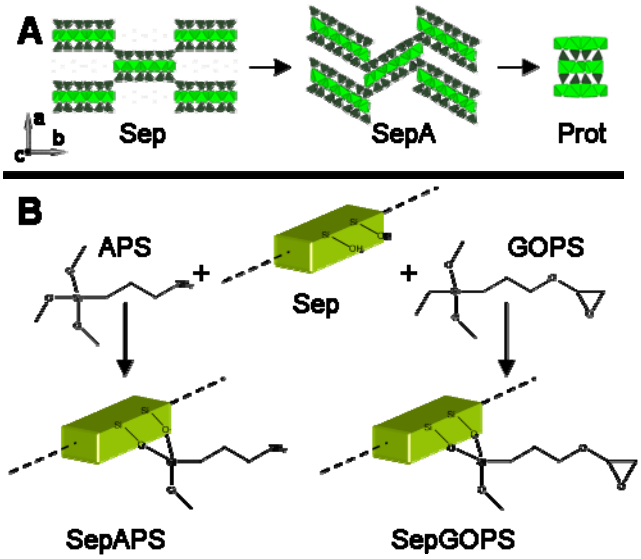


**Figure 2.2** – Schematic representation of sepiolite and the prepared derivatives. (A) Derivatives by thermal treatments: Sep, raw sepiolite; SepA, monohydrated sepiolite; Prot, protoenstatite. (B) Organic derivatives: SepAPS, aminopropyltrimethoxysilane modified sepiolite and SepGOPS, glycidoxypropyltrimethoxysilane modified sepiolite.

Higher temperature gives rise to other transitions, namely dehydroxylation of the silanol groups located in the fiber edges around 1000 ºC and the subsequent formation of a compact mineral phase named protoenstatite when submitted to temperatures above 1000 ºC. (Serna, Ahlrichs et al., 1975; Perraki and Orfanoudaki, 2008) In this work monohydrated sepiolite and protoenstatite were prepared by placing 20 g of sepiolite in a porcelain crucible and heating it

to 500 and 1100 ºC respectively. The heating was conducted in an oven under air and the heating profile was as follows. From ambient temperature, the oven temperature was raised at 10 ºC.min$^{-1}$ to the working temperature (500 or 1100 ºC) which was maintained for 5 hours. The cooling period down to ambient temperature was prolonged for at least 3 hours. The obtained samples were collected and placed in a dessicator to avoid rehydration. Samples were characterized by XRD, FTIR and SEM.

*c) Preparation of sepiolite derivatives by adsorption of gelatin*

Recently sepiolite has found increasing relevance in the context of bionanocomposites. This is partially due to its high affinity towards some biopolymers. The earliest examples are those of sepiolite-collagen hybrids (Perez-Castells, Alvarez et al., 1985) and more recently sepiolite-chitosan hybrids (Darder, Lopez-Blanco et al., 2006). These materials are prone to associate due to the establishment of hydrogen bonds between the silanol groups in the surface of sepiolite and functional groups of biopolymers such as amide groups, carboxylic acids and other hydrogen bond forming functional groups. In this work gelatin was adsorbed on sepiolite by placing different amounts of the polypeptide (from 0.1 to 4 grams) within 200 ml of sepiolite suspension (3 g.L$^{-1}$). Samples are named GSX where X stands for the initial amount of gelatin in the suspension. The mixture was left to homogenize at 60 ºC in a temperature controlled orbital mixer (50 rpm) during 48 hours. After that period the suspensions were centrifuged (4500 rpm) for 10 minutes, re-dispersed in the same volume of water (at 60ºC) and re-centrifuged. This procedure was repeated for three times to ensure a complete removal of non-adsorbed biopolymer. The obtained solids were left to dry at 40 ºC overnight. The amount of adsorbed gelatin over the inorganic particles was assessed by

two techniques, TGA and CHN chemical analysis. Sepiolite particles with adsorbed gelatin were also imaged by means of TEM microscopy.

### 2.2.2 Sepiolite-based nanocomposites

*a) Sepiolite and sepiolite-derivatives gelatin nanocomposites*

The preparation of the nanocomposite films based on the assembly of gelatin and sepiolite and its derivatives was carried out in a simple four-step procedure including dispersion, self assembly, gelation and evaporation. The appropriate amount of sepiolite derivatives (Table 2.2) was added to 40 ml of aqueous gelatin solution 5% (w/v) at 60 ºC and vigorously agitated for a 5 min period. Each of the dispersions was subsequently stored overnight in closed vessels at 60 ºC and allowed to self-assemble.

**Table 2.2 –** Sample codes of gelatin based nanocomposites and sepiolite and sepiolite-derivatives mass fraction in gelatin based nanocomposites

| | Mineral mass fraction | | | | | |
|---|---|---|---|---|---|---|
| | 0.00 | 0.01 | 0.02 | 0.05 | 0.10 | 0.20 |
| Sep | Gel | GSep1 | GSep2 | GSep5 | GSep10 | GSep20 |
| SepA | — | GSepA1 | GSepA2 | GSepA5 | GSepA10 | GSepA20 |
| Prot | — | GProt1 | GProt2 | GProt5 | GProt10 | GProt20 |
| SepAPS | — | GSepAPS1 | GSepAPS2 | GSepAPS5 | — | — |
| SepGOPS | — | GSepGOPS1 | GSepGOPS2 | GSepGOPS5 | — | — |

Afterwards mixtures were poured into 80 x 80 x 20 mm PMMA moulds, cooled down to 4 ºC and kept at this temperature for 12 h inducing gelation. Finally, gelatin–clay gels were evaporated at room temperature using a home built convection system. The obtained self-consistent films (80 x 80 x 0.2 mm approximately) were stored at room temperature in a 75% relative humidity (RH) chamber.

*b) Preparation of foam-like gelatin sepiolite nanocomposites*

Sepiolite-gelatin foams were prepared by freeze drying processes. Equal amounts of gelatin (5% w/v) and sepiolite (5% w/v) were added to bi-distilled water and left to self assemble overnight at 60 ºC. Four aliquots of 20 ml of dispersion were placed in polyethylene closed vessels. Two of them were placed at 4 ºC overnight to induce gelatin gelation while the other two were maintained at 60 ºC during the same time period. Subsequently two samples (one gelled at 4 ºC overnight and one maintained at 60 ºC) were placed at -18 ºC to freeze. The remaining samples were frozen in liquid nitrogen (-196 ºC). Table 2.3 summarizes the processing conditions of the gelatin-sepiolite foams.

**Table 2.3 –** Sample names and freezing conditions in the preparation of gelatin-sepiolite nanocomposite foams.

| Sample Name | Sample temperature before freezing / ºC | Freezing temperature / ºC |
|---|---|---|
| GSep4$N_2$ | 4 | -196 |
| GSep60$N_2$ | 60 | -196 |
| GSep4F | 4 | -18 |
| GSep60F | 60 | -18 |

Samples were lyophilized in a Cryodos -80 freeze dryer under dynamic vacuum at -80 ºC immediately after freezing. Freeze drying period was extended to 60h to ensure no residual ice would be trapped in the composite foam. The prepared foams were characterized by FE-SEM, mercury intrusion porosimetry and optical microscopy.

### 2.2.3 Sepiolite-carbonaceous materials

*a) Carbonization of gelatin-sepiolite materials*

The carbonization of gelatin-sepiolite materials was performed to generate carbonaceous materials from the biopolymer moiety on previously prepared

gelatin-sepiolite materials. In general, the carbonaceous materials prepared from gelatin were thermally treated at 800 ºC in nitrogen atmosphere. The carbonization procedure was as follows. Samples were introduced in a horizontal tubular oven (Hobersal, Spain) provided with sealed ends and controlled atmosphere. Nitrogen flow was set to 5 $ml.min^{-1}$ and temperature was risen from ambient to 800 ºC at 5 $ºC.min^{-1}$ rate and kept at this temperature for 2 hours. After this period the oven was left to cool down until ambient temperature (typically 4 hours).

Different samples were carbonized using this procedure from the different adsorbed gelatin over sepiolite samples (GS) molded into pellets to the lyophilized gelatin-sepiolite foams (GSF). Carbonized samples were characterized by different techniques such as Raman spectroscopy, four-probe electrical conductivity, mercury intrusion porosimetry, FE-SEM and TEM.

*b) Dispersion of sepiolite-MWCNT materials in water*

The dispersion of MWCNTs in presence of sepiolite was achieved by means of ultrasonic agitation using a VC750 Sonics Vibra-Cell equipment. Samples containing different amounts of MWCNTs and sepiolite in 20 ml of water were dispersed using a Ø13 mm ultrasonic horn operated at 20 kHz. Agitation was pulsed (10 sec ON followed by 10 sec OFF) to avoid overheating the sample and the amplitude of agitation was set to 50% of the equipment total capacity. The amount of energy was set between 1 and 5 KJ (per 20 ml of dispersion).

The viscosity of sepiolite suspensions and correspondent rheological percolation was determined using a Brookfield viscosimeter. Several concentrations of sepiolite (from 0.005 to 3 wt %) in water were measured after mild US dispersion (10 KJ / 100 ml).

The stability of MWCNT-Sep suspension was evaluated by observing the phase separation in the dispersions along time, FE-SEM and TEM observation as well as UV-Vis monitoring of low concentrated dispersions.

*c) Preparation of Sep-MWCNT hybrid buckypapers*

Hybrid Buckypapers (HBs) were obtained by vacuum filtration of the previously prepared sepiolite-MWCNT aqueous dispersions. Immediately after the ultrasonic agitation, the dispersions were passed through a hydrophilic membrane (MF-Millipore, VSWP04700, pore Ø = 25 nm) under vacuum. Self-supported hybrid buckypapers were easily peeled off from the membrane and dried overnight at 60 ºC.

Surface conductivity measurements were performed in galvanodynamic mode using a multichannel potentiostat (Solartron Multistat 1480). Three voltage-current curves were determined for each HB using an in-line 4 probe configuration with 0.169 cm average distance between probes determined under the optical microscope. Average resistance values were calculated for each sample and resistivity was determined based on the setup and sample geometrical configuration (Czichos, Saito et al., 2006). Prepared buckypapers were imaged under FE-SEM using two different detectors to establish a full characterization of both particles composing HBs.

*d) Functionalization of Sep-MWCNT hybrid buckypaper and biosensor preparation*

Horseradish peroxidase functionalized hybrid buckypaper (5 mg MWCNTs, 52 mg sepiolite) was functionalized using (3-aminopropyl)trimethoxysilane (APS) by immersing a dried buckypaper into 0.5 % (v/v) APS in isopropyl alcohol for 4 hours at ambient temperature. The resulting buckypaper was thoroughly washed with isopropyl alcohol, and immersed into 10 % (v/v) glutaraldehyde

aqueous solution for 30 min also at room temperature, abundantly rinsed with bidistilled water and placed at 4 ºC overnight on a 1 mg/ml aqueous solution of horseradish peroxidase. Figure 2.3 depicts sequential functionalization steps as well as an idealized view of the final material.

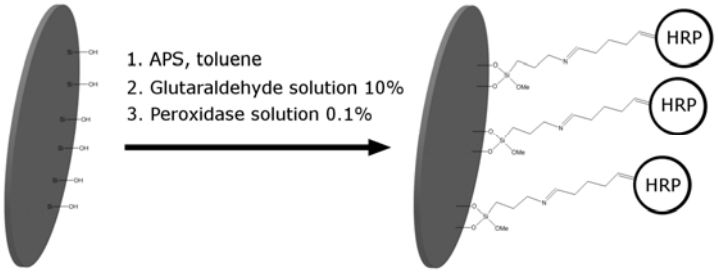


**Figure 2.3 –** Simplified reaction scheme describing the functionalization steps of HB from the as prepared HB until the HRP functionalized material.

After rinsing and drying at ambient temperature the HRP functionalized buckypaper was assembled to the graphite substrate using conductive carbon glue. After the conductive carbon was dry, the electrode was ready to use. When not in use the electrode was kept in PBS at 4 ºC. Figure 2.4 shows functionalized HB assembled HRP assembled to its biosensor form.

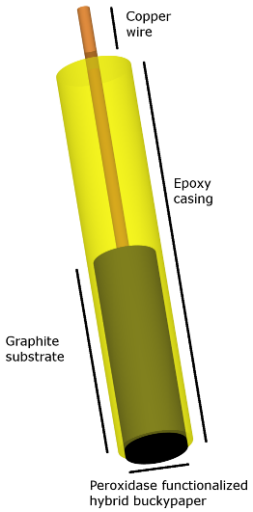


**Figure 2.4 –** HRP functionalized HB assembled into the prepared amperometric biosensor.

The graphite substrate is uniquely intended to promote electrical contact between the HRP functionalized HB with the conducting copper wire. The resulting electrode was evaluated as a $H_2O_2$ sensitive sensor based on the catalytic degradation of peroxo species by horseradish peroxidase.

### 2.2.4 Sepiolite carbon nanocomposites

*a) Preparation of carbonaceous foam epoxy composites*

The preparation of thermoset composites based on gelatin based structured foams was performed in several steps. Firstly the carbonaceous foams were prepared as described previously (§ 2.2.3a). Subsequently they were immersed in a freshly mixed stoichiometric mixture of the epoxy resin and the diamino curing agent at 40 ºC. The epoxy-diamino mixture with the carbonized foams were then degassed for 2 hours under dynamic vacuum until no further air bubbles were withdrawn from the foams. After standard curing (12 h at 60ºC followed by 2 h at 120 ºC) the epoxy-embedded foam was machined to expose the foam surfaces.

*b) Preparation of sepiolite-MWCNT nanocomposites in PVA matrix*

The preparation of PVA nanocomposites reinforced with sepiolite and MWCNTs was processed similarly to the aqueous dispersions of sepiolite and MWCNTs in water. The difference resided in the usage of PVA solution (10 % w/v) instead of water. Thirty six different compositions were prepared where both sepiolite (0, 2, 4, 6, 8 and 10 wt%) and MWCNT (0, 0.4, 0.8, 1.2, 1.6 and 2 wt.%) concentration with respect to the employed PVA mass were used. The dispersions were casted onto 80 x 80 x 20 $mm^3$ PMMA molds and left to evaporate at room temperature. After drying PVA-Sep-MWCNT nanocomposite films were peeled off and placed in a constant humidity chamber until

characterization. PVA nanocomposites were characterized by FE-SEM, DSC and mechanical testing.

## 2.3 Instrumental methods and techniques

Several characterization techniques were employed along this work to thoroughly characterize the functional and structural properties of sepiolite and the materials derived from it. Nevertheless the same amount of attention is not devoted to all of the different techniques. Some of these techniques are common and their use is defined by standard procedures that do not enclose any relevance beyond the obtained results themselves. The description of these techniques, referred to as standard techniques, consists on a mere description of the equipment and operating conditions. Among these techniques are X-ray diffraction (XRD), elemental analysis (CHN), infrared spectroscopy (FTIR), transmission electron microscopy (TEM), scanning electron microscopy (SEM), viscosimetry, thermal analysis (TG/DTG/DTA and DSC) or the mechanical characterization of materials by use of the Universal Testing Machine.

On the other hand, other techniques which due to their relevance to the present work or to their novelty in the context in which they were applied deserve special consideration will be treated in a more detailed manner. In these cases a brief conceptual remark on the technique, its relevance to the field along with some technical details are provided. Among these techniques lay the use of the AFM for the mechanical characterization of nanomaterials, the use of ultrasound to disperse nanoparticles or freeze drying technique for the formation of porous materials.

### 2.3.1 Nanomechanical properties of sepiolite using the AFM

Conceptually the caracterization of the mechanical properties of a nanofibre is simple. It consists on the deposition of a nanofibre with known dimensions over a known suspended length and measuring the required force to induce a given deformation or *vice versa*. Nevertheless, the experimental requirements to achieve such characterization of single sepiolite fibers using an AFM are far more complex than the concept itself. It involves the following steps: 1) Functionalization of sepiolite fibers, 2) Preparation of an adequate rigid patterned substrate, 3) Dispersion of sepiolite fibers over the patterned substrate, 4) Electron Microscopy (FE-SEM) detection of isolated fibers hanging over specific motifs in the patterned substrate, 5) Mechanical testing using the Atomic Force Microscope (AFM).

The first of the abovementioned steps was carried out in the context of sepiolite modification for composites preparation (§ 2.2.1a). Sepiolite-amine derivative SEP-APS was used for mechanical testing due to two key factors. Firstly, the presence of the amino functions on its surface is advantageous because it allows covalently grafting sepiolite nanofibers to the substrate. This grafting procedure minimizes the displacement of sepiolite fibers while scanning the surface with the AFM probe. The second factor resides in the nature of SEP-APS modification itself. Because sepiolite presents silanol groups only in the external blocks of its structure, its internal structure is not affected by the organosilane grafting which occurs solely on the mineral edges. The requirements for an adequate substrate for nanomechanical testing of suspended nanofibers are numerous, spanning from the substrate's rigidity to the possibility to perform nanolithography among other characteristics. One of the materials complying with all of the referred requirements is crystalline silicon wafers. Not only it presents a high rigidity (Hopcroft, Nix et al., 2010) but also there is available technology to nanopattern it and its surface can be easily

modified with organosilanes after an oxidative step with acid “piranha” solution (Faibish, Yoshida et al., 2002). Nanopatterned crystalline silicon was obtained from IMB-CNM (Barcelona, Spain). It presents numerous motifs (wells, gratings, checkboards, etc.) ranging from 1 to 500 μm in dimensions. To perform the bending tests an area with 500 nm deep and 1.5 μm in diameter wells was selected. The chemical pre-treatment was designed to ensure covalent bonds between the SEP-APS and the silicon substrate. To achieve a reactive, silanol-rich layer on silicon wafers, these were treated with “piranha” solution (7:3 volume ratio mixture of 30% $H_2O_2$ and concentrated $H_2SO_4$) for one hour at ambient temperature. After thorough rinsing with bi-distilled water, wafers were dried overnight at 60 ºC. Wafers were subsequently immersed in a solution of GOPS in toluene (0.5%) for four hours at 60 ºC. Afterwards silicon wafers were rinsed with toluene and dried under dynamic vacuum at the same temperature.

The deposition of SEP-APS nanofibres in the GOPS-modified wafer was prepared by dispersing 10 ppm SEP-APS in toluene, depositing one drop over the nanopaterned modified wafer and allowing it to dry at ambient temperature. Wafers were then placed in an oven at 60 ºC to promote covalent grafting of the APS and GOPS fraction of each substrate (fibre and wafer respectively).

FE-SEM allowed determining which fibres were individually deposited over the preselected motifs (wells). Sepiolite-modified silicon wafers were observed in a FEI Microscope, Nova NanoSEM 230 model without previous sputtering process to ensure that sepiolite’s mechanical properties would not be affected by the deposition of metallic layers. Samples were imaged at 2500X magnification throughout the entire nanopatterned area of interest. Beam landing energy (2 keV) and spot size (3.5) were kept at the equipments lowest values and unaltered throughout the imaging to minimize damaging sepiolite fibres, ensuring at the same time reproducibility throughout the different imaging sessions. FE-SEM images were juxtaposed to permit conclusive pin-pointing of nanofibres in conditions to be measured under the AFM.

AFM is the most popular form of Scanning Probe Microscopy (SPM) and was firstly described by Binnig and co-workers back in 1986 (Binnig, Quate et al., 1986). A schematic drawing of the main components of the AFM is depicted in figure 2.5. This form of microscopy is based on the mechanical interaction of a given sample and a sharp probe that scans the sample systematically on the *xy* plane. This technique can reach extremely high resolution depending on several conditions as tip radius, sample-tip interaction and effective vibration suppression, among others. Under ideal conditions atomic resolution is possible.

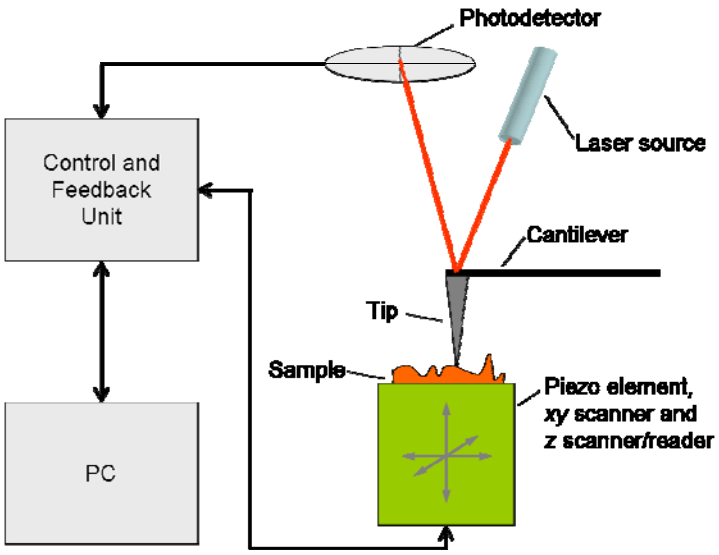


**Figure 2.5 –** Simplified schematic drawing of the AFM main elements.

The AFM has different working modes such as contact, tapping (or non-contact), force curve and force volume. In this work a conjunction of all of these modes (except for tapping mode) was used to elucidate the mechanical properties of suspended nanofibers. In contact mode the sample is brought into contact with the probe tip and the sample is scanned in the *xy* plane. The piezo element varies the height of the sample with respect to the cantilever base in order to keep a constant deflection of the cantilever (equivalent to a constant force as it is assumed that in the deflection regime to which the cantilever is

submitted it behaves in accordance to Hook's law). Collecting and merging *xy* data (position) with the correspondent piezo *z* displacement (height) gives a topographical map of the sample. This approach was used to achieve two main goals in this work. The first was to locate sepiolite fibers previously selected by FE-SEM in the pattern. This step is usually done by scanning a wide area (i.e. 50 x 50 $\mu m^2$), which is successively narrowed until the fiber and the motif over which it is located are clearly devised (typically a 3 x 3 $\mu m^2$ area). Once the fiber whose mechanical properties are to be measured is located the second step resumes. It consists on imaging the fiber at different cantilever deflections (corresponding to different forces applied on the sample) and measuring the topographical profile of the suspended fiber. By correlating the applied force to the promoted fiber deflection it is possible to estimate the fiber's mechanical properties.

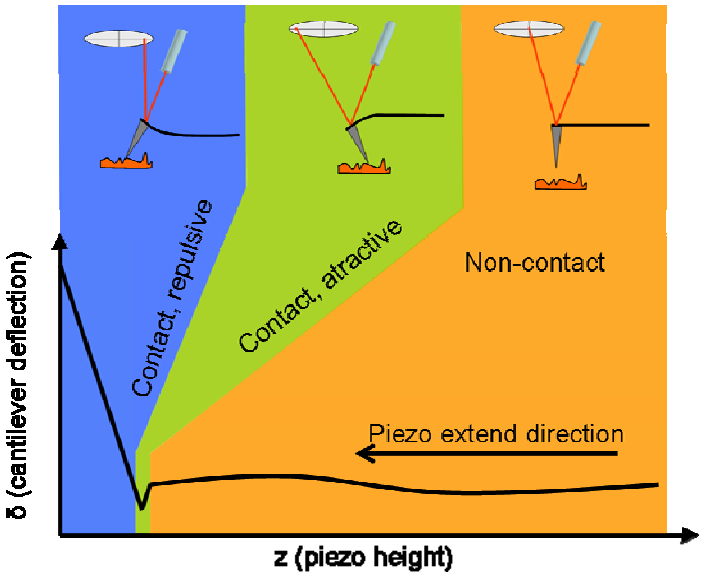


**Figure 2.6 –** Force curve example showing the different regimes of interaction between the probe tip and the sample as well as the detection setup for the different types of interaction. In orange, non-contact regime; in green, attractive contact regime and in blue, repulsive contact regime.

To extract force values from the contact mode it is necessary to use "Force Mode". This simple methodology is based on bringing the sample into contact

with the probe tip and measuring the voltage variation induced by the bending of the cantilever measured on the photodetector. Figure 2.6 illustrates the force profile as well as the contact (attractive and repulsive) and non-contact regimes. In the non-contact regime the piezo approaches the sample towards the probe tip but the only cantilever deflection registered is due to fluctuations in its position. In green, contact attractive regime, the tip jumps into contact with the sample due to their proximity. The distance is small enough for the attractive forces between the two bodies to overcome the bending energy of the cantilever. In blue, repulsive contact regime, as the piezo element carries with the upward movement the interaction between both elements becomes repulsive as the sample now forces the cantilever to deflect upwards.

To quantify the applied force in contact mode it is necessary to know the deflection voltage at which the imaging scan was performed and to perform a force curve. The height (h) between the non-contact regime (just before jumping into contact) and the deflection setpoint at which the image was taken gives the applied force by the tip on the sample. Figure 2.7 illustrates this methodology.

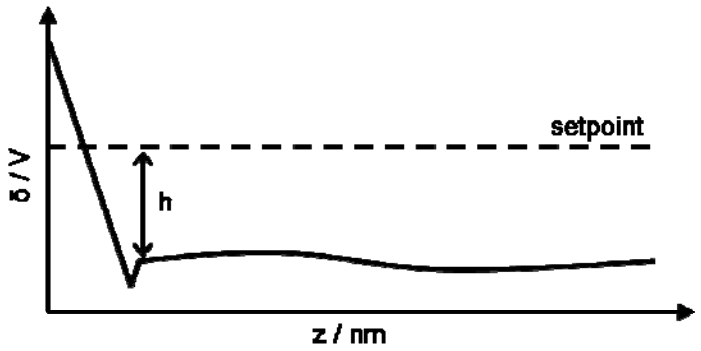


**Figure 2.7 –** Force determination in contact mode operated at a given setpoint voltage (deflection).

Another requirement to obtain absolute force values in this mode is to obtain a force profile on an infinitely hard surface. This allows calibrating the sensitivity of the experimental setup. The expression that converts the measured voltage to applied absolute force is represented in equation 2.1

$$F = hks \qquad \text{(eq. 2.1)}$$

where F stands for the applied force in nN, h for the measured voltage difference between the non-contact regime and the setpoint in V, k stands for the cantilever spring constant in $nN.nm^{-1}$ and s stands for the sensitivity in $nm.V^{-1}$.

The profile determination is performed by importing the topographic files resulting from AFM imaging at different setpoint voltages using Gwiddion 2.13 software. By correlating the force applied in each image and using the profile variation measured over the suspended length of the fiber it is possible to reproduce a simple bending test on the nanofibers. To obtain the elastic modulus of sepiolite the stress applied to the nanofiber is plotted against the measured deformation. In the ideal case where the force is applied exactly in the middle of the suspended length of the nanofiber and this presents a uniform radius and a circular cross-section the resulting slope is the elastic modulus of sepiolite in bending mode.

The last, and surely the most relevant mode to acquire force information from an AFM, is to use “Force Volume” mode (Butt, Cappella et al., 2005). This mode consists on the sequential collection of different force measurements over a given area. The procedure includes the determination of an area of interest and dividing it into a predefined grid. In this work the area was divided into a 64x64 grid, whose force profiles were collected. This technique quantitatively characterizes the mechanical properties of each point in the image. By selecting the points where the nanofiber is hanging over the well, it is possible to directly obtain a force *vs* fiber deformation information.

### 2.3.2 Dispersion of nanoparticles using ultrasonic agitation

The use of ultrasonic vibrations is finding increasing attention in materials chemistry as it configures a simple yet powerful way to disperse and homogenize different particles and/or media (Furtado, Kim et al., 2004; Seo, Sung et al., 2006; Sauter, Emin et al., 2008; Peng, Wu et al., 2011). The attention received by this technique regarding this application is also closely related to the advent of nanotechnology and nanoparticles. Due to the small dimensions of nanoparticles (and thus to their high surface to mass ratio), they show increased interfacial phenomena and consequently require more power to disrupt aggregates. Another major application of US is focused on the organic, inorganic and hybrid compounds synthesis, usually termed sonochemistry (Cintas and Luche, 1999; Bang and Suslick, 2010; Wani, Ganguly et al., 2010).

In this work, ultrasonic agitation was used to promote the dispersion of nanoparticles, namely sepiolite fibers, nanotubes and mixtures of both.

The principle of operation for the dispersion/emulsion by ultrasonic agitation relies, apart from the mechanical agitation induced by the movement of the tip, on the formation of a discontinuity on the liquid continuum (cavitation bubble). Such discontinuity tends to grow until it reaches an unstable size and collapses (Suslick and Price, 1999). The collapse of the generated cavitation bubble has two main consequences. The first is the generation of a liquid microjet caused by the abrupt entrance of liquid to the low pressure bubble and the second is the formation of a localized “hot spot” in the surroundings of the collapsing bubble. Alongside with the effects associated with the discontinuities, the application of ultrasonic energy to liquid media also induces high mechanical shear on the liquid.

In the work described in this dissertation a Sonics Vibra-Cell VCX750 was used. The dispersion experiments were carried out in a sound abating enclosure to minimize the intense high pitched noise caused by harmonics generated in the

sample and beaker. The applied energy used for each dispersing procedure was varied according to the volume of sample and the degree of disaggregation intended. The liquid media in which all experiments were conducted was water and the irradiation was pulsed to avoid generalized overheating of the sample.

### 2.3.3 Freeze drying

Freeze drying is a standard technique in the industrial process of lyophilization. It consists on freezing a dispersion or solution of any compound, followed by the removal of the solvent by the sublimation of the same. This process is usually performed at temperatures below -50º C and reduced pressure. The main uses of this technique in an industrial scale are for food processing (Shahidi and Han, 1993) and the pharmaceutical industry (Wang, 2000; Bala, Hariharan et al., 2004; Tang and Pikal, 2004). More recently, this technique has found wide use in the structuration of porous solids such as foams (Qian and Zhang, 2010). In this work, porous materials based on sepiolite and gelatin were prepared by freezing aqueous dispersions of these compounds at -196 ºC and -20 ºC. The sublimation step was conducted in a Cryodos 80 freeze fryer, operating at -80 ºC and 0.03 mbar.

### 2.3.4 Standard charaterization techniques

X-ray diffraction (XRD) was conducted in a Bruker D8-Advance diffractometer in θ–2θ configuration. The applied potential and current on the radiation source was 40 kV and 30 mA, respectively, generating a Cu-Ka radiation that was filtered through a Ni window. Diffraction patterns were collected between 2º and 60º (2θ) at a constant goniometer angular speed equal to 2º $min^{-1}$ (2θ) and detected by a SOLX detector.

X-ray scattering experiments were performed in a Nanostar (Bruker-AXS GmbH, Germany) to determine the orientation and texture of the fibres in the composites. The working distance between the sample holder and the Hi-Star two-dimensional detector (1024 x 1024 pixel$^2$) was 270 mm and Cu Ka radiation was used. These conditions allow the simultaneous collection of information in an intermediate range that spans both wide-angle X-ray diffraction pattern (WAXD) and small-angle X-ray scattering (SAXS).

Elemental analysis (CHN) was conducted in duplicate in a LECO CHNS-932 analyzer.

Infrared spectroscopy (FTIR) of sepiolite and its derivatives was conducted in attenuated total reflectance mode (ATR) using a Vertex 70 spectrometer (Bruker GmbH, Germany) connected to a Hyperion 2000 microscope equipped with a liquid nitrogen cooled mercury-cadmium-telluride (MCT) detector. Spectra were accumulated for 128 consecutive scans and collected between 4000 and 600 cm$^{-1}$. The spectral range between 4000 and 3000 cm$^{-1}$ was also measured in transmission mode using an IFS 66–v/S (Bruker GmbH, Germany).

Field emission scanning electron microscopy (FE-SEM) was carried out in a NOVA NANOSEM microscope (FEI, The Netherlands) using a solid state high contrast detector (vCD) and a trough-the-lens detector (TLD). The emission gun was operated between 5 and 5.7 kV at working distances comprised between 5 and 5.6 mm under high vacuum.

Transmission electron micrographs were obtained using a LEO-910 TEM operating at an accelerating voltage of 80 kV. Samples were deposited over Formvar coated copper grids after carbon deposition. Typically a drop of an aqueous dispersion of the particles to analyze were deposited over the copper grid and allowed to dry at ambient temperature.

Viscosimetry measurements were done in a RVDVII+ PRO Broookfield viscosimeter at 100 rpm at 25 ± 0.5 ºC.

Thermal analysis were conducted in a Seiko SSC/5200 (TG/DTG/DTA) and in a DSC 220CU (DSC).

The mechanical characterization of the prepared materials was performed in an Instron 3345 Universal Testing Machine provided with 500 and 5000 N load cells. Microtensile measurements were performed in a home built universal testing machine using a 200 N load cell, and an optical strain detection system until sample fracture. Typically, a 15 x 2 x 0.2 mm sample was elongated along its longer axis at 5 mm $s^{-1}$ rate,

# 3. Sepiolite Mechanics

According to the concept of nanomaterials research presented in the introductory chapter, the investigation of the structural properties of sepiolite has been largely unattended as compared to the research devoted to its functional properties. However, the investigation of sepiolite as reinforcing filler in nanocomposites has continuously gained momentum (Darder, Lopez-Blanco et al., 2006; Nohales, Solar et al., 2006; Zheng and Zheng, 2006; Chen, Zheng et al., 2007; Duquesne, Moins et al., 2007; Xie, Zhang et al., 2007; Fernandez-Saavedra, Darder et al., 2008; Bhattacharya, Maiti et al., 2009; Bilotti, Zhang et al., 2009; Fernandes, Ruiz et al., 2009; Chivrac, Pollet et al., 2010; Fernandes, Manjubala et al., 2010). Although little information on the mechanics of sepiolite was available until very recently (Fernandes, Castro et al., 2011), the cited examples refer to the preparation of nanocomposites where the introduction of fibrous clay mineral particles intends to improve the mechanical properties of the selected matrix. This chapter aims at disclosing the mechanical properties of sepiolite as analyzed at different length scales, from macroscopic blocks obtained directly from the pit to the mechanics of single sepiolite fibers.

## 3.1 Mechanical properties of single sepiolite fibers

The elastic properties of single sepiolite fibers were investigated,as detailed in the experimental section, using two main approaches. On the first, topographic “images” of single sepiolite fibers deposited over a nanopatterned silicon chip were imaged at different setpoint forces, using an Atomic Force Microscope. The fiber deflection determined by analyzing the fiber profile longitudinally was plotted against the force used to promote such deformation, and hence the mechanical properties could be estimated. The second strategy consisted on force-volume determinations over an area comprising the fiber to be measured. In this analysis mode, each point of the image (typically a 64 x 64 grid) is measured in force mode, allowing a detailed analysis of the mechanical behavior of every point of the image, including the sepiolite fiber suspended over the patterned well.

### 3.1.1 Sequential topographic images correlated with force measurements for flexural characterization of sepiolite fibers under the AFM

As reported earlier (§ 2.3.1) there are several steps that should be taken into account to effectively determine the mechanical properties of single sepiolite fibers using the topographic imaging approach. The first step requiring characterization is the state of dispersion of sepiolite fibers over the patterned motifs. Such characterization was performed using a FE-SEM over the area that comprises the preselected wells. Figure 3.1 displays two collages of FE-SEM images obtained at the same magnification over two similar silicon chips corresponding to samples 4 and 5. The previous sample chips (1 to 3) were prepared in an unsuccessful manner due to either inefficient functionalization or inadequate sepiolite dispersion. Such image composition covers the whole area

of interest of each chip. The numbered circles indicate possible locations for analysis under the AFM. Samples were named using the following system: SepSiO-X.y.Z, where **X** stands for the silicon chip number, **y** stands for the cantilever used for the determination (*a* for cantilever with elastic constant equal to 0.76 $N.m^{-1}$ and *b* for cantilever with elastic constant equal to 1.74 $N.m^{-1}$) and **Z** stands for the fiber location within the silicon chip, marked circle numbers in figure 3.1.

After the exhaustive determination of the single sepiolite fibers hanging over the pre-selected motifs, the mechanical properties of the fibers were investigated by AFM. For the sake of brevity only the fibers whose conditions were considered optimal are addressed. The other fibers presented different circumstances that could compromise the inference of sepiolite's mechanical properties. The most common causes behind the elimination of such fibers were insufficient adhesion to the substrate (causing the probe tip to drag the fibers away from the motif), the existence of fiber aggregates that appeared as a single fiber under the FE-SEM or fiber fracture during location or measurement with the AFM. Any of the previous causes would render non-representative measurements that would certainly maximize the error of the determinations.

Figure 3.1 summarizes the determinations performed on six sepiolite fiber-AFM tip pairs that were evaluated using the sequential images method. The samples were imaged at different setpoint conditions that ranged from 3.4 to 74.7 nN as quantified by the force determinations performed in between each image. The fiber profile obtained in each of the conditions was analyzed and the deflection of the fiber was plotted against the applied force. Such force-deflection plot is helpful to qualitatively characterize the elastic properties of sepiolite fibers as it configures a simple relationship between the applied force and the measured deflection, without the assumption of any mechanical model or geometric constraints. The appearance of a linear trend, whatever the slope, confirms the expected linear relation between the applied force and the measured deflection,

and thus indicates the absence of unexpected features such as fiber breakage, fiber displacement or overcoming the fiber elastic limit.

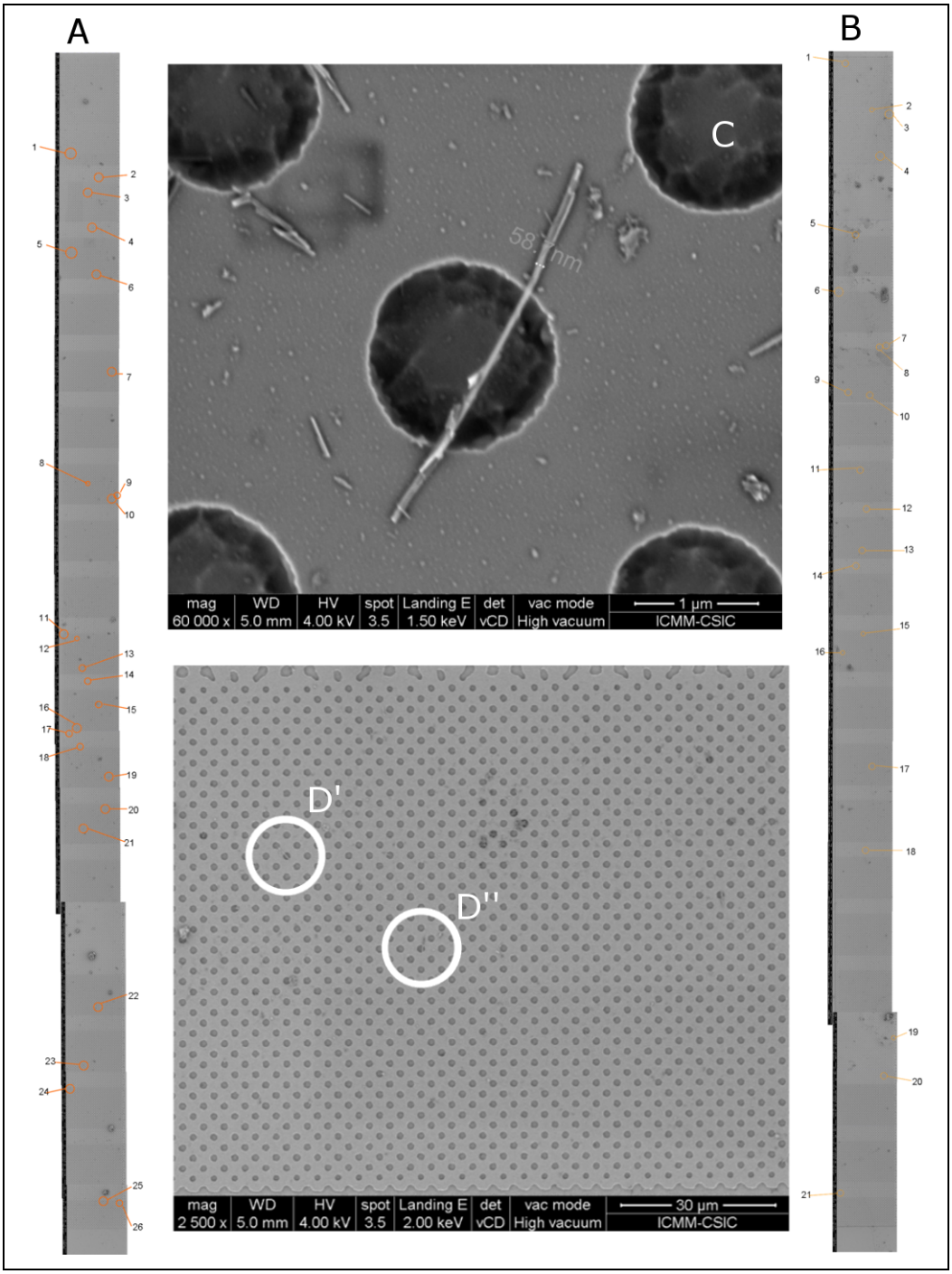


**Figure 3.1 –** FE-SEM images identification of single sepiolite fibers deposited over the Si substrates. A) Chip SepSiO4, B) Chip SepSiO5, C) detail of fiber 1 in chip SepSiO5 and D' and D'') detail of fibers 2 and 3, respectively on chip SepSiO4

As can be observed from figure 3.2 the response for each sepiolite fiber-AFM tip pair seems to be linear. Nevertheless, it is clear that the different tested systems produce notably different responses between the applied force and the measured fiber deflection. In fact, to achieve comparable values, some sort of normalization is required. Such normalization is achieved in two steps. Firstly, the geometrical characteristic of the system have to be clearly defined so both the applied force and the measured deflection are converted to applied stress and bending strain, respectively. Secondly, a mechanical model governing the response of the studied material to an applied force is critical and must be defined.

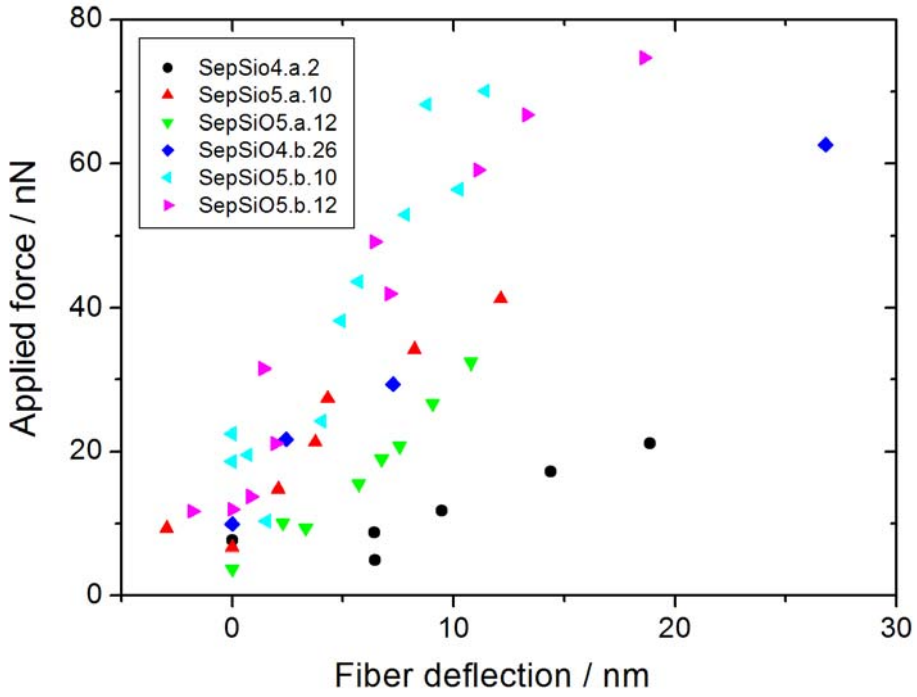


**Figure 3.2 –** Force vs. fiber deflection results measured under the AFM of six samples.

The first consideration regards the geometry of sepiolite fiber hanging over the nanosized well. As stated previously and depicted in figure 3.1C, sepiolite particles present a fiber-like morphology and high aspect ratio. When placed over a gap whose dimensions are closest to the fiber length than to the fiber

diameter, and taking into account that the fiber cross section is approximately circular, it becomes possible to consider the sepiolite fiber as a slender rod.

The bending of rods under transverse load can be described using the Euler-Bernoulli beam theory. Nevertheless, to apply such model, it should be taken in consideration that it was developed for isotropic materials. Being a crystalline material with an orthorhombic crystalline arrangement, sepiolite presents different strain tensors along its crystalline directions. When using the Euler-Bernoulli beam theory to investigate the mechanics of sepiolite, it becomes clear that the drawn information regards a “general” value for the elastic modulus of sepiolite. Consequently, the approaches and numeric values obtained from this point onwards on the mechanical characterization of sepiolite assume an approximation of the behaviour of sepiolite to an isotropic material and as such are to be regarded with caution.

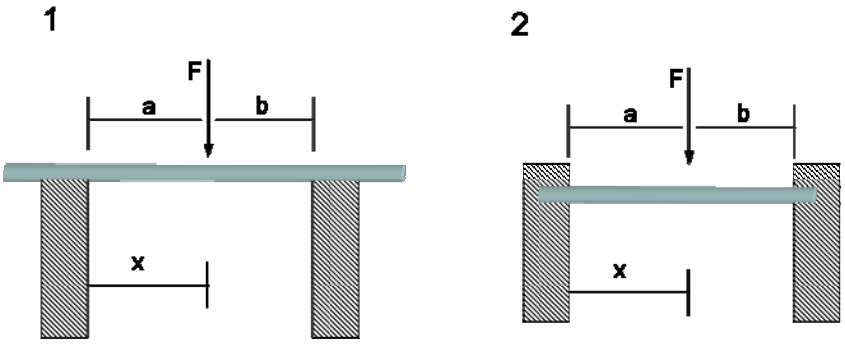


**Figure 3.3 –** Schematic illustration the two types of support for the bending of slender rods. 1) the simply supported beam case and 2) the clamped-clamped beam. **a** and **b** define the point of application of the force, where a+b corresponds to **L**, the hanging length of the rod, and **x** defines the point where the correspondent deformation is measured.

Gere and Timosheko (Gere and Timoshenko, 1998) have thoroughly reviewed some of the classic cases that derive from the Euler-Bernoulli beam theory. The two most likely cases to occur in a beam which is supported on both ends are: 1) the simply supported beam and 2) the clamped-clamped beam. These two cases refer mainly to the type of interaction between the beam and the structure that supports it. In the first case the rod is merely standing over the supporting

structure, whereas in the second case the rod ends are embedded on the structure itself. Although conceptually quite similar, these two cases reflect one different boundary condition which decisively influences the bending of the rod. Such difference resides in the moment of inertia M, of the rod ends with respect to the supporting structure. In the simply supported beam case, M is non-zero while in the clamped-clamped beam model the moment of inertia M, is zero (Gere and Timoshenko, 1998). Figure 3.3 depicts both possibilities.

One major factor accounts for the choice of the clamped-clamped beam model relates to the fact that the beam (sepiolite fiber) is functionalized with an amino-terminated organosilane and the supporting structure (silicon chip) is modified with an epoxy terminated moiety. These two functional groups react in a straightforward manner to generate a strong covalent bond, which promotes a strong adhesion between the fiber and the substrate. Given the nature of the established bond and the extended area of contact between the sepiolite fiber and the chemically modified chip, it is reasonable to assume that the clamped-clamped beam model is more fitted to describe the silicate fiber under load than the simply supported model. The behavior of a clamped-clamped beam under load is described by equation 3.1.

$$\delta = \frac{F}{6EI_0}\left(\frac{b^2x^3}{L^3}(L+2a) - \frac{3ab^2x^2}{L} - \langle x-a\rangle^3\right), \quad \begin{cases} x \le a, \langle x-a\rangle^n = 0 \\ x > a, \langle x-a\rangle^n = (x-a)^n \end{cases} \qquad \text{(eq. 3.1)}$$

Where **δ** corresponds to the measured deflection, **F** to the applied load, **E** to the elastic modulus, **a**, **b**, **x** and **L** to the location where the load is applied, and the area moment of inertia of the cylinder rod, $I_0$ is defined by equation 3.2,

$$I_0 = \frac{\pi r^4}{4} \qquad \text{(eq. 3.2)}$$

Although the Euler-Bernoulli beam theory takes into account the possibility to deflect the beam in one point while measuring or calculating the deflection in another one by appropriate use of the step function (between brackets) that case is not possible under the AFM experimental setup. This is due to fact that in an AFM the element that applies the force is the same that "reads" the deflection, which in turn means that **a = x**. Such condition simplifies the equation to the following form:

$$\delta = \frac{F}{6EI_0}\left(\frac{b^2x^3}{L^3}(L+2a) - \frac{3ab^2x^2}{L}\right) \qquad \text{(eq. 3.3)}$$

A brief analysis of equation 3.3 elucidates which are the key elements that allow to calculate the elastic bending modulus of single sepiolite fibers: the deflection, the applied load, the fiber radius and the location of the point of load.

Since the AFM topographic images (if accompanied by a measurement of the applied force at each setpoint voltage) provide the whole set of information required by equation 3.3, it is then possible to describe the elastic properties of sepiolite fibers using this approach under the AFM. Table 3.1 summarizes the main elements necessary to carry out the calculations of sepiolite fiber elastic modulus. As observed, the values for the elastic modulus do not differ considerably, being the average value for the elastic modulus of sepiolite fiber (determined with the current approach) around 11.5 GPa with a standard deviation (sd) of 5.1 GPa. Although the sd is large when compared to the absolute value of sepiolite's modulus (*circa* 50 %), it is important to take into consideration some aspects regarding the application of non-standard methods for mechanical characterization of nanomaterials.

**Table 3.1 –** Summary of the topographic images obtained from the selected fibers, the corresponding conditions of measurement and the elastic modulus obtained for each sample.

| Topographic image of deposited fibers | Sample Name | k / $Nm^{-1}$ | Sensitivity / $nmV^{-1}$ | Fiber Dimensions / nm | E / GPa |
|---|---|---|---|---|---|
| 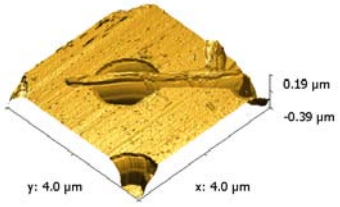 | SepSio4.a.2 | 0.76 | 63.38 | a, x = 616<br>b = 872<br>L = 1488<br><r> = 37.8 | 12.67 |
| 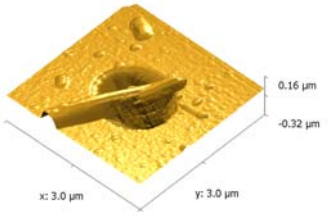 | SepSiO5.a.10 | 0.76 | 63.38 | a, x = 474<br>b = 868<br>L = 1440<br><r> = 51.5 | 5.85 |
| 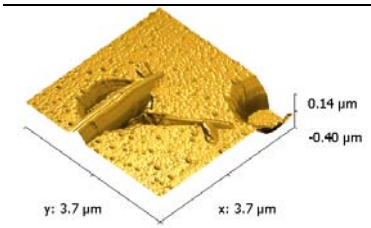 | SepSiO5.a.12 | 0.76 | 63.38 | a, x = 721<br>b = 779<br>L = 1500<br><r> = 58.8 | 9.09 |
| 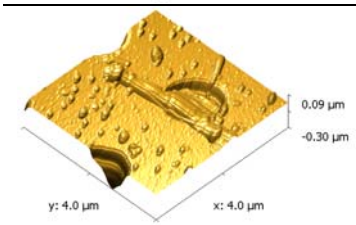 | SepSiO4.b.26 | 1.74 | 64.85 | a, x = 430<br>b = 486<br>L = 916<br><r> = 30.0 | 20.85 |
| 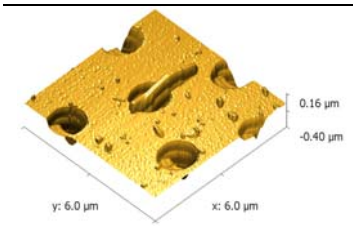 | SepSiO5.b.10 | 1.74 | 64.85 | a, x = 482<br>b = 962<br>L = 1444<br><r> = 52.6 | 10.92 |
| 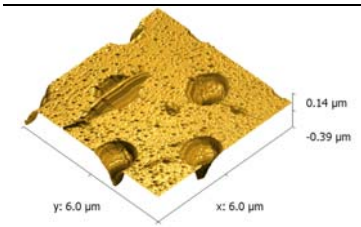 | SepSiO5.b.12 | 1.74 | 64.85 | a, x = 721<br>b = 779<br>L = 1500<br><r> = 61.5 | 10.07 |

The employment of equipment whose purpose is other than the currently explored may imply some source of error. This is especially relevant if the method used to adapt the AFM to a force analyzer has a handicap on its own.

In this case such handicap consists in the time gap between the imaging of the sample and the force determination at the same setpoint voltage. Because the AFM is drift prone, meaning that the applied force at a given voltage is likely to slowly change with time, it is possible that in some cases the effective force applied over the hanging fiber and the calculated force differ. Also the calibration of the AFM cantilever and the equipment's sensitivity measured by the user are likely to be affected by error. In the case of the cantilever calibration various simplifications and approximations are used to link the thermal noise resonant frequency to the cantilever elastic properties (Cook and et al., 2006). Also the calculation of the experimental setup sensitivity is dependent on the approximation of the silicon substrate to an infinitely hard (non-deformable) surface. Another source of error is inherent to the geometry of the experiment itself. The accuracy of rod bending models, either simply supported or clamped, is notably dependent on the precision of the geometrical term. When analyzing eq. 3.3 it is clear that the term between curved brackets is solely related to the dimensions of the rod and to the point where the force is applied. Moreover, a brief dimensional analysis leads us to ascertain that the corresponding term's dimension is $nm^3$, which suggests that a small deviation in the measurement of either **a**, **b**, **L** or **x** might have dramatic consequences on the final value of the elastic modulus. Another potential source of error regards the radius of sepiolite fibers. Since the calculus of the elastic modulus is dependent on the second moment of inertia $I_0$, defined in equation 3.2, it becomes evident that there is a fourth power dependence on the radius dimensions. Given that the fiber section (and hence its radius) is slightly variable along the fiber axis, some degree of error is expectable in the determination of the elastic properties of sepiolite. In fact, taking into account the preceding factors, the obtained results for different fibers, under different experimental setups (two AFM probes and two different silicon chips) seem especially coherent.

### 3.1.2 Determination of the mechanical properties of single sepiolite fibers using Force-Volume method

As previously referred, the use of “Force Volume” mode allows to collect spatially resolved force-distance curves along a sample (Butt, Cappella et al., 2005). In the case here reported, the determination of the mechanical properties of sepiolite using the Force-Volume mode makes use of the same mechanical concepts about the bending of isotropic rods, briefly disclosed on the preceding section (§ 3.1.1). The most notorious difference is thus of technical nature. Novel experimental procedures such as the reported in the previous section for the determination of sepiolite’s mechanical properties are (as discussed before) error prone and require validation. Since at the present state of the art, few other techniques seem to be able to cope with fibrous particles so small in dimension (McNeil and Grimsditch, 1993; Zhang, Wei et al., 2009a), other approaches based on the same technique are of great utility. In this context force-volume determinations are a valuable asset. More than a technical variation over the previously reported methodology, the change in experimental procedure relates to two main goals. In first place the need to validate the data (and thus the methodology) used in the previous approach, and as a second objective to explore the consistency between these two approaches which have not been used together in the bibliography (Salvetat, Bonard et al., 1999; Bowen, Lovitt et al., 2000; Salvetat-Delmotte and Rubio, 2002; Koenders, Yang et al., 2009).

Sample SepSiO5.b.12 was measured under force volume. It is important to note that the amount of information generated by a force-volume analysis is immense. Taking into account that the “regular” force-distance curve consists on an array of 1024 deflection points (corresponding to 512 points per direction of the piezo element), a standard 64 x 64 analysis in force mode corresponds to

4096 arrays of 1024 points. Being each of the mentioned arrays associated with one specific location in the sample. In order to cope with the amount of information generated two approaches are possible. The first is to develop software routines that efficiently analyze data, the second is to pin-point regions of interest and analyze them individually. In this work this last strategy was selected. Figure 3.4 depicts the topographic profile of the sample obtained in this analysis mode. Graphical data **a'** and **b'** reflect the force analysis performed on points **a** and **b** of the sample respectively.

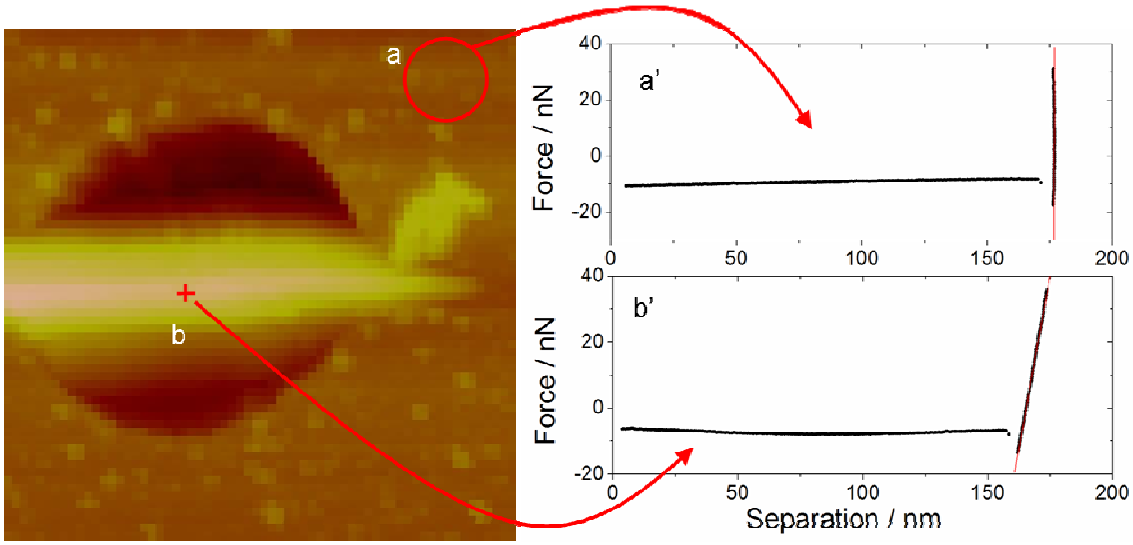


**Figure 3.4 –** Topographic image of sample SepSiO5.b.12 as imaged by Force Volume (left picture) and force profiles from two different points of the sample. Point **a**, the silicon substrate, shows a force profile **a'** typical of an infinitely hard surface with a quasi-vertical slope in the contact regime. On the other hand point **b**, half-way of the hanging profile for the sepiolite fiber, shows an interaction profile that directly reflects the relation between the applied force and the fiber deflection.

The possibility to ascribe a force (or interaction) profile to each point of the sample being analyzed permits an exhaustive examination of the mechanics throughout the sample. In the depicted case, the difference in slopes measured on the silicon substrate and on the hanging sepiolite fiber confirms the adequacy of the method to mechanically discriminate between compliant (sepiolite hanging over suspended length) and non-compliant surfaces (silicon

substrate). The slope from the contact regime was evaluated at mid-way of the hanging profile for samples SepSiO5.a.12 and SepSiO5.b.12 (i.e. same sepiolite fiber, same substrate but using a different AFM probe) and the obtained values are 2.53 and 4.24 $nN.nm^{-1}$ respectively. When such values are introduced into equation 3.3, it results that the elastic modulus of the sepiolite fiber measured with two different AFM probes in Force Volume mode is 9.45 and 13.20 GPa respectively. These values are a strong confirmation of the results obtained using the sequential topographic imaging strategy disclosed in the initial part of this section (§ 3.1.1), which were 9.09 and 10.92 GPa respectively.

Another relevant question regards the absolute value of fibrous silicate elastic modulus. Although few works are available on the mechanical properties of single clay particles, it is worth to compare these results with the few reported for other clay minerals. In general most articles devoted to the mechanical characterization of natural or synthetic silicates rely in one of the following methods: AFM or nanoindentation experiments, Brillouin scattering, neutron scattering or theoretical calculations. Given the complexity of anisotropic materials such as clays, AFM technique usually produces averaged values for the mechanical properties of clay minerals. Zhang and co-workers (Zhang, Wei et al., 2009a) have determined the “average” elastic modulus of rectorite and muscovite clay mineral tactoids by nanoindentation to be 18 and 79 GPa, respectively. Although the referred work generated considerable discussion over the definition of clay single crystal, (Bobko, Ortega et al., 2009; Zhang, Wei et al., 2009b) the elastic values determined were not disputed. Kunz et al. (Kunz, 2009) have taken the determination of the mechanical characteristic of layered silicates one step further. They have calculated the mechanical resistance opposed by fluorhectorite tactoids deposited over microstructured silicon chips and correlated it with the tactoid height. By applying the plate theory they have reached a value for fluorhectorite’s $C_{33}$ elastic modulus of 21.9

GPa. On the other hand, techniques such as Brillouin scattering allow a much more comprehensive characterization of the different elastic moduli of layered silicates. McNeil and Grimsditch quantified thirteen different elastic moduli for muscovite using this technique. Such values ranged from negative values (which is incompatible with particle stability (Lakes, Lee et al., 2001)) to values around 180 GPa. The most extended strategy to calculate the mechanics of clay minerals is based on simulations. Mazo et al. (Mazo, Manevitch et al., 2008) have recently calculated the elastic tensors of a hydrated montmorillonite using molecular dynamics methods based on the CLAYFF (i.e. clay force field) developed by Cygan et al. (Cygan, Liang et al., 2004). The so obtained elasticity values also present considerable scattering, the elasticity tensors varying between 2 and 180 GPa according to the hydration state and crystal orientation.

In summary, the elastic values calculated for sepiolite using the AFM cannot be objectively compared to the results reported in the bibliography. Although the majority of silicates whose mechanical properties have been investigated present similar structural units as sepiolite, such as silicon tetrahedra and magnesium octahedra, they are all arranged in layered manner. This layered structure gives rise to mechanical responses typical of plates. On the other hand, sepiolite is eminently fibrous in nature and therefore its mechanics is not comparable to the layered counterparts. The only comment that is possible on the mechanical properties of sepiolite is that the determined values stand within the wide dispersion of values determined for other clay minerals.

One of the most interesting characteristics of sepiolite is its diverse hierarchical order. When it is not in the form of isolated crystals as in the case evaluated this far, sepiolite presents itself as aggregates of fibers composing a bulk material. In order to investigate the mechanics of this material in its massive state and to compare its properties with the isolated fibers other techniques such as nanoindentation were used

## 3.2 Mechanical properties of sepiolite blocks by nanoindentation

One interesting aspect of nanomaterials is their expected size dependency behavior in numerous properties. Although such size dependence is usually related with the functional properties of nanomaterials (optical, electric, magnetic, etc.) it has also been described in structural properties (Bledzki and Gassan, 1999; Miller and Shenoy, 2000). To study a different length scale from the previously reported with the AFM, nanoindentation was selected as characterization technique half-way between the nano- and macroscale . In the presented case a Berkovich indenter that typically interacts with a sample surface area of around 10-100 $um^2$ was used. This technique implies thus, a variation over the previously studied length scale (the single sepiolite fiber cross section) of more than four orders of magnitude.

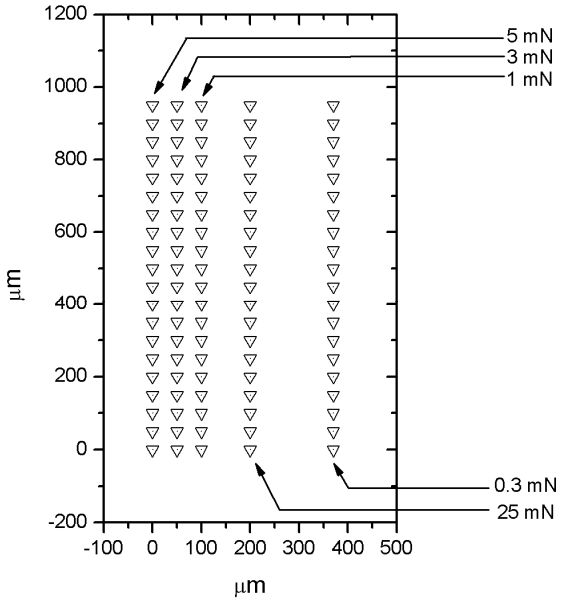


**Figure 3.5 –** Indentation scheme over the sepiolite block surface. Each load condition was essayed 20 times covering an area of 950 x 370 $\mu m^2$. The indentations performed under the same conditions were performed 50 µm apart in a straight line.

Figure 3.5 summarizes some of the measurements performed on sepiolite blocks directly obtained from the pit. The blocks were previously machined into approximately 5 x 5 x 5 $mm^3$ cubes and its surface successively polished with SiC paper into a smooth, scratch free surface under naked eye inspection. The sample surface was evaluated by means of 20 indentations per maximum load selected, 0.3, 1, 3, 5 and 25 mN. Figure 3.6 depicts the sampling points within the sepiolite block surface.

The force vs. indentation depth results obtained from the first indentation at each of the maximum loads selected are depicted in figure 3.6.

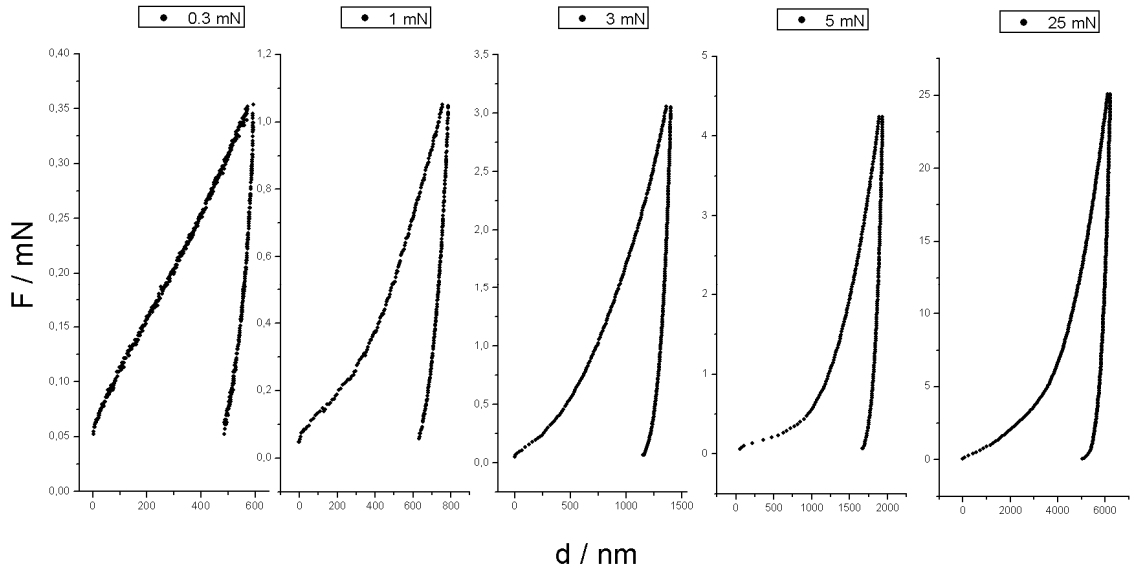


**Figure 3.6 –** Nanoindentation profile examples of the five different maximum loads essayed. From left to right 0.3, 1, 3, 5 and 25 mN of maximum load.

In order to evaluate the elastic properties of the sample the unloading curve is fitted to a power-law behavior between 100 and 20 % of maximum load. Force-depth curve in nanoindentation does not allow a direct determination of the sample mechanical properties. Instead, the elastic properties of the combination of the sample and the experimental equipment (the reduced modulus, $E_r$) can be deduced from the Oliver-Pharr model (Oliver and Pharr, 2004). Equation 3.4 describes the reduced modulus as a function of the indented area and the

stiffness **S**, which is the relation between the applied force and the unloading indenter height, S=dF/dh in the unloading curve.

$$S = \beta \frac{2}{\sqrt{\pi}} E_r \sqrt{A} \qquad \text{(eq. 3.4)}$$

where **β** stands for an empirical correction factor related to the indenter geometry. In this case the β factor was set to the unity. The factor **A** stands for the projection of the irreversibly indented area after the indentation experiment. Because it was not possible to determine such area neither by AFM nor FE-SEM microscopies after the indentation tests, A was defined according to equation 3.5 as an ideal relationship between the Berkovitch indenter form factor and the plastic indentation depth, **Pd** (Oliver and Pharr, 2004).

$$A = 24.5 Pd^2 \qquad \text{(eq. 3.5)}$$

In order to obtain the elastic modulus of the sample it is necessary to separate the effects derived from the experimental setup and the sample itself, which together account for the $E_r$. According to the theory of contact mechanics, the elasticity of the sample can be determined by direct application of equation 3.6 (Johnson, 1985),

$$\frac{1}{E_r} = \frac{1-\upsilon_i^2}{E_i} + \frac{1-\upsilon^2}{E} \qquad \text{(eq. 3.6)}$$

where $\nu_i$ and **ν** correspond to the indenter and sample Poisson ratio and $E_i$ and **E** to the indenter and sample elastic modulus respectively. Given that both the values of Poisson ratio and elastic modulus for diamond (the Berkovitch indenter material) are known, $E_i$ = 1141 GPa and $\nu_i$ = 0.07, it is possible to estimate the elastic modulus of sepiolite (Oliver and Pharr, 2004). However, because Poisson's ratio of sepiolite is unknown, some assumptions have to be

made. Excluding auxetic materials, which display negative values for Poisson's ratio, most materials present values ranging between 0 and 0.5, its upper physical limit (Gercek, 2007). In order to fully explore the possible values for the elastic modulus of sepiolite, both values were taken into account to calculate the limit values for the sepiolite's elastic modulus.

Other useful data that can be collected using nanoindentation regards the hardness of the sample, H. According to Oliver and Pharr (Oliver and Pharr, 2004), such measure can be directly obtained by dividing the maximum applied load by the projection of the plastically deformed indent, as disclosed in equation 3.7.

$$H = \frac{F_{\max}}{A} \qquad \text{(eq. 3.7)}$$

Table 3.2 summarizes the results regarding the elastic modulus and the hardness measurements on sepiolite.

**Table 3.2 –** Reduced elastic modulus, sepiolite elastic modulus calculated for $\nu$=0 and $\nu$=0.5 and hardness average data obtained by nanoindentation of sepiolite blocks. Each of the indentation conditions (five different maximum loads) were repeated 20 times. The final value (noted Average) corresponds to the average of averages for the different moduli and hardness.

| F max / mN | n | Er / Gpa | E sep $\nu$=0 | E sep $\nu$=0.5 | H / Gpa |
|---|---|---|---|---|---|
| 0.3 | 20 | 2.96 | 2.96 | 2.22 | 0.138 |
| 1 | 20 | 2.77 | 2.77 | 2.08 | 0.098 |
| 3 | 20 | 3.43 | 3.43 | 2.58 | 0.098 |
| 5 | 20 | 2.94 | 2.94 | 2.21 | 0.065 |
| 25 | 20 | 2.56 | 2.56 | 1.92 | 0.048 |
| Average | | 2.93 | 2.93 | 2.20 | 0.090 |

Taking into account that each of the reduced elastic modulus values determined by nanoindentation can be associated with a specific localization (Fig. 3.5) it is possible to map the elastic properties of the sepiolite block. This feature depicted in figure 3.7 is especially useful to determine the degree of

homogeneity of the sepiolite surface, which in turn can be a good measure of the degree of order of the sepiolite blocks.

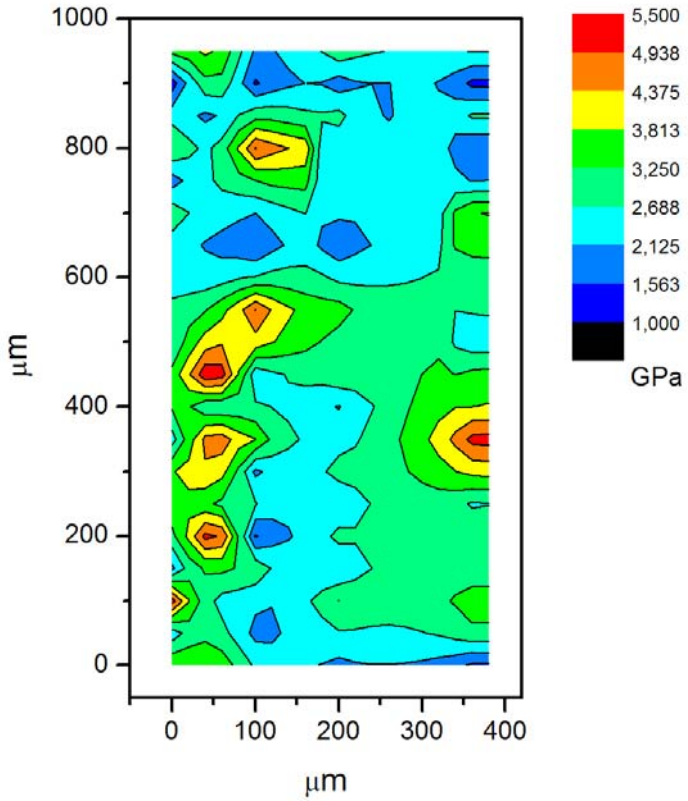


**Figure 3.7 –** Reduced modulus $E_r$, map in GPa of sepiolite block surface obtained from 100 indentations under different loading conditions. The mapping was calculated by converting $E_r$ values to a bidimensional matrix defined by the position of each indent.

Figure 3.7 illustrates how the elastic properties of sepiolite vary along its surface. In the studied region, the reduced modulus spanned from 1 to 5.5 GPa with an average value of 2.93 GPa, demonstrating the intrinsic heterogeneity of the silicate surface. The reasons behind such variability can be numerous. Sepiolite blocks are composed of aggregates of individual sepiolite fibers. When such aggregates present high packing density, it is expectable to obtain higher elastic modulus than in other zones where the fiber packing is less dense. Other reasons may relate to preferential orientation of sepiolite fibers in defined domains within the sepiolite block. In such case, areas where sepiolite fibers are oriented with a less compliant crystal orientation would naturally present

higher modulus when compared to the rest of the surface. Other hypothesis relate to the presence of impurities that may drive the elastic modulus of specific areas within the sample to higher elasticity values. A more detailed analysis of the reasons behind the heterogeneous mechanical behavior of sepiolite block falls out of the scope of this dissertation and will not be addressed.

The most notable observation related with the nanoindentation measurements performed on sepiolite blocks is its inconsistency with the values obtained for the individual fibers. While for single sepiolite fibers the elastic modulus measured under the AFM following two different strategies was around 11 GPa, the values determined under nanoindentation measurements are almost one order of magnitude below. In order to investigate the extension of the elastic properties size dependence, sepiolite was also evaluated in the form of macroscopic blocks using a standard universal testing machine in compression (see following section § 1.3).

## 3.3 Mechanical properties of macroscopic blocks of sepiolite

Sepiolite blocks obtained from the Vallecas-Vicálvaro deposit were machined to approximately 10 x 10 x 10 $mm^3$ blocks for compression testing. Figure 3.8 depicts the cutting process from a single monolith.

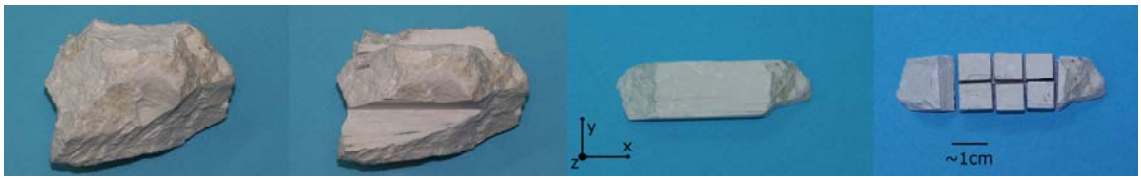


**Figure 3.8 –** Cutting process of six sepiolite monoliths for mechanical testing from a single sepiolite block. The cutting process allowed preserving information about the orientation of the single monoliths with respect to the main block.

**Table 3.3 –** Summary of the mechanical properties of sepiolite blocks determined by compression testing.

| Sample nº | Orientation | E / Mpa | $\varepsilon_{break}$ / % | $\sigma_{break}$ / MPa |
|---|---|---|---|---|
| 1 | xx | 430 | 8,94 | 33,3 |
| 2 | xx | 366 | * | * |
| 3 | yy | 409 | 8,10 | 31,7 |
| 4 | zz | 430 | 7,57 | 27,8 |
| 5 | zz | 354 | 8,14 | 26.0 |
| **Average** | | 398 | 8,19 | 29,7 |
| **sd** | | 35,8 | 0,56 | 3,38 |

***** Sample 2 did not experience fracture because it surpassed the load cell security limit (4.5 kN) before reaching fracture.

The cutting process proceeded in such manner that it was possible to maintain information about the orientation of each single sepiolite monoliths with respect to the main block. Such information is relevant as it allows discriminating the mechanical properties according to the direction of the compression experiment.

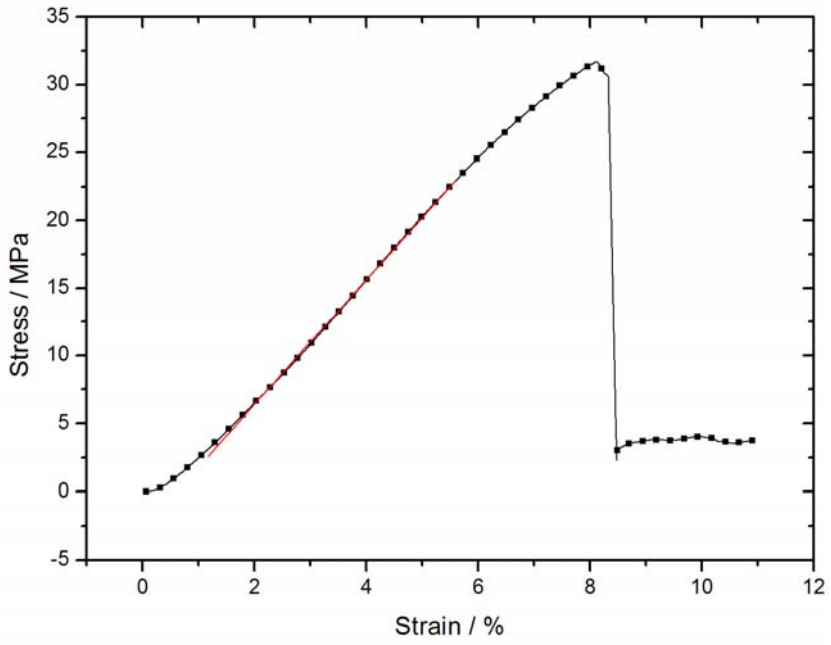


**Figure 3.9 –** Stress strain diagram in compresion for sepiolite block number 3 at 5 mm.min$^{-1}$ crosshead speed.

The obtained results from several experiments in the three different directions indicate the absence of clear detectable macroscopic anisotropy of the mechanical properties. Table 3.3 gathers information recovered from the standard compressive experiments performed on sepiolite blocks.

The compression behavior of sepiolite blocks can be observed in figure 3.9. It is characterized by a roughly linear (thus elastic) trend until around 8% deformation where it suffers the first fracture. This first crack showed random orientation among the tested blocks and generally implied a complete destruction of the sample.

## 3.4 Discussion of the multiscale mechanics of sepiolite

The first element to discuss regarding the mechanical characterization of sepiolite is its variability across the different length scales tested. In fact, from nanoscale using the AFM, to macroscale using the universal testing machine, sepiolite presents considerably different elastic moduli. Figure 3.10 displays the elastic properties of sepiolite at different length scales in a log-log plot.

As depicted in figure 3.10, not only the elastic modulus varies along the length scales but also these two parameters are related trough a linear trend in the log log plot. Such behavior follows a power law relationship of form $y = ax^b$, where a = 34.8 and the exponent b = -0.15. Typically, the reasons behind the scaling of the mechanical properties with the length scale can be of two main types. The first is characterized by a dependence of the mechanical properties along closely related dimensions (i.e. in the same order of magnitude). Chen et al., for example, have demonstrated the effect of the diameter of ZnO nanowires (NWs) on their elastic modulus (Chen, Shi et al., 2006). They have reported a surface stiffening effect, suggesting that the thinner are the nanowires the more relevant is such phenomenon. Their experimental data shows how the elastic

properties of the nanowires vary between the bulk value for ZnO monoliths (140 GPa) and around 200 GPa for 17 nm NWs. On the opposite side of the elastic properties dependence with scale, is the case of materials who display variable order across different scales.

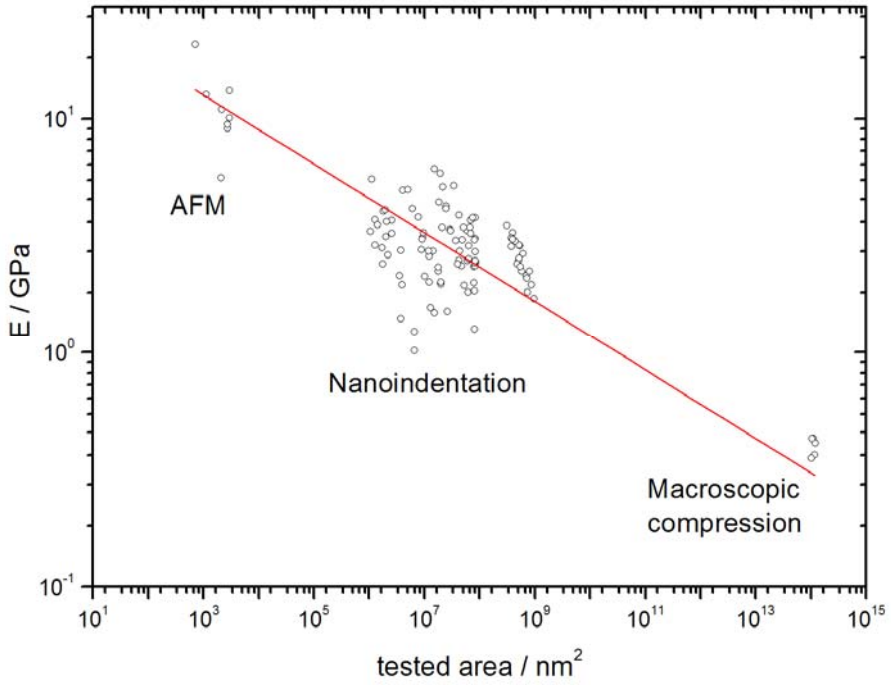


**Figure 3.10 –** Graphical representation in logarithmic scale of the elastic properties of sepiolite according to the length scale/technique employed. The length scales are defined as: for AFM, the fiber average cross-section; for nanoindentation experiments, the irreversibly indented area ($24.5xPd^2$) in each experiment; and for macroscopic compression experiments, the monolith cross-section.

One of the most paradigmatic examples is that of cellulose (Bledzki and Gassan, 1999). The paper by Bledzki and Gassan reports the elastic modulus values for cellulose across various scales. They have concluded that the elastic modulus value was inversely related to the scale at which the property was measured. The lowest scale calculated (using computational data) was the single molecular chain of cellulose in a crystalline arrangement, which displayed a Young's modulus of 250 GPa. As the measurement scale widened, the correspondent Young's modulus tended to diminish. So, for cellulose

microfibrils the elastic modulus had descended to 70 GPa and for single pulp fibers the value was even lower, 40 GPa. The extreme of the scale was wood itself, that presented a modulus of 10 GPa. It seems thus, that scaling of the elastic properties is, in the case of cellulose-wood materials dependent on the intrinsic order of the system being measured.

Another closely related concept to the order-disorder of a system composed of multiple particles (taking the upper scale materials such as wood and pulp fibers as a complex system built upon individual cellulose units) is its density. If the material order tends to diminish, that means that its apparent density will also diminish as a result of the less effective packing density of individual units.

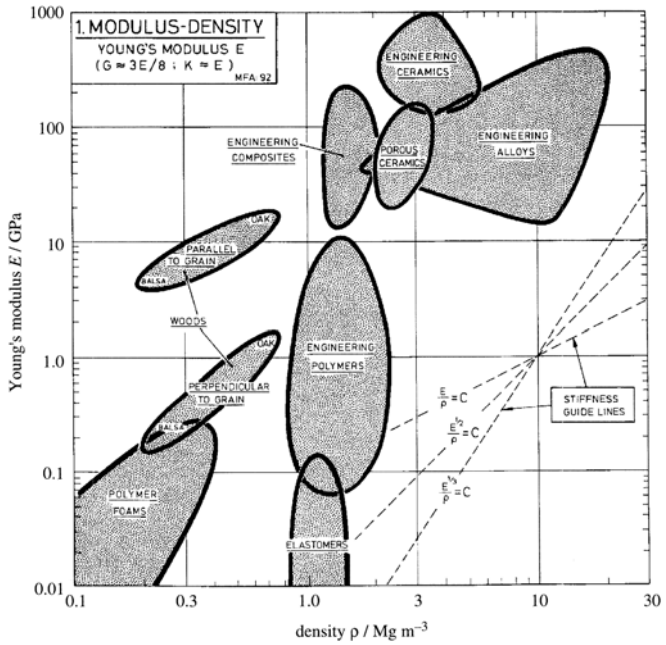


**Figure 3.11 –** Materials property chart as proposed by Ashby and co-workers (Ashby, Gibson et al., 1995). Reproduced with permission from the Royal Society.

Ashby has developed the concept of mechanical property charts (Ashby, 1989). In a later paper (Ashby, Gibson et al., 1995), devoted to the analysis of natural materials based on the mechanical chart approach, Ashby and co-workers have disclosed the close relationship between the material density and its elastic modulus. Figure 11 taken from reference (Ashby, Gibson et al., 1995) discloses

the relationship between the elastic modulus and density for several families of materials.

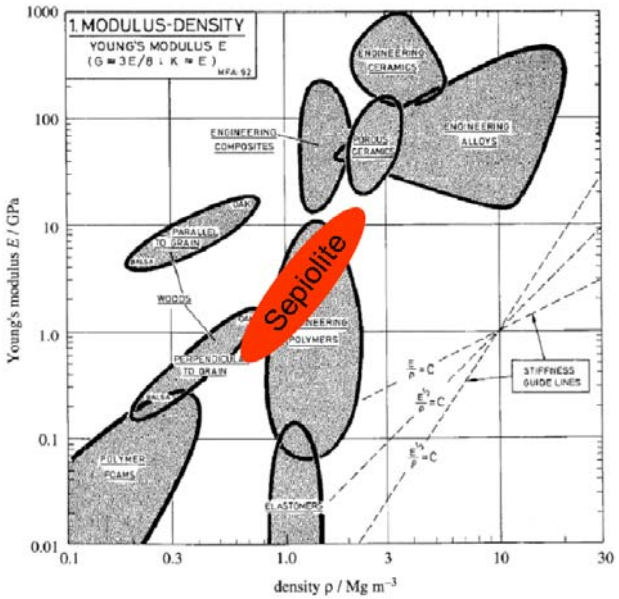


**Figure 3.12 –** Materials property chart including sepiolite measured across different scales. Adapted from reference with permission from the Royal Society (Ashby, Gibson et al., 1995).

The case of sepiolite seems to follow the same kind of behavior reported for cellulose. Here, order (and thus density) seems to be the keystone to understand the elastic properties variability. Since a single sepiolite fiber corresponds to a single sepiolite crystal, the AFM measurements (which were measured over single fibers) correspond to the highest order of sepiolite. It is therefore expected that its mechanical properties are maximized. On the other hand when analyzing sepiolite blocks (by macroscopic compression tests) the material is at its highest disorder level, because it is composed of randomly oriented sepiolite fibers aggregated into a monolith. Such disorder is consistent with the low value determined for the monolith's elastic modulus. In the sepiolite case, the density relation with the elastic modulus also seems to apply. Calculating the theoretical density for sepiolite based on its half-unit cell formula ($Si_{12}O_{30}Mg_8(OH)_4(H_2O)_4 \cdot 8H_2O$) and its unit cell volume of 1880 $A^3$ results in a theoretical density value around 2.2 $g.cm^{-3}$. On the other hand, bulk sepiolite

was historically called “Meerschaum”, which literally translated from German language means sea-foam. Such name was given after the whitish blocks of sepiolite found floating in the sea. That information indicates that the specific gravity of sepiolite blocks is inferior to that of sea water. Also, laboratory measurements performed on sepiolite blocks with a clearly defined geometry rendered specific gravity values around 0.7 $g.cm^{-3}$. Such specific gravity values also agree with the previously proposed relationship between the elastic modulus of bulk sepiolite and its density.

Another interesting aspect of the mechanical characterization of sepiolite is the determination of an absolute value describing its elastic properties. From the previous measurements it is clear that the disruption of sepiolite blocks into nanodimensional particles is advantageous. In fact, in its fundamental unit size, the single crystalline nanofiber, sepiolite presents an elastic modulus of around 11 GPa, which can be useful in numerous reinforcing purposes of low Young’s modulus matrices.

## 3.5 Concluding remarks

In summary, sepiolite’s mechanical properties could be determined at several length scales using different techniques. The results obtained using the AFM in two distinct operation modes were coherent, consisting in significant breakthrough in two different areas. The first is the knowledge of the elastic properties of single sepiolite fibers, a nanomaterial whose structural properties had not been previously determined. This result opens way to the rational use of sepiolite for mechanical reinforcing purposes as it permits to estimate (from different composite models) the elastic properties enhancement induced by the addition of the fibrous silicate. The second area is that of the application of AFM techniques to the determination of the mechanical properties of nanomaterials. Although force distance curves and Force Volume mode had been widely

reported as AFM characterization tools, there has been a continuous omission in the literature regarding the reproducibility of results between techniques. The results here reported describe that consistent results between the two approaches are possible.

Another important conclusion regards the strikingly different mechanical properties at different length scales. Using the AFM over single sepiolite fibers the elastic modulus of sepiolite is around 11 GPa, whereas sepiolite blocks measured with the nanoindenter and under macroscopic compression display much lower values around 3 and 0.4 GPa, respectively. These results suggest that the order of sepiolite fibers (also reflected in its apparent density) has a critical effect over the mechanical properties of the studied silicate.

# 4. Gelatin-sepiolite bionanocomposites

The reinforcement of polymeric matrices using sepiolite as filler has recently found increasing importance as is revealed by the number of publications devoted to this theme (Olmo, Lizarbe et al., 1987; Galan, 1996; Darder, Lopez-Blanco et al., 2006; Nohales, Solar et al., 2006; Zheng and Zheng, 2006; Duquesne, Moins et al., 2007; Gomez-Aviles, Darder et al., 2007; Fernandez-Saavedra, Darder et al., 2008; Bhattacharya, Maiti et al., 2009; Bilotti, Zhang et al., 2009; Fernandes, Ruiz et al., 2009; Chivrac, Pollet et al., 2010; Fernandes, Darder et al., 2011; Fernandes, Manjubala et al., 2011). In fact, the morphology of sepiolite fibers, which present high aspect ratio, suggests that its reinforcement efficiency when effectively dispersed in a continuous media might be considerable. On the other hand, sepiolite's similarity towards other clay minerals such as montmorillonite or illite, long used as structural and functional fillers in polymer nanocomposites (Kojima, Usuki et al., 1993; LeBaron, Wang et al., 1999; Fornes and Paul, 2003; Wang, Nakajima et al., 2003; Demirkol and Kalyon, 2007; Chen, Evans et al., 2008; Bae, Park et al., 2009), has driven researchers to explore its possible benefits as fibrous counterpart of the mentioned clay mineral fillers.

In this chapter the usage of sepiolite fibers is explored in the context of bionanocomposites, i.e. materials consisting on a biopolymer matrix where nanosized inorganic fillers are the disperse phase. To some extent this class of materials mimics Nature's high performance biological structures such as bone (Fratzl and Weinkamer, 2007), nacre (Ruiz-Hitzky, Darder et al., 2007) or ivory (Su and Cui, 1999). In such examples the inorganic phase (hydroxypatite or aragonite) is assembled to natural polymers such as lustrin, collagen or chitin to create an efficient structural material. In the same manner, the association of sepiolite (whose mechanical properties have been disclosed in the previous chapter) with gelatin (a denaturation product of structural protein collagen) is investigated in this chapter.

## 4.1 Gelatin based bionanocomposites

### 4.1.1 Gelatin-sepiolite hybrids

The understanding of the interactions established between gelatin and sepiolite is fundamental for the preparation of bionanocomposite materials addressed ijn this chapter and also for the preparation of carbonaceous materials which is addressed in the following chapter (§ 5).. One of the most important aspects is the relative quantities of gelatin that can be adsorbed onto sepiolite as it may indicate the affinity between sepiolite, the disperse phase in bionanocomposite and gelatin, the continuous phase. In that sense, the adsorption of gelatin on sepiolite was followed by means of a retention isotherm performed at 60 ºC from water solution. The selection of the temperature is related with the conformational state of gelatin and not with a thermodynamic requirement for the adsorption of the biopolymer. As seen previously (§ 2.1.2), gelatin suffers a sol-gel transition (triple helix to random coil) at *circa* 40 ºC. At high concentrations, the unique way to promote adsorption is therefore to maintain gelatin solution in the sol state. Figure 4.1 represents the retention isotherm of the biopolymer in sepiolite.

As can be observed from the retention isotherm, gelatin tends to be heavily retained by sepiolite. Given that the resulting solids have been successively washed with water above the transition temperature of gelatin, it is reasonable to expect that the biopolymer that remains adsorbed to the microporous solid is strongly attached to the surface of sepiolite. As covalent bonds between the biopolymer and sepiolite are, in principle, unexpected, the materials resulting from the association of gelatin and sepiolite can be considered as class I hybrid materials. This strong retention observed indicates that there is a strong affinity between the silicate and the biopolymer moiety. It is thus plausible that in the context of a bionanocomposite, where the interfacial forces established

between the filler and the matrix are critical, gelatin and sepiolite might form a composite where stresses are efficiently distributed along the filler-matrix interface.

In fact the cooperative behavior taking place between the biopolymer and the silicate can be also observed by the dramatic increase of the onset temperature of the main thermal degradation process in air. Figure 4.2 depicts the thermogravimetric analysis of sepiolite, gelatin and the gelatin sepiolite hybrids (GS0.1 to GS4).

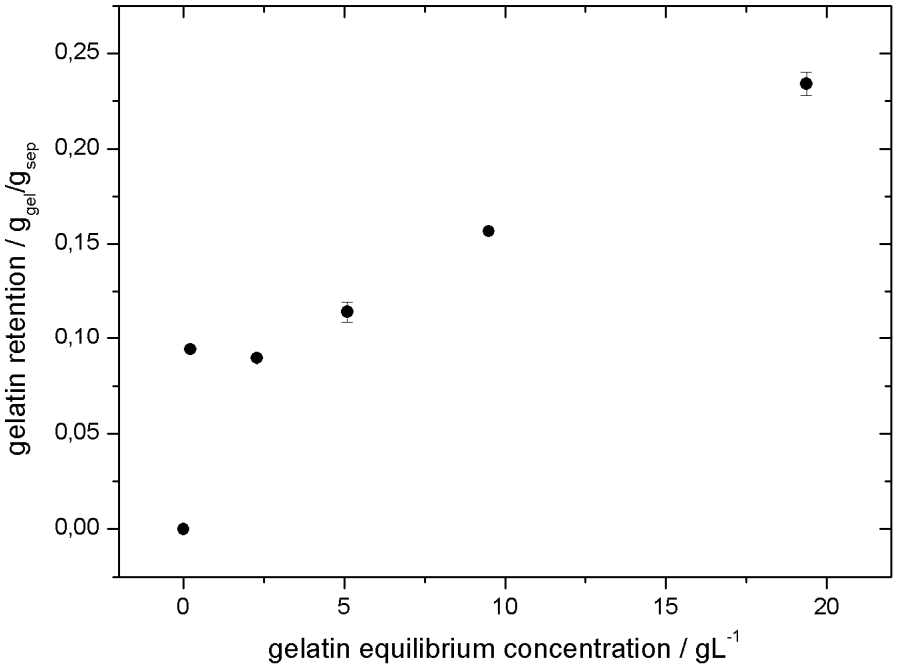


**Figure 4.1 –** Retention isotherm of gelatin over sepiolite at 60 ºC. The closed vessels were maintained under constant agitation (40 rpm) at 60 ºC during 48h. After the contact period, the dispersions were centrifuged and the collected solid resuspended in water at 60ºC. This procedure was repeated three times to ensure only strongly bonded gelatin was quantified.

While the onset of the first degradation step occurring under air that takes place around 255 ºC, sepiolite gelatin hybrids present the same degradation step over 280 ºC. The biopolymer stability enhancement of over 25 ºC indicates the stabilization effect of sepiolite over gelatin. This feature indicates that the

introduction of sepiolite in a gelatin matrix might account for an important effect over the service temperatures of the material.

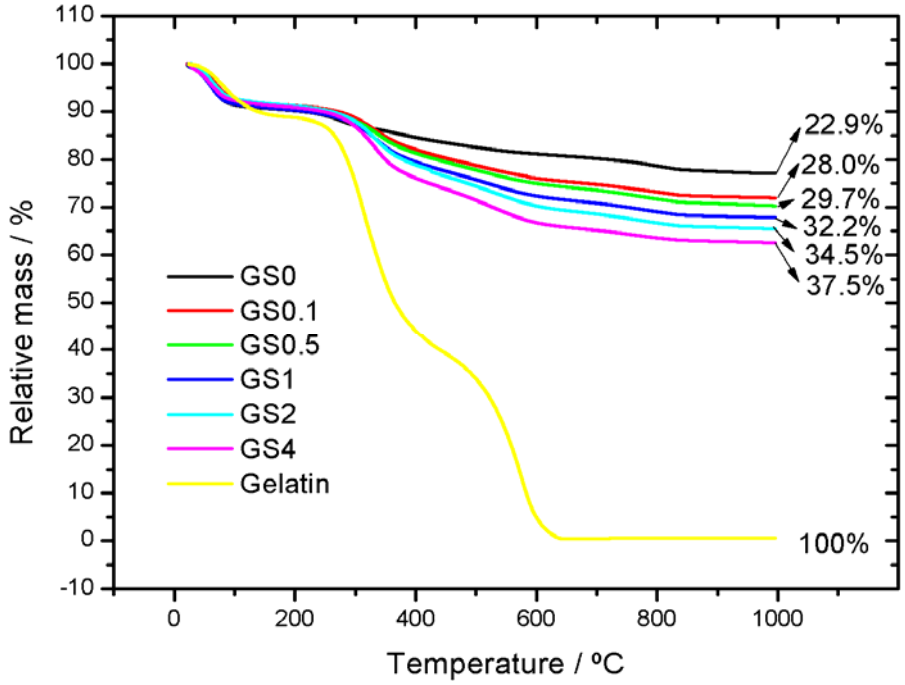


**Figure 4.2 –** Thermogravimetric analysis of sepiolite, gelatin and GS hybrids. The analysis was performed under 100 ml.min$^{-1}$ air flux at 10 ºC.min$^{-1}$ heating rate.

Besides the determination of the service temperatures of the GS hybrids (onset temperature referred to in table 4.1), the TG permits to confirm the organic matter quantification inferred from the CHN measurements.

**Table 4.1 –** Onset degradation temperatures determined by TGA. The analysis was performed under 100 ml.min$^{-1}$ air flux at 10 ºC.min$^{-1}$ heating rate.

| Sample | Onset degradation T / ºC |
|---|---|
| GS0.1 | 279.8 |
| GS0.5 | 285.9 |
| GS1 | 287.8 |
| GS2 | 286.1 |
| GS4 | 283.4 |
| Gelatin | 255.6 |

Another effective way of characterizing the association between gelatin and sepiolite regards the microscopic imaging of the resulting hybrid. Although polymers have low electronic density, which results in significant difficulties in detecting it by TEM, GS4 sample was imaged using this technique. Figure 4.3 shows the transmission microscopy of GS4 and a reference unmodified sepiolite micrograph (Fig. 4.3A) for comparison purpose.

The main observation is that the biopolymer seems to be totally associated with the fibrous silicate as no polymer aggregates are seen separately from the silicate. Sepiolite fibers, however, seem to be gathered in closely packed bundles (Fig. 4.3, images B and C). The aggregation between sepiolite fibers can be induced by an adsorbed layer of gelatin over each fiber, acting as interstitial “glue”. Micrograph C (Fig. 4.3) shows how in some locations of the sample sepiolite fibers do not show the same degree of aggregation. Moreover, that same image allows distinguishing the presence of light-shaded curved features that can be attributed to the presence of gelatin associated with sepiolite fibers.

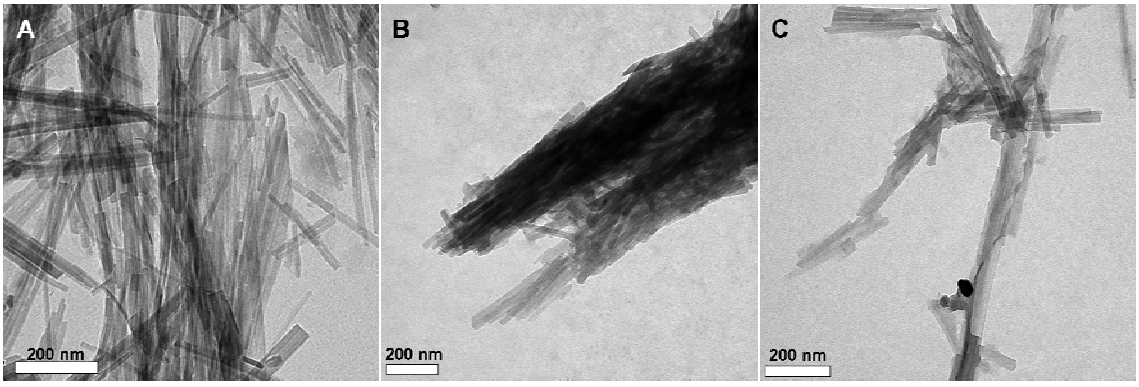


**Figure 4.3 –** TEM micrographs of unmodified sepiolite (A) and GS4 (B and C). Sample GS4 was dispersed in ethanol to prevent gelatin to desorb from sepiolite during the deposition over the TEM copper grid.

Since gelatin seems to be closely associated to sepiolite, the hybrid was considered an ideal starting material to prepare electrically conductive fibrous materials by controlled carbonization of the biopolymer. The expected material,

composed of a sepiolite fiber core surrounded by a conductive layer of nitrogen doped carbon is expected to serve both as structural and conductive filler.

## 4.2 Self assembly between gelatin, sepiolite and its derivatives

### 4.2.1 Sepiolite and sepiolite derivatives characterization

Gelatin based nanocomposites were prepared using sepiolite and the different derivatives of sepiolite previously prepared, i.e. monohydrated sepiolite, protoenstatite, sepiolite modified by reaction with 3-aminipropyltrimethoxysilane (SepAPS) and sepiolite modified by reaction with 3-glycidyloxypropyltrimethoxysilane (SepGOPS). The purpose of this preparation was to evaluate the influence of systematic variations of the mineral phase (sepiolite) on the properties of the bionanocomposites prepared thereafter. The cooperative effect between filler and matrix characteristic of nanocomposites is not exclusively dependent on the nano-dimensions of the filler, which will unquestionably promote a more efficient interaction between these. Such cooperative effect is also highly dependent on the nature of the interactions established between the two phases. By using a set of fillers whose differences can be systematized, the influence of such differences on the properties of the prepared bionanocomposites could be clearly identified.

Chemically modified sepiolite hybrids, SepAPS and SepGOPS were considered ideal candidates to evaluate the influence of the silicate surface chemistry on the polymer conformation. The rationale was: different available functional groups on the surface of sepiolite may promote diverse bonding between the hybrid and the polymeric moiety, which would in turn affect the polymer conformation in the surroundings of the modified silicate particle as well as the filler-polymer interaction strength. Amino and epoxy functional groups are known for their complementarity towards the two key functionalities of the

peptide structural units, carboxylic acids and amino groups respectively. The interaction of sepiolite amino derivative, SepAPS, with gelatin may consist on hydrogen bonds between the amino groups in the hybrid and -OH and/or –NH groups from the polypeptide. Another possibility, although less likely to occur, resides in the formation of amide bonds between amino groups from the hybrid and terminal carboxylic acid groups from the peptide chain. Also sepiolite epoxy derivative (SepGOPS) may establish covalent bonds with hydroxyl and amino groups in the polypeptide through an epoxy ring opening mechanism. In brief, both SepAPS and SepGOPS could establish hydrogen and covalent bonds with the polypeptide. Nevertheless, the epoxy derivative is considerably more prone to establish covalent bonds than the amino derivative, as the first should be, theoretically, able to covalently bond to hydroxyls or any primary or secondary amino group from the polypeptide, while the latter is limited to the polypeptide's terminal C groups.

The crystal structure of the mineral phase was also considered as a valuable tool to study the control exerted by the filler over the biopolymer matrix. The untreated silicate – sepiolite – and two derived phases – monohydrated sepiolite and protoenstatite – were used to unveil the influence of each mineral phase on the crystalline arrangement of the polymeric moiety as well as to understand its effectiveness as structural fillers in gelatin based nanocomposites.

Studies by X-ray diffraction allowed to thoroughly identify the mineral phases derived from sepiolite by thermal treatment. Figure 4.4 shows the diffraction patterns for sepiolite, monohydrated sepiolite and protoenstatite respectively. The peaks of the observed reflections were assigned to the naturally hydrated sepiolite (Brunauer and Preisinger, 1956), monohydrated sepiolite (Post, Bish et al., 2007) and protoenstatite (Yang and Ghose, 1995), which confirmed the adequacy of the selected experimental conditions to further achieve thermally controlled modification of sepiolite.

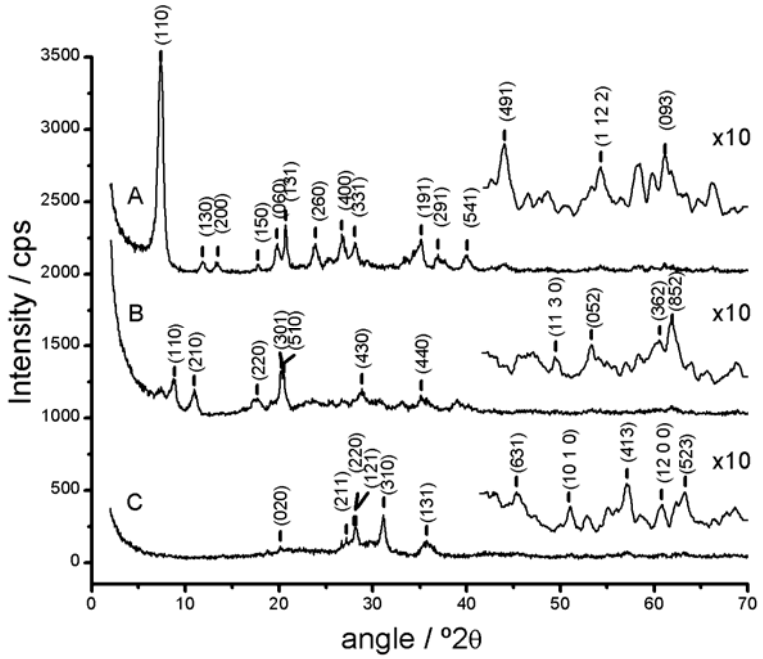


**Figure 4.4 –** XRD patterns for sepiolite, Sep (A), monohydrated sepiolite SepA (B) and protoenstatite, Prot (C). The diffraction pattern from 42 to 70º 2θ is also presented with its intensity multiplied by a factor 10 to permit detailed peak discrimination.

The infrared spectra of the derivatives obtained from sepiolite (Fig. 4.5) are usually analyzed taking into account the structural hydroxyls (Si-OH and $[Mg]_3OH$) stretching vibrations appearing at around 3710 and 3680 $cm^{-1}$, respectively, as a source of information regarding the nature of the interaction mechanisms (Ruiz-Hitzky, 2001). The relative intensity of these two bands is related to the perturbation of the external surface of sepiolite by interaction of the silanols with hydrophilic species (hydrogen bonding) or by reaction with different reagents including alkoxysilanes that can form covalent bonds (Ruiz-Hitzky and Fripiat, 1976; Fernandez-Hernandez and Ruiz-Hitzky, 1979; Van Meerbeek and Ruiz-Hitzky, 1979). It should be noted that $\nu_{Si\text{-}OH}$ vibrations are displaced towards lower frequencies due to the use of potassium bromide used for the measurements. The usage of KBr to prepare pellets implies, therefore, that no information could be drawn from this vibration as the corresponding shifted band is overlapped by the intense and broad bands assigned to O-H stretching vibrations of the water molecules associated to the silicate (Ahlrichs,

Serna et al., 1975). Hydroxyl stretching vibrations of magnesium hydroxide ($\nu_{Mg-OH}$) located inside the structural blocks of sepiolite are unaltered after interaction of this silicate with different species, in agreement with the inaccessibility to these hydroxyl groups. However it can provide useful information regarding the folding of sepiolite channels that occurs during the phase change from sepiolite to monohydrated sepiolite (Serna, Ahlrichs et al., 1975). Other hydroxyl stretching bands typical in sepiolite and its derivatives correspond to the intense broad band assigned to the $\nu_{OH}$ vibrations characteristic of the water molecules present in the untreated mineral (3630 and 3550 $cm^{-1}$: coordinated water; 3385 and 3275 $cm^{-1}$: zeolitic water) (Ruiz-Hitzky, 2001). Their shift to lower frequencies results from hydrogen-bonding interactions with adsorbed species (Kuang, Facey et al., 2003). Another important set of vibration bands corresponds to the different silicate bands between 1400 and 600 $cm^{-1}$. Among these last bands the one featured at approximately 1210 $cm^{-1}$ is especially relevant, as it corresponds to the Si-O-Si vibration of the inversion sites of the tetrahedral layer of sepiolite, the edges of each tunnel (Perraki and Orfanoudaki, 2008). The FTIR spectra of the derivatives of sepiolite (a) prepared by thermal treatments as monohydrated sepiolite (b) and protoenstatite (c), clearly show a significant variation as compared to the non-modified sepiolite. The most noticeable change in the hydroxyl bands spectral range (i) regards the disappearance of the band at 3565 $cm^{-1}$ along with a shift in the Mg-OH vibration band ($\nu_{Mg-OH}$) towards lower frequency in monohydrated sepiolite. This is indicative of a structural change in the conformation of sepiolite (folding), which is completed once the sample has been thermally treated to about 500 ºC. On the other hand, protoenstatite does not show any distinct vibration band in this spectral range. Some distinctive features can de detected in the silicate vibration range (1400-600 $cm^{-1}$). The 1209 $cm^{-1}$ band corresponding to Si-O-Si tetrahedra inversion disappears in both (500 and 1100 ºC) thermally treated sepiolite derivatives, corroborating the changes previously

detected by the Mg-OH vibration bands. Protoenstatite spectra displays bands around 1074, 933, 857 and 647, 729 $cm^{-1}$ confirming the formation of the enstatite phase (Perraki and Orfanoudaki, 2008). These features indicate that paired with dehydration, samples are experiencing the expected phase transitions.

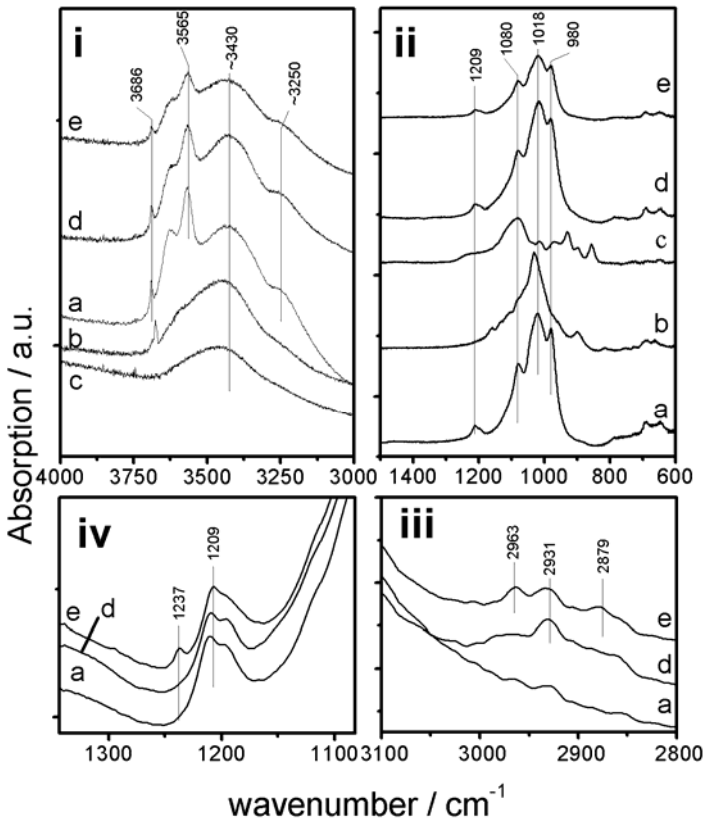


**Figure 4.5 –** FTIR spectral regions corresponding to the most relevant features of sepiolite and sepiolite's derivatives: i) Hydroxyl vibration range, ii) silicate vibrations range, iii) organic moiety related bands ($\nu_{C-H}$) stretching vibration bands, and iv) cyclic ether vibration bands. Where a) corresponds to untreated sepiolite, b) to monohydrated sepiolite, c) to protoenstatite, d) to SepAPS and e) to SepGOPS.

Infrared spectra of sepiolite chemical derivative's (SepAPS and SepGOPS) remain practically unchanged with respect to the raw sepiolite spectrum. The only significant changes consist on the appearance of weak intensity bands corresponding to the organic moiety grafted onto the sepiolite surface. Specifically, SepAPS presents C-H ($\nu_{C-H}$) stretching vibrations around 2931 $cm^{-1}$

corresponding to the alkoxysilane alkyl chain. The band characteristic of the stretching vibration of the amino group ($\nu_{NH}$) is not distinguishable in the IR spectra, probably due to overlapping with the broad band assigned to O-H stretching band of water molecules. SepGOPS presents more complete spectroscopic information. Besides the C-H ($\nu_{C-H}$) stretching vibrations at 2931 $cm^{-1}$ characteristic of alkyl chains, its spectra presents C-H ($\nu_{C-H}$) stretching vibrations associated with epoxy rings at 2963 $cm^{-1}$, the asymmetric cyclic ether vibration band ($\nu_{C-O-C}$) at 1237 $cm^{-1}$ and, finally, a weak band around 2879 $cm^{-1}$, characteristic of linear ether compounds.

**Table 4.2 –** Quantification of the organic fraction in SepAPS and SepGOPS, the chemical derivatives of sepiolite by CHN analysis.

| | Element mass ± sd (%) | | | |
|---|---|---|---|---|
| | C | H | N | Grafted species (meq/100g) |
| SepAPS | 4.8 ± 0.1 | 2.5 ± 0.1 | 1.4 ± 0.07 | 115 |
| SepGOPS | 5.9 ± 0.007 | 1.9 ± 0.06 | - | 70 |

Elemental analysis performed on sepiolite chemical derivatives is listed in table 4.2. Results indicate the presence of organic matter in both APS and GOPS modified materials, corresponding to the respective grafted organic species. APS grafts more efficiently onto the clay mineral surface than the organosilane containing epoxy groups (GOPS), as 115 meq/100 g of sepiolite reacted in the case of the first reagent whereas only 70 meq/100 g of sepiolite are incorporated in the case of GOPS.

### 4.2.2 Gelatin-Sepiolite bionanocomposite properties

The elastic properties of the composite films bearing the different sepiolite derivatives were determined under uniaxial strain and the average values of the Young's modulus were plotted against the mineral mass fraction (Fig. 4.6). The

results indicate the thermal and chemical modifications performed on sepiolite lead to dramatically different properties in gelatin-sepiolite and gelatin-sepiolite derivatives. As observed in Figure 4.6, untreated sepiolite is the most effective reinforcing filler in gelatin matrix. The inclusion of sepiolite in the gelatin matrix induces an enhancement of the composite's elastic modulus following a linear trend, reaching 220% of the initial value (from 2.8 to 6.2 GPa) at 20% (w/w) sepiolite loading.

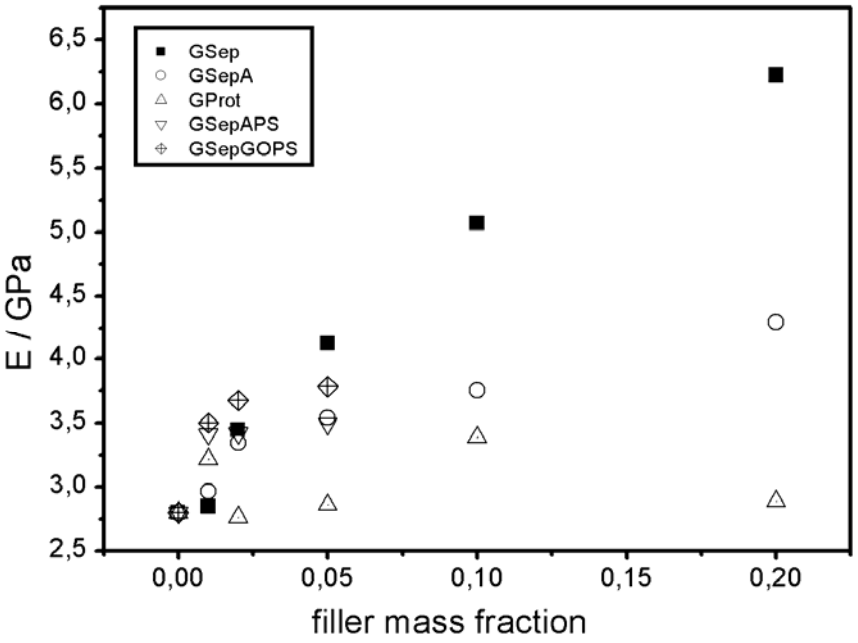


**Figure 4.6 –** Elastic modulus of gelatin's nanocomposites as a function of the sepiolite or sepiolite derivative mass fraction.

Gelatin-sepiolite nanocomposites present comparable reinforcement values when compared with the values reported in literature for neat sepiolite based composites in different polymeric matrices. In this way, Bilotti and co-workers (Bilotti, Zhang et al., 2009) reached a reinforcement value of about 166% the elastic modulus of unfilled polyamide 6 for 5% (w/w) sepiolite loaded composites. Chivrac *et al*. attained higher reinforcing values as high as 237% for 6% unmodified sepiolite loaded plasticized starch composites (Chivrac, Pollet et al., 2010). In this context it is important to stress out that the results for

sepiolite based nanocomposites referred in the bibliography rely on high shear methods to achieve homogeneous dispersion of the filler in the polymeric matrix (Nohales, Solar et al., 2006; Bilotti, Zhang et al., 2009; Chivrac, Pollet et al., 2010). The bionanocomposites reported here, on the contrary, uniquely count on self assembly between filler and matrix as the dispersion driving force. Another key observation is that sepiolite derivatives present a considerably modest enhancement of the composites' elastic modulus compared to the natural silicate. Sepiolite and its derivatives prepared by thermal treatments present some clear differences in the mechanical behavior. Among the latter, GSepA shows a roughly linear trend between clay loading and tensile modulus. Nevertheless the maximum modulus attained is around 4.3 GPa for 20% (w/w) SepA, clearly below the values obtained for raw sepiolite gelatin composites. In the case of GProt, the reinforcement limitations are even more striking as no improvement whatsoever is induced by the inclusion of 20% (w/w) protoenstatite. In the case of sepiolite organic derivatives, not only the values are considerably lower than the ones obtained for raw sepiolite but also the trend is noticeably different. GSepAPS and GSepGOPS show the development of a plateau in the Young's modulus around 2% clay loading.

One critical factor in understanding the mechanical behavior of sepiolite and its derivatives in gelatin matrix relates to the aggregation state of the fillers. It is known that fillers reinforcing efficiency is dependent on the extension of the interface between these and the continuous phase (i.e. the contact surface between sepiolite and the polymer). Therefore, the state of aggregation between filler particles will substantially alter the effectiveness of filler-polymer contact. Considering this possibility, the evaluation of clay particles aggregation in the studied matrix becomes critical to understand the influence of this factor in the observed mechanical properties.

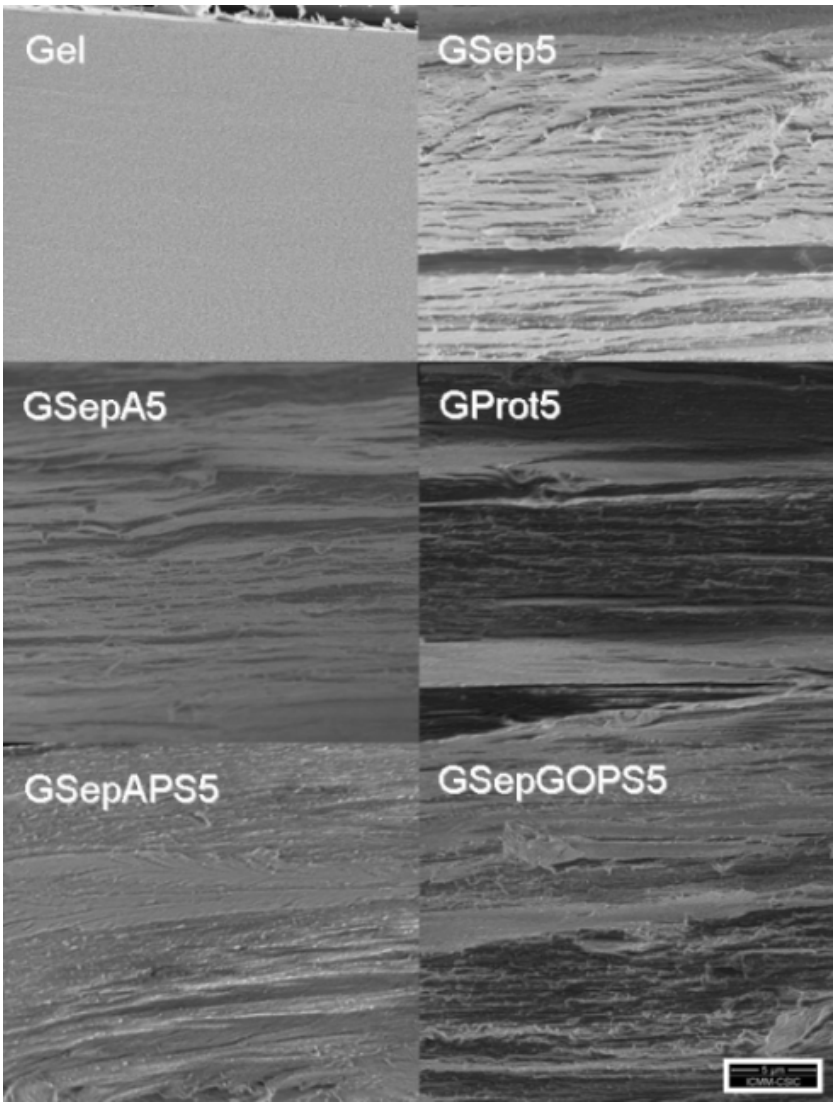


**Figure 4.7 –** FE-SEM images of the fracture zones of gelatin nanocompsoites reinforced with different sepiolite based fillers. The film plane corresponds to the micrographs horizontal direction.

FE-SEM images (Fig. 4.7) of the fracture zone of the composite films corresponding to gelatin and 5 % (w/w) loading compositions of all five different fillers reveal that non-reinforced gelatin presents markedly different fracture morphology when compared to the other composite materials (Fig. 4.5). Raw gelatin presents a smooth uniform fracture zone as expected. On the other hand, filled composites present nano- and micro-dimensioned features corresponding to particles of sepiolite and its derivatives. Although the presence of inorganic fibers is clear, the images lack sufficient resolution to allow inferring about the pull-out effect. Another noteworthy aspect of the 5 % (w/w) loaded

composites images regards the uniformity in aggregation of clay particles. All the filled composites present approximately the same size and distribution of clay aggregates. The most marked characteristic in this material's fracture zone relates to the existence of layered domains along the film plane. These domains are the result of gel collapse during drying.

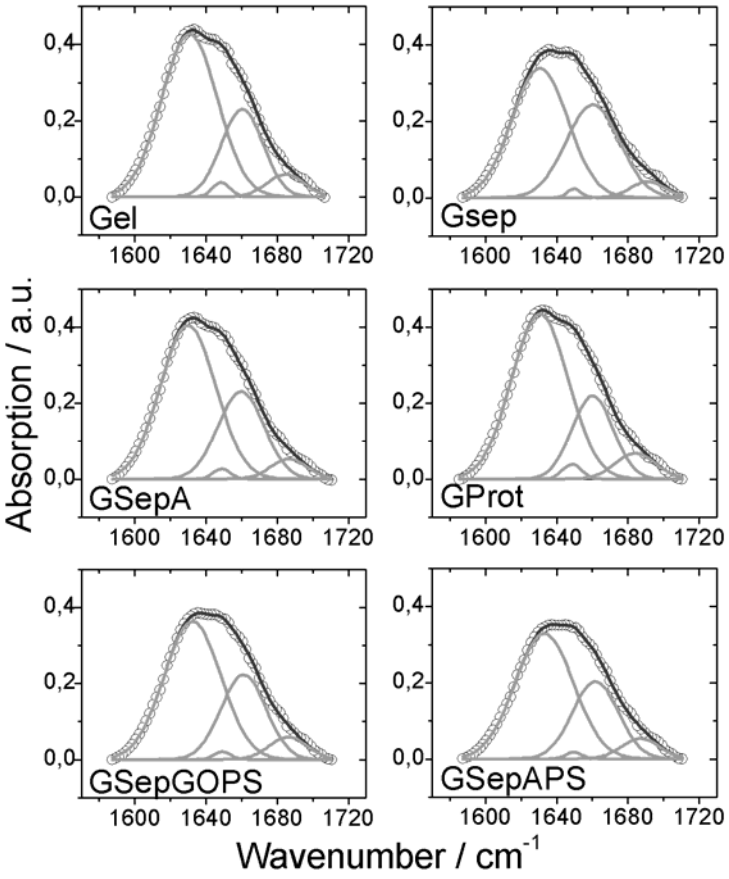


**Figure 4.8 –** Deconvolution results into four components of Amide I band in the different nanocomposites.

Biopolymers are excellent examples of the vastness of information that can be drawn from infrared spectroscopy. This technique allows, alongside with group analysis, to unveil secondary structure information by simple deconvolution procedures (Krimm, 1983; Byler and Susi, 1986; Movasaghi, Rehman et al., 2008). In this context, collagen and gelatin have been extensively studied using FTIR to discriminate and quantify crystalline triple helix and amorphous random

coil domains. According to Payne and Veis (Payne and Veis, 1988), amide bands are especially useful in this distinction since their different components provide quantitative information for each conformational state. These authors systematized the possible amide I (~1650 $cm^{-1}$) vibration components based on triple helix conformation previously proposed by Ramachandran (Ramachandran and Kartha, 1954; Ramachandran and Sasisekharan, 1965), obtaining four main components at approximately 1690, 1660, 1645 and 1630 $cm^{-1}$. One of the most relevant band components is the one detected around 1660 $cm^{-1}$ which can be directly associated to the triple helix conformation according to the Ramachandran model (Payne and Veis, 1988). Another useful amide I band component appears at 1630 $cm^{-1}$ and corresponds to the hydrogen bonding (H-bond) between amide groups and water, being therefore a good indicator of random coil conformation (Payne and Veis, 1988). The components whose vibrations appear at 1645 $cm^{-1}$, corresponding to a H-bond vibration between amide groups from the glycine residues and water, and 1690 $cm^{-1}$, assigned to triple helix aggregates vibrations, are considerably less intense (Payne and Veis, 1988; Muyonga, Cole et al., 2004). In accordance to the assignments of amide I components at 1630 and 1660 $cm^{-1}$ Payne and Veis (Payne and Veis, 1988) proposed an empirical index relating the area under these two components ($A_{1630}/_{1660}$) to infer about the prevalence of random coil versus triple helix conformations in gelatin and collagen. Figure 4.8 depicts the deconvoluted components, the experimental data and the deconvolution result for the six studied composites.

The six FTIR spectra were studied in the 1580-1720 $cm^{-1}$ range. Initially a baseline correction was performed on each spectrum in the referred range. Subsequently 4 gaussian peaks were fitted to the experimental data using initial iteration parameters $v_1$=1630 $cm^{-1}$, $v_2$=1645 $cm^{-1}$, $v_3$=1660 $cm^{-1}$, $v_4$=1690 $cm^{-1}$ and full width at half maximum $FWHM_{1-4}$=10 $cm^{-1}$. Each parameter was left

variable during the fitting session and each fitting session was repeated to ensure reproducibility. Table 4.3 summarizes the deconvolution results.

**Table 4.3 –** FTIR deconvolution results for amide I band in gelatin nanocomposites

| | v | A | $A_{1630/1660}$ | $r^2$ | $\chi^2$ |
|---|---|---|---|---|---|
| Gel | 1630.7 | 16.75 | | | |
| | 1648.6 | 0.482 | | | |
| | 1660.4 | 6.769 | | | |
| | 1684.7 | 1.576 | 2.47 | 0.9992 | $2.37E^{-05}$ |
| GSep | 1630.6 | 13.33 | | | |
| | 1649.8 | 0.237 | | | |
| | 1660.4 | 9.213 | | | |
| | 1691.1 | 1.040 | 1.45 | 0.9992 | $1.86E^{-05}$ |
| GSepA | 1629.9 | 15.83 | | | |
| | 1648.8 | 0.329 | | | |
| | 1659.7 | 7.511 | | | |
| | 1686.6 | 1.377 | 2.11 | 0.99922 | $2.16E^{-05}$ |
| GProt | 1630.6 | 17.35 | | | |
| | 1648.7 | 0.522 | | | |
| | 1660.2 | 6.383 | | | |
| | 1684.3 | 1.958 | 2.72 | 0.99928 | $2.16E^{-05}$ |
| GSepAPS | 1633.1 | 13.55 | | | |
| | 1649.6 | 0.207 | | | |
| | 1661.8 | 6.563 | | | |
| | 1687.1 | 1.438 | 2.06 | 0.99931 | $1.37E^{-05}$ |
| GSepGOPS | 1632.4 | 14.54 | | | |
| | 1649.2 | 0.255 | | | |
| | 1661.1 | 7.051 | | | |
| | 1686.2 | 1.612 | 2.06 | 0.99936 | $1.52E^{-05}$ |

Due to small intensity of 1645 $cm^{-1}$ component, deconvolution was also performed using 3 component bands solely (1630, 1660 and 1690 $cm^{-1}$ as initial iteration wavenumbers and $FWHM_{1\text{-}3}$=10 $cm^{-1}$), yielding significantly poorer fittings (results not shown). Although deconvolution procedures are considerably error prone, the analysis of the deconvolution results presented in

table 4.3 yielded strong values for square correlation coefficient, $r^2$ and reduced chi-square, $\chi^2$.

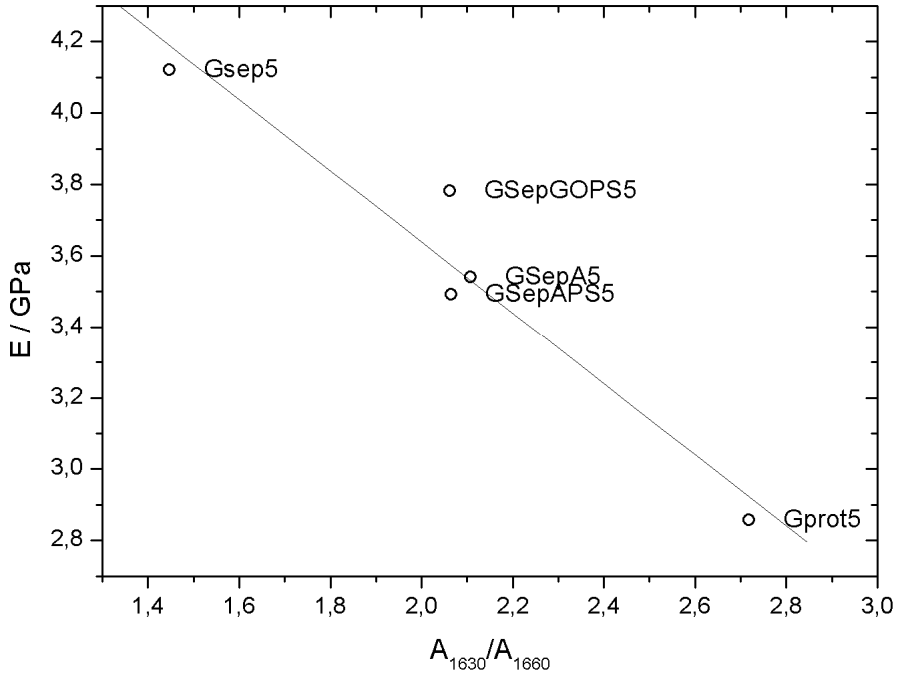


**Figure 4.9 –** Correlation between the empirical index $A_{1630/1660}$ obtained by Amide I band deconvolution and the elastic modulus of 5% w/w loaded bionanocomposites

The empirical index that relates the random coil and triple helix contents, $A_{1630/1660}$, is an important source of information regarding the crystallinity of the matrix. According to the reported results on table 4.3 the crystalline fraction in the different composites seems to vary significantly as a function of the filler used to reinforce the gelatin matrix. Raw sepiolite seems to induce highest crystalline content (lowest $A_{1630/1660}$ relationship) of all inorganic fillers. On the other hand protoenstatite induces the lowest crystalline content as expressed by the highest $A_{1630/1660}$ ratio. Taking into account that no variation, other than filler nature, has been introduced into these composites, it appears clear that the fillers are exerting some control over the polypeptide renaturation capacity.

It is widely accepted that the mechanical properties of gelatin and collagen, especially their elastic properties, are influenced by the triple helix content (Bigi, Panzavolta et al., 2004). In order to asses the interrelation between the

mechanical properties of the composite films and the empirical spectroscopic index, $A_{1630/1660}$, the Young's modulus results for 5 % (w/w) loaded composites were plotted against $A_{1630/1660}$ determined for the same set of samples (Fig. 4.9). The composites' Young's modulus measured in the microtensile experiments strongly correlate to the data inferred from spectroscopic measurements ($r^2$=0.933 and P=0.008) supporting the proposed interaction between mineral fillers and gelatin conformation.

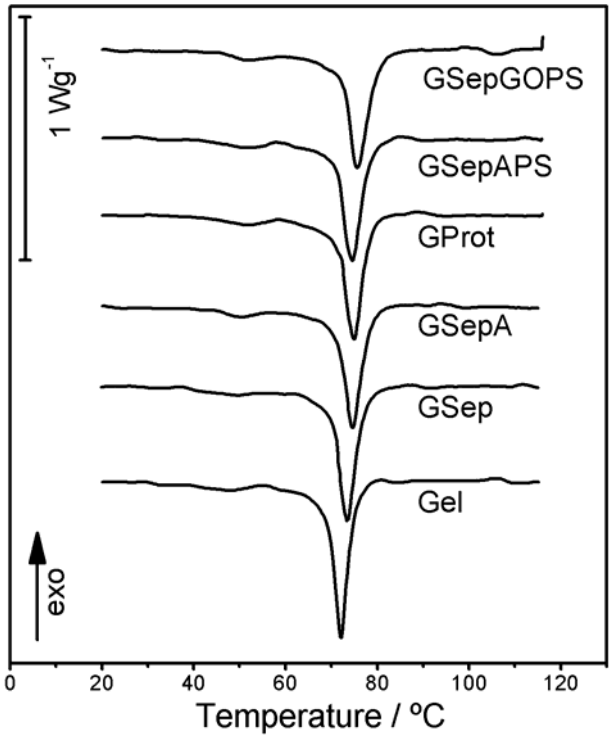


**Figure 4.10 –** DSC themograms for gelatin and gelatin reinforced with the sepiolite and its different derivatives 5% (w/w)

DSC measurements allow a precise quantification of the enthalpy of the triple helix-random coil transition (Bigi, Panzavolta et al., 2004; Brinckmann, Notbohm et al., 2005). The 5% (w/w) filler loaded samples were, along with gelatin, scanned and the results are plotted in figure 4.10. It is observed that the endothermic peak related to the triple helix-random coil transition occurs at a denaturation temperature, Td, which remains practically unchanged amongst

the entire set of samples. In the other hand the difference in the transition enthalpies recorded for each sample indicates that the crystalline fraction varies significantly. In order to quantify these differences, renaturation level was quantified using the following equation:

$$X = \frac{\Delta H_{sample}}{\Delta H_{gelatin} f} \times 100 \qquad \text{(eq. 4.1)}$$

where X corresponds to the renaturation level, $\Delta H_{sample}$ is the triple helix-random coil transition enthalpy for the composites, $\Delta H_{gelatin}$ is the triple helix-random coil transition enthalpy for neat gelatin film, and *f* is the gelatin mass fraction in the 5% loaded composite films with a value equal to 0.952.

The determined renaturation level, calculated from the triple helix-random coil transition enthalpy was plotted against the tensile modulus determined in the micromechanical experiments. The results, depicted in figure 4.11 indicate a coarse yet clear correlation between these two properties ($r^2$=0.862 and P=0.023). These results confirm that mechanical properties of the studied gelatin-sepiolite based composites are controlled by the renaturation level of gelatin, which in turn, depends entirely on the filler nature.

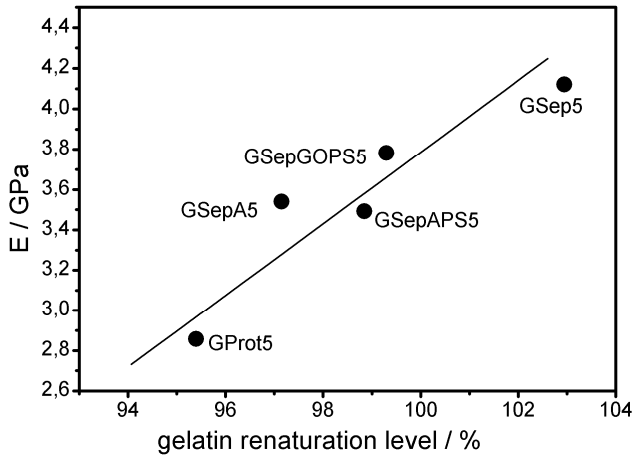


**Figure 4.11 –** Correlation between the elastic modulus of sepiolite and the degree of crystallinity of gelatin as determined by the triple helix-random coil transition enthalpy.

Ascribing a mechanism governing the renaturation process of gelatin induced by the presence of sepiolite is a difficult task. However, it seems likely that the quasi-perfect match between the dimensions of the collagen-like triple helix and the sepiolite channels might have a strong impact on the helix stability.

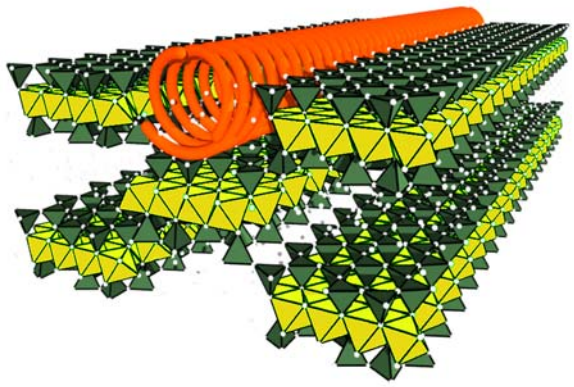

**Figure 4.12 –** Schematic representation of the association between a collagen-like domain in gelatin (orange) and a sepiolite channel

Moreover, the presence of coordinated water molecules attached to the magnesium atoms inside each channel (exterior tunnel) might provide an adequate binding site to establish hydrogen bonds between both. These considerations lay ground for a possible self-assembly mechanism between the triple helix domain of the gelatin and channels at the exterior surface of sepiolite. Figure 4.12 depicts a possible accommodation between these two supramolecular entities as previously suggested by Pérez-Castells and co-workers for collagen in collagen–sepiolite composites (Perez-Castells, Alvarez et al., 1985). This complementarity could explain the renaturation level obtained for raw sepiolite above the reference value of neat gelatin. It might also explain the lower of polymer crystallinity obtained for the nanocomposites prepared using sepiolite derivatives. Although the chemical changes produced in the mineral surface when preparing monohydrated sepiolite are very subtle, the folding of the mineral channels might hinder the same kind of interaction. Such an interaction is obviously much more improbable in the case of the other

derivatives Prot, SepAPS and SepGOPS. In the first case, protoenstatite, the channels have completely collapsed (Serna, Ahlrichs et al., 1975) and a much denser structure was formed. Also the hydroxyls and coordinated water initially present were eliminated from the structure creating a non-hydrophilic surface, which is not suitable for the interaction between the modified mineral phase and the organized biopolymer moiety. Composites prepared using SepAPS and SepGOPS might present stronger bonds between the hybrid and gelatin as covalent bonds are, in principle, possible. Nevertheless such bonds do not induce the renaturation of the collagen like triple helix because the accommodation to the clay channels is probably hindered by the interaction of the gelatin macromolecule with the alkoxysilane functionalities. In case a covalent bond is established between the sepiolite hybrids (SepAPS and SepGOPS) could also block the chain mobility required to achieve an effective renaturation degree.

## 4.3 Discussion of the mechanical properties of gelatin-sepiolite nanocomposites

A critical observation in the studied composites regards the orientation of the sepiolite fibers in the prepared films. 2D SAXS/WAXS allowed the characterization of the principal orientation of the sepiolite fibers in GSep10, a sample which was considered to be a representative example of the entire set of samples. Using a 270 mm distance between the sample holder and the detector it was possible to register a diffraction range that comprises the principal diffraction rings of sepiolite. The scattering/diffraction pattern for gelatin and gelatin–sepiolite 10% (w/w) in both orientations is presented in figure 4.13.

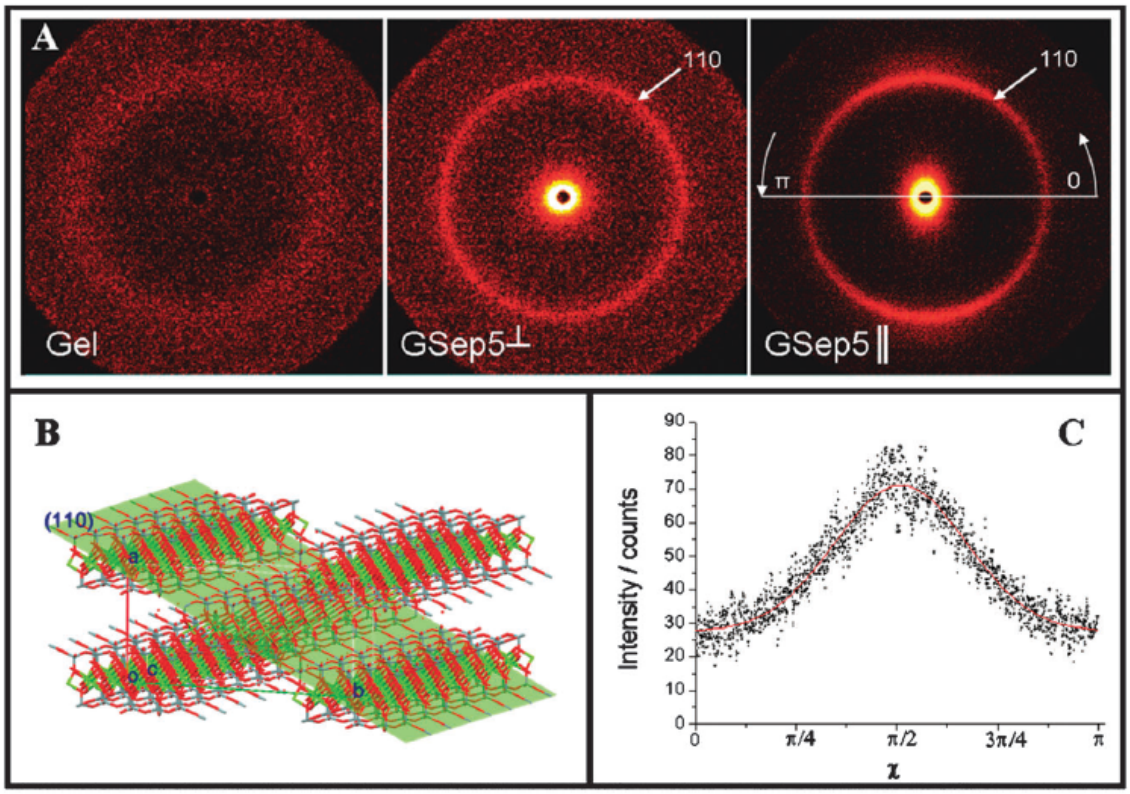


**Figure 4.13 –** (A) Gelatin and gelatin–sepiolite 10% (w/w) SAXS/WAXD patterns, (B) representation of the sepiolite *110* plane and (C) integration results for the GSep10J scattering/diffraction pattern. Azimuthal integration was performed counter clockwise from 0 to π mark and limited between radial angles 7.351–7.451 (2θ). Reproduced from (Fernandes, Manjubala et al., 2011) by permission of the PCCP Owner Societies.

The first observation is that gelatin presents a broad diffraction ring at around 7.71º (2θ) which significantly overlaps with the *110* diffraction ring of sepiolite that is observed in GSep10⊥ and GSep10‖ at around 7.41º (2θ). This observation implies some degree of difficulty in using this technique to understand for instance the degree of crystallinity of gelatin. Another noteworthy observation is that in the across the plane scattering/diffraction pattern of GSep10⊥, the rings' intensities are constant, irrespective of the azimuthal angle. This suggests that sepiolite fibers do not present any preferred radial orientation in the film plane. On the other hand, the anisotropy of the diffraction ring in the ''along the plane'' pattern obtained for GSep10‖ indicates that there is a clear preferred orientation in sepiolite fibers with respect to the composite plane. The azimuthal integration of the *110* diffraction ring in GSep10‖ is shown

in figure 4.13C along with the sepiolite *110* plane (Fig. 4.13B). The azimuthally integrated intensity fits a Gaussian distribution centered on π/2, indicating that sepiolite fibers are parallel to the composite plane. (Note: the composite film was held horizontally during the scattering experiment.) The information regarding the fiber orientation in the composites, along with the elastic properties measured should, in principle, allow drawing out some insight on the reinforcing capacity of the inorganic fiber and its derivatives. Several authors have adapted the previously mentioned Halpin–Tsai composite theory (Halpin and Kardos, 1976) (§ 1.2.2) to describe the elastic behavior of in-plane randomly oriented short fiber lamina (Mallick, 1993; Staab, 1999; Qian, Dickey et al., 2000). In such adapted model, two components, $\eta_L$ and $\eta_T$ related to the longitudinal and transversal reinforcement of the filler respectively, are taken into account.

$$E_c = \left[\frac{3}{8}\frac{1+2(l_f/d_f)\eta_L\phi}{1-\eta_L\phi} + \frac{5}{8}\frac{1+2\eta_T\phi}{1-\eta_T\phi}\right]E_m,$$
$$\eta_L = \frac{(E_f/E_m)-1}{(E_f/E_m)+2(l_f/d_f)}, \qquad \text{(eq. 4.2)}$$
$$\eta_T = \frac{(E_f/E_m)-1}{(E_f/E_m)+2}$$

Assuming that the flexural modulus of sepiolite, previously determined in the preceding chapter, is a good approach to its elasticity modulus under longitudinal strain, it is possible to compute the theoretical composite elastic modulus as a function of the volume fraction and the filler aspect ratio. Figure 4.14 depicts both the experimental and calculated values for the composite modulus. The theoretical values were simulated using equation 4.2 for three different aspect ratio values: 10, 100 and 1000.

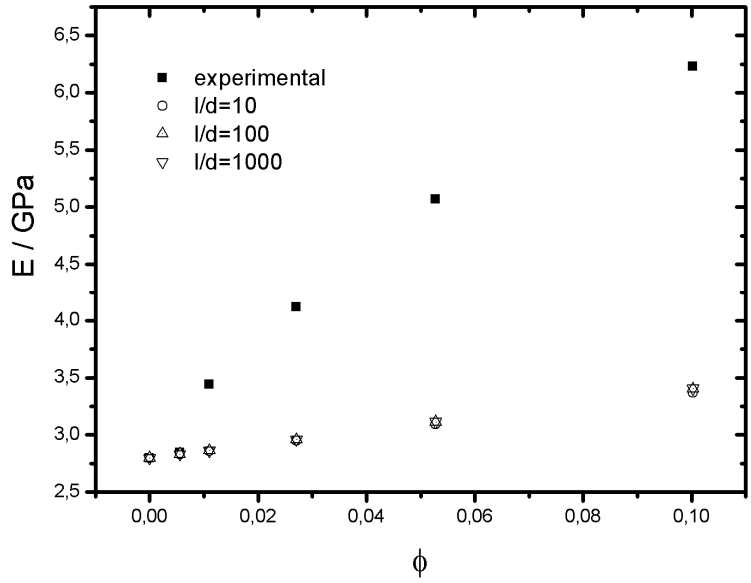


**Figure 4.14 –** Comparison between the experimental values of Young's modulus obtained for GSep composites and the theoretical values calculated from the modified HT model presented in equation 4.2 as a function of the filler volume fraction. The theoretical values were calculated for three different fiber aspect ratio (l/d= 10, 100 and 1000) using the elastic modulus of unmodified gelatin and the flexural modulus of sepiolite determined previously (§ 4.2).

Two major observations can be drawn from the data presented on figure 4.14:

a) The modified HT model does not seem to account for the aspect ratio of the filler.

In fact, the results of the theoretical calculus for the reinforcement of gelatin matrix by sepiolite as a function of sepiolite aspect ratio do not differ considerably. This fact can be explained trough a detailed analysis of the underlying reinforcement efficiency requirements of the modified HT model. Figure 4.15 maps the reinforcement efficiency ($E_c/E_m$) for a 0.1 (v/v) loaded sample as a function of two variables, the relation between the elastic modulus of filler and matrix ($E_f/E_m$) and the filler aspect ratio (l/d).

As can be observed in figure 4.15, to achieve an effective reinforcement of a continuous matrix using random-in-plane oriented fibers, there are two main requirements that have to be fulfilled simultaneously. The first regards the need for a high aspect ratio particle. Examining the map displayed on figure 4.15

leads to the observation that for low aspect ratio particles, the reinforcement values obtained are considerably more modest than the ones obtained for high aspect ratio particles.

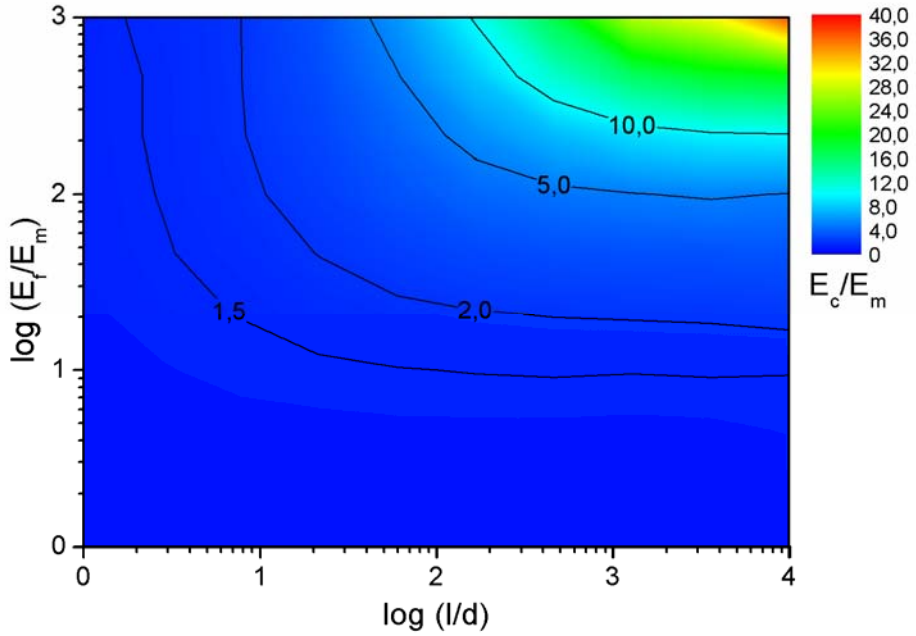


**Figure 4.15 –** Map displaying the reinforcement factor as function of the filler aspect ratio and the quotient between the filler elastic modulus and the matrix elastic modulus. The black lines define borders for the depicted reinforcement factor. The values are based on the modified HT equation for $\Phi = 0.1$

Let's consider two composite systems consisting on the same polymeric matrix loaded with 10 %(v/v) of particles. On the first system the particle's aspect ratio is 10, and in the second system 1000. In case such particles present the same modulus (*e.g.* an elastic modulus 1000 times higher than the matrix elastic modulus), the highest reinforcing efficiency that could be attained for the two systems varies greatly. The shorter particles would account solely for a two-fold increase of the elastic modulus, whereas the longer particles would promote an increase of the composite elastic modulus far superior to 20. The second requirement to induce an effective reinforcement of the composite implies that the ratio between the elastic modulus' of the filler and the matrix is maximized. To demonstrate such requirement let's take into account two systems loaded

with the same amount of filler in the same polymeric matrix. Let's also consider that the fillers present high aspect ratio (*e.g.* l/d = 1000) and the only difference between the two systems resides in the filler's elastic modulus. For a composite whose filler modulus is ten times superior with respect to the matrix the modulus increase of the composite ($E_c/E_m$) would be uniquely of 1.5. On the other hand, for a composite system presenting a filler whose elastic modulus is 100 times superior to the matrix's modulus, the reinforcement factor would be close to 5.

In summary, both criteria (aspect ratio and the relation between the filler and the matrix modulus) turn out to be critical in achieving an effective reinforcement of a composite elastic modulus.

Given the previous criteria for the reinforcement of composites, it becomes appropriate to analyze the role of sepiolite in the mechanical reinforcement of a gelatinous matrix. Although the first criteria of particle aspect ratio is fulfilled – sepiolite presents at least an aspect ratio equal to 100 – it fails to comply with the second criteria. The elastic modulus of sepiolite determined on the previous chapter (§ 3) of 11.5 GPa is clearly insufficient to effectively reinforce gelatin, whose elastic modulus is 2.8 GPa. In fact, sepiolite's characteristics in gelatin should account uniquely for a reinforcement value of around 1.2. Surprisingly, sepiolite seems to reinforce gelatin matrix in an effective manner as can be deduced from the obtained reinforcement values. Such remark leads us to the second observation related to the reinforcement efficiency depicted in figure 4.15.

b) There is a noticeable discrepancy between the theoretical and experimental data, irrespective of the aspect ratio of the filler.

According to figure 4.14, the experimental values measured for GSep are far superior to the ones calculated using the modified HT model, for random in plane discontinuous lamina. This efficiency does not seem to be related to the pure mechanical reinforcement discussed above. It is rather related to the

renaturation degree of gelatin in presence of sepiolite discussed in section §4.2. As referred earlier, Bigi and co-workers revealed a linear positive trend between the renaturation level of gelatin and the elastic modulus of gelatin gels (Bigi, Panzavolta et al., 2004) and films (Bigi, Bracci et al., 1998). This fact along with the crystallinity values obtained for GSep composites by the two characterization techniques used in this work (FTIR and DSC) leads us to assume that the crystalline fraction of gelatin is variable along the different compositions. Given that gelatin presents variable mechanical properties as a function of the different crystalline contents, it becomes clear that the HT or the modified HT equations do not account for an important feature in semi-crystalline composites: the variability of the matrix's elastic properties. A simple analysis of equation 4.3 (a simplified version of the HT model) yields a constant term for the matrix properties.

$$\begin{aligned} E_c &= f(l_f / d_f, E_f / E_m, \phi_f) E_m, \\ E_m &= k \end{aligned} \qquad \text{(eq. 4.3)}$$

A more accurate model should take into account the matrix variability (Fernandes, Darder et al., 2011) in the form presented in equation 4.4.

$$\begin{aligned} E_c &= f(l_f / d_f, E_f / E_m, \phi_f) E_m, \\ E_m &= f(l_{cryst} / d_{cryst}, E_{cryst} / E_{am}, \phi_{cryst}) E_{am} \\ \phi_{cryst} &= f(\phi_f) \end{aligned} \qquad \text{(eq. 4.4)}$$

where subscripts *cryst* and *am* refer to the crystalline and amourphous phases of the matrix respectively.

For the specific case of a gelatin matrix, this variation over the HT model seems especially fit, as the crystalline domains (collagen-like triple helixes) show fiber-like morphology with high aspect ratio and an elastic modulus superior to the corresponding value of the amorphous fraction, and can therefore be regarded

as a filler on their own. Halpin and Kardos (Halpin and Kardos, 1972) have discussed the use of their composite theory to describe the reinforcing effect of crystallites in semi-crystalline polymers. They have concluded that, if the crystallite had a sufficient aspect ratio and the orientation functions were known, the HT model would be adequate to describe its reinforcing effect on the composites. The case of gelatin seems to fit the requirements. Surprisingly, neither Halpin, Tsai nor Kardos (the chief developers of the HT model) have prolonged their research on the relation between the filler volume fraction and the development of the crystalline phase.

In the present case, sepiolite induces the renaturation of the collagen-like domains functioning as a nucleation agent. Such function can be described by, $\Phi_{cryst}=f(\Phi_{filler})$, in equation 4.4, which defines a relationship between the amount of polymeric crystalline domains and the volume fraction of filler introduced into the polymeric matrix. This relation can be understood as a functional role of sepiolite on the mechanical reinforcement of gelatin matrix. Such role of sepiolite can be extrapolated to other polymers where sepiolite has a seeding effect of the development of polymer crystallites.

## 4.4 Concluding remarks

This section, devoted to the reinforcement of gelatin matrix by sepiolite, allows drawing some particular conclusions regarding the reinforcing efficiency of sepiolite in gelatin.

Sepiolite has proven to be an adequate filler to improve gelatin's tensile properties, inducing an increase by a factor of 2.2 of the neat polymer elastic modulus by the inclusion of 20% (w/w). Surprisingly, chemically modified sepiolite hybrids (SepAPS and SepGOPS) do not improve the elastic properties of the resulting composites any more than unmodified sepiolite. This feature indicates that the expected interactions through hydrogen and covalent bonding

between the organo-modified sepiolite derivatives and the biopolymer matrix do not provide sufficient stress transfer to significantly enhance the bionanocomposites mechanical properties. On the other hand these organomodified hybrids seem to drive the random coil/triple helix equilibrium towards the random coil configuration. The reduction of the triple helix content as compared to the neat gelatin results in poor matrix mechanical properties and consequently low mechanical reinforcement as compared to the neat gelatin. On the contrary, untreated sepiolite, whose interactions with the polymer matrix are restricted to hydrogen bonding, provides a much higher mechanical reinforcement. This effect is due to the fact that not only sepiolite is acting as a mechanical filler, but also it is driving the random coil/triple helix to the triple helix conformation as deduced from the spectroscopic and thermal data. It seems thus plausible to consider that some fillers may act as nucleating agents for gelatin triple helix whereas others actually impair such phenomenon, with obvious consequences on the mechanical properties of the composites. Sepiolite channels might act as adequate environments to displace gelatin's crystalline–amorphous equilibrium towards the generation of higher crystallinity as it has been previously suggested for collagen (Perez-Castells, Alvarez et al., 1985). The mechanical properties results also corroborate this view, since the differences in the elastic properties measured in the different composite materials seem to relate strongly to gelatin's crystalline fraction.

Another relevant issue regards the inadequacy of composite models to describe the elastic properties of composites. The present case reveals that the introduction of a variable regarding the variability of the matrix elastic properties as a function of the filler would describe the reinforcing phenomenon more accurately.

# 5. Carbon materials from sepiolite and gelatin

The development of nanocomposites based on the assembly of gelatin and sepiolite (reported in the previous chapter) stands as a natural starting point to the preparation of gelatin sepiolite based carbon materials.

Carbon materials are ubiquitous in materials science. These materials can be formed in a natural manner such as in coal, pitch, graphite or diamond or through synthetic procedures resulting in activated carbons, CNTs, fullerenes or graphene.

The wide range of applications of carbons is related (with the exception of diamond) with two main properties, electrical conductivity and high specific surface area. The first of these properties relies on the extensive conjugated systems that compose the graphitic part of carbons. Some of these materials that, besides from the presence of large graphitic domains present high aspect ratio have been selected as the most advantageous choice in the reinforcing of polymer matrices for structural and electrical applications. Above a critical volume fraction (percolation threshold), materials such as carbon nanofibers, CNTs or graphene sheets establish an electrically conducting path throughout the insulating matrix and provide the final materials with electrical conductivity (Hammel, Tang et al., 2004; Coleman, Khan et al., 2006a; Grossiord, Loos et al., 2006; Zhang, Mine et al., 2009).

The specific surface area is another important characteristic of carbonaceous materials particularly in the case of activated carbons with applications in the technologically relevant process of adsorption (Lozano-Castelló, Lillo-Ródenas et al., 2001; De La Casa-Lillo, Lamari-Darkrim et al., 2002; Chen, Duan et al., 2007; Yang and Xing, 2010). This process finds use in many applications, from wastewater treatment (Monser and Adhoum, 2002) to gastric *lavage* (Bond, 2002)

## 5.1 Preparation of carbonaceous materials from gelatin-sepiolite hybrids

Gelatin was tested as a starting compound for the preparation of carbonaceous materials since the works by Walton et al. in the early forties of the last century (Larsen and Walton, 1940; Bente and Walton, 1943). In those initial reports, the protein was used to prepare activated carbons for catalytic applications. However, since those works, the use of gelatin-based materials to prepare carbonaceous materials has been scarce and mostly used as a sacrificial template to be degraded upon thermal oxidation (Nabeta and Sano, 2005).

In this section we report a new approach in which gelatin adsorbed over sepiolite fibers was submitted to a carbonization process with the aim of preparing electrically conducting silicate-carbon fibers. The use of gelatin comes from two main factors. The first is the fact that nitrogen-doped carbons are known for its interesting electronic properties (Marchand and Zanchetta, 1966; Ayala, Arenal et al., 2010) with enhanced electronic conductivity. The other derives from the known association between the silicate and the biopolymer as portrayed by the retention isotherm presented in figure 4.1.

To asses the formation of nitrogen-doped carbon over the sepiolite fibers CHN quantification was performed on gelatin, gelatin after the carbonization process, gelatin adsorbed over gelatin (sample GS4) and the correspondent carbonized sample. Results are indicated in Table 5.1.

The first important information arising from the CHN data regards the raw amount of carbon left upon carbonization of gelatin. GelatinC sample presents a content in carbon close to 80 wt.% whereas initially presented solely 44.4 %. This feature indicates that the used carbonization process, 800 ºC under nitrogen flow is adequate for the preparation of carbonaceous materials. Also interesting to note is that the amount of nitrogen initially present on gelatin (*circa*

17 wt.%) tends to be eliminated upon carbonization. This tendency can be more clearly illustrated by the ratio of carbon to nitrogen referred in the last column of table 5.1. In gelatin such relation is 2.7 while after carbonization it rises to 6.6. The same tendency is observed when gelatin is adsorbed onto sepiolite (sample GS4 and GS4C) where the carbon to nitrogen ratio maintains the values previously determined for gelatin and its carbonized counterpart. Another interesting feature that arises from the CHN data is the atomic ratio between carbon and nitrogen. The ratio that relates the atomic carbon to nitrogen quantities reflects only the amino acids composition of the proteinous starting material. However, the atomic ratio between carbon and nitrogen in the carbonized gelatins provides interesting insight on the properties of the produced carbonaceous material. According to the quantification determined by CHN, the carbonized samples (either gelatinC or GS4C) posses one nitrogen atom per 8 carbon atoms.

**Table 5.1 –** CHN quantification (in wt.%) and respective standard deviation of gelatin and sample GS4 before and after carbonization (noted with a final "C" in the sample name).

| Sample | C / wt.% | H / wt.% | N / wt.% | C/N |
|---|---|---|---|---|
| Gelatin | 44.4 ± 0.1 | 6.8 ± 0.2 | 16.6 ± 0.08 | 2.7 |
| GelatinC* | 78.9 | 1.0 | 12.0 | 6.6 |
| GS4 | 12.1 ± 0.1 | 3.0 ± 0.01 | 4.3 ± 0.1 | 2.8 |
| GS4C | 5.0 ± 0.1 | 0.14 ± 0.03 | 0.75 ± 0.01 | 6.7 |

* Sample GelatinC was not analyzed in duplicate. Standard deviation values are thus not available for this sample.

Also important to note is that the presence of sepiolite (GS4) on the precursor materials does not affect the ratio of carbon to nitrogen obtained in the final material. This feature indicates that sepiolite does not directly take part on a specific elimination process of any of those type of atoms.

Another useful way to characterize the carbonaceous materials produced from the carbonization of gelatinous materials is the observation by electronic

microscopy of the resulting materials. Figure 5.1 displays scanning electron micrographs of the gelatinC and GS4C samples at two different scales. The most distinct feature regards the final form of the obtained materials. Carbonized gelatin (GelC), prepared by thermal treatment of the pure protein presents itself as massive bulk material. The initial gelatin pellet size expands severely to approximately the double of the initial volume. Upon mild manual milling it is characterized by large particle size (Ø > 50 μm) and some distinct pores in the sub-micron range (see lower GelC image). In fact due to their morphology it is reasonable to think that their formation is the result of the evolution of gases during the carbonization process.

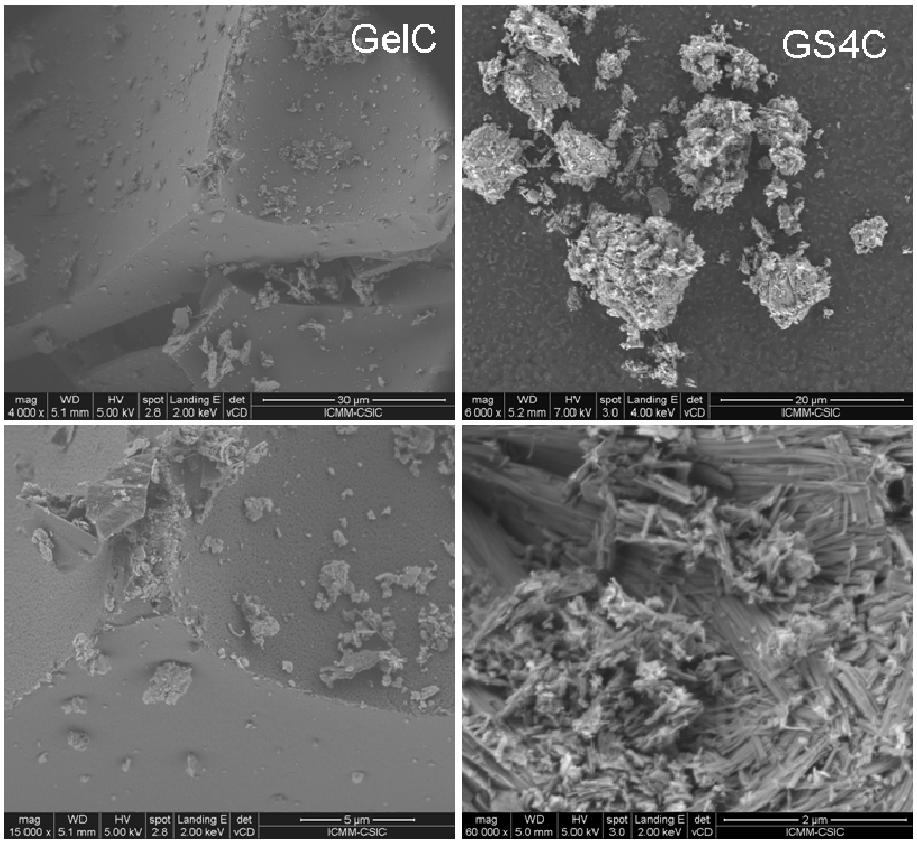


**Figure 5.1 –**FE-SEM images of GelC (left-hand side images) and GS4C (right-hand side images) at two different magnifications.

GS4C also results in a bulk material. However the final carbonized pellet shows minimal volume variation. On the other hand, upon mortar and pestle milling it

presents a particulated state where sepiolite fibers maintain its high aspect ratio and remain aggregated in micron range sized particles. It is especially interesting to note that GS4C particles maintain under the FE-SEM the same morphology as previously determined for the non-carbonized counterpart (i.e. GS4, figure 5.4 B and C). This feature suggests that the carbonization of gelatin adsorbed onto sepiolite proceeds mainly with gelatin still adsorbed over sepiolite. Not only the morphology of the sample varies, also the texture is distinct from the carbonaceous material derived from gelatin alone. In GS4C, a clear rugosity associated with sepiolite fibers is observable while in GelC the sample presents a smooth surface often presenting pores.

Also TEM serves as useful tool in characterization of the morphology of carbonaceous materials. Figure 5.2 displays images of GS4C under TEM in different areas of the sample. The first meaningful observation regards the differences between the left-hand side images and the opposed right-hand side of the image. Contrary to what had been previously observed under SEM, the sample presents zones where no sepiolite is observable. However, in both areas (named “sepiolite rich”, SR, and “sepiolite poor”, SP, for convenience), the obtained carbonaceous material presents itself as a thin layered material. Detailed observation of SR areas (images 1 and 3 in figure 5.1) shows that the formed carbon layers are placed closely to sepiolite fibers suggesting that these carbonaceous materials derive from gelatin previously attached to sepiolite. In some cases the formed layered carbon spanned over several sepiolite fibers (image 3 in figure 5.2) whereas in other cases it stood by one single sepiolite fiber (image 1 in figure 5.2). Interestingly, the SP zones also displayed layered carbon structures. Images 2 and 4 in figure 5.2 show several layers of carbonaceous material disposed in a semi-overlapping manner.

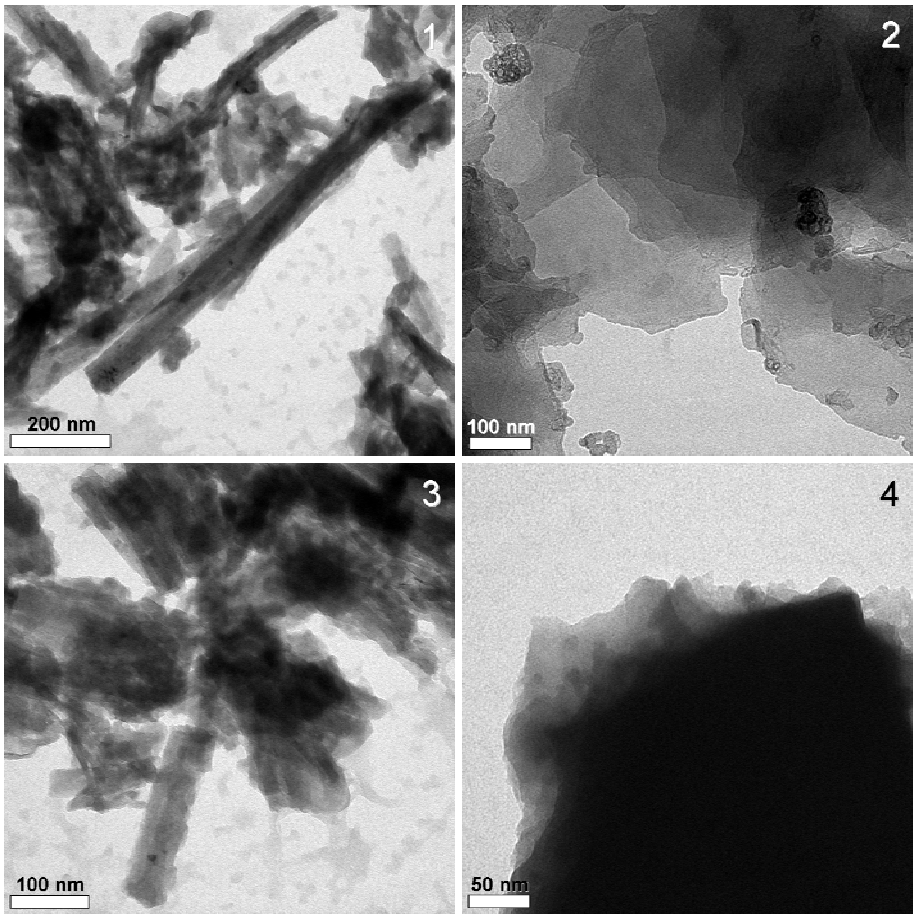


**Figure 5.2 –** TEM images of GS4C sample displaying sepiolite rich SR (1,3) and sepiolite poor SP (2,4) zones in the carbonized sample.

Raman spectroscopy is one of the most useful techniques to unveil the chemical nature of carbonaceous materials. The usefulness of the technique relates to the possibility to directly discriminate between carbon atoms hybridized in a $sp^2$ or $sp^3$ fashion. This information is especially relevant because the nature of carbon materials can be, in great part, deduced from the relation between these two types of carbon hybridization. As an example diamond, one of the fundamental carbon allotropes that is completely based on sp3 carbon presents an intense D band around 1355 $cm^{-1}$ while the G band (featured at 1575 $cm^{-1}$) is totally absent. Graphite monocrystals carbon nanotubes and graphene, on the other hand, only present a sharp and intense G band (Dresselhaus, Dresselhaus et al., 2005; Ferrari, 2007). In between these two extreme allotropes lie other carbonaceous materials such as carbon

blacks, charcoal, graphene oxide, etc. (Cuesta, Dhamelincourt et al., 1994) where both G and D bands are present and from which relative intensities the sample graphitization level can be inferred.

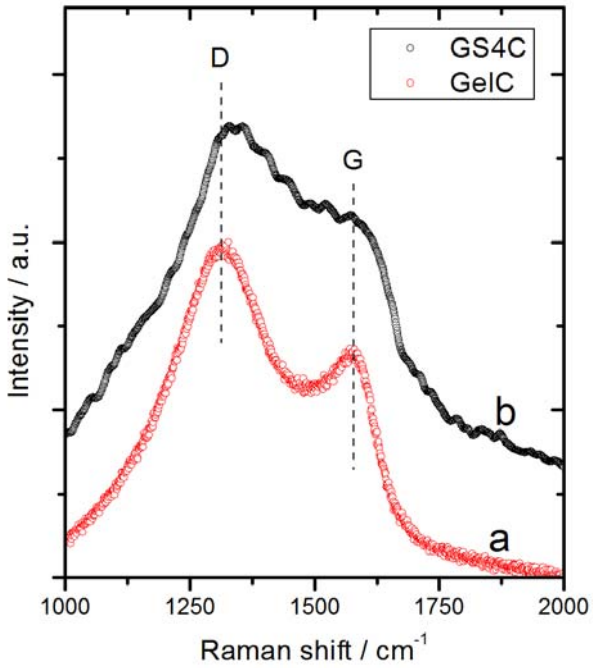


**Figure 5.3 –** Raman spectra of a) carbonized gelatin and b) carbonized GS4 hybrid (GS4C) measured under irradiation by a 2.41 eV laser (514 nm). The luminescent background present on the spectrum of sample GS4C due to the presence of sepiolite was subtracted. Additionally the curves have been normalized and artificially displaced for clarity of interpretation.

In the case of carbonized gelatin and GS4C samples there are some critical observations regarding their respective Raman spectra (Figure 5.6). The first is the relative intensities of the D and G band. As can be clearly seen, D band, which reflects the degree of disorder or defects in a graphitic system, is considerably more intense that the G band. This feature indicates that the carbonaceous material produced is dominantly composed of $sp^3$ non-graphitic carbon. To some extent, this indication contradicts the results observed by TEM where the GS4C material displayed a morphology that could easily be ascribed to a graphenic system. Also interesting to note is that the relative intensities between the two characteristic bands is not altered by the presence of sepiolite. This suggests that the presence of the silicate is not influencing the outcome of

the carbonization process of gelatin in the adopted experimental conditions. Another important observation is that G and D bands in both materials present considerable width, which results in an overlapping of both bands. Such overlap is probably magnified by a large D'' band at 1500 $cm^{-1}$ attributable to amorphous carbon or oxygenated functions (Cuesta, Dhamelincourt et al., 1994).

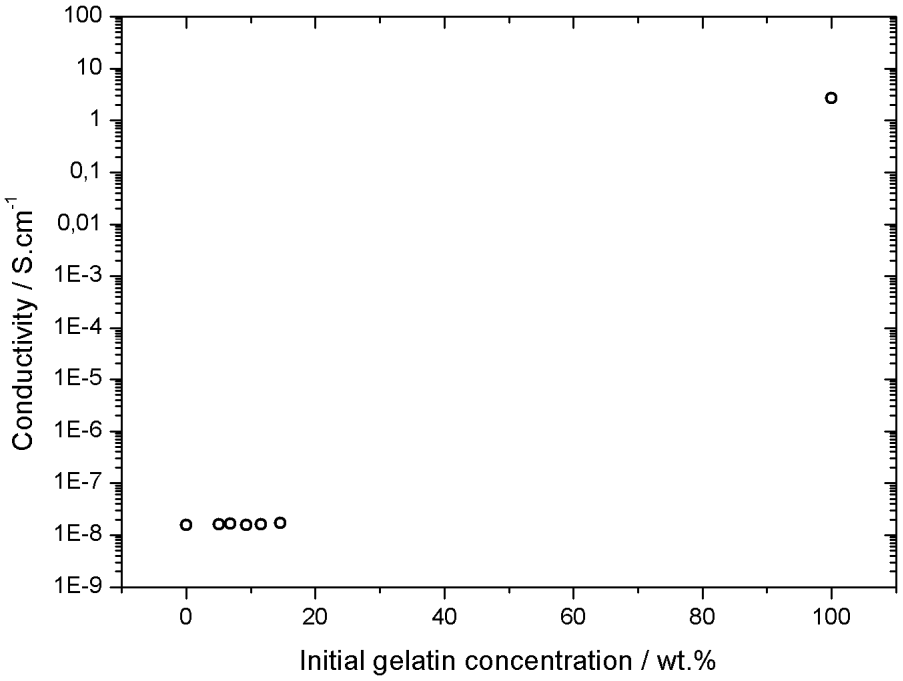


**Figure 5.4 –** Electric conductivity of carbonized GS samples as function of gelatin composition prior to carbonization.

Electric conductivity is another important property of carbonaceous materials in numerous applications such as sensors, conductive fillers for functional composites, etc.. In order to evaluate the electric properties of gelatin-sepiolite derived carbons, these were grinded with mortar and pestle and pressed into 22 mm Ø pellets. The faces of the resulting pellets were sputtered with gold and their resistivity measured in AC mode using Electrochemical Impedance Spectroscopy (EIS). Similarly, carbonized gelatin was also subjected to the same essay to determine the potentialities of gelatin derived carbons in

applications where electrical conductivity was a requisite. Figure 5.4 depicts the volumetric electric conductivity as a function of the gelatin content prior to carbonization.

Carbonized sepiolite and gelatin containing samples display an electrical insulator behavior as is depicted in figure 5.7 (Czichos, Saito et al., 2006). In fact, the absolute conductivity is similar to that of calcined sepiolite alone and is probably due to some ionic mobility and residual water adsorbed onto sepiolite during measurement at ambient conditions. Surprisingly, carbon derived from gelatin present in the tested materials does not seem to account for any enhancement of conductivity. This fact is interesting when compared with the electrical conductivity of gelatin derived carbon (in the absence of sepiolite, data point at 100% initial gelatin concentration in the preceding graph), that yields a highly conductive material (2.5 $S.cm^{-1}$). Therefore gelatin is capable of, upon carbonization, generating a highly conductive material, the quantities retained in sepiolite are not sufficient to establish a percolating path of electrons across the material. This indication suggests that to prepare conductive sepiolite-carbon materials derived from sepiolite-gelatin materials higher gelatin concentrations are needed. Also important is to note that although Raman spectroscopy indicates low graphitic carbon content, carbonized gelatin presents interesting electronic behavior. This feature indicates that the graphitic domains within the material are sufficiently wide to generate a percolating path and therefore gelatin is a suitable raw material to prepare conductive carbonaceous materials.

Another vital property in carbon materials due to their wide applicability in adsorption and decontamination processes is the specific surface area. Figure 5.5 depicts the nitrogen adsorption isotherms of sepiolite, gelatine and sample GS4 after thermal treatment under inert atmosphere. The most striking observation regarding the adsorption profiles is the correspondent to carbonized gelatine. Contrarily to the other two samples, CGel is unable to adsorb nitrogen yielding a specific surface area close to zero. CSep, on the other hand presents

a type II isotherm with a small H3 hysteresis loop (Sing, Everett et al., 1985) yielding a specific surface area $a_s$(BET) = 106 $m^2.g^{-1}$. According to the adorption isotherm, CGS4 sample presented a specific surface area $a_s$(BET) = 79 $m^2.g^{-1}$ which can be explained as a mixed behaviour between the specific surface area of sepiolite submitted to thermal treatment and the gelatine derived carbon specific surface area (close to zero).

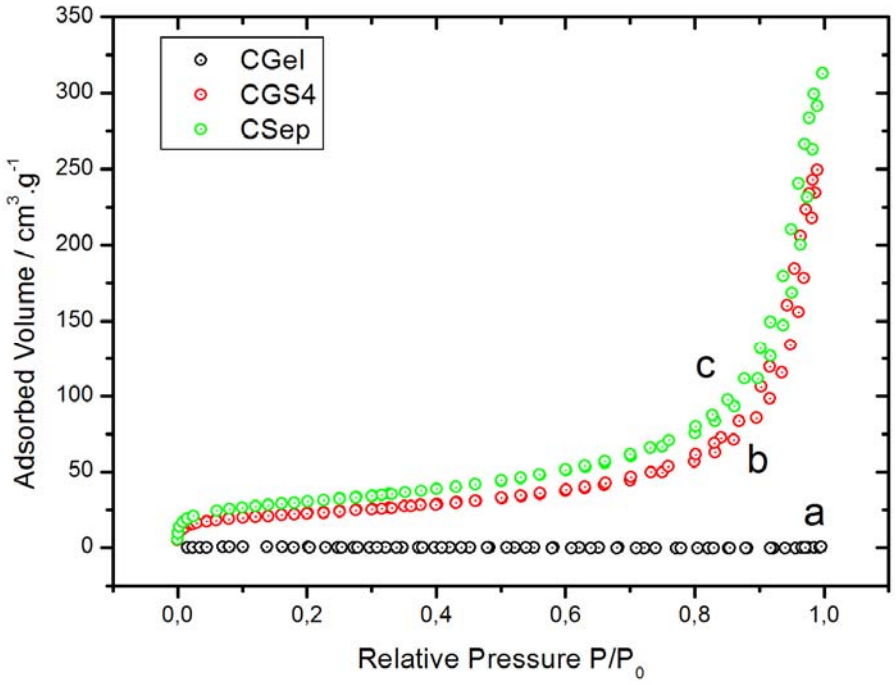


**Figure 5.5 –** Nitrogen adsorption isotherms carried out at 77 K in a) gelatine (CGel) b) CGS4 and c) sepiolite (CSep), after thermal treatment at 800 ºC.

Further studies are currently being made to clarify the reasons behind the low surface area of the generated carbon. The work being currently undertaken is especially focused in distinguishing between the existence of closed pores and the real non-porosity of the material. Meanwhile, the results give a clear indication that the adsorption properties of the prepared materials are probably not very high and will rely uniquely on sepiolite as adsorbent.

## 5.2 Preparation of carbon materials from gelatin-sepiolite foams

Polymer or polymer nanocomposite foams share one common feature, being a dispersion of a gas within a solid. In general the preparation of these materials varies greatly according to the nature of the polymer. Polyurethane (PU) foams, generally taken as reference foam like material, rely on *in situ* polymerization of the isocyanate with water and a polyol (Montminy, Tannenbaum et al., 2004; Seo, Sung et al., 2006; Chen, Zheng et al., 2007; Istrate and Chen, 2011). The reaction's outcome generates both the polymerization of PU and the formation of carbon dioxide. In this case, $CO_2$ acts as a blowing agent inducing the foaming of the material being formed. In other cases the foaming of the materials is induced by other foaming agents such as CFCs (which are presently in the process of being removed from most markets), or by porogens such as salts that are subsequently leached to generate pores corresponding to the size of the leached particles. Another approach to prepare porous materials is the usage of freeze drying techniques as mentioned in the experimental section. In the present section gelatin sepiolite foams are prepared using this technique to subsequently generate carbon-sepiolite foams upon carbonization.

### 5.2.1 Nanocomposite foams as precursors

The use of sepiolite-biopolymer foams prepared under freeze drying techniques has been previously reported for acoustic and thermal insulation-related applications (Ruiz-Hitzky, Aranda et al., 2009). In the present case gelatin sepiolite foams were prepared as an initial step in the preparation of nanocomposite carbon foams.

To evaluate the influence of the processing conditions on the porous structure formed, gelatin sepiolite (1:1) suspensions (10 wt.% total sepiolite + gelatin)

were frozen under different conditions. Table 5.2 summarizes the freezing conditions as well as the sample names.

**Table 5.2 –** Summary of processing temperatures in Gelatin Sepiolite Foams (GSF).

| Sample | Conditioning temperature / ºC | Freezing temperature / ºC |
|---|---|---|
| GSF60/-20 | 60 | -20 |
| GSF60/-196 | 60 | -196 |
| GSF4/-20 | 4 | -20 |
| GSF4/-196 | 4 | -196 |

The rationale behind the selection of the freezing and conditioning temperatures was related with two main factors. The first is that the temperature at which the suspensions are maintained before freezing may influence the renaturation level of gelatin, and therefore the mechanical properties of the resulting foam (Bigi, Panzavolta et al., 2004). Although the foams are not intended for mechanical applications on their own, the structural stability of the foam might be endangered by the low mechanical properties of the foam walls. In that sense, the use of a pre-conditioning temperature below the renaturation temperature of gelatin might induce an enhacement of the foam structural integrity. The second factor is the influence of the freezing temperature (and thus the velocity at which the ice forms) on the pore dimensions, form and number.

After freeze drying the four different foams presented a foam-like aspect and variable handling properties. As an example, sample GSF60/-20 was very prone to disaggregate into lamellar flakes upon manual handling while sample GSF4/-20 presented much more resistance to handling and maintained integrity. Both GSFs frozen under liquid nitrogen presented smaller pore size. The sample that had been preconditioned at 4 ºC presented much stronger mechanical properties and was not deformed by manual handling while sample which had been preconditioned at 60 ºC was easily deformable. In fact, the

preconditioning temperature seems to be determinant for the preparation of mechanically stable foam materials. This observation confirms the hypothesis that the conditioning temperature is critical in promoting gelatin renaturation which is later reflected in the foams' mechanical properties.

Optical microscopy was used to further assess the structure of the generated foams. As can be observed in figure 5.6 both GSFs frozen at -20 ºC present interconnected pores in the hundreds of micrometer range. However, the structure of the pores in these two samples varies significantly. Sample GSF60/-20 displays an anisotropic pore orientation while sample GSF4/-20 presents a much more isotropic structure. This observation was confirmed by the macroscopic aspect of the samples which presented markedly different appearance. It is reasonable to assume that the ice forming process in samples frozen at relatively high temperature (-20 ºC) is highly dependent on the ability of water molecules to move to the ice growing front (*i.e.* the water mobility in the dispersion) (Blond, 1988). The preconditioning of the gelatin-sepiolite at 4 ºC induces the gelling of gelatin dramatically enhancing the viscosity of the dispersion and to the formation of a stable three-dimensional network of the polymer together with sepiolite. These two parameters may be responsible for the interruption of ice crystal growth and the reduced mobility of water (Blond, 1988). On the other hand, GSF60/-20 is a much less viscous system which may lead to facile growth of ice in the preferred (heat difference driven) orientation without the resistance of a viscous system. This effect may result in anisotropic foam whose pores reflect the ice growing direction determined by temperature differences within the sample. Moreover, since the gelatin sepiolite suspension is initially at higher temperature, the freezing process is slower, leading to bigger ice crystals and consequently bigger pores.

Samples frozen under liquid nitrogen present considerably reduced pore size when compared with samples frozen at -20 ºC. This effect is mainly attributable to the fast kinetics of ice formation that leads to a big number of nucleation sites

for ice but a short period of time for crystal development. In fact the size of the pores is not detectable by optical microscopy. Figure 5.9 depicts a low magnification image of the four GSF samples under the optical microscope.

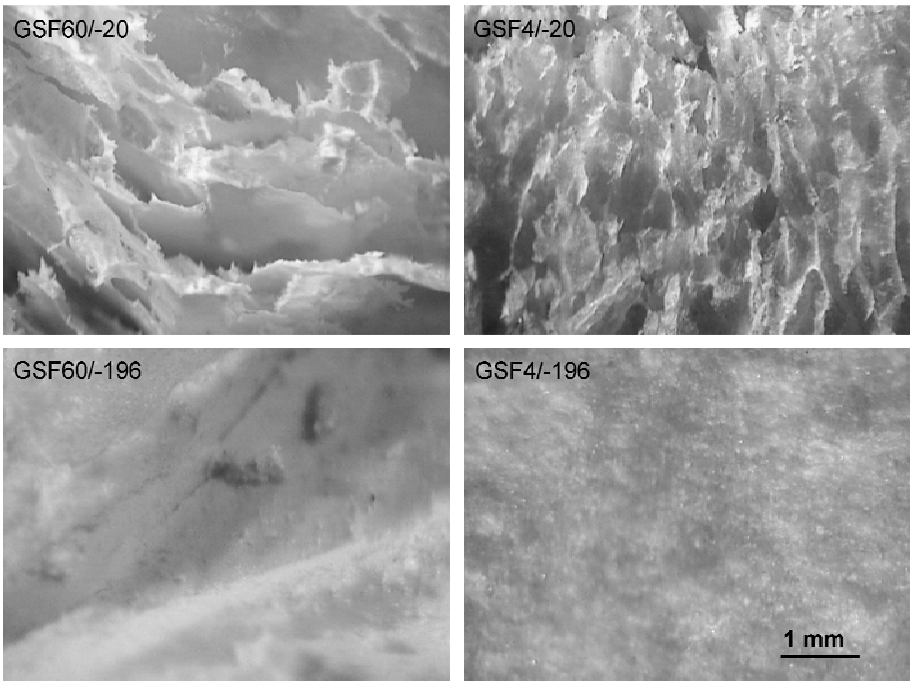


**Figure 5.6 –** Optical micrographs of the four GSF samples. Scale bar is common to the entire sample set.

Apart from the microscopy images, the analysis of the pore size distribution was performed using mercury porosimetry. Figure 5.7 depicts the main results obtained from the mercury intrusion isotherms. As is clearly observable, the pore size distribution follows, practically in all samples, a monomodal distribution. The most notable observation is, however related with the influence of the freezing conditions in the pore size distribution. Samples GSFX/-196 present considerably smaller pore sizes with a modal value in the micrometer range (around 5 μm). It is also interesting to note that sample GSF4/-196 presents a much narrower pore size distribution whereas sample GSF60/-196 presents a wide pore size distribution ranging from some micrometers to hundreds of micrometers. Samples frozen at -20 ºC present monomodal pore

size distribution bigger pores, ranging between the hundreds of micrometers to the millimetric scale.

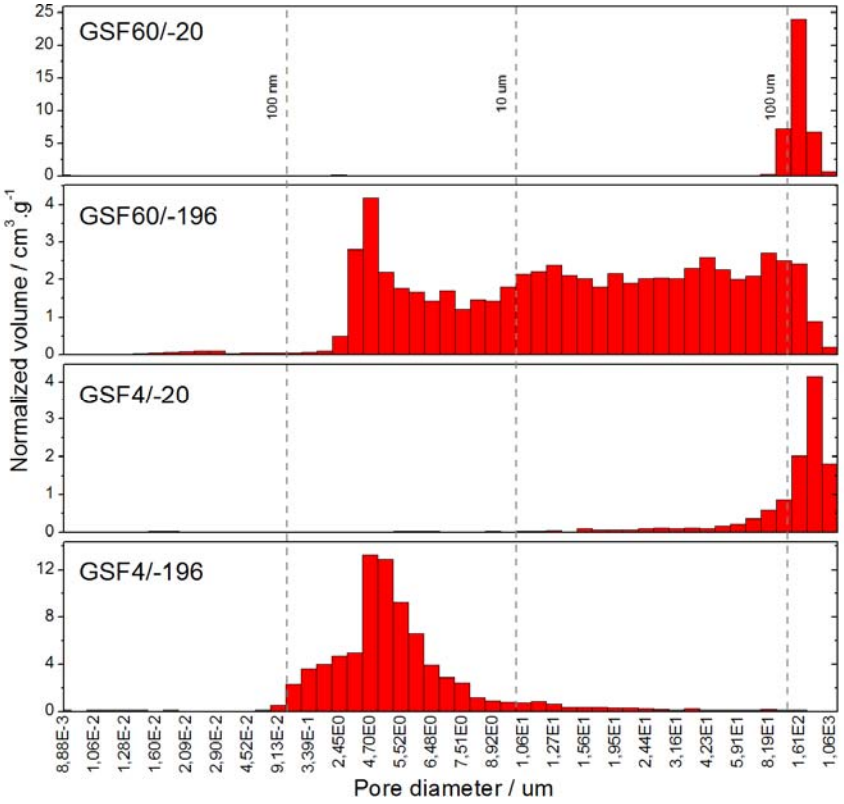


**Figure 5.7 –** Pore size distribution of GSF samples as measured by the intrusion isotherm of mercury.

Samples conditioned at 4 ºC were further characterized by FE-SEM to fully determine the microarchitecture of the pores and pore walls. To do so, SGF4/-20 and GSF4/-196 samples were gold sputtered to allow thorough imaging at different length scales without compromising the biopolymer stability while exposed to the microscope electron beam. As can be clearly observed from the consecutive micrographs taken at increasing magnifications the structure of the two foams varies considerably in the entire imaged scale range. The top images in figure 5.8 display a general view of the two prepared foams where the typical pore dimensions, previously determined by mercury porosimetry, are clearly visible. Sample GSF4/-20 displays a wide and irregular

pore structure while sample frozen under liquid nitrogen presents smaller and more homogeneous pores.

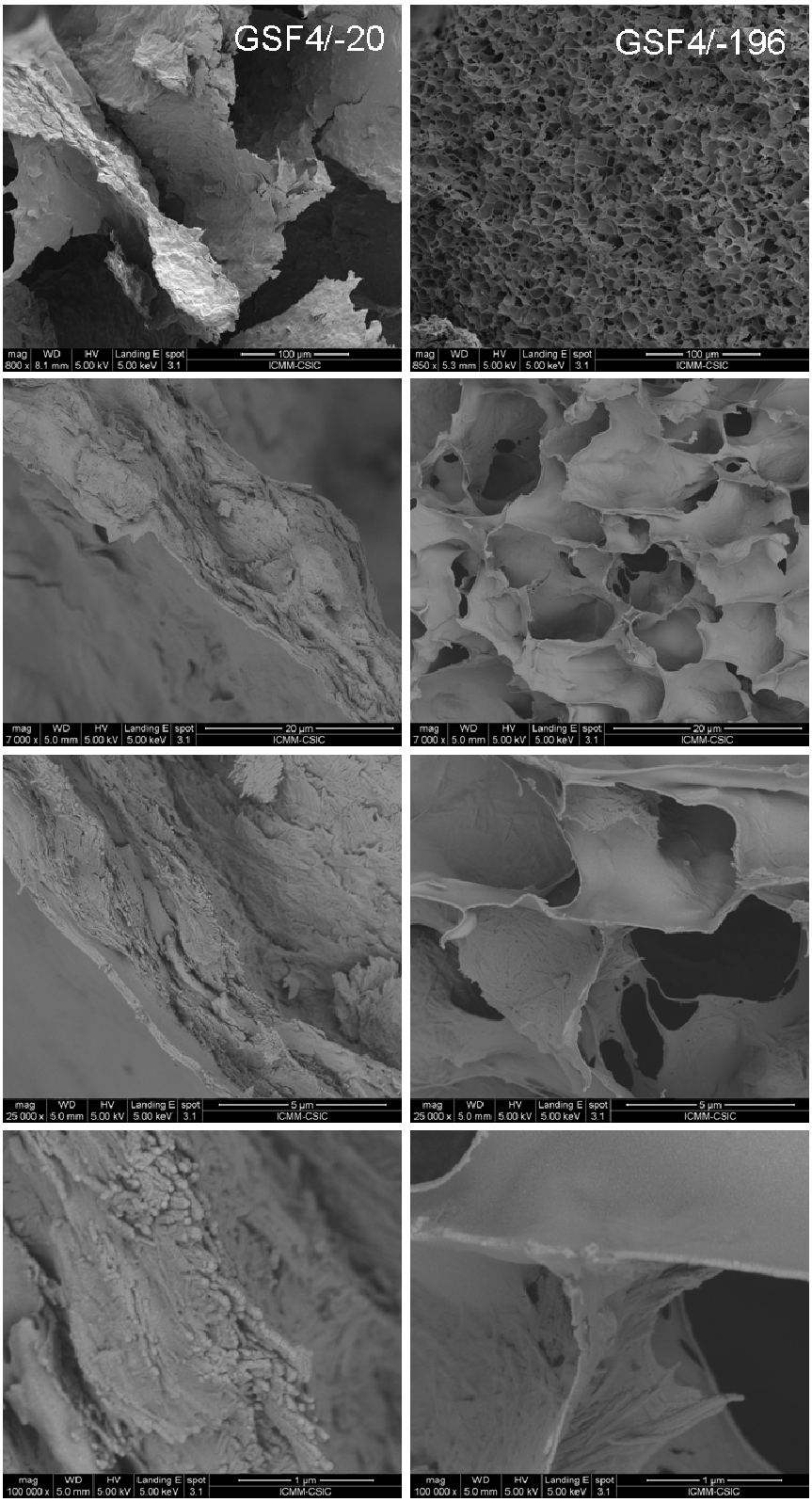


**Figure 5.8 –** Multi-scale FE-SEM micrographs corresponding to GSFs prepared from gel state and frozen at -20 ºC (left hand-side images) and -196 ºC (right hand-side images).

Also interesting to note is the differences in the wall thickness in both materials. GSF4/-20 presents wall thickness around 10-20 μm while the corresponding thickness in GSF4/-196 is below 100 nm. Although both materials display a visible (under the microscope) integration of sepiolite fibers in the pore walls, the sample frozen under liquid nitrogen presents much smoother pore walls. Another important feature is the orientation of sepiolite fibers inside the composite walls. Sepiolite fibers display random-in-plane orientation within the pore wall plane. In fact, such orientation has been previously reported for gelatin-sepiolite bionanocomposites processed as films (Fernandes, Ruiz et al., 2009; Fernandes, Manjubala et al., 2011). Such orientation of the silicate fibers is critical in the maximization of the mechanical properties of the foams as it induces a magnified reinforcing effect when compared with a totally isotropic orientation of sepiolite fibers. The arrangement of fibers within the foams is likely to be related with the ice-growing process. Hypothetically, when two vicinal ice crystals grow they tend to segregate the polymer and filler away from the ice growing front. As those ice fronts become closer and with coincident trajectory they generate high shear forces over the reinforced polymer layer that lies in between the two ice fronts. Forced by the growing ice fronts, sepiolite fibers may therefore tend to align perpendicularly to the ice crystals.

### 5.2.2 Carbon materials derived from gelatin-sepiolite foams

In order to prepare conductive materials based on gelatin sepiolite foams the same carbonization procedures were used as for gelatin sepiolite hybrids. The obtained materials were characterized by their mechanical stability, Raman spectra and electrical conductivity.

In order to use carbon foams, some degree of mechanical stability is required. In this work the criterion to accept the resulting carbon foams as useful

materials was that of self support. This means that if the carbonized foam was able to inherit both the structure and structural stability of the original GSF it was considered for application as carbon-sepiolite foam. Table 5.3 summarizes the mechanical integrity of the prepared carbon foams.

**Table 5.3 –** Summary of structural stability of the carbon foams resulting from the carbonization process of gelatin sepiolite foams. Samples that maintained their structure and mechanical stability are noted **OK**, while samples that have lost their mechanical stability are marked **X**.

| Sample | Structural Stability |
|---|---|
| GSF60/-20C | X |
| GSF60/-196C | X |
| GSF4/-20C | OK |
| GSF4/-196C | OK |

Interestingly, gelatin sepiolite foams that had been conditioned at 4 ºC present a stable structure upon carbonization, wheres GSFs prepared from gelatin sepiolite sols at 60 ºC became powdery carbonous solids when submitted to the same process. This feature extends the idea that the renaturation process of gelatin is critical to achieve mechanically resistant foams to the result of the carbonization process. Putting it in a brief manner, not only the conditioning of gelatin sepiolite suspensions at 4 ºC induces a mechanical stronger behavior to the nanocomposite foams, but also the resulting sepiolite-carbon foam maintains its structural integrity.

The conductivity of carbon foams is often an underestimated property as compared with the correspondent thermal and mechanical properties (Gallego and Klett, 2003; Chen, Kennel et al., 2006; Wang, Zhong et al., 2006; Li, Guo et al., 2007). However, the electrical properties play a major role in many applications such as antistatic materials (Kupke, Wentzel et al., 1998; Pokhmurs'kyi, Piddubnyi et al., 2005), sensors (Davis, Weber et al., 1990) among other applications. In order to evaluate the applicability of the prepared carbon foams for conductivity-related applications, the electrical properties of

the prepared materials were assessed after grinding and compaction of the foams into disk-like pellets. The conductivity results measured by EIS are displayed in Table 5.4.

**Table 5.4 –** Conductivity of gelatin sepiolite foams (GSF) after the carbonization step.

| Sample | Conductivity / S.cm$^{-1}$ |
|---|---|
| GSF60/-20C | 1.7 E-04 |
| GSF60/-196C | 1.7 E-05 |
| GSF4/-20C | 1.6 E-04 |
| GSF4/-196C | 2.1 E-05 |

The major observation related with the conductivity of the sepiolite-carbon foams is that they display a significantly higher conductivity as compared with the carbonized gelatin sepiolite hybrids previously reported (§ 5.1.1). However, the conductivity values for these materials, between 1x10$^{-5}$ and 1x10$^{-4}$ S.cm$^{-1}$, still remain distant from the conductivity values described for gelatin alone.

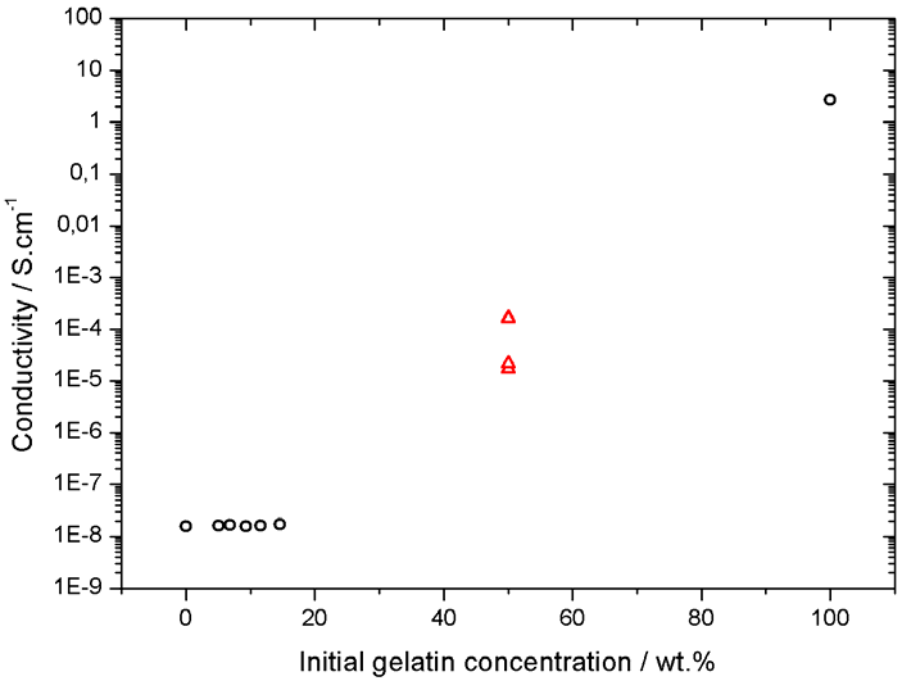


**Figure 5.9 –** Electric conductivity of carbonized gelatin sepiolite hybrids (black circles) and carbonized gelatin sepiolite foams (red triangles) as function of initial gelatin composition.

Figure 5.9 depicts the conductivity values of carbonized gelatin sepiolite hybrids, foams and carbonized gelatin alone. On the other hand it is also interesting to note that the processing conditions, especially the freezing temperature of the foams, are responsible for one order of magnitude of difference in conductivity of the grinded GSFs. Foams prepared from materials frozen at -20 ºC display conductivity around $1.6x10^{-4}$ $S.cm^{-1}$ while foams prepared from materials frozen at -196 ºC are around $2x10^{-5}$ $S.cm^{-1}$. The reasons behind these differences are difficult to establish, moreover since the samples have suffered a grinding process before the measurement.

Another important characteristic that allows a clear overview about the nature of the type of carbon materials obtained is Raman spectroscopy. Figure 5.13 displays the two main bands that characterize the obtained carbon sepiolite foams in all four different processing conditions.

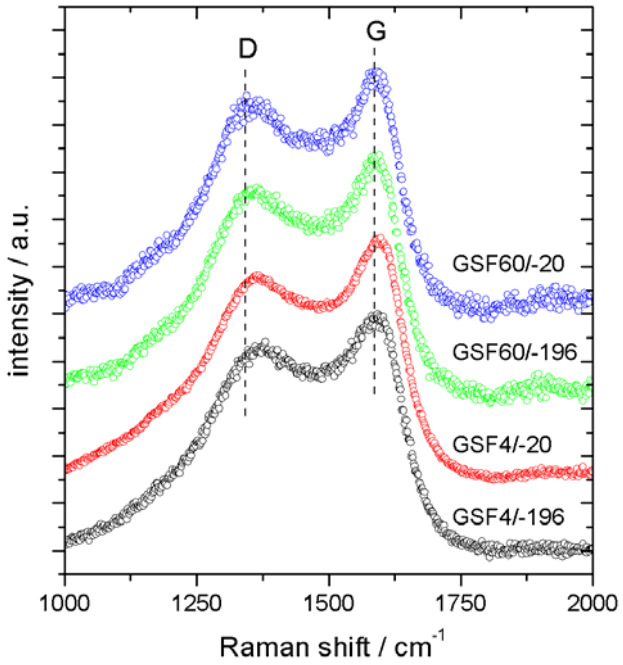


**Figure 5.10 –** Raman spectra of carbonized gelatin sepiolite foams measured under irradiation by a 2.41 eV laser (514 nm). The luminescent background present on the spectrum of sample GS4C due to the presence of sepiolite was subtracted. Additionally the curves have been normalized and artificially displaced for clarity of interpretation.

Once again, the relative intensity of the D and G bands is a critical parameter to establish the relation between the amounts of carbon atoms in $sp^2$ or $sp^3$ hybridization. Contrarily to the results obtained for the carbonized hybrids GS4C and carbonized gelatin alone, the prepared carbonized foams display a G band significantly more intense than the D band. This feature indicates that the conditions under which the foams were prepared are more suitable for the generation of highly conjugated graphenic systems. Once again, the Raman spectra does not present any second order features such as 2D band.

There are two main differences between the carbonized gelatin sepiolite hybrids and the carbonized gelatin sepiolite foams that may account for the different Raman profile. On the first hand the processing conditions of the foams force the gelatin moiety to undergo negative temperatures and considerable shear forces. These conditions may, hypothetically, drive the biopolymer to organize into different conformational states more prone to graphitization upon thermal treatment. On the other hand, the morphology of the materials before carbonization may also account for significant differences in the carbonization process. Taking into account that gelatin contains a fair amount of oxygen atoms, it is plausible to assume that these along with other volatiles will be responsible for some degree of oxidation upon thermal treatment. In the case of bulk materials such as the compacted pellets (carbonized gelatin sepiolite hybrids) the diffusion of such volatiles should be slower due to the denser nature of the pellets, favoring the partial oxidation of the material and thus resulting in higher concentration of defects in the resulting carbon. For carbonized gelatin sepiolite foams, the diffusion of volatiles should, in principle, be facilitated by the extensive porosity in the material and the thin walls. This characteristic of the foams can therefore act as a limiting factor, preventing or minimizing, the oxidation processes in the resulting materials. This feature could explain the decrease in defects that are characterized by the inversion of the D to G band ratio.

*a) Carbonized Gelatin Sepiolite Foams in composite materials*

In order to elucidate about the applicability of the prepared carbonized gelatin sepiolite foams, these were used to produce conductive composites based on thermosetting epoxy resin.

Carbonized gelatin sepiolite foams GSF4/-20 and GSF4/-196 were immersed in an uncured mixture of DGEBA and the corresponding diamine under vacuum at 40 ºC. After the vacuum induced evacuation of air trapped inside the carbonized foams these plunged to the bottom of the uncured mixture indicating that their density had surpassed that of the uncured resin and thus confirming the filling of the pores by the resin had occurred extensively. After standard curing the obtained blocks were machined to expose the carbonized foam surface. Figure 5.14 illustrates the aspect of both foams before and after carbonization along with the corresponding epoxy-filled foams.

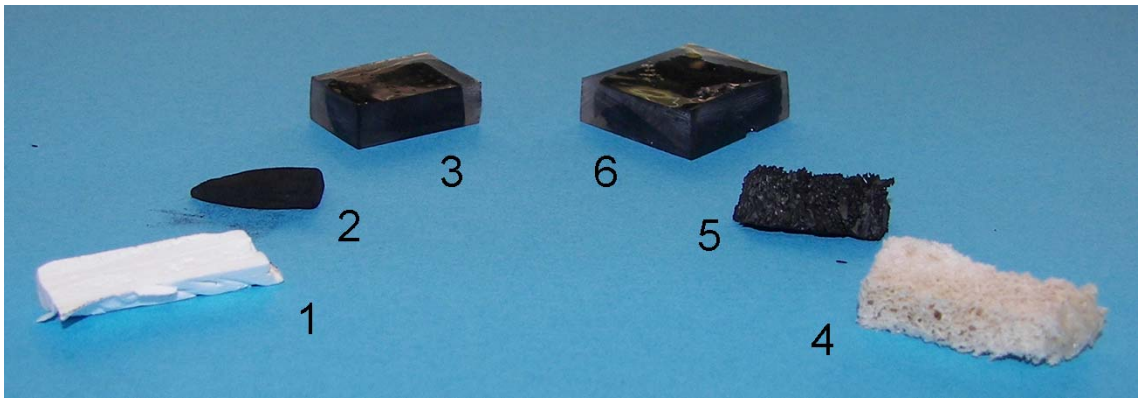


**Figure 5.11 –** Gelatin sepiolite foams displaying structural integrity before carbonization, after carbonization and after immersion in epoxy resin. 1) GSF4/-196, 2) GSF4/-196C, 3) epoxy-GSF4/-196C, 4) GSF4/-20, 5) GSF4/-20C, 6) epoxy- GSF4/-20C.

During the immersion process in the epoxy resin the carbonized foams did not experience any visible apparent volume change.

Achieving conductive epoxy system is of paramount importance in many technological fields such as electronic circuitry and packaging (Li and Wong,

2006), electromagnetic/radio frequency interference (EMI/RFI) shielding (Azim, Satheesh et al., 2006) and static charge dissipation among other applications. To establish the applicability of the prepared epoxy filled foams their volumetric conductivity was measured yielding the values presented in Table 5.6.

**Table 5.5 –** Volumetric conductivity values determined under DC mode for epoxy-filled carbonized gelatin sepiolite foams.

| Sample | Conductivity / $S.cm^{-1}$ |
|---|---|
| Epoxy-GSF4/-20C | 8.6 E-03 |
| Epoxy-GSF4/-196C | 1.5 E-02 |

Interestingly the electrical conductivity determined in the epoxy filled carbonized foams surpasses the values previously determined in the grinded foams. This fact may be associated with the destruction of the porous structure upon grinding and consequent loss of connectivity of the grinded particles. Moreover the differences in conductivity determined in the grinded foams between the materials processed at -20 ºC and the materials processed at -196 ºC seems to dissipate when they are measured in the epoxy-filled system. This feature indicates that more than an absolute difference in the conductivity of the samples, the differences determined in the grinded carbonized foams correspond to different results of the grinding and compaction process.

## 5.3 Concluding remarks

The reported strategies of preparing nitrogen-doped carbons from gelatin sepiolite hybrids and foams resulted in different materials and significant insight. Firstly, the sepiolite containing carbonized materials obtained from gelatin-sepiolite hybrids were found to display a layered structure resembling that of graphene associated with the silicate fibers. Raman spectroscopy of this material also proved the existence of considerable amount of graphitic domains.

The material obtained from the carbonization of the more gelatin rich hybrid (GS4C), however insufficient to promote the generation of an extensively conductive system. Further development of hybrids with higher concentration in gelatin may provide sufficient carbon network to generate a fully percolating network of conductive material. In such case, gelatin-derived carbon associated with sepiolite fibers could provide an interesting filler for structural and electrical applications in polymers.

Gelatin sepiolite foams were successfully prepared by freeze drying process of gelatin sepiolite aqueous suspensions. Their morphology and mechanical behavior seem to be controllable upon precise selection of the processing temperatures, especially the conditioning temperature (that determined if the freezing process occurs from the sol or gel states) and freezing temperature. A set of complementary essays are necessary to optimize this system.

The chemical nature of the carbon atoms in the final carbonized structures was also affected by the processing conditions. In the case of carbonized foams, the $sp^2$ to $sp^3$ ratio (as determined by Raman spectroscopy) was inverted when compared with carbons derived from GS hybrids. The enhancement of graphitic domains could be explained by the porous structure of the starting foam that may provide a more effective way to eliminate volatile subproducts of the carbonization or even oxidizing species such as molecular oxygen. The produced foams, that display electrically conductive behavior with conductivities in the $1x10^{-2}$ $S.cm^{-1}$ range, were applied as proof of concept in epoxy resin in which the foams were embedded.

# 6. Sepiolite-Carbon Nanotube materials and nanocomposites

Since its discovery, large scale application of carbon nanotubes (CNTs) has been systematically postponed due to the inherent difficulties in handling this material (Iijima, 1991). Such difficulty in handling has, alongside with its high cost, impaired the extended use of CNTs in the industrial applications where it is expected that CNT's would excel due to their outstanding properties (electrical, mechanical, thermal, optical, etc.). One of the most relevant questions in solving the handling of CNTs is to achieve a homogeneous degree of dispersion in different aqueous media (as it would permit easy handling in most industrial processes) and polymeric matrices for the preparation of high performance nanocomposites. Although different approaches have been developed to achieve a homogeneous dispersion of CNTs, no single one seems to solve the problem thoroughly, especially at high CNTs concentration. In fact, the strategies developed so far, have proven effectiveness only in very dilute systems.

## 6.1 Sepiolite as a mediator for CNT dispersion in aqueous media

This section is devoted to a new approach designed to effectively disperse CNTs making use of fibrous clay mineral sepiolite. The proposed strategy allowed dispersing multiwall carbon nanotubes (MWCNTs) in water both in low and high concentration regimes and to prepare a new type of buckypaper materials from these dispersions. The reported co-dispersion approach opens a clear pathway to use CNTs in aqueous media without the use of chemical entities such as surfactants, and thus enabling water-based chemistry in pristine nanotubes.

### 6.1.1 CNT dispersion stability using sepiolite

Two main approaches have been reported so far to handle the difficulties of CNT dispersion. The more chemical approach consists on the deep modification of CNT walls and can be regarded as a functionalization approach (Tasis, Tagmatarchis et al., 2006). This strategy is usually preceded by an oxidative step that generates, in a not always controlled manner, some degree of damage into the CNT walls. These defects, usually in the form of carboxylic acids, are the functionalization cornerstone as they convert the inert rolled up graphitic outer sheet into an easily available organic chemistry building block. More subtle approaches have been developed, among others, by Prato and co-workers who proposed a chemical functionalization mechanism based on the 1,3-dipolar cycloaddition of azomethine ylides to the nanotube walls (Georgakilas, Kordatos et al., 2002; Tagmatarchis and Prato, 2004). Other authors have also developed other cycloaddition mechanisms such as the Diels-Alder reaction to functionalize Carbon Nanofibers (CNFs) (Araujo, Fernandes et al., 2007; Fernandes, Araujo et al., 2007). However, it should be

taken into consideration that no matter how subtle the chemical pathway might be, it will still generate considerable damage to the highly conjugated π system with the corresponding decrease of the CNTs mechanical properties (Garg and Sinnott, 1998). Also the grafting of an organic moiety, usually insulating, onto the tube wall will most likely affect electronic conductivity. The second chief concept in the dispersion of CNT is when it is mediated by molecular or macromolecular entities such as surfactants (Jiang, Gao et al., 2003; Moore, Strano et al., 2003), or polymeric chains that interact with the CNT surface (Zheng, Jagota et al., 2003; Lee, Huh et al., 2007). In these cases the involved mechanism is considered as a steric stabilization (Penicaud, Poulin et al., 2005). From a fundamental point of view, steric stabilization consists on the enhancement of the repulsive forces between two adjacent particles that hold an adsorbed species on its outer surface, thus augmenting the net stability of the colloid (Birdi, 2009). From a more practical point of view, using steric stabilization to disperse CNTs requires applying ultrasounds that promote temporary separation of CNTs while molecules in solution are adsorbed onto the nanotube surface (Szleifer and Yerushalmi-Rozen, 2005; Yerushalmi-Rozen and Szleifer, 2006). These molecules (*e.g.* tethered polymers) account for the repulsive forces between adjacent nanotubes, and therefore for the potential wall that will likely prevent CNT from rebundling (Girifalco, Hodak et al., 2000; Shvartzman-Cohen, Nativ-Roth et al., 2004; Yerushalmi-Rozen and Szleifer, 2006). Although this strategy might not give rise to thermodynamically or kinetically stable dispersions, it will produce a metastable state of CNTs dispersion typical of colloids (Yerushalmi-Rozen and Szleifer, 2006).

This section focuses on a variation over the steric stabilization approach. Here the interposed species is not a molecular or macromolecular entity but another nanoparticle, fibrous clay mineral sepiolite. Few works have been reported on the concomitant use of CNTs and silicates. The most notorious, reports the formation of micelle-like aggregates between micas and CNTs allowing the

irreversible dispersion of CNTs in either water or organophilic solvents such as toluene (Lan and Lin, 2009).

The main goal of this section regards the preparation of stable co-dispersions of CNTs and sepiolite in water. The resulting water-based dispersions are crucial as they configure a starting point allowing to prepare other materials as for instance CNT-based bionanocomposites and self supported films similar to buckypapers (Rinzler, Liu et al., 1998). To demonstrate the stability of MWCNTs dispersions in high concentration regime, 1% (w/v) MWCNTs were dispersed in the presence and absence of 5% (w/v) sepiolite by applying 1KJ of ultrasonic energy per 20 ml of dispersion. Scheme 6.1 depicts the dispersion procedure based on the concomitant dispersion of sepiolite and CNT under ultrasonic irradiation.

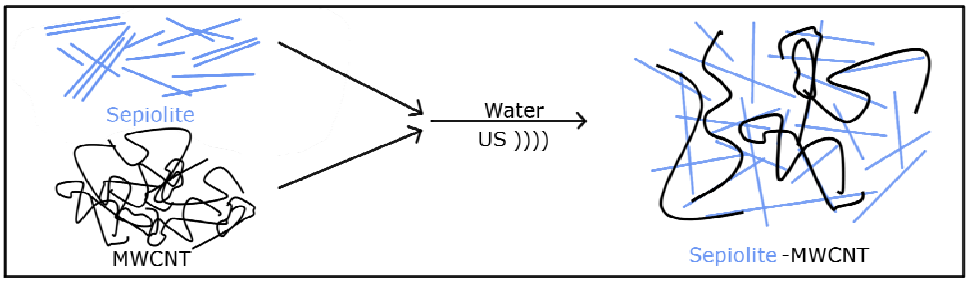


**Scheme 6.1 –** Dispersion scheme for sepiolite-CNT materials using ultrasonic agitation in water.

Interestingly, the resulting dispersions imaged six month after sonication, display high macroscopic homogeneity and stability of the dispersion of MWCNTs in presence of sepiolite as opposed to the flock morphology observed in the MWCNTs dispersed without the silicate. Figure 6.1 depicts the macroscopic aspect of the obtained dispersions. This observation suggests that the presence of sepiolite nanofibers prevents re-aggregation of the MWCNTs and thus keeps them in suspension. In order to investigate the extension of the observed dispersion, some parameters were studied. The optimization of the dispersion conditions was carried out taking into account factors, such as sepiolite concentration and the amount of ultrasonic energy involved to disperse

the system. The stability of the dispersions was monitored for 10 days starting from the moment of the ultrasonic dispersion (Fig. 6.1).

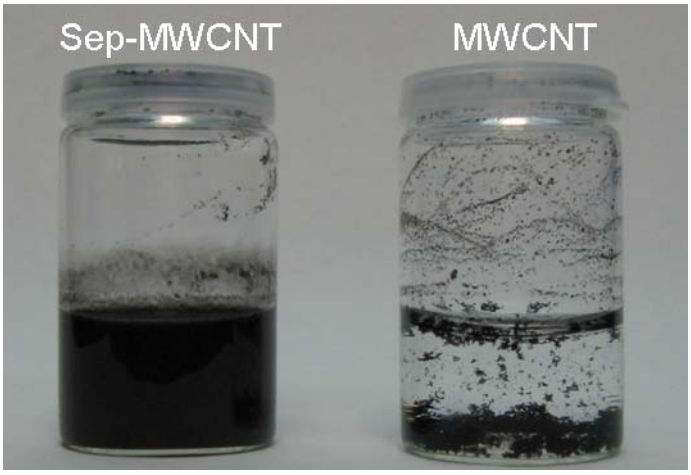


**Figure 6.1 –** Macroscopic aspect of the dispersions of 1% MWCNT in water using sepiolite as a dispersant (left vial) and without the presence of sepiolite (right vial). The image was taken six month after sonication.

A key concept to understand the behavior of sepiolite dispersions is its rheological percolation threshold. The percolation threshold ($q_p$) is defined as the concentration (number of particles per unit volume of continuous medium) at which all the discrete particles dispersed in a continuous phase become influenced by at least one adjacent particle. A complementary notion, which is helpful in overcoming the gap between the concept of percolation threshold and its relation with a relative quantity such as concentration, is that of excluded volume ($V_{ex}$).

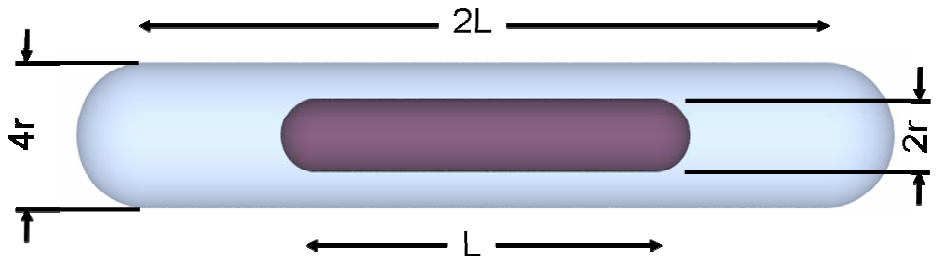


**Figure 6.2 –** Excluded volume (blue) calculated for a single spherocylinder (purple) of radius r, and legth L. The excluded volume is calculated based on the presence of another fiber (spherocylinder) aligned with the first (i.e. angle defined by the spherocylinders axes, θ = 0).

The excluded volume corresponds to a volume around each particle where no other particle is allowed, i.e. the necessary volume of particle-free continuous matrix that each particle needs in order to remain isolated from other particles in the vicinity. Figure 6.2 depicts one example of the exclude volume of a spherocylinder (Balberg, Anderson et al., 1984).

As seen in the previous image to define an excluded volume for a given particle it is necessary to take into account another particle forming an angle θ with the previous particle. As it is unpractical to define all the angles formed between adjacent fibers present in a continuous medium, average values are used instead. Equation 6.1 decribes the calculus of an average excluded volume, $\langle V_{ex} \rangle$, assuming an isotropic distribution of the fibers. The previous condition permits to calculate an average angular relationship between the fibers (Balberg, Anderson et al., 1984; Berhan, 2007). A full derivation of such angular term is available from reference (Balberg, Anderson et al., 1984) and will not be detailed here.

$$\langle V_{ex} \rangle = \frac{32\pi}{3} r^3 \left[ 1 + \frac{3}{4}\left(\frac{L}{r}\right) + \frac{3}{32}\left(\frac{L}{r}\right)^2 \right] \qquad \text{(eq. 6.1)}$$

Taking into account that the volume of a spherocylinder is defined by equation 6.2,

$$V = \frac{4\pi}{3} r^3 + \pi r^2 L \qquad \text{(eq. 6.2)}$$

and that $\phi_c$, the fiber volume fraction at percolation, is defined by equation 6.3,

$$\phi_c = \frac{V}{\langle V_{ex} \rangle} \qquad \text{(eq. 6.3)}$$

comes that for sepiolite fibers with average radius of 20 nm and an average length of 3 μm dispersed in water, the volume fraction of sepiolite at percolation is around 1.4 % (w/w). According to these calculations, the rheological behaviour of sepiolite suspensions in water should change dramatically at this concentration. Figure 6.3 illustrates de variation of the viscosity of a sepiolite suspension as function of sepiolite concentration.

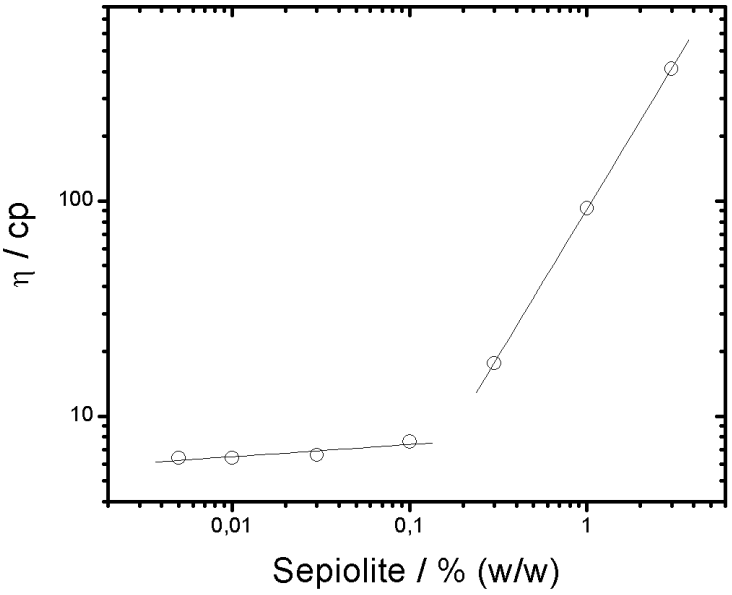


**Figure 6.3 –** Apparent viscosity of sepiolite suspensions as function of its concentration measured using a Brookfield viscosimeter.

Although the variation of viscosity follows the expected concentration dependence above percolation (*circa* 0.2 % w/w), the value at which the suspension displays a percolating network behavior is far below the one predicted using equation 6.3. Since the gap between the predicted (1.4 %) and observed (0.2 %) values is significant, one must conclude that the interaction between sepiolite fibers in water takes place at higher distances than the ones assumed in the referred model. Other model is described in the literature that accounts for systems that percolate without an actual contact between its particles (Berhan, 2007). Unfortunately, unless the interaction distance is know for a given system, only numerical solutions are available.

Regardless of these differences, the influence of sepiolite concentration (especially below and above the percolation threshold) on the capacity to disperse MWCNT was assessed. Figure 6.4 displays the stability over time of sepiolite-MWCNT suspensions using sepiolite concentrations below (left vials) and above (right vials) the percolation threshold of sepiolite in water. The applied energy to disperse the system using ultrasounds (US) is also accounted for.

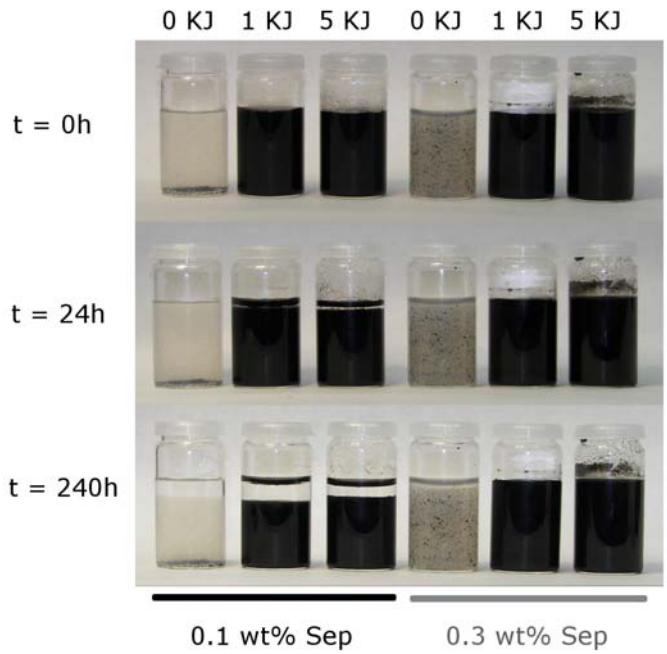


**Figure 6.4 –** Stability evaluation of sepiolite-MWCNT suspensions as a function of time, applied US energy and sepiolite concentration. The weight relation between sepiolite and MWCNT was kept constant, Sep-MWCNT 5:1. Vials marked 0 KJ correspond to manual vigorous agitation during one minute.

The observation of the dispersions stability indicates that one key criterion to obtain a stable dispersion is the application of ultrasonic agitation. In both sepiolite concentrations, the vial correspondent the manual agitation displays a flock like morphology of MWCNT. An interesting feature is that the stability of the suspension where US agitation was applied seems to be independent of the amount of US energy applied. Such information is of great utility as it permits to establish minimum US energy values to disperse the system, avoiding

extensive damage into the MWCNT walls. Another critical observation is related to the stability of the suspensions over time. Although all suspensions where US was applied were homogeneous at t=0h, during the course of the first 24h the suspensions prepared with the lowest sepiolite concentration started to segregate into two phases. On the other hand, Sepiolite-MWCNT suspension prepared using 0.3 wt% sepiolite maintained their stability during the monitored time period. In fact, this observation agrees well with the postulated idea that the concentration of sepiolite is a key factor in promoting the stability of MWCNT aqueous suspension. More precisely, the use of sepiolite concentrations just below and above percolation defines the stability of the suspension. Briefly put, to effectively disperse sepiolite using sepiolite in water the following criteria must be fulfilled.

1) The use of at least 1KJ of US energy per 20 ml of suspension.
2) The use of a concentration of sepiolite above its percolation threshold.

Another relevant point concerning the dispersion of MWCNT in presence of sepiolite is the need to use US agitation. This technique, as briefly discussed in the experimental section, is essential to achieve the dispersion of CNTs. All of the techniques described in the literature to homogeneously disperse CNTs in aqueous environments, based on steric stabilization, are dependent on US. Yerushalmi-Rozen and co-workers have shown that the role of sonication is critical in that context (Shvartzman-Cohen, Levi-Kalisman et al., 2004; Shvartzman-Cohen, Nativ-Roth et al., 2004; Yerushalmi-Rozen and Szleifer, 2006). The US energy applied promotes a temporary separation of adjacent CNTs forming bundles. By separating the individual CNTs, the steric stabilizer in solution (end-tethered polymer, biomolecule, etc.) is able to adsorb onto the previously occluded walls of the CNTs that were interacting with adjacent nanotubes forming CNT bundles. Such adsorbed moieties will subsequently create a potential barrier that hampers the CNTs from rebundling. To describe such phenomenon the referred authors have used the intertube potential

defined by Girifalco et al. as the driving force for nanotube bundle cohesion (Girifalco, Hodak et al., 2000). In the approach described in this dissertation, the interposed species is sepiolite. Figure 6.5 shows microscopic images of the dry residue of Sep-MWCNT suspensions.

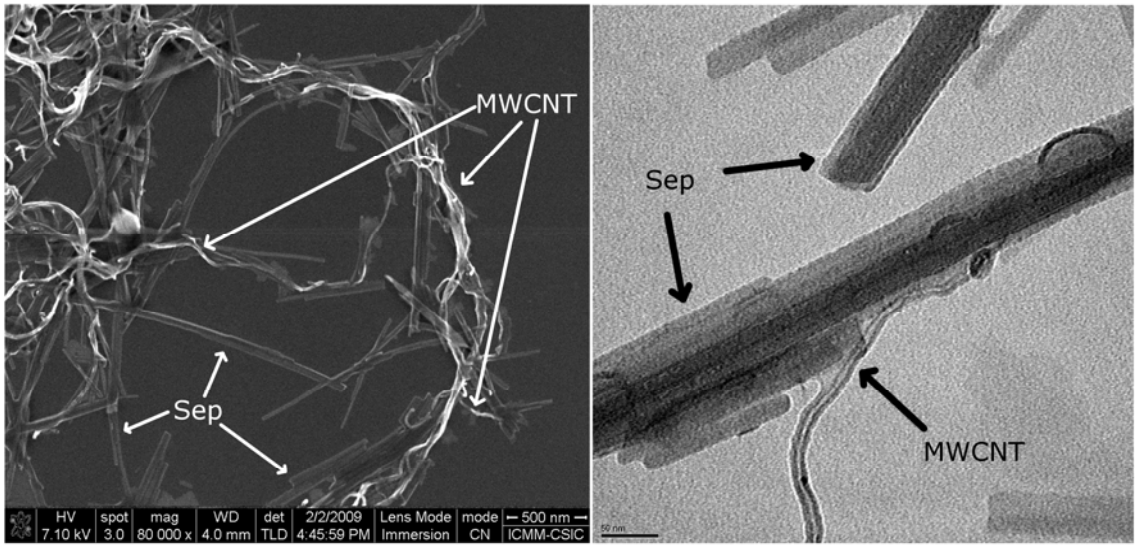


**Figure 6.5 –** Microscopy images of Sep-MWCNT materials. Left image was obtained under a FE-SEM. Due to their electrical conductivity MWCNT appear as bright materials. Another feature helping to distinguish between sepiolite fibers and MWCNT is that the latter show high degree of waviness. Right hand image was acquired using a TEM where sepiolite fibers appear as straight particles with different shades of grey and MWCNT as curved, hollow fibers, thinner than sepiolite.

In fact, TEM and FE-SEM (Fig. 6.5) images of the dry residue of MWCNTs-sepiolite suspensions, reveal that MWCNTs tend to associate to sepiolite after sonication rather that to rebundle. Is this sense, although sepiolite fibers are not adsorbed onto the nanotube walls, the network of sepiolite fibers in between the nanotubes can be considered as steric stabilizer, since it prevents MWCNTs from rebundling.

Another relevant factor contributing to the unexpected cooperativeness between such different materials is related to the rheological properties of sepiolite in the domains of time. Maqueda et al. have studied the viscosity of sepiolite suspensions at different shear rates (Maqueda, Partal et al., 2009). They have

demonstrated that similarly to what happens with other clay slurries (Abou, Bonn et al., 2003; Tombacz and Szekeres, 2006), sepiolite suspensions in water present a markedly shear thinning behavior. Shear thinning is a non-Newtonian rheological behavior characterized by a variable viscosity of the material being tested as a function of the frequencies at which the shear is applied (shear rate). More specifically, it behaves as a less and less viscous material as the shear rate increases. Sepiolite suspensions studied by Maqueda and co-workers displayed an intense shear thinning effect reaching a minimum in viscosity of 5 mPa.s at 1 kHz shear rate while for 1mHz shear rate it displayed a maximum in viscosity of $5x10^5$ mPa.s (Maqueda, Partal et al., 2009). Figure 6.6, reproduced from Maqueda et al. with permission from Elsevier, represents the pseudo-plastic (i.e. shear thinning) behavior of sepiolite suspensions dispersed in water (Maqueda, Partal et al., 2009).

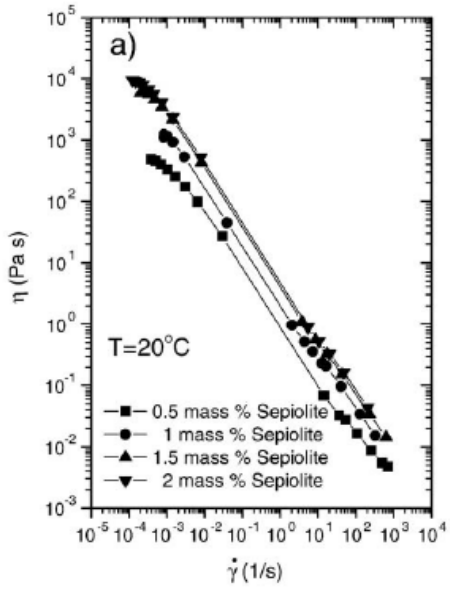


**Figure 6.6 –** Shear-thinning behavior of sepiolite suspensions at four different concentrations, 0.5, 1, 1.5 and 2 wt.% in water. Reproduced from Maqueda et al. (2009) with permission from Elsevier (Maqueda, Partal et al., 2009).

As depicted in figure 6.6, sepiolite slurries between 0.5 and 2 wt.% show a noticeable shear thinning effect. This behavior is critical in many industrial

applications such as drilling muds or ink additives, where the low viscosity at high shear rate and high viscosity at low shear rate is of great interest. In the case of the dispersion of MWCNT in aqueous environments it also seems to play an important role. Taking into consideration that the US dispersion of sepiolite occurs at the resonant frequency of the piezo element (20 kHz), and that the role of the piezo is to induce shear in the dispersion; one can assume that the behavior of a sepiolite suspension under US agitation is comparable to the one it would display under rotational shear. The notion that shear applied to a non-Newtonian material using either rotational or US are comparable is validated by some non-standard rheological techniques (Longin, Verdier et al., 1998; Leroy, Pitura et al., 2010). In the referred papers, the authors made use of US emission to study the rheological properties of materials at frequencies which are prohibitive for a rotational rheometer. In summary, they show that it is expected that a material behaves under US induced shear as it would under rotational shear at comparable frequencies. As sepiolite slurries studied by Maqueda et al. show a steady shear thinning behavior across seven orders of magnitude it is expectable that such trend will decisively influence the viscosity of sepiolite when subjected to the US shear at 20 kHz. To put it briefly, sepiolite viscosity under US agitation is expected to be several orders of magnitude below the viscosity detected at 1 Hz (which can be considered a typical precipitation frequency). Since during sonication MWCNTs debundle temporarily and the mobility of sepiolite is maximized due to the shear induced decrease in viscosity, it is then likely that sepiolite fibers diffuse into the inter-nanotube spaces previously unavailable. The diffusion of sepiolite into such spaces might consequently generate a potential barrier that hampers MWCNTs from rebundling. Figure 6.7 displays a schematic presentation of the concepts detailed above.

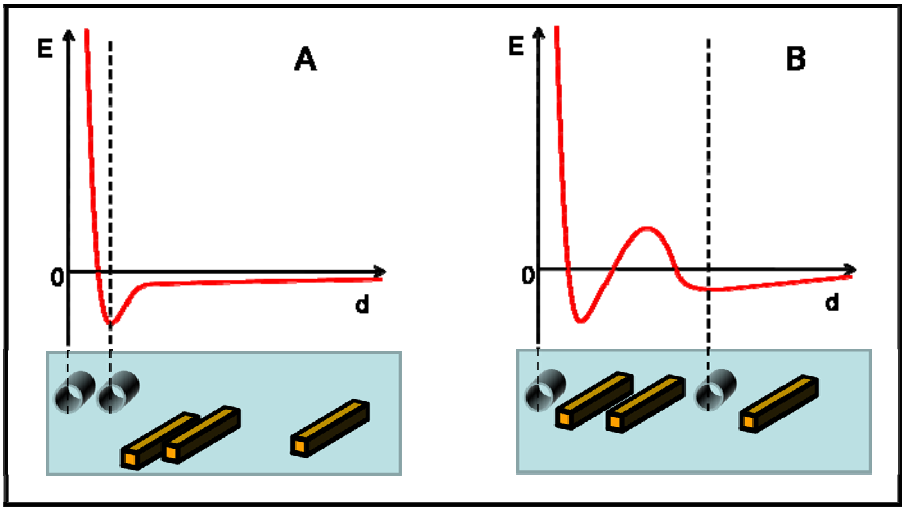


**Figure 6.7 –** Proposed schematic representation of the debundling of MWCNT (hollow tubes) induced by US agitation in presence of sepiolite fibers (orange rectangular prisms). The upper part of the scheme represents the energy potential between a pair of nanotubes as a function of their distance. The lower parts of the scheme (blue rectangles) depict the dispersion state/spatial distribution of MWCNT and Sep. A) before sonication. The potential between bundled nanotubes is defined by the Lennard-Jones carbon-carbon potential well described by Girifalco et al. (Girifalco, Hodak et al., 2000). B) after sonication. The MWCNTs remain debundled after sonication due the potential barrier that arises from the presence of sepiolite particles in between the previously adjacent nanotubes.

The dispersion of MWCNT in low concentration regime using sepiolite as a co-dispersant was also assessed by means of UV absorption. To assess the effectiveness in dispersing MWCNT the dispersion was evaluated in the presence and absence of sepiolite and also in presence of a common surfactant used in nanotube stabilization, sodium dodecyl sulphate. Figure 6.8 displays the results for the stability evaluation of low concentration of MWCNTs in aqueous media.

Immediately after sonication (t=0h) both MWCNT dispersions obtained in presence of an adjuvant (sepiolite and SDS) display higher absorption than the dispersion obtained in water indicating a higher concentration of MWCNTs in suspension. Given that MWCNTs are active in the visible range only if they are in isolated state, the absorption at 500 nm ($A_{500}$) directly reflects the amount of isolated MWCNTs present in the dispersion (Yu, Grossiord et al., 2007; Rastogi,

Kaushal et al., 2008). After 24 hours the concentration of individual MWCNTs suspended dropped significantly in the three dispersions. The most noticeable variation regards MWCNTs in water, where the absorption value dropped from $A_{500}$=0.31 to $A_{500}$=0.05, corresponding to the rebundling of approximately 84% of the previously suspended individual MWCNTs. The results concerning the adjuvant (Sep and DDS) aided dispersions also present an important decrease of the individually suspended MWCNTs. Adjuvant aided dispersions, MWCNT-Sep and MWCNT-DDS, present approximately the same absorption after a settling period of 96 hours, corresponding to approximately $A_{500}$=0.3. After the same period of time, the remaining individual MWCNTs from the water based dispersion present absorption, $A_{500}$=0.01.

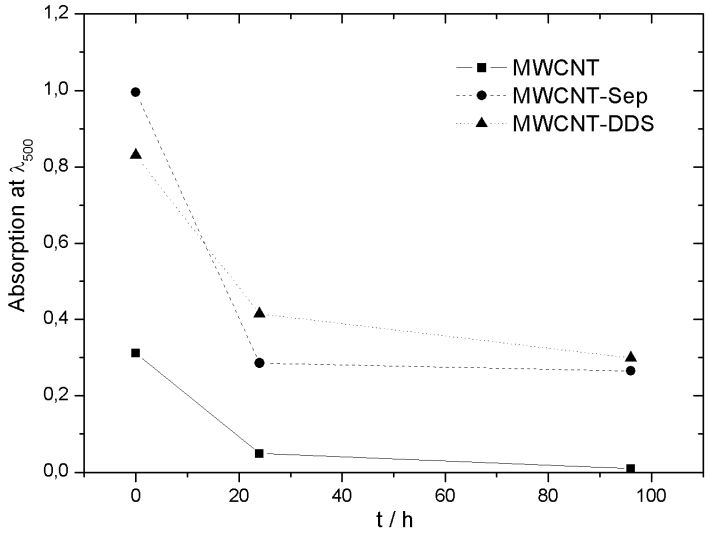


**Figure 6.8 –** Variation of the absorption of MWCNT suspensions using different co-adjuvants at 500nm along 96 hours.

In summary, both sepiolite and DDS promote the stabilization of 30 times the amount of individual CNTs dispersed in water. The mechanism governing the suspension of MWCNT below the percolation threshold of sepiolite fibers is still unclear and cannot be explained by the arguments used for the highly concentrated dispersions. Nevertheless, the result itself is of great relevance as sepiolite aided dispersion was proven to be as effective as surfactant aided

dispersion, which is in the present the most used non-covalent approach to disperse CNTs.

### 6.1.2 Sepiolite-CNT nanocomposites

The dispersion of MWCNT in hydrophilic polymeric moieties is another field of major interest. Due to their excellent mechanical properties, MWCNTs are expected to greatly improve the performance of water soluble polymers. However the problems mentioned for the dispersion of CNTs in aqueous dispersions hold for aqueous polymer solutions. To ascertain the applicability of sepiolite mediated dispersion of CNT in polymeric matrices several weight relations between Sep and MWCNT were tested in polyvinyl alcohol (PVA). Figure 6.9 is composed of different photographic images of the macroscopic aspect of each of PVA-Sep-MWCNT nanocomposites.

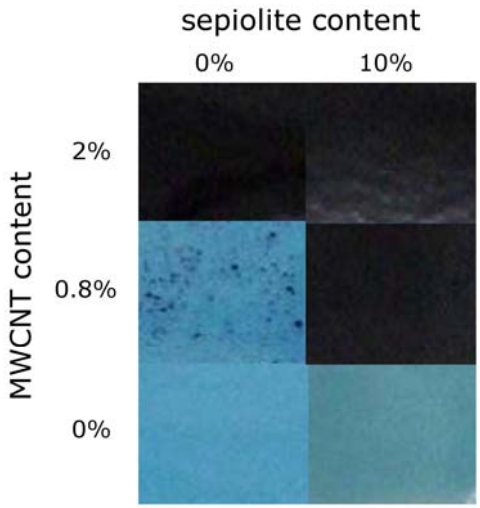


**Figure 6.9 –** Photographic images of PVA-Sep-MWCNT nanocomposite films with variable composition. The film thickness was approximately 300 μm. The composite films were photographed against a blue background to help evaluate the dispersion state of the filler.

The PVA-Sep-MWCNT nanocomposite films present different homogeneity as a function of the proportion between sepiolite and MWCNTs used as filler. According to figure 6.9, nanocomposite films containing 10 % (w/w) of sepiolite

(right column) display a much higher macroscopic homogeneity regardless of the MWCNT content. On the other hand, there are clearly visible aggregates of carbonaceous material in composites prepared without sepiolite (left column). It seems thus clear that in the presence of a hydrophilic polymer, sepiolite works as a mediator and a stabilizer in the dispersion of MWCNTs. In order to assess the ideal weight relation between sepiolite and MWCNT the mechanical (elastic) properties of PVA-Sep-MWCNT nanocomposites were evaluated. Sepiolite content was varied from 0 to 10 % (w/w) while the MWCNT content varied from 0 to 2 % (w/w). Figure 6.10 displays the elastic modulus, the ultimate tensile strength and the elongation at break of PVA nanocomposites measured in traction.

The introduction of sepiolite nanofibers along with MWCNTs in the PVA matrix allowed to dramatically increase the elasticity modulus of PVA based composites. The modulus of pure PVA (783.5 MPa) was systematically enhanced by the introduction of sepiolite together with MWCNTs. The highest reinforcement efficiency in the composite's Young's modulus (orange-red zone in fig. 6.10A) was attained at a composition of 10% (w/w) sepiolite and 0.8% (w/w) MWCNTs, where the modulus increased up to a factor of 2.8 (2221 MPa). Apart from the referred composition (10% Sep + 0.8% MWCNT) which displayed especially increased values for the elastic modulus, other compositions above 4% (w/w) Sep and/or 0.8% (w/w) MWCNT also induced an important increase in the elastic properties (green plateau in fig. 6.10A). The right-hand image (fig. 6.10a) depicts the percent relative error of the Young's modulus. It was calculated by dividing the standard deviation of all measurement for a given composition by the corresponding average value. As can be observed the relative error for the Young's modulus is in average around 10%. A small area corresponding to 4-6% Sep in absence of MWCNTs shows some increased variability. In general the error variability seems to decrease

with the introduction of higher loadings of both fillers as seen in the upper right area of the error map.

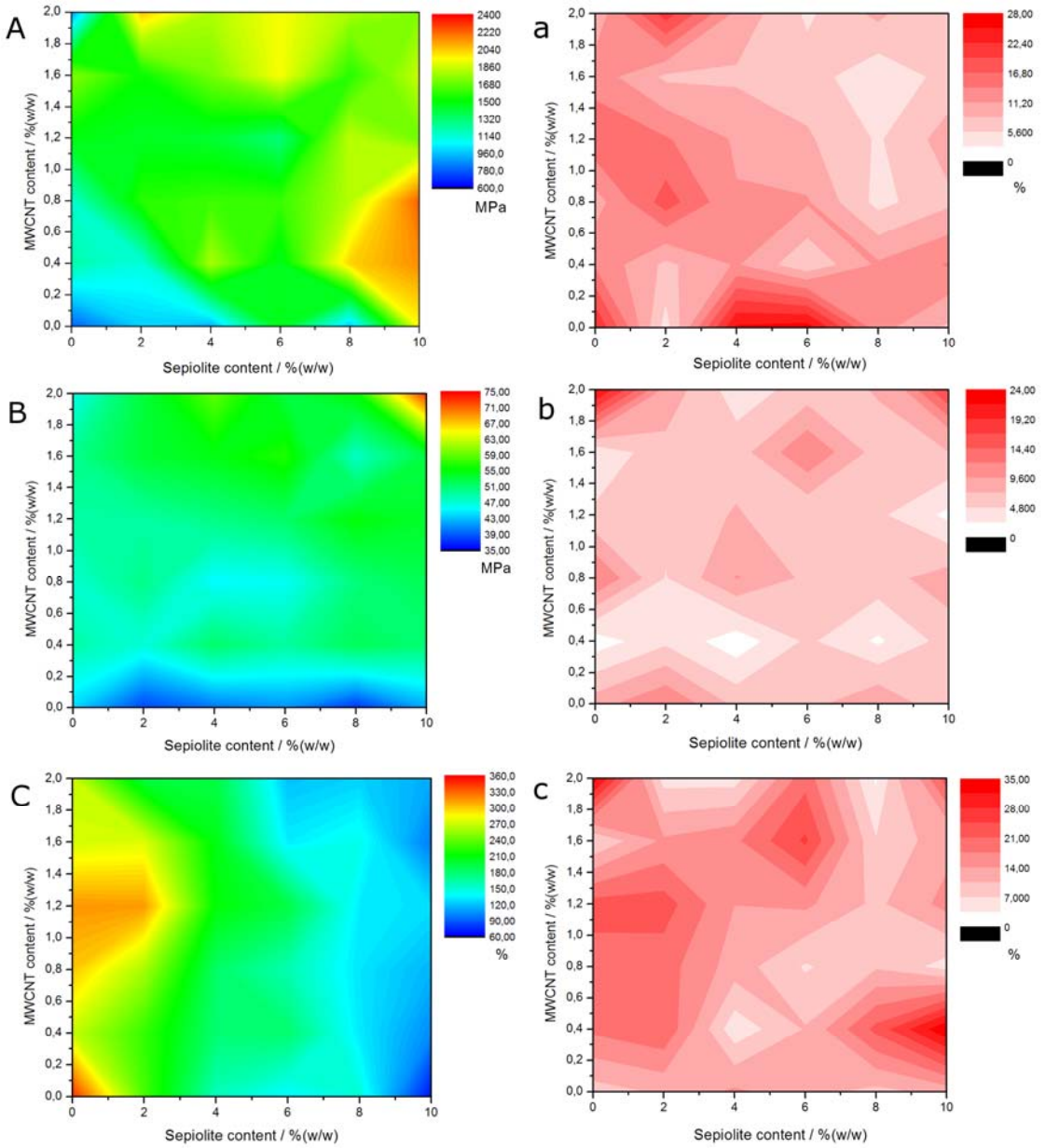


**Figure 6.10 –** Mechanical properties and respective relative error of PVA-Sep-MWCNT nanocomposites. A) Young's modulus, B) ultimate tensile stress (UTS) and C) elongation at break; a, b and c (lower case) correspond to the percent relative error of Young's modulus, UTS and elongation at break, respectively.

If the elastic properties of PVA-Sep-MWCNT nanocomposites present a rather unexpected behavior with a spot of efficiency at a defined filler composition, the ultimate tensile strength (UTS) displays a much more gradual evolution. The

introduction of sepiolite alone (0-10%) does not affect the strength as can be observed by the dark blue area in figure 6.10B. Also MWCNTs alone (0-2%) seem to just barely increase the UTS. On the other hand when both fillers are used simultaneously they promote a gradual increase in the UTS until it reaches a plateau around 50 – 55 MPa whereas unfilled PVA displays an UTS of approximately 40 MPa. The highest improvement in the UTS is verified at the highest filler concentration tested (10% Sep + 2% MWCNT). At this composition the UTS suffers a dramatic increase to *circa* 73 MPa. However, this result should be analyzed with caution since the relative error for that specific composition (fig. 6.10b) is abnormally high as compared to the average relative error values.

The elongation at break (ε) is the only mechanical characteristic that displays a reduction of performance linked to the introduction of sepiolite. As depicted in figure 6.10C, the introduction of sepiolite seems to be related to a significantly lower ε, irrespective of the MWCNT loading. Such behavior is consistent with a more brittle behavior of the composites also observed by an increase in Young's modulus. The relative error map concerning the elongation at break (fig. 6.10c) doesn't evidence any specific error trend.

Although the reasons behind the effectiveness of specific compositional relationship between sepiolite and MWCNT are unclear, this result is of major importance as it largely surpasses previously reported values for CNT reinforced PVA. Wagner and co-workers reported the preparation and characterization of PVA filled with functionalized SWCNT (0.8% w/v) loading, achieving an enhancement of the elastic modulus by a factor of 1.8 (Liu, Barber et al., 2005). Also Cadek et al. reported the same improvement in the Young's modulus of PVA reinforced with MWCNT with respect to the polymeric matrix modulus (Cadek, Coleman et al., 2002). It is widely known that semi-crystalline polymers such as PVA and their composites may present large variations in the elastic modulus due to changes in the polymer's crystalline fraction.

Additionally, MWCNT might act as nucleating agents in nanotube based PVA composites, driving the crystallinity to significantly higher values that the observed for raw PVA (Cadek, Coleman et al., 2002). Nevertheless the crystalline fraction of PVA does not seem to be the reason behind the differences in elastic modulus of the prepared composites. Table 6.1 provides the values for the crystalline fraction obtained for some of the most relevant nanocomposite formulations. The crystalline fraction values were calculated by the enthalpy of fusion of PVA measured by DSC.

**Table 6.1 –** Degree of crystallinity as a function of the filler composition in PVA nanocomposites. The quantification was performed from the DSC endotherms of PVA nanocomposites.

| Sep / % (w/w) | MWCNT / % (w/w) | Crystalinity / % |
|---|---|---|
| 0 | 2 | 30.7 |
| 0 | 0.8 | 34.1 |
| 0 | 0 | 30.0 |
| 10 | 0 | 30.0 |
| 10 | 0.8 | 30.8 |
| 10 | 2 | 26.4 |

In summary, the use of sepiolite and MWCNT in PVA based nanocomposites displays a cooperative effect as it allows the preparation of homogeneous films up to 2 % (w/w) in MWCNT. The concomitant use of the two fillers also accounts for the high improvement of the elastic modulus as compared to the PVA matrix alone and also with respect with sepiolite alone reinforced system.

## 6.2 Hybrid buckypapers

As referred in the preceding section (§ 6.1), the preparation of stable aqueous dispersions of MWCNTs finds many useful applications. One of the most

remarkable of those applications regards the preparation of self-supported mats of nanotubes. Such materials, commonly known as *buckypapers*, are prepared by a very simple method, vacuum filtration of CNT aqueous suspensions (Wang, Liang et al., 2004). Obviously, the difficulty to prepare these materials is not related to the processing method, but with the pre-requisite of having a water-based suspension of CNTs. In this context, the preparation of a stable aqueous suspension of MWCNTs using sepiolite as a mediator configures a simplified starting point to achieve buckypapers.

A brief analysis of buckypaper-based materials shows that the evolution of applications envisaged for these materials has significantly changed throughout its short life. Initially, buckypapers were mostly conceived for structural reinforcement of polymeric matrices (Wang, Liang et al., 2004). However, the difficulties in handling CNTs in suspension at large scales along with the raw material price have hampered its widespread use in structural applications. In the other hand, conductivity related applications have emerged, most notably, for the preparation of sensors (Smajda, Gyori et al., 2007; Smajda, Kukovecz et al., 2007; Kukovecz, Smajda et al., 2008; Meng, Liu et al., 2009; Zhang, Zheng et al., 2010; Zhu, Ku et al., 2010).

### 6.2.1 Hybrid Buckypaper Morphology

Hybrid buckypapers (HBs) containing sepiolite and MWCNTs were prepared by the procedure described in the experimental section (§ 2.2.3c). Taking into account that the sepiolite, an insulator, represents the biggest fraction of the material, it becomes relevant to understand its electric behavior as a function of the conductor load. Figure 6.11 displays hybrid buckypapers prepared using between 0 and 10% (w/w) MWCNTs.

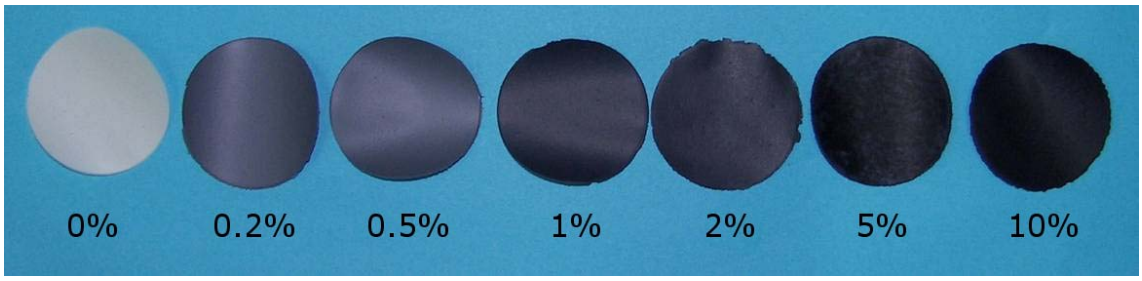


**Figure 6.11 –** Photographic image of hybrid buckypapers prepared using different relative ammounts of MWCNTs and sepiolite. The percentual values underneath each buckypaper refer to the MWCNT content in % (w/w). The buckypapers dimensions are: diameter 45 mm and thickness 60 μm.

One interesting observation is that the association of MWCNTs with sepiolite in water permits to readily obtain self-supported buckypapers, as opposed to what happens in the absence of the silicate. In fact, the difficulties in preparing a dimensionally stable buckypaper in absence of a surfactant, is one of the major drawbacks when preparing buckypapers. Although surfactants are exceptionally useful to disperse the CNTs, they need to be removed in a later step in most conductivity related-applications. Such removal processes is usually done using a solvent such as short-chain alcohol and often implies cracking of the prepared buckypaper. Using sepiolite instead of a surfactant to disperse CNTs means that no washing step is required and therefore the mechanical stability of the buckypaper is preserved.

The homogeneity of the HBs was also assessed at higher magnification under a FE-SEM (fig. 6.12). Hybrid buckypapers were imaged using a FE-SEM to ascertain the degree of dispersion of the MWCNTs within the material as well as to gain insight on the spatial arrangement of the two fibrous particles in the prepared HBs. Figure 6.12 depicts the microscopic images of the surface of HBs. The experimental setup (vCD detector) utilized is useful to asses the surface morphology of the HBs. However, apart from the curvature – a characteristic attribute of MWCNTs which is not expectable to observe in crystalline sepiolite fibers – it is difficult to unambiguously ascribe each of the fibrous particles observed to a given particle type.

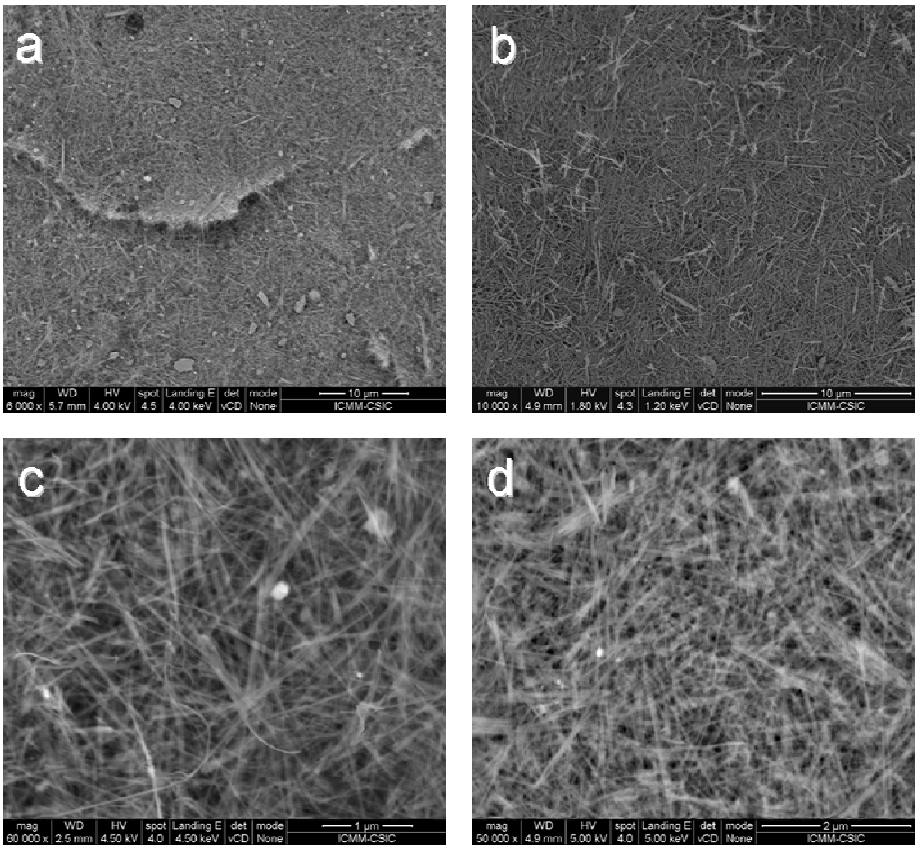


**Figure 6.12 –** Mycroscopic images (FE-SEM) of the surface of two HBs: a) and c) HB0.2% observed under two different magnifications and b) and d) HB10% observed at comparable magnification.

To tackle this problem other detector was used that can discriminate between conductive and insulating particles. Figure 6.13 depicts a HB composed of 10% (w/w) MWCNTs. As can be readily observed from FE-SEM imaging (Fig. 6.13) the adequate choice of a scintillation trough the lens detector (TLD) which collects secondary electrons from the sample, provides elements to discriminate between MWCNTs and sepiolite fibers, allowing therefore to asses the connectivity of the conducting particles. It is also possible to ascertain the dispersion state of MWCNTs as well as the type of structures generated in the prepared HB.

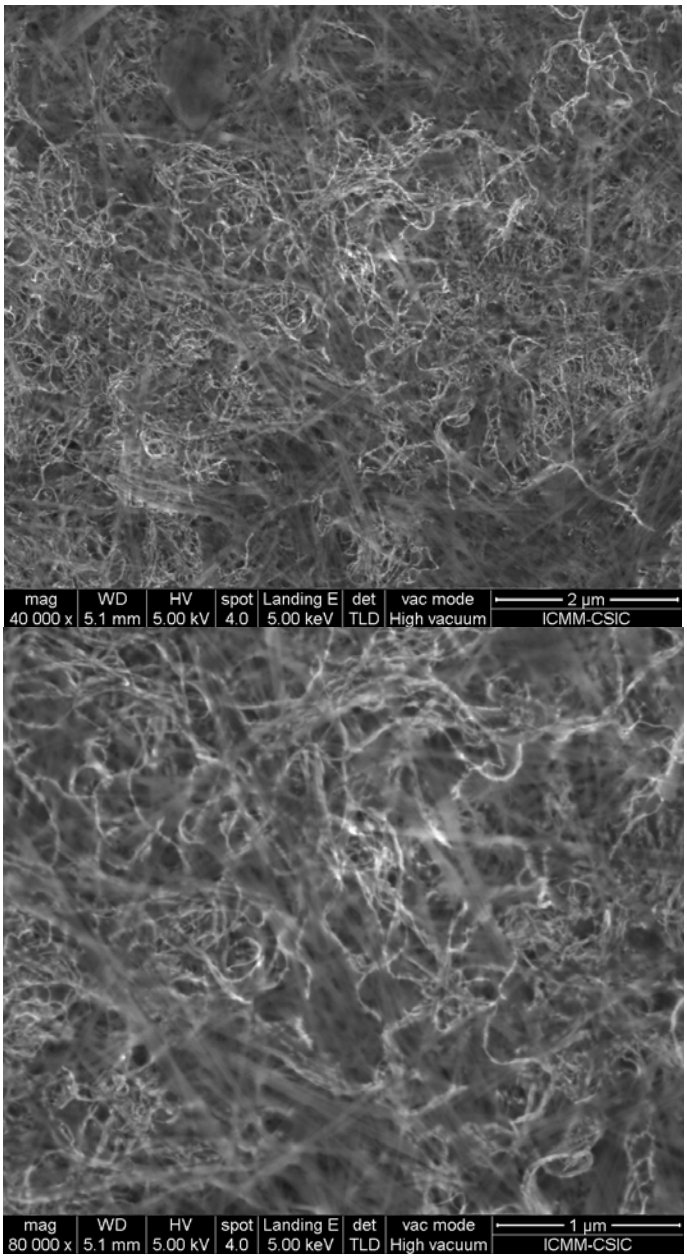


**Figure 6.13 –** FE-SEM microscopic images at different magnifications of HB 10% obtained using a TLD detector allowing to observe the percolating network of MWCNTs (bright curved particles).

Another key characteristic of both sepiolite and MWCNTs is their specific surface area. Sepiolite, when degassed at temperatures between 25 and 200 ºC, is known to posses a specific surface area as high as 340 $m^2.g^{-1}$ (Ruiz-Hitzky and Casal, 1985). This feature is, in fact, behind the use of sepiolite in many applications where its interfacial role is important, such as adsorption of contaminants (Kara, Yuzer et al., 2003; Alkan, Demirbas et al., 2004; Ozcan,

Oncu et al., 2006) or nanocomposite materials (Darder, Lopez-Blanco et al., 2006; Nohales, Solar et al., 2006; Zheng and Zheng, 2006; Duquesne, Moins et al., 2007; Fernandes, Ruiz et al., 2009; Chivrac, Pollet et al., 2010; Fernandes, Manjubala et al., 2011). Also MWCNTs are known to posses a high specific surface area which is, according to theoretical and experimental studies highly dependent on the number of walls (Peigney, Laurent et al., 2001; Li, Pan et al., 2004). For MWCNTs a typical value for the specific surface area is 250 $m^2.g^{-1}$.

To evaluate the effect of the assembly of sepiolite and MWCNTs into hybrid buckypapers, nitrogen adsorption isotherm experiments at 77 K of hybrid buckypaper containing 10% (w/w) MWCNTs, sepiolite and raw MWCNTs. These results are summarized in table 6.2.

**Table 6.2 –** Micropore, external and total specific surface area of sepiolite, MWCNT and HB10 measured by $N_2$ adsorption at 77 K. The samples were degassed at 150 ºC under dynamic vacuum prior to the measurements.

| | $S_{micro}$ / $m^2.g^{-1}$ | $S_{ext}$ / $m^2.g^{-1}$ | $S_{total}$ / $m^2.g^{-1}$ |
|---|---|---|---|
| **Sep** | 123 | 221 | 344 |
| **MWCNT** | 52 | 201 | 253 |
| **HB10** | 95 | 178 | 274 |

According to the specific surface area determinations HB materials maintain the high surface area characteristic of its components. This feature, which could be somehow anticipated from microscopic images, confirms that the compatibilization of sepiolite and MWCNTs does not suppose a depletion of the material's surface properties and that application depending on the surface area of the material should not loose applicability due to the processing methodology.

Another important criterion to asses HB materials and their possible application regards their carbon chemistry as compared to raw MWCNTs. As previously seen for carbon materials derived from gelatine (§ 5.1) Raman spectroscopy

provides deep understanding of the chemistry of carbon atoms, namely by the relation between the G and D bands intensity which reflect the sp2 and sp3 character of carbon atoms respectively. Figure 6.14 summarizes the main Raman spectroscopic features of sepiolite, MWCNTs and HB.

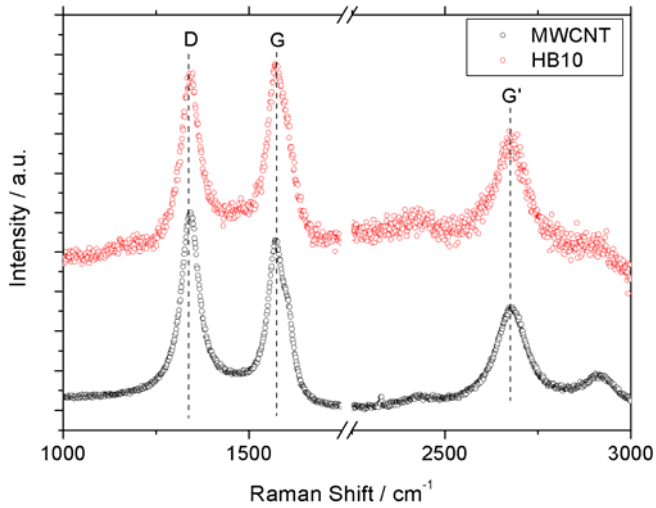


**Figure 6.14 –** Raman scattering spectra of MWCNTs (black circles) and HB10 (red circles) measured under irradiation by a 2.41 eV laser (514 nm).

As observed in figure 6.14, Raman spectra of hybrid buckypaper indicates that the chemical nature of carbon atoms remains unaltered after the procedure that give rise to the formation of hybrid buckypapers. The relation between $sp^3$ and $sp^2$ carbon atoms, given by the relative intensity of the D and G bands remains practically unaltered. In fact one can even detect a slight enhancement of the G band in the hybrid buckypaper. This slight variation is not, however, related to an increase of the conjugated system in the nanotubes composing the HB. It is more probably ascribed to a higher level or error in the determination of the Raman spectra when sepiolite is present. In fact the luminescent behavior of sepiolite when irradiated with a 514 nm laser source had been already reported by McKeown and co-workers (McKeown, Post et al., 2002), who also reported the adequacy of 1064 nm laser to characterize the vibration modes of sepiolite and palygorskite. Since a laser source with such characteristics was not

available, HB spectra presented in figure 6.14 corresponds to the subtraction of the luminescence profile of sepiolite to HB spectra, which accounts for the poor baseline observed. Given this circumstance, the evaluation of the relative intensities of D and G bands in sample HB10 must be addressed with caution. Also G' band suffers no alteration in its shape or intensity, further confirming the preservation of the chemical nature of MWCNTs in HBs. In summary, Raman data permits to state that no considerable damage was produced to nanotubes, and therefore HB materials are expected to partially maintain the properties of pristine nanotubes.

### 6.2.3 Bio-sensors based on Hybrid Buckypapers

Another example of the interest of this new type of CNT-sepiolite materials concerns their use as active components in amperometric biosensors.

There are three main requirements that characterize materials with good electrochemical sensing properties, its **electronic properties**, the ability to be **functionalized** and the ease of **handling/producing** the sensor (Jacobs, Peairs et al., 2010). The first is naturally of paramount importance since the electronic properties will decisively influence the electrode performance. A good electronic conductor will induce faster electronic response and consequently improve the electrode response kinetics, sensitivity, etc.. In fact, the replacement of other carbon forms for CNTs is directly related to these materials' superior electronic properties and consequent better electrochemical performance. On the other hand the second and third criteria are often problematic. In order to be functionalized (fundamental for the introduction of active species), CNTs often need to be heavily oxidized using strong acids. Such treatment promotes the appearance of oxygen containing functions (hydroxyls, carboxylic acids, etc.) on the surface of the nanotube that, in turn, are vital to achieve functionalization. Also, the incorporation of these functions plays a major role in dispersing the

nanotubes in aqueous environments (Qureshi, Kang et al., 2009; Jacobs, Peairs et al., 2010). Although the acid treatment seems, at first sight, to solve the two last requirements for a good electrode material, it also carries along a downside. When oxidizing CNTs its electronic properties are severely damaged due to the rupture of the highly conjugated graphitic network. In summary, achieving a good CNT based electrode relies on a compromise between the electronic properties and the functionalization/dispersion ability of these materials.

The proposed approach in this work explores the usage of another particulate material, sepiolite, to overcome the need for a compromise between CNTs dispersability and electrical properties. Sepiolite not only presents, as previously demonstrated, an easily available surface chemistry, but also is a key material in achieving water based dispersions of CNTs without any chemical oxidation step. In summary, sepiolite should enable to fully explore CNTs potential as an electrochemical sensor material.

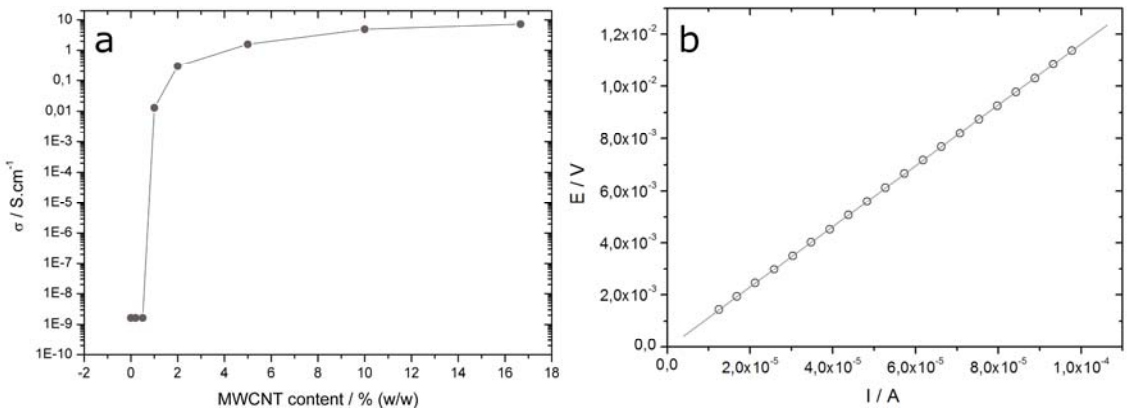


**Figure 6.15 –** a) Electrical conductivity of HB films as function of the MWCNT content, b) DC electrical resistance of HB 1% measured using the four probe method between 0.01 and 0.1mA.

The first criteria when preparing materials for electrochemical applications is, as previously stated, their conductivity. The surface conductivity of the prepared HB films was assessed using a 4 point probe as previously described (§ 2.3.4). Figure 6.15 depicts the surface conductivity of the different HBs prepared as

well as one example of resistance measurement used to calculate the HBs conductivity.

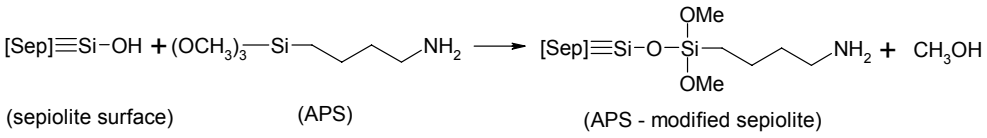


(eq. 6.4)

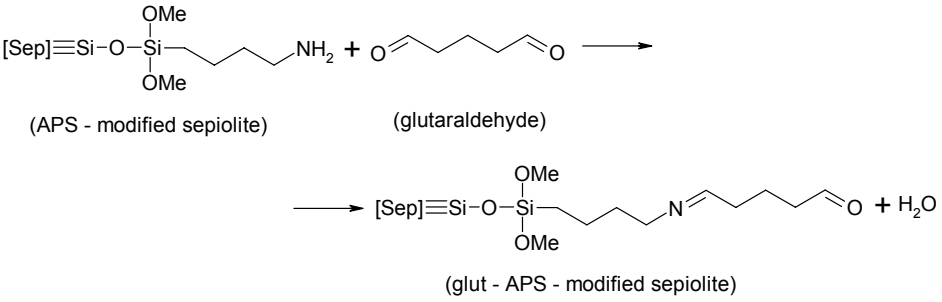


(eq. 6.5)

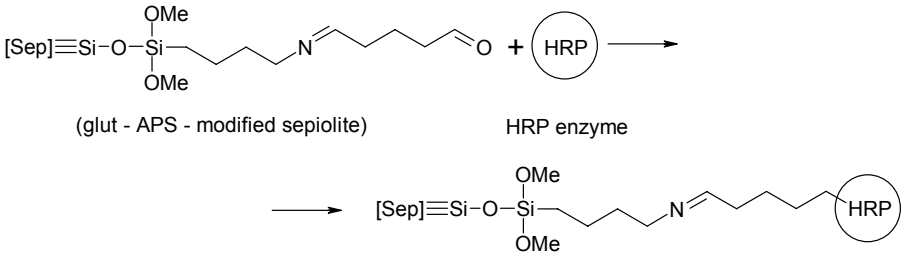


(eq. 6.6)

As is depicted in figure 6.15 the electrical percolation threshold of MWCNTs in HB films is around 1%. Also it is relevant to note that the electrical conductivity of the HB films above such MWCNT loading value is considerably high (> 1S.cm$^{-1}$) which is a decisive characteristic for an electrochemical sensor.

Since the electric conductivity requirement is fulfilled by the presence of small amounts of MWCNTs the other requirements gain importance. The obtention of HBs is a straightforward process that results in materials that can be directly used as sensors. HB films are self-supported (fig. 6.11) and stable when immersed in a variety of solvents, including water.

The functionalization requirement can also be simply solved. Sepiolite, the main component in HB composition allows for metal alkoxide covalent grafting via

condensation mechanism. In this work horseradish peroxidase (HRP), was covalently grafted to the silicate (eq. 6.4) through a preliminary grafting of APS followed by treatment with glutaraldehyde solution (eq. 6.5) and finally incubated with the enzyme (eq. 6.6). When HRP is in its active conformation it catalyses hydrogen peroxide to water, according to the following reaction scheme:

$$[Fe(CN)_6]^{3-} + e^- \rightarrow [Fe(CN)_6]^{4-}$$
$$[Fe(CN)_6]^{4-} + HRP_{ox} \rightarrow [Fe(CN)_6]^{3-} + HRP_{red} \qquad \text{(eq. 6.7)}$$
$$HRP_{red} + H_2O_2 + 2H^+ \rightarrow HRP_{ox} + 2H_2O$$

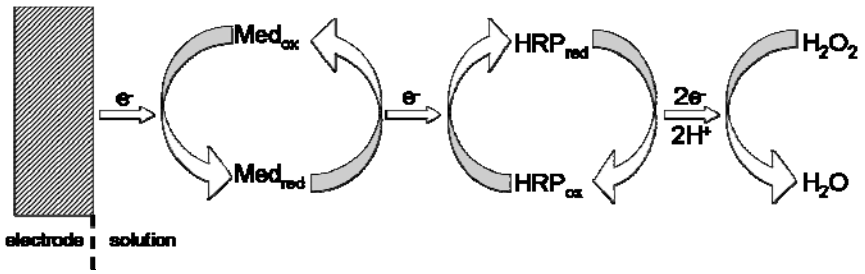


**Figure 6.16 –** Schematic representation of the catalytic reduction of hydrogen peroxide by horseradish peroxidase in presence of an electronic mediator

As described by the preceding equations and scheme, during the reducing step in cyclic voltammetry, ferricyanide ion (acting as electronic mediator) is reduced to ferrocyanide, which in turn reduces HRP. The enzyme's reduced form is then capable of catalytically reducing hydrogen peroxide to water. In the case that no hydrogen peroxide is present on the solution, the process is reversible and both the enzyme's oxidized form and the mediators reduced form can be regenerated upon the cyclic voltammetry (CV) oxidizing step.

The prepared biosensor was evaluated by means of cyclic voltammetry to asses its capacity to catalytically degrading $H_2O_2$. Prior to the CV experiment, the electrode was immersed in a mixture of ABTS and $H_2O_2$ to check if the enzyme maintained its activity. The mixture turned blue/green immediately

indicating that the enzyme kept its activity. The CV results for phosphate buffer solution (PBS) + ferricyanide as well as PBS + ferricyanide + $H_2O_2$ are depicted in figure 6.17.

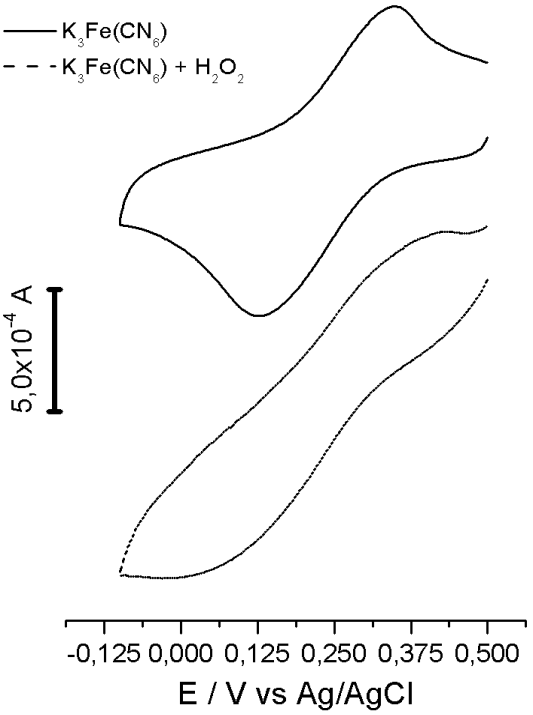


**Figure 6.17 –** Cyclic voltammograms of the electronic mediator (full line) and catalytic degradation of hydrogen peroxide (0.5M) in presence of mediator (dotted line) using a HRP modified HB electrode. Cyclic voltammograms were performed at 5 $mVs^{-1}$ between 0.5 and -0.1 V vs Ag/AgCl. Voltammograms are artificially displaced in the yy axis for clarity.

As clearly depicted in figure 6.17 the cyclic voltamogram obtained using HRP modified HB electrode as a working electrode in the presence of ferricyanide ion (the electronic mediator) displays a reduction potential $E_{pc}$ = 130 mV ($E_{p/2c}$ = 243 mV) vs Ag/AgCl with a cathodic current $I_{pc} = 5x10^{-4}$ A, whereas its oxidation potential is $E_{pa}$ = 340 mV ($E_{p/2a}$ = 253 mV) vs Ag/AgCl and an anodic current $I_{pa} = 3.8x10^{-4}$ A. Although these values are relatively far from the expected reversible one electron process, where the difference between the anodic peak potential and the cathodic peak potential should be equal to 57 mV and the differences between the peak potential and the potential at half height of the peak should be equal to 56.6 mV, the system does seems to be able to re-

oxidize the generated ferrocyanide ion to ferricyanide ion. In fact, the relationship between the anodic and cathodic currents is relatively close to the expected value for a reversible process $I_{pa}/ I_{pc}$ = 0.76. When the cyclic voltammogram was performed in presence of $[H_2O_2]$ = 0.5 M the voltammetric profile changed considerably. The first difference relates to the enhancement of the cathodic current to approximately the double of the absolute value measured in the absence of peroxide species at similar potential values. This indicates the occurrence of an electrochemical reaction induced by the reduction of the electron transfer (ET) shuttle species formerly measured alone. On the other hand, the disappearance of the cathodic process on the oxidative step of the voltammogram is, once again, coincident with the catalytic reduction of hydrogen peroxide to water by the HRP modified HB electrode.

Although the catalytic reduction of $H_2O_2$ to water was successfully achieved, the results deserve some comment. The high concentration of substrate ($H_2O_2$) needed to achieve an enhancement of the cathodic current indicates that the prepared sensor has a very high limit of detection. According to Habermüller et al. (Habermüller, Mosbach et al., 2000) the main aim in the design of amperometric biosensors is promoting fast electron transfer processes by the development of electrode architectures with predefined ET pathways. Later on the same review article, the authors distinguish between mediated and non-mediated electron transfer. In direct (non-mediated) electron transfer, the authors state that the determinant step is the tunnelling distance between the enzyme active center and the electrode. In the case of mediated electron transfer (as the case of the electrode presented in this section) the authors have stated that the determinant step is the diffusion of the mediator species between the active moiety and the electrode. In this context it is interesting to analyze the architecture of the HRP modifies HB electrode as it presents some characteristics that might explain the detected lack of sensitivity. Sepiolite and MWCNTs are integrated in a mesh-like structure where sepiolite fibers are the

most abundant particles. Although the HB material is conductive in a macroscopic scale, its conductivity is the result of the mixture of insulating (sepiolite) and conductive (MWCNTs) particles. This means that locally (i.e. at the nanometric scale) only a small fraction of the fibers are conductive and therefore able to work as an electronic collector. Also the covalent grafting of HRP proceeds in a manner that the enzyme ends up grafted onto the insulating moiety. The result of this asymmetric structure is that although the MWCNTs structure is preserved due to the absence of aggressive oxidative steps, and as a result its intrinsic conductivity should remain unaltered, the bioactive centers (heme group in the case of HRP) are located at a distant position from the conductive moiety. Although there is a mediator present in the solution, this species should diffuse between the intricate mat of sepiolite and MWCNT fibers to “connect” these two moieties. This path can be several nanometers long as can be observed from the FE-SEM images presented in figure 6.13 and thus the time of diffusion, a decisive factor in achieving good communication between the enzyme and the conducting moiety of the electrode. Other strategies to reduce such distance such as the adsorption of other species at the HB that might work as relays, thus promoting electron hopping between the redox centre and the MWCNT collectors.

In fact, the reported experiment can be solely regarded as a proof of concept of the ability of HRP modified HB electrodes to work as a peroxide sensitive biosensor. Further experimental data are needed to fully characterize the system. In particular, the kinetics of the electron transfer process are key to understand the feasibility of this system as a competitive hydrogen peroxide biosensor.

## 6.3 Concluding remarks

In summary the compatibilization of sepiolite nanofibers with MWCNTs permits to widen the perspectives of use of MWCNTs in aqueous media.

In this context it was possible to produce kinetically stable dispersions of MWCNTs in presence of sepiolite fibers without the addition of any molecular or macromolecular species such as surfactants or polymeric chains (Takahashi, Tsunoda et al., 2002; Moore, Strano et al., 2003; Lee, Huh et al., 2007; Rastogi, Kaushal et al., 2008; Su, Wang et al., 2008; Sun, Nicolosi et al., 2008; Krause, Petzold et al., 2009; Lan and Lin, 2009) or the severe oxidation treatments described in literature (Georgakilas, Kordatos et al., 2002; Grossiord, Loos et al., 2006; Tasis, Tagmatarchis et al., 2006). The stability of these particles in water is of major importance as it configures a starting point to generalize the use of MWCNTs in industrial water based processes. On the other hand, also the scientific aspect of this achievement is of great relevance as it opens doors to water based chemistry (*Green Chemistry*) on CNTs.

This chapter has demonstrated that the use of a co-dispersant particle with high affinity towards the solvent (instead of a molecular or macromolecular species) is an effective colloidal way to stabilize nanotubes. In particular, two rheological properties of the co-stabilizer seem to be especially relevant in this process. The first is the use of a co-dispersant concentration above its percolation threshold in a way that CNTs will be surrounded by particles that are stable in the used medium. The other is the selection or high aspect-ratio particles capable of inducing a shear-thinning behaviour to the dispersion. Lastly, the use of a high frequency dispersing technique such as ultrasonic dispersion is fundamental to achieve high mobility of the co-dispersant particles while promoting the temporary separation of bundled CNTs. In conjunction, these factors permit to achieve stable high concentrated dispersions of CNTs in water.

Regarding the applications, this approach allowed to prepare nanocomposites based on the dispersion of both sepiolite nanofibers and MWCNTs which showed high reinforcing efficiency in PVA matrix. Some specific compositional relations between the two fillers show especially efficient reinforcement capacity for this system. Such is the case for 10% Sepiolite + 0.8% MWCNTs (w/w) which displayed an enhancement of the young's modulus of PVA as high as 280 % with respect to the raw PVA matrix. Further studies must be performed to understand if the relative amount between fillers reflects some sort of balance between the two types of fillers or if this proportion is also dependent on the nature of the polymeric matrix.

The co-dispersion of sepiolite and MWCNTs allowed as well the preparation of hybrid buckypapers (HB). These materials that show electrical percolation threshold above 1% (w/w) MWCNTs are especially fit for electrochemical application as potentiometric, amperometric (as described in the present chapter by the preparation of a HRP based biosensor) or even structural integrity sensors. The advantage of incorporating sepiolite into buckypapers (a previously reported and explored concept) regards simplification of the processing steps (no washing step required) and also the easiness of chemical functionalization of the material based on sepiolite's straightforward reactivity with functionalized silicon alkoxides.

Another advantage of the proposed co-dispersing strategy regards the maintenance of the electrical and chemical properties of MWCNTs as no decrease of the $sp^2$ hybridized carbon was detected by Raman spectroscopy as opposed to most of the standard techniques in use.

# 7 Conclusions

The work reported in this dissertation allows drawing some general conclusions regarding the use of sepiolite in the context of nanocomposites. It permits as well to establish specific conclusions that highlight the findings reported in each different chapter. These particular findings are referred to in the following paragraphs while the general conclusions are mentioned at the end of each chapter as final remarks.

Sepiolite is a microfibrous clay mineral that presents a wide array of potential applications. One of the most interesting aspects in Materials Science regards its use as reinforcing filler in polymer-clay nanocomposites. However, the mechanical properties of this type of clay had not been previously studied. Taking into account that these properties provide deep understanding of the reinforcing potential of the clay, the first part of the work was devoted to the measurement of such properties. The measurements performed under the AFM over single sepiolite fibers yielded a Young's modulus around 10 GPa. However the same material measured at different length scales (measured under a nanoindenter and compression tests of macroscopic blocks obtained from the pit) yielded significantly lower values. This feature indicates that, as the dimensions of the filler decrease (and therefore its organization level increases), sepiolite's mechanical efficiency rises.

Once the elastic properties of sepiolite fibers were known, the effect arising from their introduction in a biopolymer matrix was studied. Sepiolite proved to be an excellent reinforcing filler for gelatin-based bionanocomposites. The raw silicate presented a much more pronounced effect over the elastic properties of the composites than the modified clay counterparts. Sepiolite alone accounted for an increase of the elastic modulus around 220 % with respect to non-reinforced gelatin, way above the effect detected for the modified materials. The enhancement of the composite elastic properties as compared to the raw polymer matrix can be attributed to two main factors. The first is the mechanical reinforcing effect of high aspect ratio particles displaying an elastic modulus superior to that of the matrix. The second is the effect of sepiolite in the mechanical properties of sepiolite-gelatin bionanocomposites, related to the conformational changes induced in the polymer matrix. Since the differences between modified and unmodified sepiolite are considerable (and the elastic properties of some of the silicate derivatives are not expected to present any variation), one must conclude that the second factor (i.e. the conformational change induced over the biopolymer structure) accounts for a more relevant effect on the reinforcement of gelatin by sepiolite.

The close interaction between sepiolite and gelatin were used as a starting point to prepare nitrogen-rich carbon materials in the presence of sepiolite. Two main strategies were followed. The first relied on the preparation of gelatin sepiolite class I hybrids by means of adsorption, using the obtained material for carbonization under controlled conditions. The carbonaceous moiety of the resulting materials presents a layered nature resembling that of graphene. Carbonized gelatin presented high electrical conductivity ($\sigma$ = 2.5 $S.cm^{-1}$), however the same did not occur with gelatin sepiolite hybrids as precursors of carbonaceous materials. The second strategy was based on the preparation of gelatin-sepiolite foam and subsequent carbonization. The obtained materials

not only presented better conductivity properties but also were mechanically stable, permitting its use in epoxy formulations. This last strategy stands as a viable route for the preparation novel polymer-based materials provided with electrical conductivity.

Finally, sepiolite was successfully used in the stabilization of carbon nanotubes. Stable suspensions of MWCNTs were achieved by the joint dispersion of sepiolite and non-modified nanotubes. The stability of carbon nanotubes in water is of crucial importance as it opens a clear pathway to apply CNTs in clean processes. Sepiolite-MWCNT suspensions are stable after at least one year over their preparation. The stability of CNTs co-dispersed with sepiolite was found to be dependent on two main features. The use of a concentration of sepiolite superior to the one required for rheological percolation of the silicate in water and the use of ultrasound in the dispersion process.

The proposed strategy allowed as well the preparation of PVA nanocomposites reinforced with sepiolite and MWCNTs. The mechanical enhancement of the elastic properties was maximized for the composite prepared with 10% Sepiolite + 0.8% MWCNTs (w/w), which displayed an enhancement of the elastic modulus of 280 % with respect to pure PVA. The application of the sepiolite-CNT materials in the electroanalytical field was also pursued by the preparation of self-supported sepiolite-CNT films, hybrid buckypapers. This material was functionalized to prepare HRP enzyme modified conductive material that showed activity towards the degradation of hydrogen peroxide. An amperometric biosensor was successfully prepared from this material.

The most general conclusion that can be drawn from the presented work is that sepiolite, a fibrous clay mineral known for its adsorption properties, can be widely used in the field of composites and bionanocomposites.

The diversity of applications briefly mentioned in this dissertation consist in no more than a grasp of the potential of this silicate not only in polymer-clay nanocomposites but, in general, in the field of the so-called advanced materials.

# 8. Bibliography

Abou, B., Bonn, D. and Meunier, J. (2003). "Nonlinear rheology of Laponite suspensions under an external drive." Journal of Rheology **47**(4): 979-988.

Addadi, L. and Weiner, S. (1985). "Interactions between acidic proteins and crystals: stereochemical requirements in biomineralization." Proceedings of the National Academy of Sciences **82**(12): 4110-4114.

Addadi, L. and Weiner, S. (1986). "Iinteractions between acidic macromolecules and structured crystal surfaces - Stereochemistry and biomineralization." Molecular Crystals and Liquid Crystals **134**(1-4): 305-322.

Ahlrichs, J. L., Serna, C. and Serratosa, J. M. (1975). "Structural hydroxyls in sepiolites." Clays and Clay Minerals **23**(2): 119-124.

Ajayan, P. M., Stephan, O., Colliex, C. and Trauth, D. (1994). "Aligned Carbon Nanotube Arrays Formed by Cutting a Polymer Resin-Nanotube Composite." Science **265**(5176): 1212-1214.

Alivisatos, A. P. (1996). "Semiconductor Clusters, Nanocrystals, and Quantum Dots." Science **271**(5251): 933-937.

Alkan, M., Demirbas, O., Celikcapa, S. and Dogan, M. (2004). "Sorption of acid red 57 from aqueous solution onto sepiolite." Journal of Hazardous Materials **116**(1-2): 135-145.

Aranda, P. and Ruiz-Hitzky, E. (1992). "Poly(ethylene oxide)-silicate intercalation materials." Chemistry of Materials **4**(6): 1395-1403.

Aranda, P., Serratosa, J. M. and Ruiz-Hitzky, E. (2004). Clay-Organic Interactions. Handbook of Layered Materials. Dutta, P. K., Auerbach, S. M. and Carrado, K. A. New York, CRC Press.

Araujo, R., Fernandes, F. M., Proenca, M. F., Silva, C. J. R. and Paiva, M. C. (2007). "The 1,3-dipolar cycloaddition reaction in the functionalization of carbon nanofibers." Journal of Nanoscience and Nanotechnology **7**(10): 3441-3445.

Ashby, M. F. (1989). "Overview No. 80: On the engineering properties of materials." Acta Metallurgica **37**(5): 1273-1293.

Ashby, M. F., Gibson, L. J., Wegst, U. and Olive, R. (1995). "The Mechanical Properties of Natural Materials. I. Material Property Charts." Proceedings: Mathematical and Physical Sciences **450**(1938): 123-140.

Ayala, P., Arenal, R., Rümmeli, M., Rubio, A. and Pichler, T. (2010). "The doping of carbon nanotubes with nitrogen and their potential applications." Carbon **48**(3): 575-586.

Azim, S. S., Satheesh, A., Ramu, K. K., Ramu, S. and Venkatachari, G. (2006). "Studies on graphite based conductive paint coatings." Progress in Organic Coatings **55**(1): 1-4.

Bae, H. J., Park, H. J., Hong, S. I., Byun, Y. J., Darby, D. O., Kimmel, R. M. and Whiteside, W. S. (2009). "Effect of clay content, homogenization RPM, pH, and ultrasonication on mechanical and barrier properties of fish gelatin/montmorillonite nanocomposite films." LWT - Food Science and Technology **42**(6): 1179-1186.

Bala, I., Hariharan, S. and Kumar, M. (2004). "PLGA nanoparticles in drug delivery: The state of the art." Critical Reviews in Therapeutic Drug Carrier Systems **21**(5): 387-422.

Balberg, I., Anderson, C. H., Alexander, S. and Wagner, N. (1984). "Excluded volume and its relation to the onset of percolation." Physical Review B **30**(7): 3933.

Bang, J. H. and Suslick, K. S. (2010). "Applications of Ultrasound to the Synthesis of Nanostructured Materials." Advanced Materials **22**(10): 1039-1059.

Baughman, R. H., Cui, C. X., Zakhidov, A. A., Iqbal, Z., Barisci, J. N., Spinks, G. M., Wallace, G. G., Mazzoldi, A., De Rossi, D., Rinzler, A. G., Jaschinski, O., Roth, S. and Kertesz, M. (1999). "Carbon nanotube actuators." Science **284**(5418): 1340-1344.

Bauhofer, W. and Kovacs, J. Z. (2009). "A review and analysis of electrical percolation in carbon nanotube polymer composites." Composites Science and Technology **69**(10): 1486-1498.

Bensaude-Vincent, B., Arribart, H., Bouligand, Y. and Sanchez, C. (2002). "Chemists and the school of nature." New Journal of Chemistry **26**(1): 1-5.

Bente, P. F. and Walton, J. H. (1943). "The Catalytic Activity of Activated Nitrogenous Carbons." The Journal of Physical Chemistry **47**(2): 133-148.

Bergaya, F., Theng, B. K. G. and Lagaly, G., Eds. (2006). Handbook of clay science. Developments in clay science. Oxford, Elsevier.

Berhan, L. (2007). "Modeling percolation in high-aspect-ratio fiber systems. I. Soft-core versus hard-core models." Physical review. E, Statistical, nonlinear, and soft matter physics **75**(4).

Bhattacharya, M., Maiti, M. and Bhowmick, A. K. (2009). "Tailoring Properties of Styrene Butadiene Rubber Nanocomposite by Various Nanofillers and Their Dispersion." Polymer Engineering and Science **49**(1): 81-98.

Bigi, A., Bracci, B., Cojazzi, G., Panzavolta, S. and Roveri, N. (1998). "Drawn gelatin films with improved mechanical properties." Biomaterials **19**(24): 2335-2340.

Bigi, A., Panzavolta, S. and Rubini, K. (2004). "Relationship between triple-helix content and mechanical properties of gelatin films." Biomaterials **25**(25): 5675-5680.

Bilotti, E., Zhang, R., Deng, H., Quero, F., Fischer, H. R. and Peijs, T. (2009). "Sepiolite needle-like clay for PA6 nanocomposites: An alternative to layered silicates?" Composites Science and Technology **69**(15-16): 2587-2595.

Binnig, G., Quate, C. F. and Gerber, C. (1986). "Atomic Force Microscope." Physical Review Letters **56**(9): 930.

Birdi, K. S., Ed. (2009). Handbook of Surface and Colloid Chemistry. Boca Raton, USA, CRC Press.

Bledzki, A. K. and Gassan, J. (1999). "Composites reinforced with cellulose based fibres." Progress in Polymer Science **24**(2): 221-274.

Blond, G. (1988). "Velocity of linear crystallization of ice in macromolecular systems." Cryobiology **25**(1): 61-66.

Blumstein, A. (1965). "Polymerization of adsorbed monolayers. I. Preparation of the clay–polymer complex." Journal of Polymer Science Part A: General Papers **3**(7): 2653-2664.

Bobko, C. P., Ortega, J. A. and Ulm, F.-J. (2009). "Comment on "Elastic modulus and hardness of muscovite and rectorite determined by nanoindentation" by G. Zhang, Z. Wei and R.E. Ferrell [Applied Clay Science 43 (2009) 271-281]." Applied Clay Science **46**(4): 425-428.

Bond, G. R. (2002). "The role of activated charcoal and gastric emptying in gastrointestinal decontamination: A state-of-the-art review." Annals of Emergency Medicine **39**(3): 273-286.

Bowen, W. R., Lovitt, R. W. and Wright, C. J. (2000). "Application of atomic force microscopy to the study of micromechanical properties of biological materials." Biotechnology Letters **22**(11): 893-903.

Bradley, W. F. (1945). "Molecular associations between montmorillonite and some polyfunctional organic liquids." Journal of the American Chemical Society **67**(6): 975-981.

Brinckmann, J., Notbohm, H. and Müller, P. K., Eds. (2005). Collagen, Primer in Structure, Processing and Assembly Topics in Current Chemistry. Berlin, Springer.

Brunauer, K. and Preisinger, A. (1956). "Struktur und Entstehung des Sepioliths." Tschermaks Mineralogische und Petrographische Mitteilungen **6**(1-2): 120-140.

Burgos-Asperilla, L., Darder, M., Aranda, P., Vazquez, L., Vazquez, M. and Ruiz-Hitzky, E. (2007). "Novel magnetic organic-inorganic nanostructured materials." Journal of Materials Chemistry **17**(40): 4233-4238.

Butt, H.-J., Cappella, B. and Kappl, M. (2005). "Force measurements with the atomic force microscope: Technique, interpretation and applications." Surface Science Reports **59**(1-6): 1-152.

Byler, D. M. and Susi, H. (1986). "Examination of the secondary structure of proteins by deconvolved FTIR spectra." Biopolymers **25**(3): 469-487.

Cadek, M., Coleman, J. N., Barron, V., Hedicke, K. and Blau, W. J. (2002). "Morphological and mechanical properties of carbon-nanotube-reinforced semicrystalline and amorphous polymer composites." Applied Physics Letters **81**(27): 5123-5125.

Caruso, F. (2001). "Nanoengineering of Particle Surfaces." Advanced Materials **13**(1): 11-22.

Cascone, M., Barbani, N., Cristallini, C., Giusti, P., Ciardelli, G. and Lazzeri, L. (2001). "Bioartificial polymeric materials based on polysaccharides." Journal of biomaterials science. Polymer edition **12**(3): 267-281.

Cintas, P. and Luche, J.-L. (1999). "Green chemistry . The sonochemical approach." Green Chemistry **1**(3): 115-125.

Coleman, J. N., Khan, U., Blau, W. J. and Gun'ko, Y. K. (2006a). "Small but strong: A review of the mechanical properties of carbon nanotube-polymer composites." Carbon **44**(9): 1624-1652.

Coleman, J. N., Khan, U. and Gun'ko, Y. K. (2006b). "Mechanical Reinforcement of Polymers Using Carbon Nanotubes." Advanced Materials **18**(6): 689-706.

Cook, S. M. and et al. (2006). "Practical implementation of dynamic methods for measuring atomic force microscope cantilever spring constants." Nanotechnology **17**(9): 2135.

Cuesta, A., Dhamelincourt, P., Laureyns, J., Martínez-Alonso, A. and Tascón, J. M. D. (1994). "Raman microprobe studies on carbon materials." Carbon **32**(8): 1523-1532.

Cygan, R. T., Liang, J.-J. and Kalinichev, A. G. (2004). "Molecular Models of Hydroxide, Oxyhydroxide, and Clay Phases and the Development of a General Force Field." The Journal of Physical Chemistry B **108**(4): 1255-1266.

Czichos, H., Saito, T. and Smith, L., Eds. (2006). Handbook of Materials Measurement Methods. Heidleberg, Springer.

Chang, L. N. and Chow, W. S. (2010). "Accelerated Weathering on Glass Fiber/Epoxy/Organo-montmorillonite Nanocomposites." Journal of Composite Materials **44**(12): 1421-1434.

Chen, B., Evans, J. R. G., Greenwell, H. C., Boulet, P., Coveney, P. V., Bowden, A. A. and Whiting, A. (2008). "A critical appraisal of polymer-clay nanocomposites." Chemical Society Reviews **37**(3): 568-594.

Chen, C., Kennel, E. B., Stiller, A. H., Stansberry, P. G. and Zondlo, J. W. (2006). "Carbon foam derived from various precursors." Carbon **44**(8): 1535-1543.

Chen, C. Q., Shi, Y., Zhang, Y. S., Zhu, J. and Yan, Y. J. (2006). "Size Dependence of Young's Modulus in ZnO Nanowires." Physical Review Letters **96**(7): 075505.

Chen, H. X., Zheng, M. S., Sun, H. Y. and Jia, Q. M. (2007). "Characterization and properties of sepiolite/polyurethane nanocomposites." Materials Science and Engineering a-Structural Materials Properties Microstructure and Processing **445**: 725-730.

Chen, W., Duan, L. and Zhu, D. Q. (2007). "Adsorption of polar and nonpolar organic chemicals to carbon nanotubes." Environmental Science & Technology **41**(24): 8295-8300.

Cheng, X. H., Xue, Y. J. and Xie, C. Y. (2002). "Effect of rare earths modification of glass fiber on friction and wear properties of PTFE composite." Journal of Inorganic Materials **17**(6): 1321-1326.

Chiellini, E., Cinelli, P., Fernandes, E. G., Kenawy, E.-R. and Lazzeri, A. (2001). Composite Materials Based on Gelatin and Fillers from Renewable Resources: Thermal and Mechanical Properties. Biorelated Polymers: Sustainable Polymer Science and Technology. Chiellini, E., Gil, E., Braunegg, G., Buchert, J., Gatenholm, P. and van der Zee, M. New York, Kluwer Academic: 101-114.

Chivrac, F., Pollet, E., Schmutz, M. and Avérous, L. (2010). "Starch nano-biocomposites based on needle-like sepiolite clays." Carbohydrate Polymers **80**(1): 145-153.

Chua, C. K., Leong, K. F., Tan, K. H., Wiria, F. E. and Cheah, C. M. (2004). "Development of tissue scaffolds using selective laser sintering of polyvinyl alcohol/hydroxyapatite biocomposite for craniofacial and joint defects." Journal of Materials Science-Materials in Medicine **15**(10): 1113-1121.

Daniel, M.-C. and Astruc, D. (2003). "Gold Nanoparticles: Assembly, Supramolecular Chemistry, Quantum-Size-Related Properties, and Applications toward Biology, Catalysis, and Nanotechnology." Chemical Reviews **104**(1): 293-346.

Darder, M., Colilla, M. and Ruiz-Hitzky, E. (2003). "Biopolymer-clay nanocomposites based on chitosan intercalated in montmorillonite." Chemistry of Materials **15**(20): 3774-3780.

Darder, M., Colilla, M. and Ruiz-Hitzky, E. (2005). "Chitosan-clay nanocomposites: application as electrochemical sensors." Applied Clay Science **28**(1-4): 199-208.

Darder, M., Lopez-Blanco, M., Aranda, P., Aznar, A. J., Bravo, J. and Ruiz-Hitzky, E. (2006). "Microfibrous chitosan-sepiolite nanocomposites." Chemistry of Materials **18**(6): 1602-1610.

Darder, M., Ruiz, A. I., Aranda, P., Van Damme, H. and Ruiz-Hitzky, E. (2006). "Bio-nanohybrids based on layered inorganic solids: Gelatin nanocomposites." Current Nanoscience **2**(3): 231-241.

Davis, B. K., Weber, S. G. and Sylwester, A. P. (1990). "Electrochemical characterization of a microcellular carbon foam/epoxy composite electrode." Analytical Chemistry **62**(10): 1000-1003.

De La Casa-Lillo, M. A., Lamari-Darkrim, F., Cazorla-Amorós, D. and Linares-Solano, A. (2002). "Hydrogen storage in activated carbons and activated carbon fibers." Journal of Physical Chemistry B **106**(42): 10930-10934.

Demirkol, E. A. and Kalyon, D. M. (2007). "Batch and continuous processing of polymer layered organoclay nanocomposites." Journal of Applied Polymer Science **104**(3): 1391-1398.

Dresselhaus, M. S., Dresselhaus, G. and Jorio, A. (2004). "Unusual properties and structure of carbon nanotubes." Annual Review of Materials Research **34**: 247-278.

Dresselhaus, M. S., Dresselhaus, G., Saito, R. and Jorio, A. (2005). "Raman spectroscopy of carbon nanotubes." Physics Reports **409**(2): 47-99.

Dunlop, J. W. C. and Fratzl, P. (2010). "Biological Composites." Annual Review of Materials Research **40**(1): 1-24.

Duquesne, E., Moins, S., Alexandre, M. and Dubois, P. (2007). "How can nanohybrids enhance polyester/sepiolite nanocomposite properties?" Macromolecular Chemistry and Physics **208**(23): 2542-2550.

Faibish, R. S., Yoshida, W. and Cohen, Y. (2002). "Contact Angle Study on Polymer-Grafted Silicon Wafers." Journal of Colloid and Interface Science **256**(2): 341-350.

Fernandes, F. M., Araujo, R., Proenca, M. F., Silva, C. J. R. and Paiva, M. C. (2007). "Functionalization of carbon nanofibers by a Diels-Aider addition reaction." Journal of Nanoscience and Nanotechnology **7**(10): 3514-3518.

Fernandes, F. M., Castro, M., Carnicero, A., Ruiz-Hitzky, E. and Vazquez, L. (2011). "Multiscale mechanics of sepiolite nanofibres." in preparation.

Fernandes, F. M., Darder, M., Ruiz, A. I., Aranda, P. and Ruiz-Hitzky, E. (2011). Gelatine-based bio-nanocomposites. Nanocomposites with Biodegradable Polymers. Synthesis, Properties, and Future Perspectives Mittal, V. New York, Oxford University Press.

Fernandes, F. M., Manjubala, I. and Ruiz-Hitzky, E. (2010). "Gelatin renaturation, a new approach to filler role in bionanocomposites." Physical Chemistry Chemistry of Physics.

Fernandes, F. M., Manjubala, I. and Ruiz-Hitzky, E. (2011). "Gelatin renaturation, a new approach to filler role in bionanocomposites." Physical Chemistry Chemistry of Physics **13**(11): 4901-4910.

Fernandes, F. M., Ruiz, A. I., Darder, M., Aranda, P. and Ruiz-Hitzky, E. (2009). "Gelatin-clay bio-nanocomposites: structural and functional properties as advanced materials." Journal of Nanoscience and Nanotechnology **9**(1): 221-229.

Fernandez-Hernandez, M. N. and Ruiz-Hitzky, E. (1979). "Interactions of isocyanate and sepiolite." Clay Minerals **14**(4): 295-305.

Fernandez-Saavedra, R., Darder, M., Gomez-Aviles, A., Aranda, P. and Ruiz-Hitzky, E. (2008). "Polymer-clay nanocomposites as precursors of nanostructured carbon materials for electrochemical devices: Templating effect of clays." Journal of Nanoscience and Nanotechnology **8**(4): 1741-1750.

Ferrari, A. C. (2007). "Raman spectroscopy of graphene and graphite: Disorder, electron-phonon coupling, doping and nonadiabatic effects." Solid State Communications **143**(1-2): 47-57.

Feynman, R. (1960). "There is plenty of room at the bottom." Engineering & Science **23**: 22.

Fornes, T. D. and Paul, D. R. (2003). "Modeling properties of nylon 6/clay nanocomposites using composite theories." Polymer **44**(17): 4993-5013.

Franckel, R. B. and Mann, S. (1994). Biomineralization. Encyclopedia of Inorganic Chemistry. King, R. B. Chichester, John Wiley & Sons. **1:** 269-279.

Fratzl, P., Gupta, H. S., Paschalis, E. P. and Roschger, P. (2004). "Structure and mechanical quality of the collagen-mineral nano-composite in bone." Journal of Materials Chemistry **14**(14): 2115-2123.

Fratzl, P. and Weinkamer, R. (2007). "Nature's hierarchical materials." Progress in Materials Science **52**(8): 1263-1334.

Fukushima, Y., Okada, A., Kawasumi, M., Kurauchi, T. and Kamigaito, O. (1988). "Swelling behaviour of montmorillonite by poly-6-amide." Clay Minerals **23**(1): 27-34.

Furtado, C. A., Kim, U. J., Gutierrez, H. R., Pan, L., Dickey, E. C. and Eklund, P. C. (2004). "Debundling and Dissolution of Single-Walled Carbon Nanotubes in Amide Solvents." Journal of the American Chemical Society **126**(19): 6095-6105.

Galan, E. (1996). "Properties and applications of palygorskite-sepiolite clays." Clay Minerals **31**(4): 443-453.

Galán, E. and Singer, A., Eds. (1984). Palygorskite - Sepiolite Occurences, Genesis and Uses. Developments in sedimentology. Amsterdam, Elsevier.

Gallego, N. C. and Klett, J. W. (2003). "Carbon foams for thermal management." Carbon **41**(7): 1461-1466.

Gao, B., Chen, G. Z. and Li Puma, G. (2009). "Carbon nanotubes/titanium dioxide (CNTs/TiO2) nanocomposites prepared by conventional and novel surfactant wrapping sol-gel methods exhibiting enhanced

photocatalytic activity." Applied Catalysis B: Environmental **89**(3-4): 503-509.

Garg, A. and Sinnott, S. B. (1998). "Effect of chemical functionalization on the mechanical properties of carbon nanotubes." Chemical Physics Letters **295**(4): 273-278.

Georgakilas, V., Kordatos, K., Prato, M., Guldi, D. M., Holzinger, M. and Hirsch, A. (2002). "Organic Functionalization of Carbon Nanotubes." Journal of the American Chemical Society **124**(5): 760-761.

Gercek, H. (2007). "Poisson's ratio values for rocks." International Journal of Rock Mechanics and Mining Sciences **44**(1): 1-13.

Gere, J. M. and Timoshenko, S. P. (1998). Mecánica de Materiales. Mexico, Mexico, International Thomson Editores.

Gieseking, J. E. (1939). "The mechanism of cation exchange in the montmorillonite-beidellite-nontronite type of clay minerals." Soil Science **47**(1): 1-13.

Girifalco, L. A., Hodak, M. and Lee, R. S. (2000). "Carbon nanotubes, buckyballs, ropes, and a universal graphitic potential." Physical Review B **62**(19): 13104.

Gomez-Aviles, A., Darder, M., Aranda, P. and Ruiz-Hitzky, E. (2007). "Functionalized carbon-silicates from caramel-sepiolite nanocomposites." Angewandte Chemie-International Edition **46**(6): 923-925.

Gong, K., Zhang, M., Yan, Y., Su, L., Mao, L., Xiong, S. and Chen, Y. (2004). "Sol Gel-Derived Ceramic Carbon Nanotube Nanocomposite Electrodes: Tunable Electrode Dimension and Potential Electrochemical Applications." Analytical Chemistry **76**(21): 6500-6505.

Grossiord, N., Loos, J., Regev, O. and Koning, C. E. (2006). "Toolbox for dispersing carbon nanotubes into polymers to get conductive nanocomposites." Chemistry of Materials **18**(5): 1089-1099.

Habermüller, K., Mosbach, M. and Schuhmann, W. (2000). "Electron-transfer mechanisms in amperometric biosensors." Fresenius Journal of Analytical Chemistry **366**(6): 560-568.

Halpin, J. C. and Kardos, J. L. (1972). "Moduli of crystalline polymers employing composite theory." Journal of Applied Physics **43**(5): 2235-2241.

Halpin, J. C. and Kardos, J. L. (1976). "The Halpin-Tsai equations: A review." Polymer Engineering & Science **16**(5): 344-352.

Hammel, E., Tang, X., Trampert, M., Schmitt, T., Mauthner, K., Eder, A. and Pötschke, P. (2004). "Carbon nanofibers for composite applications." Carbon **42**(5-6): 1153-1158.

Hashin, Z. (1983). "Analysis of composite materials: a survey." Journal of Applied Mechanics-Transactions of the Asme **50**(3): 481-505.

Hatto, P. (2008). Nanotechnologies - Terminology and definitions for nano-objects - Nanoparticle, nanofibre and nanoplate. Geneva, Switzerland, International Organization for Standardization

Hendricks, S. B. (1941). "Base exchange of the clay mineral montmorillonite for organic cations and its dependence upon adsorption due to Van Der Waals forces." Journal of Physical Chemistry **45**(1): 65-81.

Hopcroft, M. A., Nix, W. D. and Kenny, T. W. (2010). "What is the Young's Modulus of Silicon?" Microelectromechanical Systems, Journal of **19**(2): 229-238.

Iijima, S. (1991). "Hellical microtubules of graphitic carbon." Nature **354**(6348): 56-58.

Istrate, O. M. and Chen, B. (2011). "Relative modulus-relative density relationships in low density polymer-clay nanocomposite foams." Soft Matter **7**(5): 1840-1848.

Jacobs, C. B., Peairs, M. J. and Venton, B. J. (2010). "Review: Carbon nanotube based electrochemical sensors for biomolecules." Analytica Chimica Acta **662**(2): 105-127.

Ji, B. H. and Gao, H. J. (2004). "Mechanical properties of nanostructure of biological materials." Journal of the Mechanics and Physics of Solids **52**(9): 1963-1990.

Jiang, L., Gao, L. and Sun, J. (2003). "Production of aqueous colloidal dispersions of carbon nanotubes." Journal of Colloid and Interface Science **260**(1): 89-94.

John, M. J. and Thomas, S. (2008). "Biofibres and biocomposites." Carbohydrate Polymers **71**(3): 343-364.

Johnson, K. L. (1985). Contact Mechanics. Cambridge, University Press.

Jones, T. R. (1983). "The properties and uses of clays which swell in organic solvents." Clay Minerals **18**(4): 399-410.

Jordan, J. W. (1949). "Organophilic Bentonites. I. Swelling in Organic Liquids." The Journal of Physical and Colloid Chemistry **53**(2): 294-306.

Kamrani, S., Hesabi, Z. R., Riedel, R. and Reihani, S. M. S. (2010). "Synthesis and Characterization of Al-SiC Nanocomposites Produced by Mechanical Milling and Sintering." Advanced Composite Materials **20**(1): 13-27.

Kara, M., Yuzer, H., Sabah, E. and Celik, M. S. (2003). "Adsorption of cobalt from aqueous solutions onto sepiolite." Water Research **37**(1): 224-232.

Kikuchi, M., Ikoma, T., Itoh, S., Matsumoto, H. N., Koyama, Y., Takakuda, K., Shinomiya, K. and Tanaka, J. (2004). "Biomimetic synthesis of bone-like nanocomposites using the self-organization mechanism of hydroxyapatite and collagen." Composites Science and Technology **64**(6): 819-825.

Kikuchi, M., Itoh, S., Ichinose, S., Shinomiya, K. and Tanaka, J. (2001). "Self-organization mechanism in a bone-like hydroxyapatite/collagen nanocomposite synthesized in vitro and its biological reaction in vivo." Biomaterials **22**(13): 1705-1711.

Kim, H. M., Kishimoto, K., Miyaji, F., Kokubo, T., Yao, T., Suetsugu, Y., Tanaka, J. and Nakamura, T. (1999). "Composition and structure of the apatite formed on PET substrates in SBF modified with various ionic activity products." Journal of Biomedical Materials Research **46**(2): 228-235.

Kittelson, D. B. (1998). "Engines and nanoparticles: a review." Journal of Aerosol Science **29**(5-6): 575-588.

Kobayashi, M., Chang, Y. S. and Oka, M. (2005). "A two year in vivo study of polyvinyl alcohol-hydrogel (PVA-H) artificial meniscus." Biomaterials **26**(16): 3243-3248.

Koenders, M. M. J. F., Yang, L., Wismans, R. G., van der Werf, K. O., Reinhardt, D. P., Daamen, W., Bennink, M. L., Dijkstra, P. J., van Kuppevelt, T. H. and Feijen, J. (2009). "Microscale mechanical properties of single elastic fibers: The role of fibrillin-microfibrils." Biomaterials **30**(13): 2425-2432.

Kojima, Y., Usuki, A., Kawasumi, M., Okada, A., Fukushima, Y., Kurauchi, T. and Kamigaito, O. (1993). "Mechanical properties of Nylon 6-clay hybrid." Journal of Materials Research **8**(5): 1185-1189.

Kong, L. J., Gao, Y., Lu, G. Y., Gong, Y. D., Zhao, N. M. and Zhang, X. F. (2006). "A study on the bioactivity of chitosan/nano-hydroxyapatite composite scaffolds for bone tissue engineering." European Polymer Journal **42**(12): 3171-3179.

Krause, B., Petzold, G., Pegel, S. and Pötschke, P. (2009). "Correlation of carbon nanotube dispersability in aqueous surfactant solutions and polymers." Carbon **47**(3): 602-612.

Krimm, S. (1983). "Vibrational analysis of conformation in peptides, polypeptides, and proteins." Biopolymers **22**(1): 217-225.

Kuang, M., Wang, D., Gao, M., Hartmann, J. r. and MÃ¶hwald, H. (2005). "A Bio-inspired Route to Fabricate Submicrometer-Sized Particles with Unusual Shapes - Mineralization of Calcium Carbonate within Hydrogel Spheres." Chemistry of Materials **17**(3): 656-660.

Kuang, W. X., Facey, G. A., Detellier, C., Casal, B., Serratosa, J. M. and Ruiz-Hitzky, E. (2003). "Nanostructured hybrid materials formed by sequestration of pyridine molecules in the tunnels of sepiolite." Chemistry of Materials **15**(26): 4956-4967.

Kukovecz, A., Smajda, R., Oze, M., Schaefer, B., Haspel, H., Konya, Z. and Kiricsi, I. (2008). "Multiwall carbon nanotube films surface-doped with electroceramics for sensor applications." Physica Status Solidi B-Basic Solid State Physics **245**(10): 2331-2334.

Kunz, D. A. (2009). "Deformation measurements on thin clay tactoids." Small **5**(16): 1816-1820.

Kupke, M., Wentzel, H.-P. and Schulte, K. (1998). "Electrically conductive glass fibre reinforced epoxy resin." Materials Research Innovations **2**(3): 164-169.

Lakes, R. S., Lee, T., Bersie, A. and Wang, Y. C. (2001). "Extreme damping in composite materials with negative-stiffness inclusions." Nature **410**(6828): 565-567.

Lan, Y. F. and Lin, J. J. (2009). "Observation of Carbon Nanotube and Clay Micellelike Microstructures with Dual Dispersion Property." Journal of Physical Chemistry A **113**(30): 8654-8659.

Larsen, E. C. and Walton, J. H. (1940). "Activated Carbon as a Catalyst in Certain Oxidation-Reduction Reactions." The Journal of Physical Chemistry **44**(1): 70-85.

Laura, D. M., Keskkula, H., Barlow, J. W. and Paul, D. R. (2000). "Effect of glass fiber and maleated ethylene-propylene rubber content on tensile and impact properties of Nylon 6." Polymer **41**(19): 7165-7174.

LeBaron, P. C., Wang, Z. and Pinnavaia, T. J. (1999). "Polymer-layered silicate nanocomposites: an overview." Applied Clay Science **15**(1-2): 11-29.

Lee, J. U., Huh, J., Kim, K. H., Park, C. and Jo, W. H. (2007). "Aqueous suspension of carbon nanotubes via non-covalent functionalization with oligothiophene-terminated poly(ethylene glycol)." Carbon **45**(5): 1051-1057.

Lehn, J. (1988). "Supramolecular chemistry - Scope and perspectives molecules, supermolecules and molecular devices." Angewandte Chemie. International edition in English **27**(1): 89-112.

Leroux, F. and Besse, J. P. (2001). "Polymer interleaved layered double hydroxide: A new emerging class of nanocomposites." Chemistry of Materials **13**(10): 3507-3515.

Leroy, V., Pitura, K. M., Scanlon, M. G. and Page, J. H. (2010). "The complex shear modulus of dough over a wide frequency range." Journal of Non-Newtonian Fluid Mechanics **165**(9-10): 475-478.

Li, R. H. (1998). "Materials for immunoisolated cell transplantation." Advanced Drug Delivery Reviews **33**(1-2): 87-109.

Li, S., Guo, Q., Song, Y., Liu, Z., Shi, J., Liu, L. and Yan, X. (2007). "Carbon foams with high compressive strength derived from mesophase pitch treated by toluene extraction." Carbon **45**(14): 2843-2845.

Li, X. D., Chang, W. C., Chao, Y. J., Wang, R. Z. and Chang, M. (2004). "Nanoscale structural and mechanical characterization of a natural nanocomposite material: The shell of red abalone." Nano Letters **4**(4): 613-617.

Li, Y. and Wong, C. P. (2006). "Recent advances of conductive adhesives as a lead-free alternative in electronic packaging: Materials, processing, reliability and applications." Materials Science and Engineering: R: Reports **51**(1-3): 1-35.

Li, Z., Pan, Z. and Dai, S. (2004). "Nitrogen adsorption characterization of aligned multiwalled carbon nanotubes and their acid modification." Journal of Colloid and Interface Science **277**(1): 35-42.

Lin, J. H., He, C. Y., Zhang, L. J. and Zhang, S. S. (2009). "Sensitive amperometric immunosensor for alpha-fetoprotein based on carbon nanotube/gold nanoparticle doped chitosan film." Analytical Biochemistry **384**(1): 130-135.

Liu, L., Barber, A., Nuriel, S. and Wagner, H. (2005). "Mechanical Properties of Functionalized Single-Walled Carbon-Nanotube/Poly(vinyl alcohol) Nanocomposites." Advanced Functional Materials **15**(6): 975-980.

Liz-Marzán, L. M. (2005). "Tailoring Surface Plasmons through the Morphology and Assembly of Metal Nanoparticles." Langmuir **22**(1): 32-41.

Longin, P. Y., Verdier, C. and Piau, M. (1998). "Dynamic shear rheology of high molecular weight polydimethylsiloxanes: comparison of rheometry and ultrasound." Journal of Non-Newtonian Fluid Mechanics **76**(1-3): 213-232.

Lowenstam, H. A. (1981). "Minerals Formed by Organisms." Science **211**(4487): 1126-1131.

Lowenstam, H. A. and Weiner, S. (1989). On biomineralization. New York, Oxford University Press.

Lozano-Castelló, D., Lillo-Ródenas, M. A., Cazorla-Amorós, D. and Linares-Solano, A. (2001). "Preparation of activated carbons from Spanish anthracite - I. Activation by KOH." Carbon **39**(5): 741-749.

MacDonald, R. A., Laurenzi, B. F., Viswanathan, G., Ajayan, P. M. and Stegemann, J. P. (2005). "Collagen–carbon nanotube composite materials as scaffolds in tissue engineering." Journal of Biomedical Materials Research Part A **74A**(3): 489-496.

MacEwan, D. M. C. (1946). "Halloysite-organic complexes." Nature **157**(3980): 159-160.

Mallick, P. K. (1993). Fiber-reinforced composites: materials, manufacturing, and design. New York, Marcel Dekker Inc.

Manchado, M. A. L., Valentini, L., Biagiotti, J. and Kenny, J. M. (2005). "Thermal and mechanical properties of single-walled carbon nanotubes-polypropylene composites prepared by melt processing." Carbon **43**(7): 1499-1505.

Mann, S. (1986a). "Biomineralization - A new branch in bioinorganic chemistry." Chemie in Unserer Zeit **20**(3): 69-76.

Mann, S. (1986b). "Oon the nature of boudary organized biomineralizatio (BOB)." Journal of Inorganic Biochemistry **28**(2-3): 363-371.

Mann, S., Hannington, J. P. and Williams, R. J. P. (1986). "Phospholipid-vesicles as a model system for biomineralization." Nature **324**(6097): 565-567.

Maqueda, C., Partal, P., Villaverde, J. and Perez-Rodriguez, J. L. (2009). "Characterization of sepiolite-gel-based formulations for controlled release of pesticides." Applied Clay Science **46**(3): 289-295.

Marchand, A. and Zanchetta, J. V. (1966). "Proprietes electroniques d'un carbone dope a l'azote." Carbon **3**(4): 483-491.

Mazo, M. A., Manevitch, L. I., Gusarova, E. B., Berlin, A. A., Balabaev, N. K. and Rutledge, G. C. (2008). "Molecular Dynamics Simulation of Thermomechanical Properties of Montmorillonite Crystal. II. Hydrated Montmorillonite Crystal." The Journal of Physical Chemistry C **112**(44): 17056-17062.

McKeown, D. A., Post, J. E. and Etz, E. S. (2002). "Vibrational analysis of palygorskite and sepiolite." Clays and Clay Minerals **50**(5): 667-680.

McNeil, L. E. and Grimsditch, M. (1993). "Elastic moduli of muscovite mica." Journal of Physics-Condensed Matter **5**(11): 1681-1690.

Meng, C. Z., Liu, C. H. and Fan, S. S. (2009). "Flexible carbon nanotube/polyaniline paper-like films and their enhanced electrochemical properties." Electrochemistry Communications **11**(1): 186-189.

Merkoci, A. (2006). "Carbon nanotubes in analytical sciences." Microchimica Acta **152**(3-4): 157-174.

Mileiko, S. T., Rudnev, A. M. and Gelachov, M. V. (1995). "Carbon-fibre/titanium silicide interphase/titanium-matrix composites: Fabrication, structure and mechanical properties." Composites Science and Technology **55**(3): 255-260.

Miller, R. E. and Shenoy, V. B. (2000). "Size-dependent elastic properties of nanosized structural elements." Nanotechnology **11**(3): 139-147.

Mizutani, K. and Iwatsu, T. (1980). "Temperature dependence of tensile properties of composites consisting of carbon fiber tow in thermosetting polymers." Journal of Applied Polymer Science **25**(11): 2649-2652.

Monser, L. and Adhoum, N. (2002). "Modified activated carbon for the removal of copper, zinc, chromium and cyanide from wastewater." Separation and Purification Technology **26**(2-3): 137-146.

Monthioux, M. and Kuznetsov, V. L. (2006). "Who should be given the credit for the discovery of carbon nanotubes?" Carbon **44**(9): 1621-1623.

Montminy, M. D., Tannenbaum, A. R. and Macosko, C. W. (2004). "The 3D structure of real polymer foams." Journal of Colloid and Interface Science **280**(1): 202-211.

Moore, V. C., Strano, M. S., Haroz, E. H., Hauge, R. H., Smalley, R. E., Schmidt, J. and Talmon, Y. (2003). "Individually Suspended Single-Walled Carbon Nanotubes in Various Surfactants." Nano Letters **3**(10): 1379-1382.

Mori, T. and Tanaka, K. (1973). "Average stress in matrix and average elastic energy of materials with misfitting inclusions." Acta Metallurgica **21**(5): 571-574.

Moropoulou, A., Bakolas, A. and Anagnostopoulou, S. (2005). "Composite materials in ancient structures." Cement and Concrete Composites **27**(2): 295-300.

Movasaghi, Z., Rehman, S. and Rehman, I. U. (2008). "Fourier transform infrared (FTIR) spectroscopy of biological tissues." Applied Spectroscopy Reviews **43**(2): 134-179.

Muyonga, J. H., Cole, C. G. B. and Duodu, K. G. (2004). "Fourier transform infrared (FTIR) spectroscopic study of acid soluble collagen and gelatin

from skins and bones of young and adult Nile perch (Lates niloticus)." Food Chemistry **86**(3): 325-332.

Nabeta, M. and Sano, M. (2005). "Nanotube Foam Prepared by Gelatin Gel as a Template." Langmuir **21**(5): 1706-1708.

Nohales, A., Solar, L., Porcar, I., Vallo, C. I. and Gomez, C. M. (2006). "Morphology, flexural, and thermal properties of sepiolite modified epoxy resins with different curing agents." European Polymer Journal **42**(11): 3093-3101.

Nuttelman, C. R., Henry, S. M. and Anseth, K. S. (2002). "Synthesis and characterization of photocrosslinkable, degradable poly(vinyl alcohol)-based tissue engineering scaffolds." Biomaterials **23**(17): 3617-3626.

Oliver, W. C. and Pharr, G. M. (2004). "Measurement of hardness and elastic modulus by instrumented indentation: Advances in understanding and refinements to methodology." Journal of Materials Research **19**(1): 3-20.

Olmo, N., Lizarbe, M. A. and Gavilanes, J. G. (1987). "Biocompatibility and degradability of sepiolite-collagen complex." Biomaterials **8**(1): 67-69.

Oyane, A., Uchida, M., Yokoyama, Y., Choong, C., Triffitt, J. and Ito, A. (2005). "Simple surface modification of poly(epsilon-caprolactone) to induce its apatite-forming ability." Journal of Biomedical Materials Research Part A **75A**(1): 138-145.

Ozcan, A., Oncu, E. M. and Ozcan, A. S. (2006). "Adsorption of Acid Blue 193 from aqueous solutions onto DEDMA-sepiolite." Journal of Hazardous Materials **129**(1-3): 244-252.

Ozin, G. A. and Arsenault, A. C. (2005). Nanochemistry A Chemical Approach to Nanomaterials. Cambridge, UK, RSC Publishing.

Parkinson, D. (1951). "The reinforcement of rubber by carbon black." British Journal of Applied Physics **2**(10): 273.

Payne, K. J. and Veis, A. (1988). "Fourier transform ir spectroscopy of collagen and gelatin solutions: Deconvolution of the amide I band for conformational studies." Biopolymers **27**(11): 1749-1760.

Peigney, A., Laurent, C., Flahaut, E., Bacsa, R. R. and Rousset, A. (2001). "Specific surface area of carbon nanotubes and bundles of carbon nanotubes." Carbon **39**(4): 507-514.

Peng, B., Wu, H., Bao, W. T., Guo, S. Y., Chen, Y., Huang, H., Chen, H. Y., Lai, S. Y. and Jow, J. (2011). "Effects of ultrasound on the morphology and properties of propylene-based plastomer/nanosilica composites." Polymer Journal **43**(1): 91-96.

Penicaud, A., Poulin, P., Derre, A., Anglaret, E. and Petit, P. (2005). "Spontaneous dissolution of a single-wall carbon nanotube salt." Journal of the American Chemical Society **127**(1): 8-9.

Perez-Castells, R., Alvarez, A., Gavilanes, J., Lizarbe, M. A., Martinez Del Pozo, A., Olmo, N. and Santaren, J. (1985). Adsorption of collagen by sepiolite. Proceedings of the International Clay Conference, Denver, The Clay Minerals Society.

Perraki, T. and Orfanoudaki, A. (2008). "Study of raw and thermally treated sepiolite from the Mantoudi area, Euboea, Greece." Journal of Thermal Analysis and Calorimetry **91**(2): 589-593.

Pinnavaia, T. J. and Beall, G., Eds. (2000). Polymer - Clay Nanocomposites. New York, John Willey & Sons.

Pokhmurs'kyi, V., Piddubnyi, V., Zin, I., Lavryshyn, B., Bilyi, L. and Voloshyn, M. (2005). "Influence of Surface-Modified Conducting Fillers on the Properties of Epoxy Coatings." Materials Science **41**(4): 495-500.

Post, J. E., Bish, D. L. and Heaney, P. J. (2007). "Synchrotron powder X-ray diffraction study of the structure and dehydration behavior of sepiolite." American Mineralogist **92**(1): 91-97.

Pötschke, P., Andres, T., Villmow, T., Pegel, S., Brünig, H., Kobashi, K., Fischer, D. and Häussler, L. (2010). "Liquid sensing properties of fibres prepared by melt spinning from poly(lactic acid) containing multi-walled carbon nanotubes." Composites Science and Technology **70**(2): 343-349.

Qian, D., Dickey, E. C., Andrews, R. and Rantell, T. (2000). "Load transfer and deformation mechanisms in carbon nanotube-polystyrene composites." Applied Physics Letters **76**(20): 2868-2870.

Qian, L. and Zhang, H. (2010). "Controlled freezing and freeze drying: a versatile route for porous and micro-/nano-structured materials." Journal of Chemical Technology & Biotechnology **86**(2): 172-184.

Qureshi, A., Kang, W. P., Davidson, J. L. and Gurbuz, Y. (2009). "Review on carbon-derived, solid-state, micro and nano sensors for electrochemical sensing applications." Diamond and Related Materials **18**(12): 1401-1420.

Ramachandran, G. N. and Kartha, G. (1954). "Structure of Collagen." Nature **174**(4423): 269-270.

Ramachandran, G. N. and Sasisekharan, V. (1965). "Refinement of the structure of collagen." Biochimica et Biophysica Acta (BBA) - Biophysics including Photosynthesis **109**(1): 314-316.

Rastogi, R., Kaushal, R., Tripathi, S. K., Sharma, A. L., Kaur, I. and Bharadwaj, L. M. (2008). "Comparative study of carbon nanotube dispersion using surfactants." Journal of Colloid and Interface Science **328**(2): 421-428.

Rho, J.-Y., Kuhn-Spearing, L. and Zioupos, P. (1998). "Mechanical properties and the hierarchical structure of bone." Medical Engineering & Physics **20**(2): 92-102.

Rinzler, A. G., Liu, J., Dai, H., Nikolaev, P., Huffman, C. B., Rodríguez-Macías, F. J., Boul, P. J., Lu, A. H., Heymann, D., Colbert, D. T., Lee, R. S., Fischer, J. E., Rao, A. M., Eklund, P. C. and Smalley, R. E. (1998). "Large-scale purification of single-wall carbon nanotubes: process, product, and characterization." Applied Physics A: Materials Science & Processing **67**(1): 29-37.

Ruiz-Hitzky, E. (1988). "Genie Cristallin Dans Les Solides Organo-Mineraux." Molecular Crystals and Liquid Crystals Incorporating Nonlinear Optics **161**: 433-452.

Ruiz-Hitzky, E. (1993). "Conducting polymers intercalated in layered solids." Advanced Materials **5**(5): 334-340.

Ruiz-Hitzky, E. (2001). "Molecular access to intracrystalline tunnels of sepiolite." Journal of Materials Chemistry **11**(1): 86-91.

Ruiz-Hitzky, E. (2004). Organic-Inorganic materials: from intercalation chemistry to devices. Functional Hybrid Materials. Gómez-Romero, P. and Sanchez, C. Weinheim, Wiley-VCH.

Ruiz-Hitzky, E. and Aranda, P. (1990). "Polymer-salt intercalation complexes in layer silicates." Advanced Materials **2**(11): 545-547.

Ruiz-Hitzky, E., Aranda, P. and Darder, M. (2008). Bionanocomposites. Kirk-Othmer Enciclopedia of Chemical Technology. Hoboken, NJ, John Wiley & Sons: 1-28.

Ruiz-Hitzky, E., Aranda, P., Darder, M., Fernandes, F. M. and Matos, R. (2009). Espumas rigidas de tipo composite basadas en biopolímeros combinados con arcillas fibrosas y su método de preparación. Spain, CSIC.

Ruiz-Hitzky, E., Aranda, P., Darder, M., Fernandes, F. M. and Matos, R. (2010). Espumas rigidas de tipo composite basadas en biopolímeros combinados con arcillas fibrosas y su método de preparación. **WO 2010081918**. Spain, CSIC.

Ruiz-Hitzky, E., Aranda, P., Darder, M. and Ogawa, M. (2011). "Hybrid and biohybrid silicate based materials: molecular vs. block-assembling bottom-up processes." Chemical Society Reviews **40**(2): 801-828.

Ruiz-Hitzky, E. and Casal, B. (1985). "Epoxide rearrangements on mineral and silica-alumina surfaces." Journal of Catalysis **92**(2): 291-295.

Ruiz-Hitzky, E., Darder, M. and Aranda, P. (2005). "Functional biopolymer nanocomposites based on layered solids." Journal of Materials Chemistry **15**(35-36): 3650-3662.

Ruiz-Hitzky, E., Darder, M. and Aranda, P. (2007). An introduction to Bio-nanohybrid materials. Bio-inorganic Hybrid Nanomaterials, Strategies, Syntheses, Characterization and Applications. Ruiz-Hitzky, E., Ariga, K. and Lvov, Y. M. Weinheim, Wiley-VCH: 1-32.

Ruiz-Hitzky, E., Darder, M. and Aranda, P. (2010). Progress in bionanocomposite materials. Annual Review of Nanoresearch. Cao, G., Zhang, Q. and Brinker, C. J. Singapore, World Scientific Publishing. **3:** 149-189.

Ruiz-Hitzky, E., Darder, M., Aranda, P., del Burgo, M. A. M. and del Real, G. (2009). "Bionanocomposites as New Carriers for Influenza Vaccines." Advanced Materials **21**(41): 4167-+.

Ruiz-Hitzky, E. and Fripiat, J. J. (1976). "Organomineral derivatives obtained by reacting organochlorosilanes with surface of silicates in organic solvents." Clays and Clay Minerals **24**(1): 25-30.

Ruiz-Hitzky, E. and Van Meerbeek, A. (2006). Clay mineral- and organoclay-polymer nanocomposite. Handbook of clay science. Bergaya, F., Theng, B. K. G. and Lagaly, G. Amsterdam, Elsevier.

Salvetat-Delmotte, J.-P. and Rubio, A. (2002). "Mechanical properties of carbon nanotubes: a fiber digest for beginners." Carbon **40**(10): 1729-1734.

Salvetat, J. P., Bonard, J. M., Thomson, N. H., Kulik, A. J., Forro, L., Benoit, W. and Zuppiroli, L. (1999). "Mechanical properties of carbon nanotubes." Applied Physics a-Materials Science & Processing **69**(3): 255-260.

Sanchez, C., Arribart, H. and Guille, M. (2005). "Biomimetism and bioinspiration as tools for the design of innovative materials and systems." Nature Materials **4**(4): 277-288.

Santaren, J., Sanz, J. and Ruiz-Hitzky, E. (1990). "Structural fluorine in sepiolite." Clays and Clay Minerals **38**(1): 63-68.

Sauter, C., Emin, M. A., Schuchmann, H. P. and Tavman, S. (2008). "Influence of hydrostatic pressure and sound amplitude on the ultrasound induced dispersion and de-agglomeration of nanoparticles." Ultrasonics Sonochemistry **15**(4): 517-523.

Schaefer, D. W. and Justice, R. S. (2007). "How Nano Are Nanocomposites?" Macromolecules **40**(24): 8501-8517.

Seo, W. J., Sung, Y. T., Kim, S. B., Lee, Y. B., Choe, K. H., Choe, S. H., Sung, J. Y. and Kim, W. N. (2006). "Effects of ultrasound on the synthesis and properties of polyurethane foam/clay nanocomposites." Journal of Applied Polymer Science **102**(4): 3764-3773.

Serna, C., Ahlrichs, J. L. and Serratosa, J. M. (1975). "Folding in sepiolite crystals." Clays and Clay Minerals **23**(6): 452-457.

Shahidi, F. and Han, X. Q. (1993). "Encapsulation of food ingredients." Critical Reviews in Food Science and Nutrition **33**(6): 501-547.

Shvartzman-Cohen, R., Levi-Kalisman, Y., Nativ-Roth, E. and Yerushalmi-Rozen, R. (2004). "Generic Approach for Dispersing Single-Walled Carbon Nanotubes: The Strength of a Weak Interaction." Langmuir **20**(15): 6085-6088.

Shvartzman-Cohen, R., Nativ-Roth, E., Baskaran, E., Levi-Kalisman, Y., Szleifer, I. and Yerushalmi-Rozen, R. (2004). "Selective Dispersion of

Single-Walled Carbon Nanotubes in the Presence of Polymers: the Role of Molecular and Colloidal Length Scales." Journal of the American Chemical Society **126**(45): 14850-14857.

Sing, K. S. W., Everett, D. H., Haul, R. A. W., Moscou, L., Pierotti, R. A., Rouquerol, J. and Siemieniewska, T. (1985). "Reporting physisorption data for gas/solid systems with special reference to the determination of surface area and porosity." Pure and Applied Chemistry **57**(4): 603-619.

Sinha Ray, S. and Bousmina, M. (2005). "Biodegradable polymers and their layered silicate nanocomposites: In greening the 21st century materials world." Progress in Materials Science **50**(8): 962-1079.

Smajda, R., Gyori, Z., Sapi, A., Veres, M., Oszko, A., Kis-Csitari, J., Kukovecz, A., Konya, Z. and Kiricsi, I. (2007). "Spectroscopic studies on self-supporting multi-wall carbon nanotube based composite films for sensor applications." Journal of Molecular Structure **834**: 471-476.

Smajda, R., Kukovecz, A., Hopp, B., Mohl, M., Konya, Z. and Kiricsi, I. (2007). "Morphology and N-2 permeability of multi-wall carbon nanotube - Teflon membranes." Journal of Nanoscience and Nanotechnology **7**(4-5): 1604-1610.

Staab, G. H. (1999). Laminar composites. Boston, Butterwoth Heinemann.

Sturcová, A., Davies, G. R. and Eichhorn, S. J. (2005). "Elastic Modulus and Stress-Transfer Properties of Tunicate Cellulose Whiskers." Biomacromolecules **6**(2): 1055-1061.

Su, J. X., Wang, Q., Su, R., Wang, K., Zhang, Q. and Fu, Q. (2008). "Enhanced compatibilization and orientation of polyvinyl Alcohol/Gelatin composite fibers using carbon nanotubes." Journal of Applied Polymer Science **107**(6): 4070-4075.

Su, X. W. and Cui, F. Z. (1999). "Hierarchical structure of ivory: from nanometer to centimeter." Materials Science and Engineering: C **7**(1): 19-29.

Sun, J., Gao, L. and Li, W. (2002). "Colloidal Processing of Carbon Nanotube/Alumina Composites." Chemistry of Materials **14**(12): 5169-5172.

Sun, Z., Nicolosi, V., Rickard, D., Bergin, S. D., Aherne, D. and Coleman, J. N. (2008). "Quantitative evaluation of surfactant-stabilized single-walled

carbon nanotubes: Dispersion quality and its correlation with zeta potential." Journal of Physical Chemistry C **112**(29): 10692-10699.

Suslick, K. S. and Price, G. J. (1999). "Applications of ultrasound to materials chemistry." Annual Review of Materials Science **29**: 295-326.

Szleifer, I. and Yerushalmi-Rozen, R. (2005). "Polymers and carbon nanotubes--dimensionality, interactions and nanotechnology." Polymer **46**(19): 7803-7818.

Tagmatarchis, N. and Prato, M. (2004). "Functionalization of carbon nanotubes via 1,3-dipolar cycloadditions." Journal of Materials Chemistry **14**(4): 437-439.

Takahashi, T., Tsunoda, K., Yajima, H. and Ishii, T. (2002). "Isolation of single-wall carbon nanotube bundles through gelatin wrapping and unwrapping processes." Chemistry Letters(7): 690-691.

Talibudeen, O. (1950). "Intralemmelar adorption of protein monolayers on pure montmorillonoid clays." Nature **166**(4214): 236-236.

Talibudeen, O. (1955). "Complex formation between montmorillonoid clays and amino-acids and proteins." Transactions of the Faraday Society **51**(4): 582-590.

Tang, X. L. and Pikal, M. J. (2004). "Design of freeze-drying processes for pharmaceuticals: Practical advice." Pharmaceutical Research **21**(2): 191-200.

Tasis, D., Tagmatarchis, N., Bianco, A. and Prato, M. (2006). "Chemistry of Carbon Nanotubes." Chem. Rev. **106**(3): 1105-1136.

Theng, B. K. G. (1974). The chemistry of clay-organic reactions. New York, Wiley.

Theng, B. K. G. (1979). Formation and Properties of Clay-Polymer Complexes. New York, Elsevier.

Tombacz, E. and Szekeres, M. (2006). "Surface charge heterogeneity of kaolinite in aqueous suspension in comparison with montmorillonite." Applied Clay Science **34**(1-4): 105-124.

Usuki, A., Kojima, Y., Kawasumi, M., Okada, A., Fukushima, Y., Kurauchi, T. and Kamigaito, O. (1993). "Synthesis of Nylon 6-clay hybrid." Journal of Materials Research **8**(5): 1179-1184.

Van Meerbeek, A. and Ruiz-Hitzky, E. (1979). "Mechanism of the grafting of organosilanes on mineral surfaces. 2 Secondary reaction during the grafting of akenylchlorosilanes." Colloid and Polymer Science **257**(2): 178-181.

Veis, A. (1964). The macromolecular chemistry of gelatin. New York, Academic Press.

Veitch, N. C. (2004). "Horseradish peroxidase: a modern view of a classic enzyme." Phytochemistry **65**(3): 249-259.

Wakayama, H., Hall, S. R. and Mann, S. (2005). "Fabrication of CaCO3-biopolymer thin films using supercritical carbon dioxide." Journal of Materials Chemistry **15**(11): 1134-1136.

Wan, Y. Z., Wang, Y. L., Luo, H. L., Cheng, G. X. and Yao, K. D. (2000). "Carbon fiber-reinforced gelatin composites. I. Preparation and mechanical properties." Journal of Applied Polymer Science **75**(8): 987-993.

Wang, R. Z., Suo, Z., Evans, A. G., Yao, N. and Aksay, I. A. (2001). "Deformation mechanisms in nacre." Journal of Materials Research **16**(9): 2485-2493.

Wang, S.-F., Shen, L., Zhang, W.-D. and Tong, Y.-J. (2005). "Preparation and Mechanical Properties of Chitosan/Carbon Nanotubes Composites." Biomacromolecules **6**(6): 3067-3072.

Wang, W. (2000). "Lyophilization and development of solid protein pharmaceuticals." International Journal of Pharmaceutics **203**(1-2): 1-60.

Wang, X., Zhong, J., Wang, Y. and Yu, M. (2006). "A study of the properties of carbon foam reinforced by clay." Carbon **44**(8): 1560-1564.

Wang, Z., Liang, Z., Wang, B., Zhang, C. and Kramer, L. (2004). "Processing and property investigation of single-walled carbon nanotube (SWNT) buckypaper/epoxy resin matrix nanocomposites." Composites Part A: Applied Science and Manufacturing **35**(10): 1225-1232.

Wang, Z. M., Nakajima, H., Manias, E. and Chung, T. C. (2003). "Exfoliated PP/Clay Nanocomposites Using Ammonium-Terminated PP as the Organic Modification for Montmorillonite." Macromolecules **36**(24): 8919-8922.

Wani, I. A., Ganguly, A., Ahmed, J. and Ahmad, T. (2010). "Silver nanoparticles: Ultrasonic wave assisted synthesis, optical characterization and surface area studies." Materials Letters **65**(3): 520-522.

Wei, H., Ma, N., Shi, F., Wang, Z. and Zhang, X. (2007). "Artificial nacre by alternating preparation of layer-by-layer polymer films and CaCO3 strata." Chemistry of materials **19**(8): 1974-1978.

Whitesides, G. M., Mathias, J. P. and Seto, C. T. (1991). "Molecular Self-Assembly and Nanochemistry: A Chemical Strategy for the Synthesis of Nanostructures." Science **254**(5036): 1312-1319.

Xie, S. B., Zhang, S. M., Wang, F. S., Yang, M. S., Seguela, R. and Lefebvre, J. M. (2007). "Preparation, structure and thermomechanical properties of nylon-6 nanocomposites with lamella-type and fiber-type sepiolite." Composites Science and Technology **67**(11-12): 2334-2341.

Xu, A. W., Ma, Y. R. and Colfen, H. (2007). "Biomimetic mineralization." Journal of Materials Chemistry **17**(5): 415-449.

Xu, J. Z., Zhu, J. J., Wu, Q., Hu, Z. and Chen, H. Y. (2003). "An Amperometric Biosensor Based on the Coimmobilization of Horseradish Peroxidase and Methylene Blue on a Carbon Nanotubes Modified Electrode." Electroanalysis **15**(3): 219-224.

Yang, H. X. and Ghose, S. (1995). "High temperature single-crystal X.ray diffraction studies of ortho-proto phase transition in enstatite, $Mg_2Si_2O_6$ at 1360 K." Physics and Chemistry of Minerals **22**(5): 300-310.

Yang, K. and Xing, B. (2010). "Adsorption of Organic Compounds by Carbon Nanomaterials in Aqueous Phase: Polanyi Theory and Its Application." Chemical Reviews **110**(10): 5989-6008.

Yano, K., Usuki, A., Okada, A., Kurauchi, T. and Kamigaito, O. (1993). "Synthesis and properties of polyimide–clay hybrid." Journal of Polymer Science Part A: Polymer Chemistry **31**(10): 2493-2498.

Yerushalmi-Rozen, R. and Szleifer, I. (2006). "Utilizing polymers for shaping the interfacial behavior of carbon nanotubes." Soft Matter **2**(1): 24-28.

Yu, J., Grossiord, N., Koning, C. E. and Loos, J. (2007). "Controlling the dispersion of multi-wall carbon nanotubes in aqueous surfactant solution." Carbon **45**(3): 618-623.

Zhang, G., Wei, Z. and Ferrell, R. E. (2009a). "Elastic modulus and hardness of muscovite and rectorite determined by nanoindentation." Applied Clay Science **43**(2): 271-281.

Zhang, G., Wei, Z. and Ferrell, R. E. (2009b). "Reply to the Comment on "Elastic modulus and hardness of muscovite and rectorite determined by nanoindentation" by G. Zhang, Z. Wei and R.E. Ferrell [Applied Clay Science 43 (2009) 271-281]." Applied Clay Science **46**(4): 429-432.

Zhang, G. Q., Zheng, J. P., Liang, R., Zhang, C., Wang, B., Hendrickson, M. and Plichta, E. J. (2010). "Lithium-Air Batteries Using SWNT/CNF Buckypapers as Air Electrodes." Journal of the Electrochemical Society **157**(8): A953-A956.

Zhang, J., Mine, M., Zhu, D. and Matsuo, M. (2009). "Electrical and dielectric behaviors and their origins in the three-dimensional polyvinyl alcohol/MWCNT composites with low percolation threshold." Carbon **47**(5): 1311-1320.

Zhang, R. and Ma, P. X. (1999). "Porous poly(L-lactic acid)/apatite composites created by biomimetic process." Journal of Biomedical Materials Research **45**(4): 285-293.

Zhang, R. Y. and Ma, P. X. (2004). "Biomimetic polymer/apatite composite scaffolds for mineralized tissue engineering." Macromolecular Bioscience **4**(2): 100-111.

Zheng, M., Jagota, A., Semke, E. D., Diner, B. A., McLean, R. S., Lustig, S. R., Richardson, R. E. and Tassi, N. G. (2003). "DNA-assisted dispersion and separation of carbon nanotubes." Nat Mater **2**(5): 338-342.

Zheng, X., Zhang, B., Zhang, J., Xue, Y. and He, J. (2003). "Flow properties and morphology of PC/LCP blends affected by the addition of glass fiber and resulted mutual influences." International Polymer Processing **18**(1): 3-11.

Zheng, Y. and Zheng, Y. (2006). "Study on sepiolite-reinforced polymeric nanocomposites." Journal of Applied Polymer Science **99**(5): 2163-2166.

Zhu, W., Ku, D., Zheng, J. P., Liang, Z., Wang, B., Zhang, C., Walsh, S., Au, G. and Plichta, E. J. (2010). "Buckypaper-based catalytic electrodes for

improving platinum utilization and PEMFC's performance." Electrochimica Acta **55**(7): 2555-2560.

Zhuang, H., Zheng, J., Gao, H. and De Yao, K. (2007). "In vitro biodegradation and biocompatibility of gelatin/montmorillonite-chitosan intercalated nanocomposite." Journal of Materials Science: Materials in Medicine **18**(5): 951-957.